The elastic anisotropy and mechanical behaviour of the Whitby Mudstone

The elastic anisotropy and mechanical behaviour of the Whitby Mudstone

Proefschrift

Ter verkrijging van de graad van doctor
aan de Technische Universiteit Delft,
op gezag van Rector Magnificus, prof. dr. ir. T.H.J.J. van der Hagen,
voorzitter van het College van promoties,
in het openbaar te verdedigen op
Vrijdag 13 Maart 2020 om 12:30 uur

door

Lisanne Aurora Natascha Rosalie DOUMA

Master in de aardwetenschappen, Universiteit Utrecht, Nederland
Geboren te Groningen, Nederland

Dit proefschrift is goedgekeurd door de promotor en copromotor.

Samenstelling promotiecommissie bestaat uit:

Rector Magnificus,	voorzitter
Prof. dr. ir. C. P. A. Wapenaar,	Technische Universiteit Delft, promotor
dr. A. Barnhoorn,	Technische Universiteit Delft, copromotor

onafhankelijke leden:

Prof. dr. G. Bertotti,	Technische Universiteit Delft
Prof. dr. D. F. Bruhn,	Technische Universiteit Delft; GFZ
Prof. dr. A. Ferrari,	École Polytechnique Fédérale de Lausanne
dr. S. J. T. Hangx,	Universiteit Utrecht

overig lid:

dr. D. N. Dewhurst,	CSIRO Energy

Keywords: mudstones, elastic anisotropy, mechanical behaviour, ultrasonic velocities, triaxial deformation tests

Cover illustration: photograph of the outcropping Whitby Mudstone Formation

ISBN 978-94-6366-249-9

Printed in the Netherlands by Gildeprint, Enschede.

'If you act like you've only got fifteen minutes, it will take all day. Act like you've got all day, it will take fifteen minutes.'

Monty Roberts

Summary

Mudstones play an important role in hydrocarbon exploration and production, carbon capture and storage, and nuclear waste disposal. The high concentration of clay minerals contribute to the high intrinsic anisotropy (e.g., velocity, strength, permeability, and resistivity changes with direction) of mudstones. This high anisotropy complicates, among other things, seismic interpretation for hydrocarbon exploration and production, as well as predictions on the mechanical behaviour of these clay-rich rocks. Mudstones are also characterized by a low-permeability matrix, which makes it difficult for fluids to flow through the rock. This impermeable character of mudstones makes them a potential natural seal for long-term CO_2 storage and a potential host rock for nuclear waste disposal. For hydrocarbon production, open fractures are needed to enhance the productivity of oil and gas reservoirs, whereas the presence of such fractures can result in unwanted leakage of CO_2 or nuclear waste in the subsurface. Fracture formation depends on, among other things, the mechanical properties of the mudstone. It is thus important to understand the elastic anisotropy and mechanical properties of mudstones for successful hydrocarbon exploration and production, and to safely store CO_2 and radioactive waste in the subsurface. Although mudstones are important in the energy sector, the understanding of their elastic anisotropy and deformation behaviour under various physical conditions is limited, due to their complex character and the lack of laboratory experiments performed on well-preserved samples.

In this thesis, the elastic anisotropy and deformation behaviour of mudstones and their evolution due to changes in water saturation are analysed in detail, with the main focus on hydrocarbon exploration and production in the Netherlands. Mudstone samples originating from the Whitby Mudstone Formation were studied as an analogue for the Dutch Posidonia Shale, the main shale-gas prospect in the Netherlands. The mineralogy and petrophysical properties were characterized using various techniques, such as x-ray fluorescence, x-ray diffraction, x-ray computed tomography, and nuclear magnetic resonance. The elastic anisotropy and mechanical behaviour of the Whitby Mudstone were obtained by performing deformation experiments and ultrasonic measurements in the laboratory at a range of temperature and pressure conditions on mudstone core plugs with varying water content.

To avoid confusion, in this thesis a clear and unambiguous definition of the term *shale* is provided, which closely follows the definition used in the petroleum industry (chapter 2). Here, the term *shale* is used in a generic way, describing all fine-grained, laminated, and low-permeability sedimentary rocks, having a clay content between 20% and 90% and a small pore size. However, there is a major difference in mechanical behaviour, elastic anisotropy, and core handling and preservation between shales, depending on their clay content (mineralogy) (chapter 3). Therefore, *shales* are divided into *mudstones* and *gas shales*. A mudstone is a shale consisting of clay minerals (>40%), whereas a gas shale contains less clay minerals (>20% but <40%). The Whitby Mudstone is classified as a *mudstone*.

The Whitby Mudstone has an extremely high elastic anisotropy (velocity anisotropy) compared to other sedimentary rocks, due to its high clay content and the presence of lamination (chapter 4). This anisotropy increases further with decreasing water content. There are three competing mechanisms which play a key role in the anisotropy increase due to dehydration. This includes (1) density contrast in the pore space, (2) formation of bedding-parallel dehydration fractures, and (3) frame stiffening. Increasing the mean effective stress leads to a decrease in the elastic anisotropy parameters ε and γ (Thomsen's parameters), because of the closure of defects, such as natural and dehydration fractures, and the formation of stress-induced fractures. The high elastic anisotropy of the Whitby Mudstone should be considered for geophysical interpretation for hydrocarbon exploration and production.

In terms of mechanical behaviour, the relatively stiff Whitby Mudstone behaves in a macroscopically brittle manner (chapter 5). The stiffness and rock strength, as well as the deformation mechanisms (contraction/dilatancy) acting on the microscopic scale (grain scale/microstructure), are highly dependent on the saturation state. Loss of pore water leads to a significant increase in cohesive strength and stiffness due to increasing capillary forces. Dilative shear fractures are formed in the partially-saturated Whitby Mudstone, suggesting that cataclastic deformation mechanisms are operating. Contractive shear fractures are formed when the Whitby Mudstone is fully saturated with brine, suggesting that ductile deformation mechanisms are also operating under these conditions. Dilative shear fractures are most favourable for hydrocarbon production, since they are likely to enhance the permeability of the rock.

Mudstones can be buried a few kilometres in the subsurface, where pressure and temperature increases with depth. These parameters affect the elastic properties and mechanical behaviour of sedimentary rocks (chapters 5, 6, 7). At higher pressures, the Whitby Mudstone is mechanically stronger and stiffer, whereas the elastic anisotropy decreases, due to the closure of imperfections (e.g., bedding-parallel fractures). Localized shear fractures can be dilative or contractive, depending on both the degree of saturation and pressure conditions (chapter 5). Dilative shear fractures are likely to enhance the permeability, and can form fluid-flow pathways when efficiently connected. The applied pressure in combination with the rock strength determines whether such flow paths will form in layered sequences in the subsurface (chapter 7).

An increase in temperature enhances the elastic anisotropy of the Whitby Mudstone when partially saturated (chapter 6). Two key mechanisms are responsible for the velocity changes, including (1) a change in pore fluid properties, and (2) grain contact stiffening. This latter property results in an increase in rock strength and cohesion at high temperatures, where the Whitby Mudstone behaves in a macroscopically brittle manner when partially-saturated. It is likely that the elastic and mechanical behaviour of the Whitby Mudstone are different when fully saturated at subsurface conditions.

The findings presented in this thesis improve the understanding of the elastic anisotropy and mechanical behaviour of mudstones. The degree of saturation should always be mentioned when performing laboratory experiments on mudstones. The elastic anisotropy and mechanical behaviour obtained from partially-saturated mudstones should be treated with care when extrapolating them to *in situ* fully saturated conditions. Additionally, the lab-derived properties cannot be used directly as input parameters for mechanical and geophysical models at the reservoir scale without upscaling.

For shales containing gas, it is recommended to obtain the elastic and mechanical properties of mudstones saturated with formation brine and gas, instead of air and gas, at subsurface conditions. In addition, it is essential to perform additional work on brine-saturated Whitby Mudstones at high temperatures, to better predict their elastic and mechanical behaviour at reservoir conditions, improving hydrocarbon exploration and production in the Netherlands.

Samenvatting

Kleistenen spelen een belangrijke rol bij het winnen van olie en gas, maar ook bij de opslag van koolstofdioxide (CO_2) en radioactief afval in de ondergrond. Doordat kleistenen voor het grootste gedeelte uit kleimineralen bestaan, zijn de golfsnelheden niet in alle richtingen gelijk. Deze elastische anisotropie maakt het moeilijker de seismiek te interpreteren, die wordt gebruikt in de olie- en gasindustrie om de ondergrond weer te geven. Ook zijn kleistenen laag permeabel, waardoor vloeistoffen er nauwelijks doorheen kunnen stromen. Open breuken zorgen voor een hogere productiviteit van olie- en gasreservoirs, maar vormen ook een verhoogd risico voor lekkage van CO_2 of radioactief afval in de ondergrond. Of een breuk ontstaat in de ondergrond, hangt onder andere af van de mechanische eigenschappen van het gesteente. Het is dus van belang de elastische- en mechanische gesteente-eigenschappen van kleistenen te begrijpen, om succesvol olie en gas te kunnen exploiteren en op een veilige manier CO_2 en radioactief afval te kunnen opslaan. Het is niet eenvoudig deze eigenschappen te begrijpen. Dit kleirijke gesteente droogt namelijk gemakkelijk uit en er zijn weinig experimenten uitgevoerd met kleistenen uit de ondergrond, die op de juiste manier bewaard zijn gebleven om uitdroging te voorkomen.

In dit proefschrift worden de elastische- en mechanische eigenschappen van kleistenen bestudeerd, waarbij de focus ligt op olie- en gaswinning in Nederland. Ook wordt er gekeken hoe uitdroging deze gesteente-eigenschappen beïnvloedt. De kleistenen die worden gebruikt in dit proefschrift, zijn afkomstig van een geologische formatie uit Engeland, genaamd de *Whitby Mudstone Formation*. Deze kleistenen zijn analoog aan de Posidonia schalie; een potentieel schaliegashoudend gesteente dat in de Nederlandse ondergrond gevonden kan worden. De mineraalsamenstelling en gesteente-eigenschappen van de *Whitby Mudstone* zijn geanalyseerd met behulp van verschillende technieken, zoals röntgenfluorescentie (XRF), röntgencomputertomografie (X-ray CT) en kernmagnetische resonantie (NMR). Om de mechanische eigenschappen en het mechanische gedrag van de *Whitby Mudstone* te onderzoeken, zijn vervormingsexperimenten uitgevoerd in het laboratorium. Tijdens deze experimenten zijn de omstandigheden in de aardkorst zo goed mogelijk nagebootst, door de omgevingsdrukken en de temperatuur te verhogen. Onder deze omstandigheden zijn ook de snelheden van ultrasone geluidsgolven gemeten om de elastische eigenschappen van dit gesteente te kunnen bepalen.

Om verwarring te voorkomen in dit proefschrift zijn de termen *schalie*, *kleisteen* en *gasschalie* als volgt gedefinieerd: een schalie is een sedimentair gesteente dat wordt gekenmerkt door een fijne korrelgrootte, aanwezigheid van gelaagdheid en een lage permeabiliteit. Het bevat 20% - 90% aan kleimineralen en heeft kleine poriën. Schalies kunnen worden onderverdeeld in kleistenen en gasschalies. Een kleisteen is een schalie die voor meer dan 40% uit kleimineralen bestaat en waarvan de gesteente-eigenschappen veranderen wanneer het in aanraking komt met een vloeistof of lucht. Een gasschalie bestaat uit minder kleimineralen dan een kleisteen (>20% maar <40%). De *Whitby Mudstone* is geclassificeerd als kleisteen.

De resultaten in dit proefschrift laten zien dat de *Whitby Mudstone* erg anisotroop is vanwege de grote hoeveelheid kleimineralen en de gelaagdheid in deze kleisteen. Uitdroging zorgt ervoor dat de elastische anisotropie van de *Whitby Mudstone* groter wordt. Er zijn drie aspecten die de toenemende anisotropie bij uitdroging veroorzaken:

- veranderingen in porievloeistof;
- het ontstaan van horizontale scheuren;
- het stijver worden van het gesteente.

Er moet rekening gehouden worden met de hoge elastische anisotropie van de *Whitby Mudstone* tijdens de geofysische interpretatie van de seismiek voor olie- en gaswinning.

Wat betreft mechanische gesteente-eigenschappen, is de *Whitby Mudstone* een stijf en bros gesteente. De mate van stijfheid, de sterkte en de aard van vervorming zijn afhankelijk van de hoeveelheid water in deze kleisteen. Uitdroging van de *Whitby Mudstone* zorgt ervoor dat het gesteente sterker en stijver wordt. Dat komt door toenemende capillaire krachten. De vervormingsbreuken die zijn ontstaan in het laboratorium, laten vloeistoffen door wanneer de *Whitby Mudstone* niet volledig gesatureerd is. Wanneer deze kleisteen gesatureerd is, kan er geen vloeistof doorheen stromen. Dit is ongunstig voor olie- en gaswinning.

Kleistenen bevinden zich op een paar kilometer diepte in de ondergrond. Hoe dieper in de grond, hoe hoger de druk en temperatuur van de omgeving. Deze parameters beïnvloeden de elastische- en mechanische gesteente-eigenschappen van kleistenen. Bij hogere omgevingsdrukken wordt de gesatureerde *Whitby Mudstone* mechanisch stijver en sterker, maar minder anisotroop. Oneffenheden, zoals kleine breuken, gaan onder een hoge omgevingsdruk dicht, waardoor de elastische anisotropie afneemt. Onder lage drukken zijn de in het laboratorium gecreëerde vervormingsbreuken open. Ook die breuken sluiten bij hogere omgevingsdrukken. Hogere temperaturen veroorzaken een hogere anisotropie bij de onvolledig gesatureerde *Whitby Mudstone*. Dit komt doordat de eigenschappen van de porievloeistof veranderen en doordat het contact tussen de korrels sterker wordt. Dit laatste zorgt ervoor dat de sterkte en de cohesie van de Whitby Mudstone toeneemt bij hogere temperaturen. Het is aannemelijk dat de Whitby Mudstone ander elastisch en mechanisch gedrag vertoont, wanneer het volledig gesatureerd is en zich daadwerkelijk in de ondergrond bevindt.

De bevindingen in dit proefschrift helpen om het elastische en mechanische gedrag van kleistenen beter te begrijpen. Bij het uitvoeren van laboratoriumexperimenten met kleistenen, moet de mate van verzadiging altijd genoemd worden. De elastische- en mechanische eigenschappen van onvolledig gesatureerde kleistenen, zijn niet te vergelijken met de gesteente-eigenschappen van gesatureerde kleistenen op diepte. De waardes die zijn verkregen door het uitvoeren van laboratoriumexperimenten, kunnen niet direct gebruikt worden voor mechanische- en geofysische modellen. Dit komt doordat de experimenten niet op werkelijke schaalgrootte worden uitgevoerd.

Vervolgonderzoek moet uitwijzen wat het effect is van gas op het elastische- en mechanische gedrag van schalies. In poriën van schalies in de ondergrond zit namelijk natuurlijk gas opgesloten. Ook moet worden gekeken naar hoe de volledig gesatureerde *Whitby Mudstone* zich gedraagt bij hogere temperaturen, om zo beter het elastische- en mechanische gedrag te kunnen bepalen in de ondergrond. Dit zal bijdragen aan de olie- en gasontdekkingen en de winning hiervan in Nederland.

Contents

1

Introduction

1.1 Rationale

Mudstones make up a large part of the sedimentary rocks in the world [e.g., *Garrels and Mackenzie*, 1969]. These clay-rich rocks are characterized by a tight matrix, making them relatively impermeable with respect to fluid flow unless natural fractures develop [*Best and Katsube*, 1995; *Horsrud et al.*, 1998; *Aplin and Macquaker*, 2011]. This makes a mudstone an important natural seal for conventional petroleum reservoirs, as it is responsible for trapping large volumes of hydrocarbons [*Dewhurst et al.*, 2011], as well as for geo-sequestration projects, such as long-term CO_2 storage in the subsurface [*Busch et al.*, 2008; *Dewhurst et al.*, 2019]. In addition, their low permeability matrix (Nano-Darcy) makes mudstones potential host rocks for nuclear waste disposal [*Bossart et al.*, 2002]. Mudstones containing sufficient organic material can also generate oil and gas when sufficiently heated and, under the right conditions, act as an, so called, unconventional reservoir of natural oil or gas. Although the low-permeability matrix is favoured for hydrocarbon trapping and storage of CO_2 or radioactive waste in the subsurface, it complicates production from unconventional hydrocarbon reservoirs.

For successful hydrocarbon production from unconventional reservoirs, open fractures are needed to create a source for connectivity, allowing hydrocarbons to flow [*Newhouse*, 1942; *Ferrill et al.*, 2017]. Such fractures improve the hydrocarbon production from mudstone reservoirs significantly if they are effectively connected within the reservoir or within high-permeability layers. In contrast, when fractures do not stay in the target zone and propagate through layer boundaries, unwanted leakage pathways are created due to the loss of seal integrity.

Another property complicating production from mudstone reservoirs is their high clay content, making them highly anisotropic (e.g., velocity, strength, permeability, and resistivity changes with direction) [e.g., *Vernik and Liu*, 1997; *Dewhurst and Siggins*, 2006]. Layering of lithologies and the presence of fractures enhance the anisotropy of mudstones even further [*Hudson*, 1981; *Vernik and Nur*, 1992; *Vernik and Liu*, 1997; *Sayers*, 2013]. The elastic anisotropy (velocity anisotropy) is known to cause significant problems for geophysical interpretation, such as depth conversion for sweet spot mapping in seismic exploration, fluid identification, or monitoring subsurface reservoirs during production.

The mechanical behaviour and elastic anisotropy of mudstones are dependent on a number of factors, including their depositional environment, mineralogy, the presence of organic matter, and compaction [e.g., *Vernik and Liu*, 1997; *Dewhurst et al.*, 1998]. The deposition process of mudstones is rarely constant [*Trabucho-Alexandre*, 2015], resulting in highly-laminated successions with significant variation and a complex mineralogy on various scales. This heterogeneity tends to result in notable dissimilarities in mechanical and elastic properties throughout the mudstone formation [e.g., *Ghadeer and Macquaker*, 2012; *Douma et al.*, 2017], complicating predictions of the deformation behaviour and elastic anisotropy of mudstones [*Passey et al.*, 2010].

Understanding the elastic anisotropy and deformation behaviour of mudstones, their causes and magnitude are critical components of hydrocarbon exploration and production workflows [*Ewy et al.*, 2010; *Dewhurst et al.*, 2011].

Although mudstones have a primary economic importance, the understanding of their deformation behaviour and elastic anisotropy under various physical conditions is very limited. The difficulties in understanding these properties are mainly due to (1) the complex character of a mudstone, and (2) the lack of laboratory experiments performed on well-preserved samples. Mudstones are rarely recovered from the subsurface due to the costs of acquisition, and even when they are, often no precautions are taken to preserve them in their original state during storage [*Dewhurst et al.*, 2008].

Realistic mechanical properties and elastic anisotropy measurements of clay-rich rocks could only be obtained in the laboratory if the rocks are preserved immediately after recovery and if the pore pressure is measured throughout the sample [*Ewy*, 2018]. Poor preservation leads to a loss of *in situ* pore fluids which can alter the rock properties, no matter whether the clay-rich rock is soft, weak and ductile, or hard, strong and brittle [*Dewhurst et al.*, 2019]. In addition, dehydration can result in cracking, porosity reduction, and shrinkage of the core plugs [*Montes et al.*, 2004; *Romera et al.*, 2011; *Ferrari et al.*, 2014], making the mudstones unsuitable for mechanical and anisotropy testing [*Ewy*, 2015].

A majority of the published laboratory studies report experiments with no pore pressure control and/or on unsaturated (unpreserved) clay-rich rocks, without stating the degree of saturation, if known at all [e.g., *Sone and Zoback*, 2013; *Zhubayev et al.*, 2016; *Jin et al.*, 2018]. Only a few studies [e.g., *Dewhurst and Siggins*, 2006; *Delle Piane et al.*, 2011; *Sarout et al.*, 2014; *Ewy*, 2018; *Giger et al.*, 2018] performed experiments on well-preserved and saturated mudstones to get insight into their elastic anisotropy and deformation behaviour. The mechanical and anisotropy results obtained in the laboratory from unpreserved mudstone do not represent the *in situ* conditions of the sediments, resulting in ambiguities in the elastic anisotropy and deformation behaviour of mudstones.

1.2 Whitby Mudstone Formation: an analogue for the Dutch Posidonia Shale Formation

[1] During the Early Jurassic, the Neotethyan shelf was located near the tropic of Cancer. Present-day Europe was on the extensive Laurussian continental shelf, which opened towards the southeast into the deep Tethyan Ocean [*Song et al.*, 2015]. This shallow shelf area represented the northwestern European seaway, connecting the arctic sea and the Neo-Thethys. The global climate and ocean currents, in com-

---

[1] This section is modified from *Douma et al.* [2017, 2019a,b]

bination with the divers topographical feature on the shelf area lead to restriction of the water circulation across the shallow shelf sea, resulting in organic matter-rich Lower Toarcian shales widely distributed in northwestern Europe [*Schwark and Frimmel*, 2004; *Trabucho-Alexandre et al.*, 2012; *Song et al.*, 2015]. The present-day distribution of these Early-Jurassic shales spans from central to northwestern Europe, comprising the surface and subsurface of the Netherlands (West and Central Netherlands Basin; Broad Fourteens Basin, locally named Posidonia Shale), United Kingdom (Yorkshire Basin, locally named Whitby Mudstone), Germany (Lower Saxony Basin and Southwest German Basin, locally named Posidonienschiefer), and France (Paris Basin, locally named Schistes Carton) [*Littke et al.*, 1991; *Hesselbo et al.*, 2000] (Figure 1.1).

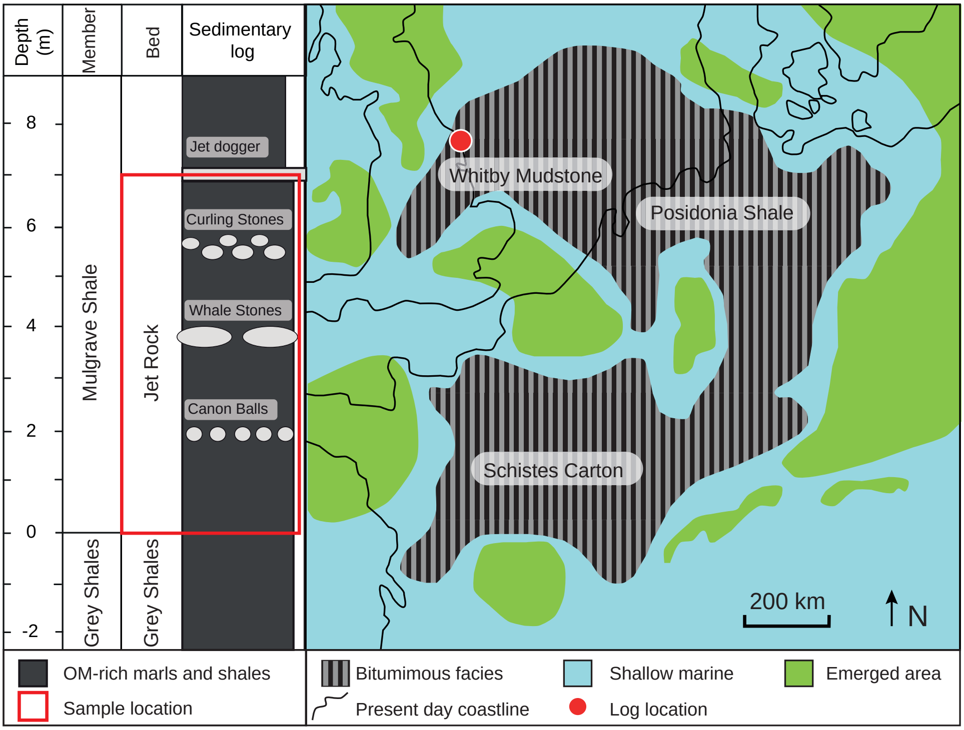

Figure 1.1: *Left: the mudstone samples tested in this thesis were collected from the base of the Mulgrave Shale Member (Jet Rock Bed) in the Whitby Mudstone Formation (WMF). The stratigraphic log is modified after Hesselbo et al. [2000]; Houben et al. [2016a]. Right: the present day distribution of the Early Jurassic WMF, spanning from central to northwest Europe, comprising the (sub)surface of the UK (WMF), the Netherlands (PSF), Germany (Posidonienschiefer), and France (Schistes Carton). Modified after Douma et al. [2017]; Frimmel et al. [2004].*

The Dutch Posidonia Shale Formation (PSF) is the main shale-gas prospect in the Netherlands [*Herber and Jager*, 2010]. It is a proven oil source rock for conventional reservoirs and considered as a potential source rock for unconventional reservoirs in northwest Europe [*Herber and Jager*, 2010]. The PSF is relatively constant in thickness (30 m average) [*Zijp et al.*, 2015], and has uniform lithological characteristics across the basins [*Houben et al.*, 2016b]. The Dutch PSF does not outcrop in the Netherlands. Current data available on the PSF only includes (vintage) well logs from around 100 wells and well-preserved samples from cored well intervals of the Dutch PSF are lacking [*Zijp et al.*, 2015]. Therefore, the time and depositional equivalent Whitby Mudstone Formation (WMF) outcropping in the United Kingdom (UK) is used as an analogue for the Dutch PSF.

The WMF belongs to the Lias Group (199.6 – 175.6 Ma) of the East-English Cleveland Basin (also known as Yorkshire Basin), and comprises 105 m of mudstone of Lower to Late Toarcian Age (Lower Jurassic) [*Powell*, 2010]. The Cleveland Basin formed part of a system of shallow epicontinental seas and small extensional tectonic basins, linked via the Sole Pit Basin (half-graben) to the North Sea Basin. During the Late Triassic, marine sedimentation was initiated and a succession of marine siliciclastic mudstones accumulated during the Early Jurassic. The Cleveland Basin was affected by a number of extensional faults and strike-slip fault complexes, which roughly define the present-day outcrop [*Powell*, 2010]. Petrophysical studies show that the maximum burial depth of the mudstones in the Cleveland Basin is estimated at 4 km [*Kemp et al.*, 2005], where the top of the Lower Jurassic (Toarcian) does not exceed 2.5 km [*Pye*, 1985].

The WMF comprises three members: the Grey Shale Member, Mulgrave Shale Member (formerly Jet Rock Member), and Alum Shale Member [*Powell*, 2010]. The Mulgrave Shale Member is deposited in anoxic bottom conditions and is the lateral-equivalent of the Dutch PSF [e.g., *Littke et al.*, 1991; *Powell*, 2010; *Ghadeer and Macquaker*, 2012]. This member is very similar to the Dutch PSF with respect to age, overall thickness, depositional environment (paleowater depth 20 – 100 m), TOC distribution, and mineralogy. The Mulgrave Shale Member consists of fissile, bituminous, dark-grey mudstones with abundant ammonites [*Powell*, 2010; *Houben et al.*, 2016b]. This member is relatively clay rich, essentially composed of sheet silicates (50 – 70%, interlayered illite/smective, illite, and kaolinite) (Houben et al., 2016b), and is enriched in organic matter (average TOC 6%; type II kerogen) [*Song et al.*, 2015; *Zijp et al.*, 2015], often interlayered within the matrix [*Houben et al.*, 2016a]. The Mulgrave Shale comprises the Jet Rock Bed and Bituminous Shale Bed (Figure 1.1). The shales from the Jet Rock Bed are rich in organic matter and approach the oil window maturity (vitrinite reflectance of 0.61-0.74%) [*Song et al.*, 2015]. In this thesis, laboratory experiments are performed on mudstone samples originating from the lower base of the Mulgrave Shale Member (Jet Rock Unit) in the outcropping WMF (Figure 1.1).

1.3 Scope of the thesis

In this thesis, the elastic anisotropy and deformation behaviour of mudstones and their evolution due to changes in water saturation are analysed in detail, with the main focus on hydrocarbon exploration and production in the Netherlands. Deformation experiments were performed in the Geoscience and Engineering Laboratory at *Delft University of Technology* (Delft, the Netherlands) and at the Geomechanics and Geophysics Laboratory at *CSIRO* (Perth, Australia), on mudstone core plugs originating from the outcropping WMF. The results obtained through the laboratory experiments provide insight into the elastic anisotropy and mechanical behaviour of the WMF and their evolution due to changes in water saturation. The findings raise awareness about the importance of preserving clay-rich rocks and carrying out their testing adequately to minimize the risk of reporting ambiguous laboratory results in the future. In addition, the results could help to understand the deformation behaviour of the Whitby Mudstone and improve geophysical interpretation for hydrocarbon exploration and production in the Netherlands.

1.4 Thesis outline

This thesis starts by proposing a clear and unambiguous definition of the term *mudstone* in chapter 2. This is needed, since the term *mudstone* is used inconsistently in the literature.

Chapter 3 introduces the Whitby Mudstone Formation, focussing on its heterogeneities in mineralogy, rock-physical and rock-mechanical properties at an outcrop scale. As heterogeneities are scale dependent, existing trends as reported in the literature obtained from a wide range of shales originating from different basins may not be applicable on all scales. This chapter discusses the validation of existing trends on various scales between heterogeneities in mineralogy and petrophysical properties, and rock-mechanical and rock-physical properties of mudstones. The results in this chapter are obtained from dry mudstone samples.

For further characterization of the Whitby Mudstone, the elastic anisotropy of this clay-rich formation is presented in chapter 4. This chapter focusses mainly on how the elastic anisotropy of the Whitby Mudstone is affected by the degree of water saturation by using P-wave and S-wave velocities at various ray paths and assuming a vertical transversely isotropic medium (VTI). The classical method is applied to obtain Thomsen's anisotropy parameters (ε, γ, δ).

To get a better insight into the deformation behaviour of the Whitby Mudstone, the mechanical properties and fracture behaviour of this mudstone are discussed in detail in chapter 5. The effect of water saturation on the deformation behaviour of the Whitby Mudstone is emphasized in this chapter.

Chapter 6 discusses the impact of temperature on the elastic anisotropy and mechanical behaviour of the partially-saturated Whitby Mudstone. The temperature in the subsurface increases with depth. Since mudstones are buried at a few kilometres depth, the effect of temperature on the elastic anisotropy and mechanical properties needs to be considered for better subsurface predictions. Mudstone core plugs with a water saturation of 58% are used in this chapter. The elastic anisotropy is determined using a P-wave inversion algorithm recently published by *Kovalyshen et al.* [2017], using only P-wave velocities along multiple ray paths and assuming a transversely isotropic (TI) medium.

Chapter 7 discusses the effect of the variation in rock strength in finely-layered rocks on the fracture propagation and arrests within the succession. The experimental results presented in this chapter are not performed on the laminated Whitby Mudstone core plugs due to its complex character and time consuming nature of laboratory tests on this low-permeability rock. Instead, various silica-rich rocks with different strengths where used. The results assist substantially in predicting fluid flow pathways in layered reservoirs.

The last chapter (chapter 8) touches upon the findings of the previous chapters, discusses the relevance and limitations of the study, and provides an outlook of future work.

2

A definition of a mudstone

Abstract Mudstones are presented in the literature as the most abundant rock formations worldwide and play an important role in various industries. However, the term mudstone is used inconsistently in the literature and often mixed with shales, gas shales, or (tight) sandstones. The absence of a clear and unambiguous definition can lead to uncertainties and misinterpretation of published data, and complicates the communication between scientists. This chapter provides a definition of the term mudstone, to avoid confusion in this thesis. An overview is given of ambiguous definitions of mudstones and (gas) shales as reported in the literature, followed by a proposed definition, putting the Whitby Mudstone in context.

2.1 Introduction

‘*Mudstones dominate sedimentary basins*’ [*Dewhurst et al.*, 1998] and ‘*Shales are the dominant clastic component in sedimentary basins*’ [*Dewhurst and Siggins*, 2006] are statements often red in the literature on low-permeability, clay-bearing, laminated sedimentary rocks. It is physically not possible that mudstones as well as shales dominate the sedimentary basins. Therefore, it is likely that the authors of the above mentioned statements are referring to the same lithology, using different terms.

The above mentioned statements are just an example of the inconsistent use of the term *shale* and *mudstone*. The main problem is the diversity of definitions, if defined at all. Literature shows that a main source of ambiguity is the application of these terms, which are defined on either visual appearance (fissility/lamination) [*Grainger*, 1984], clay content (mineralogy) [*Horsrud et al.*, 1998], particle size [*Trabucho-Alexandre*, 2015], their role in the subsurface (e.g., reservoir rock or overburden), or a combination of them. For example, the term *shale* refers to laminated and fissile sedimentary rocks, whereas mudstones lack bedding plane fissility [*Grainger*, 1984]. *Horsrud et al.* [1998] uses the term *shale* as a sedimentary rock containing up to 30% clay minerals, whereas *Trabucho-Alexandre* [2015] states that a shale represents a sedimentary rock composed of predominantly muds particles ($>4\phi$ or <0.0625 mm). This latter definition is used by *Aplin and Macquaker* [2011] for mudstones suggesting that mud particles (<0.0625 mm) become mudstones as a result of physical and chemical changes driven by burial diagenesis.

Accurate identification of rock types is of fundamental importance in the field of geomechanics and rock physics. This holds especially for shales/mudstones, since these rocks have characteristics which make them difficult to handle correctly during rock-mechanical testing, due to their low permeability, clay content, and sensitivity to contacting fluids [*Horsrud*, 2001]. The usefulness of lithological names is diminished without a consistent set of criteria to classify the rock material [*Grainger*, 1984]. This chapter provides a definition of shale and mudstone as used in this thesis and puts the Whitby Mudstone in context, to avoid miscommunication and misinterpretation of the data presented in this thesis.

2.2 Mudstones, shales, gas shales: how are they defined?

The most common definition of shales is based on the presence of laminations and bedding-plane fissility, due to the orientation of clay particles parallel to the bedding planes [*Ingram*, 1953; *Grainger*, 1984; *Horsrud et al.*, 1998; *Dusseault*, 2004]. In contrast, mudstones lack the bedding-plane fissility [*Ingram*, 1953; *Horsrud et al.*, 1998; *Dusseault*, 2004]. Shales and mudstones are deposited in low energetic environments with a quiet water column, for example large lakes, on floods planes, or on the continental shelf in relatively deep, quiet water [*Dayal and Mani*, 2017]. Due to the slow deposition process, influx of different fine grained sediments, and mechanical diagenetic compaction processes, these layered (laminated) rocks are formed [*Haldar and Tisljar*, 2014]. *Lamination* has a descriptive definition with sedimentological implications [*McKee and Weir*, 1953; *Campbell*, 1967], whereas *fissility* is defined as a secondary property largely related to weathering [*Ingram*, 1953; *Trabucho-Alexandre*, 2015]. Classifying shales and mudstones in this restricted sense alone would suggest that '*there are no shales in the subsurface, only potential shales*' [*Weaver*, 1989]. Shales will then only exist in outcrops or core stores.

Another problem appears from the dual meaning of clay/mud, which can refer to grain size, but also to mineralogy. In addition, the thresholds for which grain-size range and mineral content belongs to a shale or a mudstone are ambiguous. Sedimentary rocks composed predominantly of silt-sized (1/16 – 1/256 mm) and clay-sized (<1/256 mm) particles [*Wentworth*, 1922] are classified as shales [*Boggs*, 2006; *Dayal and Mani*, 2017]. *Trabucho-Alexandre* [2015] uses another name, namely mud (>4ϕ or <1/16 mm), to describe the particle size comprising a shale, whereas *Aplin and Macquaker* [2011] uses the same criteria to describe mudstones.

Definitions for shales/mudstones are also based on the amount of clays (mineralogy). Clay minerals enhance the capillary suction, affect the elastic anisotropy and geomechanical properties. The amount of clay minerals which should be present in a shale is not something scientists agree on. A sedimentary rock is defined as a shale when the clay content is >15% [*Dusseault*, 2004], >25% [*Picard*, 1953; *Shaw and Weaver*, 1965], or >30% [*Horsrud et al.*, 1998; *Dusseault*, 2004]. More often, it is only mentioned that a shale contains clay minerals, without stating the percentage at all. Table 2.1 summarizes the different criteria found in the literature to describe mudstones, shales, and gas shales.

Table 2.1: *Mudstones, shales, and gas shales are defined based on [1], visual appearance (fissility, lamination), [2] particle size, [3] mineralogy or a combination of them. The criteria used to define these rocks is not always consistent.*

Existing definitions based on			
	1. Fissility	*2. Particle size*	*3. Mineralogy*
Mudstone	No bedding-plane fissility	- Mud size (<1/16 mm)	- Clay >40%
Shale	Bedding-plane fissility	- Silt and clay size (1/16 - 1/256 mm and <1/256 mm) - Mud size (<1/16 mm)	- Clay 15% - 90% - Clay >25% - Clay >30%
Gas shale			- Clay >20% but <40% - Quartz; carbonate

When plotting mineral content of different lithologies encompassed by the term *shale*, it is clear that a wide variety of clay content is accepted for shales (Figure 2.1). The variability in mineralogy between lithologies from different basins is large, as well as within the same formation. For example, some samples taken from the Bakken Formation have a clay content (sheet silicates) of only a few percent, whereas the Dutch Posidonia Shale consists up to ~75% of sheet silicates (mainly clays).

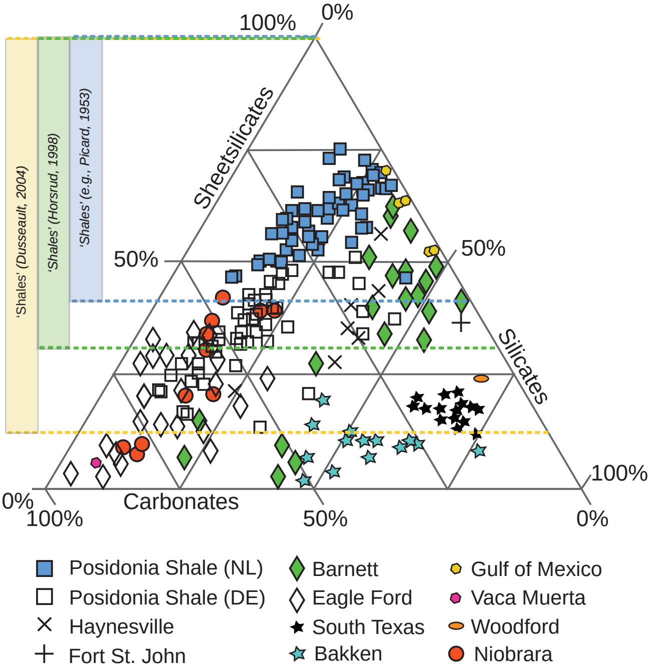

Figure 2.1: *Mineralogy composition plotted for different lithologies encompassed by the term shale [Ross and Bustin, 2009; Chesapeake, 2010; Chalmers et al., 2012; Kanitpanyacharoen et al., 2012; Sone and Zoback, 2013; Clarkson et al., 2013; Gasparik et al., 2014; Ghanizadeh et al., 2014; Rexer et al., 2014; Klaver et al., 2015; Rybacki et al., 2015; Houben et al., 2016b; Mathia et al., 2016]. These lithologies are not always actual shales, depending on which definition (based on mineral content) is used.*

A more general definition for a shale is used in the petroleum industry [*Dusseault*, 2004]. Here, shales are described as all clayey fine-grained rocks, where the clay content varies from 15% to >90% [*Dusseault*, 2004]. *Ewy* [2015] uses this general definition of a shale, but subdivides the term shale into (1) claystones, and (2) gas shales, due their differences in mineralogy and characteristics. A claystone is a clay-dominated mudstone lacking fissility, whereas the mineralogy of a gas shale is different and more complex [*Ewy*, 2015]. The clay content in a gas shale is often not higher than 40%, and often down around 20%, and significant amounts of carbonate or quartz are present [*Ewy*, 2015]. The differences in mineralogical content results in different mechanical properties, where gas shales are generally stronger and stiffer than claystones. Claystones have in general a relatively high water content, whereas gas shales have a naturally low water saturation, since gas generation has already driven the water saturation down [*Ewy*, 2015]. Both claystones and gas shales alter their water content when exposed to air. However, a claystone is more sensitive to shrinkage and swelling than a gas shale, due to the significant amount of clay minerals present. Clay minerals have a characteristic surface charge and high specific surface area, creating various problems [*Horsrud et al.*, 1998]. Loss of pore water in a claystone results in the formation of dehydration (shrinkage) cracks, making them unsuitable for mechanical testing [*Ewy*, 2015]. Contacting a claystone with brine (pore fluid) leads to water increase between clay layers, causing the claystone to swell.

2.3 A classification: where does the Whitby Mudstone belong?

■ 2.3.1 A definition of a mudstone

The definition of a mudstone, shale, or gas shale is often contradictory. However, when comparing the presented definitions, there are some rock characteristics which the definitions have in common. Whether it is called a mudstone, shale or gas shale, they are all laminated, fine grained, have a low matrix permeability, and contain clay minerals (we can argue about the percentage).

Since the definitions of a mudstone, shale, and gas shale have many things in common, I have chosen to closely follow the definition in the petroleum industry. In this thesis the term *shale* is used as a generic term, referring to *a fine-grained, laminated, low-permeability sedimentary rock, containing clay minerals ranging from ∼20% to >90% and having a small pore size.*

The small pore size in combination with the presence of clay minerals results in high capillary pressures, which also distinguishes shales from other lithologies. However, there is a major difference in mechanical behaviour, elastic anisotropy, and core handling and preparation between shales, depending on their clay content (mineralogy). Therefore, as suggested by *Ewy* [2015], shales can be divided into two groups, namely (1) mudstones (or claystones), and (2) gas shales (Figure 2.2). *Mudstones* are shales, having a relatively high clay content (>40%), consists mainly of clay and (very fine) silt sized particles [Wentworth scale; *Wentworth*, 1922], are very sensitive to contacting fluids, and are damaged when in contact with air. Mudstones obtained from the subsurface should be sealed immediately in a non-aqueous fluid after recovering them when using them for rock-mechanical testing. In this thesis, the term *claystone* has the same definition as *mudstone.* Gas shales have a lower clay content (>20% but <40%) with significant amount of quartz or carbonate present, they remain intact when in contact with air, and are often partially saturated when recovered from the subsurface.

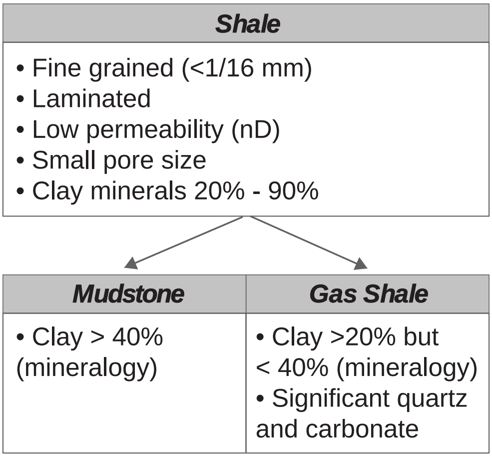

Figure 2.2: *There is a major difference in mechanical behaviour, elastic anisotropy, and core handling and preparation between shales, depending on their clay content (mineralogy). Therefore, in this thesis, shales are divided into mudstones and gas shales, based on their mineral content (clays).*

2.3.2 Putting the Whitby Mudstone in context

The Whitby Mudstone meets all the criteria to be classified as a shale: it is a laminated sedimentary rock, has a low permeability (10^{-23} – 10^{-18} m^2), a low porosity (0.3% – 7%, gas adsorption), a fine-grained matrix consisting of clay and silt sized grains [Wentworth scale; *Wentworth*, 1922], small pore diameters (between 114 – 1000 nm, SEM mosaics) [*Houben et al.*, 2016b], and has a relatively high clay content (in general 50% - 75%) [*Houben et al.*, 2016b; *Douma et al.*, 2017].

The mineral content of the Whitby Mudstone is presented in Figure 2.3 [*Houben et al.*, 2016b; *Douma et al.*, 2017]. The Whitby Mudstone mainly consists of sheet silicates (mainly clays), and thus, based on the mineralogy alone, the Whitby Mudstone can be categorized as a *mudstone*. In addition, this clay-rich rock is very sensitive to air, resulting in shrinkage fractures due to dehydration (chapters 4 and 5). This supports the idea that the Whitby Mudstone is classified as a *mudstone*.

Lithologies encompassed by the term shale in the literature, which are not actual shales following the definition used in this thesis (Figure 2.3), are referred to either (tight) sandstones or (tight) carbonates, depending on their mineral content.

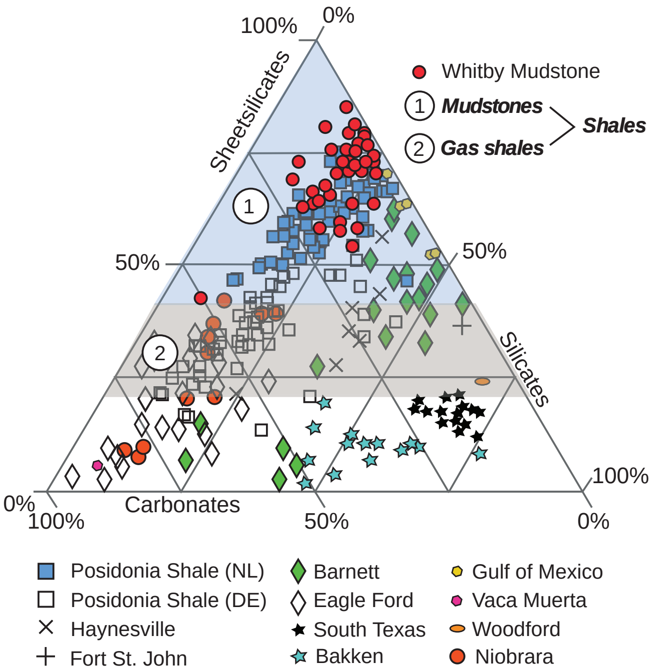

Figure 2.3: *In this thesis, the Whitby Mudstone is referred to as a mudstone. Lithologies encompassed in the literature as shale, might not be actual shales according to the definitions used in this thesis. These lithologies can be better referred to as (tight) sandstones (e.g., South Texas, Bakken) or (tight) carbonates (e.g., Vaca Muerta).*

2.4 Conclusions

- The terms *shale* and *mudstone* are used inconsistently in the literature, diminishing the usefulness of lithological names.
- In this thesis, the term shale is used in generic way, describing all sedimentary rocks which are fine-grained, laminated, low-permeable, contain clay minerals ranging from ~20% to >90% and have small a small pore size.
- Shales are divided into mudstones and gas shales, due to their different mechanical behaviour, and different response to air and fluids. This results in

different handling and preservation of mudstone and gas shale core plugs, which are needed for geomechanical testing.

- A *mudstone* is a shale consisting mainly of clay minerals (>40%) and is very sensitive to contacting fluids and air.
- A *gas shale* is a shale containing less clay minerals than a mudstone (>20% but <40%) and a significant amount of quartz or carbonate is present.
- In this thesis, the Whitby Mudstone is referred to as a *mudstone*.

3

The validity of generic trends on multiple scales in rock-physical and rock-mechanical properties of the Whitby Mudstone

Abstract Correlations between mineralogy and petrophysical properties, and mechanical properties can help to predict the deformation behaviour of rocks. The mineral content of shales varies significantly between different basins, as well as within a single formation (chapter 2). The correlations available in the literature are obtained by comparing a wide range of relatively quartz-rich shales (gas shales) from different basins. Little effort has been made on the applicability of these trends in clay-rich shales (mudstones) originating from a single basin on an outcrop scale. This chapter examines the applicability of existing trends in rock-physical and rock-mechanical properties obtained from a wide range of gas shales on clay-rich mudstones from a single basin. It addresses the question where and why the breakdown in scaling does occur with regard to petrophysical and mechanical property coupling of gas shales and mudstones. First, the Whitby Mudstone Formation is introduced, presenting the petrophysical and rock-mechanical properties of the Whitby Mudstone on an outcrop and at hand sample scale. Second, comparisons with a wide range of gas shales from the United States are made to assess the validity of existing trends.

Published as: Douma, L.A.N.R., M.I.W. Primarini, M.E. Houben, and A. Barnhoorn (2017), The validity of generic trends on multiple scales in rock-physical and rock-mechanicsl properties of the Whitby Mudstone, United Kingdom, *Marine and Petroleum Geology*, 84, 135-147.
Note that minor changes have been introduced to make the text consistent with the other chapters.

3.1 Introduction

Shales are characterized by a very fine-grained, tight matrix, making them relatively impermeable to fluid flow [*Aplin and Macquaker*, 2011].For successful hydrocarbon production, shale reservoirs generally require hydraulic fracturing to create open fractures, allowing hydrocarbons to flow in otherwise low-permeability rocks [*Newhouse*, 1942]. The presence of bedding planes, faults and joints are known to strongly impact fracture propagation and the overall fracture geometry [*Warpinski and Teufel*, 1987]. Additionally, rock-mechanical properties are required to understand the strength and stiffness (Young's modulus) of shales, and to assess whether the shale will be brittle enough to initiate fractures [*Josh et al.*, 2012]. For example, low Young's modulus and high Poisson's ratio shales are generally ductile, and allow fracture closure and self-healing [*Britt and Schoeffler*, 2009; *Josh et al.*, 2012].

The deposition process of shales is rarely constant [*Trabucho-Alexandre*, 2015], resulting in highly-laminated successions with significant variation in mineralogy, organic content, maturity, and microstructure on various scales [*Dewhurst and Siggins*, 2006; *Passey et al.*, 2010; *Houben et al.*, 2016a]. This heterogeneity results in notable differences in rock-physical and rock-mechanical properties throughout the formation [*Ghadeer and Macquaker*, 2012], which complicates predictions of fracture behaviour. This lead to erroneous interpretations when upscaling to wireline-log, outcrop, or reservoir scale. Understanding the controls on mechanical behaviour is important for the successful development of hydrocarbon reservoirs.

Previous studies have shown that the mechanical properties of shales are controlled by mineralogy and petrophysical properties, including clay and organic content, shale fabric, porosity and mechanical anisotropy [*Sone and Zoback*, 2013; *Fjær and Nes*, 2014; *Rybacki et al.*, 2016]. *Sone and Zoback* [2013] showed a correlation between clay and organic matter content, and elastic properties. Such correlations in rock physics help to predict the rock-mechanical behaviour of shales, improving predictions of the fracture response in shales. However, these correlations are obtained by comparing a wide range of relatively quartz-rich shales (gas shales) from different basins, including Barnett, Haynesville, Fort St. John, and Eagle Ford shale. Little effort has been made on the applicability of these trends in mudstones originating from a single basin on an outcrop scale.

This study examines the applicability of existing trends in rock-physical and rock-mechanical properties obtained from a wide range of quartz-rich shales (gas shales) and clay-rich shales (mudstones) from a single basin. Petrophysical and rock-mechanical analyses of relatively quartz-rich shales originating from the United States is extended to the petrophysics and geomechanics of relatively clay-rich shales. These mudstones are a potential target for future shale gas exploration in Northwest Europe. Considerable amounts of gas are potentially present in these clay-rich shales, but the degree of brittle deformation is a challenge that may hinder economic hydrocarbon production [*Van Bergen et al.*, 2013; *Ter Heege et al.*, 2015]. Mudstone samples were taken along a stratigraphic section in a single basin in order to investigate the heterogeneities and possible trends in rock-physical and rock-mechanical properties on an outcrop scale. Comparisons were made with a wide range of US shales from different basins to assess the validity of generic trends.

3.2 Materials and Methodology

■ 3.2.1 Sample material and preparation

Mudstone blocks were collected along the coastal cliffs of the Whitby Mudstone Formation (WMF) north of Whitby (UK), near Runswick Bay and Port Mulgrave [see also: *Houben et al.*, 2016b; *Zhubayev et al.*, 2016] (Figure 3.1). Twenty-one mudstone blocks were collected at different heights along 6 m of stratigraphic section and within 5 km laterally (Figure 3.1) to study the heterogeneity of the Whitby Mudstone on an outcrop scale. The mudstone blocks were taken from the Jet Rock Member because of its accessibility and high organic content (TOC = 4–15%) [*Hesselbo et al.*, 2000; *Powell*, 2010].

Large mudstone blocks of about 30 by 30 by 6 cm were collected using a geological hammer and chisel. The mudstone blocks were wrapped in cling film immediately after recovering. Note that wrapping the sample blocks in cling film only slows down the desiccation of the mudstone blocks, but does not prevent *in situ* pore fluids to escape. However, since the blocks originate from outcropping coastal cliffs, it is assumed that pore fluid loss already occurred over geological time scale. The initial saturation state was not measured from these outcropping mudstone blocks.

Twenty-two cubic subsamples were cut out of the larger mudstone blocks using a saw cooled by air. Each sample was cut with an angle of 90° with respect to the bedding plane (i.e., horizontal bedding). The subsamples were manually sanded into cylinders, having a 60 mm length and 30 mm diameter. The top and bottom ends of the mudstone core plugs were ground flat. It is likely that the process of producing the cylindrical samples would have led to significant pore fluid loss. Since the initial saturation state was unknown and the water loss due to sample preparation was not measured, the mudstone blocks are therefore classified as ‘dry’, without knowing the saturation state. In the next chapters (chapters 4 and 5) the effect of water saturation on the elastic anisotropy and mechanical properties of the Whitby Mudstone is discussed. The dry core plugs were used to investigate the mineralogical, petrophysical, rock-mechanical, and ultrasonic velocity characteristics.

■ 3.2.2 Mudstone characterization

Geochemical analysis was performed on twelve Whitby Mudstone samples located at different heights in the stratigraphic section. The analysed mudstone samples were powdered and dried in the oven at a temperature of 70°C for at least 24

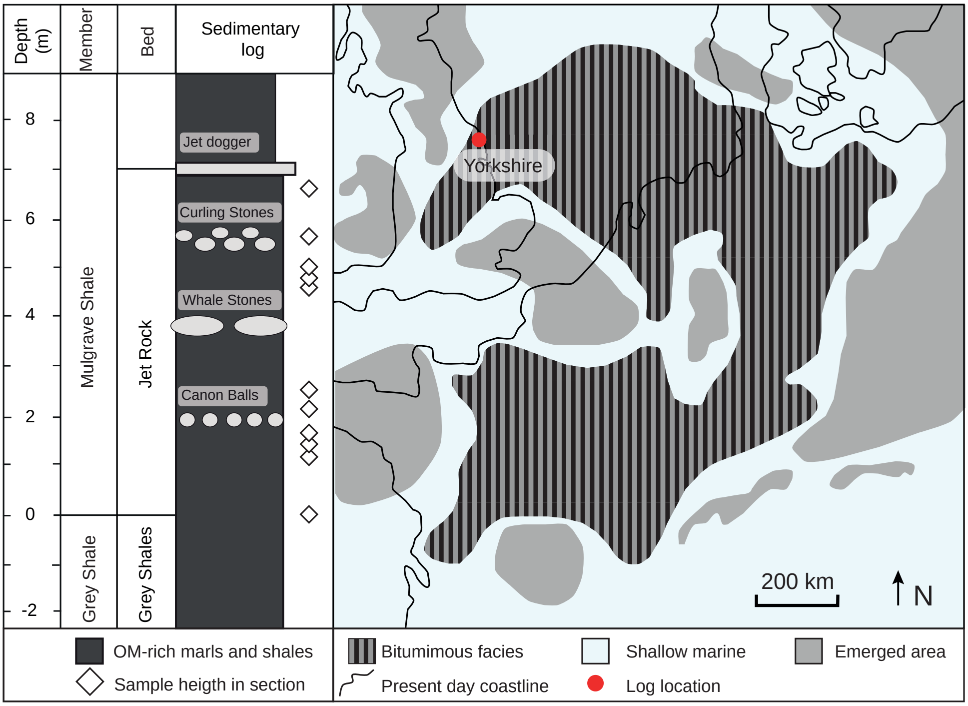

Figure 3.1: *Mudstone blocks were collected from the coastal cliffs of the Whitby Mudstone Formation deposited in the Yorkshire Basin, United Kingdom. To assess the heterogeneity of the WMF at an outcrop scale, the mudstone samples were collected at different heights in the stratigraphic section. Modified from Hesselbo et al. [2000]; Frimmel et al. [2004]; Houben et al. [2016b].*

hours. X-ray fluorescence (XRF) was performed to measure the mineral composition and associated weight of the mudstone samples. A spectrometer (*Panalytical Axios Max WD-XRF*) was used for XRF analysis measurements. Data evaluation was performed using the *Super Q5.0i/Omnian* software. The porosity and matrix density was measured on cores using a pycnometer (*Ultra pycnometer 1000 version 2.12*). Helium (He) gas was used to measure the porosity and matrix density because of its small atomic dimensions enabling measuring pores with diameters down to nm-scale. The porosity values represent the effective porosity, connected to the samples outside, which was connected with pore throats wide enough for He to enter.

Ultrasonic P- (V_p) and S-wave (V_s) velocities of seventeen mudstone core plugs were recorded parallel (V_{ph}; horizontal direction) and perpendicular (V_{pv}; vertical direction) to the horizontal bedding plane to estimate the dynamic elastic properties and elastic anisotropy (i.e., difference in velocity with direction) of the Whitby Mudstone at ambient conditions (i.e. room temperature, no confining pressure applied).

Benchtop measurements were performed by attaching P- or S-wave transducers (central frequency of 1 MHz) directly to the core plug. During each measurement, one transducer acts as a source, whereas the opposed transducer acts as a receiver, recording the transmitted signal (waveform). The arrival times were picked manually from the oscilloscope.

The dynamic elastic moduli were obtained from the measured P- and S-wave velocities and bulk rock density (ρ). The P- and S-wave velocities represent the velocities in the vertical direction. The dynamic elastic parameters, including Young's modulus (E_{31}) and Poisson's ratio (ν_{31}), were estimated from the elastic wave equation in isotropic media [e.g., *Mavko et al.*, 2003]. The dynamic Young's modulus is calculated from the following equation:

$$E_{31dyn} = \frac{9K\mu}{3K + \mu} \tag{3.2.1}$$

where the bulk modulus (K) is expressed by $K = (V_p^2 - \frac{4}{3}V_s^2)\rho_m$ and the shear modulus (μ) by $\mu = V_p^2$. The dynamic Poisson's ratio is expressed by the elastic moduli K and μ following:

$$\nu_{31dyn} = \frac{3K - 2\mu}{2(3K + \mu)}. \tag{3.2.2}$$

Note that the Young's modulus and Poisson's ratio are likely to be different when measured in other directions (e.g., parallel to the bedding), since mudstones are often anisotropic. Thomsen's P- and S-wave anisotropy parameters (ε, γ, respectively) [*Thomsen*, 1986] were used to describe the elastic anisotropy of the WMF and were obtained from the horizontal and vertical ultrasonic P- and S-wave velocities [see also: *Zhubayev et al.*, 2016]. The reader is referred to chapter 4, subsection 4.2.4 for a detailed explanation of the relation between the ultrasonic velocities and elastic coefficients, and the definition of the anisotropy parameters ε and γ.

To obtain the static elastic properties (Young's modulus and Poisson's ratio) and the rock strength, unconfined compression tests were performed under room humidity conditions on fifteen dry mudstone core plugs. The experiments were conducted at room temperature (20°C). Cylindrical samples were placed in a pressure bench with a 50 – 500 kN load frame and deformed until failure. The uniaxial compressive loading axis was oriented 90° to the bedding plane. The axial and circumferential strain were recorded by linear variable differential transformers (LVDTs) and extensometers mounted on the shale sample. Axial strain rates of 10^{-6} s^{-1} were used. This loading rate might be too fast for the Whitby Mudstone when fully saturated (chapter 5). Chapter 5 shows the calculations for appropriate strain rates of the Whitby Mudstone, and details the consequences of using inappropriate strain rates on the mechanical behaviour of clay-rich rocks based on the work of *Giger et al.* [2018]. However, the core plugs used here are partially saturated, and therefore the effect of inappropriate loading rates is less significant. The pore pressure was not controlled or monitored during deformation.

■ 3.2.3 Brittleness indices

Brittleness is used to describe the brittle deformation behaviour of materials [*Holt et al.*, 2015; *Rybacki et al.*, 2015], where the brittleness index is used to quantify the degree of brittle deformation behaviour of rocks. A high brittleness index (max. value of 1) indicates the highest degree of brittle deformation, whereas a low value (close to 0) indicates more ductile behaviour. However, there is not one definition of brittleness index [*Hucka and Das*, 1974; *Holt et al.*, 2011, 2015; *Yang et al.*, 2013; *Rybacki et al.*, 2015]. Four different definitions that could quantify the brittleness of the WMF were used (Table 3.1), including a brittleness index based on mineralogy (B_1) [*Jarvie et al.*, 2007], one based on the relation between elastic strain and total strain at failure (B_2) [*Coates and Parsons*, 1966], and two based on the combination of dynamic Young's modulus and Poisson's ratio (B_3; B_4) [*Rickman et al.*, 2008; *Jin et al.*, 2014].

Table 3.1: *Brittleness indices as found in the literature to quantify the brittleness of the WMF [Coates and Parsons, 1966; Jarvie et al., 2007; Rickman et al., 2008; Jin et al., 2014].*

Brittleness indices	**Comments**
$B_1 = \frac{Qtz}{(Qtz+C+Cl)}$	Qtz, C, and Cl are weight fractions of quartz, carbonate, and clay, respectively.
$B_2 = \frac{C_{el}}{C_{tot}}$	C_{el} and C_{tot} are the elastic strain and total strain prior to failure, respectively.
$B_3 = \frac{1}{2}(\frac{E_{dyn}(0.8-\phi)}{8-1} + \frac{\nu_{dyn}-0.4}{0.14-0.4}) \times 100$	E_{dyn}, ν_{dyn}, and ϕ are the dynamic Young's modulus (Mpsi), Poisson's ratio, and porosity, respectively.
$B_4 = (\frac{\frac{E-E_{min}}{E_{max}-E_{min}} + \frac{\nu_{max}-\nu}{\nu_{max}-\nu_{min}}}{2})$	E_{min}, E_{max} and ν_{min}, ν_{max} are the minimum and maximum Young's modulus and Poisson's ratio, respectively. E and ν are the Young's modulus and Poisson's ratio over depth.

3.3 Heterogeneities in the Whitby Mudstone Formation

■ 3.3.1 Mineralogy and petrophysical properties

Basic mineralogical composition and petrophysical properties information such as total organic carbon (TOC), effective porosity for helium, and matrix density of the stratigraphic section are summarised in Figure 3.2. The mineral composition of seven samples analysed by *Houben et al.* [2016b] were included in the results (Figure 3.2a).

The main fraction of the mineralogy consists of clay minerals, mainly kaolinite and illite. The clay content varies throughout the Jet Rock Member from about 40 weight percentage (wt%) to approximately 75 wt%. The clay content is higher at the base of the Jet Rock member than in its upper part. Additionally, the measured clay content seems to decrease in the vicinity of the Whale Stones. The combined quartz and pyrite content ranges from 18 to 29 wt%, with the maximum values occurring in the same interval as the Whale Stones. Locally, the section is calcite rich (up to 45 wt%), due to the presence of fossils.

Zijp et al. [2015] measured TOC throughout the section (Figure 3.2b). The TOC measurements show a gradual increase from about 4% at the base of the Grey Shale Member to approximately 15% in the middle of the Jet Rock Member. Above this maximum, the TOC values decrease again to approximately 4% in the upper part of the Jet Rock Member. The level of maximum TOC values seems to correspond to maximum levels of quartz and pyrite content.

The porosity values from twenty-six samples of *Houben et al.* [2016b] are included in the section (Figure 3.2c). The porosity values range from approximately 0.3% to approximately 5.2%. The porosity values vary between different samples taken from the same sample block as well as between different samples, implying that there is variation in porosity laterally on centimetre scale as well as vertically through the section [*Houben et al.*, 2016b].

The bulk-density profile displays a vertical and lateral variation with a maximum value of approximately 2.2 to 2.8 $g.cm^{-3}$ (Figure 3.2d). Measured bulk-density values are similar in the upper part and the base of the Jet Rock Member and decrease towards the middle of the Jet Rock Member.

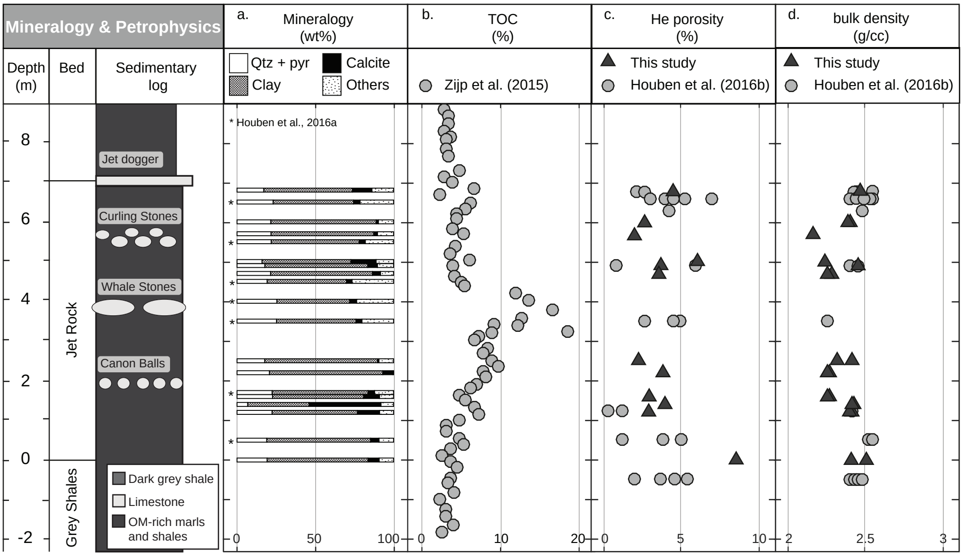

Figure 3.2: *Mineralogical composition and petrophysical properties of the Whitby Mudstone throughout the stratigraphic section. a. Mineralogical data from this study and [Houben et al., 2016b]. b. TOC data [Zijp et al., 2015]. c. Connected porosity data from this study and Houben et al. [2016b]. d. Bulk density from this study and Houben et al. [2016b].*

■ 3.3.2 Ultrasonic velocities

[1]Figure 3.3 shows the P- and S-wave velocities and corresponding elastic anisotropy parameters for the dry Whitby Mudstone core plugs. P-wave velocities measured perpendicular to the bedding (V_{pv}) range between 1530 m/s and 2520 m/s. P-wave velocities measured parallel to the bedding (V_{ph}) are higher, varying between 2480 m/s to 3790 m/s (Figure 3.3a). S-wave velocities measured perpendicular to the bedding (V_{sv}) decrease from 1580 m/s at the base of the Jet Rock Member to 1450 m/s in the vicinity of the Whale Stones (Figure 3.3b). The V_{sv} values increase again towards the top of the Jet Rock Member to a maximum of approximately 1760 m/s. The variation in recorded V_{sh} values is limited at the base of the Jet Rock Member, whereas they vary both laterally and vertically in the upper half of the Jet Rock Unit. The P-wave anisotropy (ε) ranges from approximately 0.33 to approximately

---

[1] The ultrasonic velocity data are taken from M. Primarini, 2015, Fracture Mode Analysis, Geomechanics, Petrophysics and fracture characterization, M.Sc. thesis. No waveforms were presented and the P- and S-wave uncertainties were not reported in the M.Sc. thesis, therefore the quality of the data could not be verified. Especially S-wave picking is often difficult in clay-rich rocks (see chapter 4).

0.56 (Figure 3.3c). The S-wave anisotropy (γ) varies from approximately 0.25 to approximately 0.66 (Figure 3.3d).

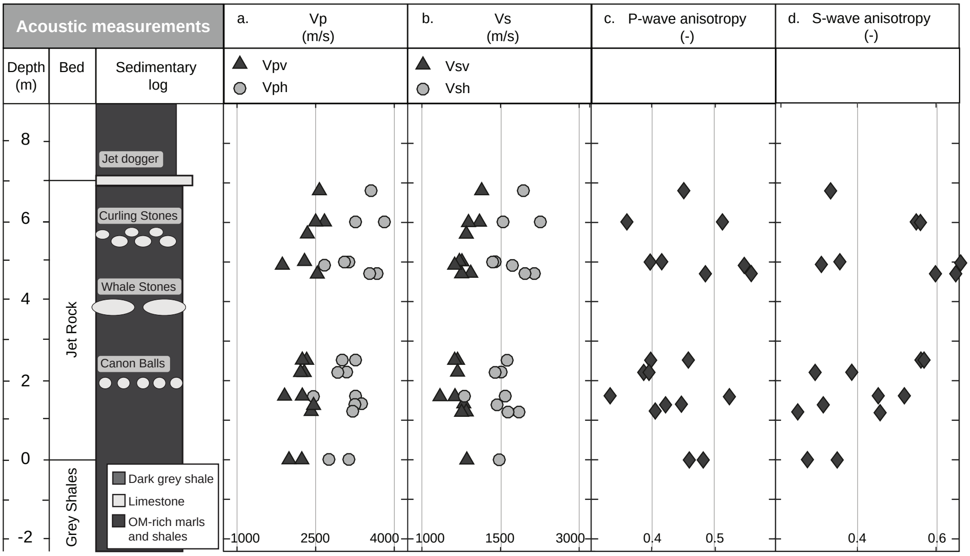

Figure 3.3: Acoustic measurements of the Whitby Mudstone throughout the stratigraphic section. a. P-wave velocities parallel (V_{ph}) and perpendicular (V_{pv}) to the bedding. b. S-wave velocities parallel (V_{sh}) and perpendicular (V_{sv}) to the bedding. c. P-wave anisotropy (ε). d. S-wave anisotropy (γ).

The elastic anisotropy parameters are plotted against the amount of clay content for each Whitby Mudstone sample (Figure 3.4). Clay content is expected to have a great effect on the overall rock properties, since clay content is an important constituent of a shale/mudstone [*Sone and Zoback*, 2013]. The data show that there is no clear correlation between the clay content and the P- and S-wave anisotropy of the Whitby Mudstone.

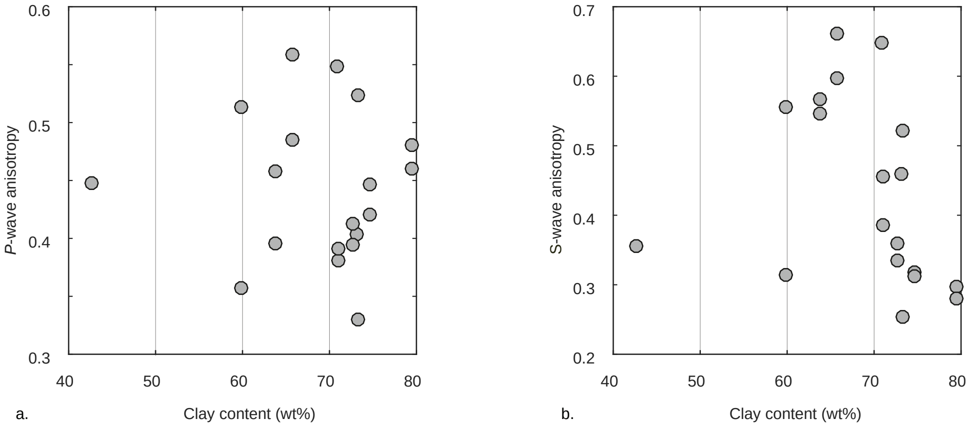

Figure 3.4: *Correlation between clay content and P- and S-wave anisotropy for the Whitby Mudstone samples. a. Clay content versus P-wave anisotropy (ε). b. Clay content versus S-wave anisotropy (γ).*

▪ 3.3.3 Rock-mechanical properties

[2] The dynamic Young's modulus has a minimum value of 8 GPa at the base of the Jet Rock Member and increases to approximately 16 GPa towards the top of the Jet Rock Member (Figure 3.5a). The dynamic Young's modulus is lower than the static Young's modulus, which is opposite to what one might expect *in situ*. The static Young's modulus varies from approximately 12 GPa at the base of the Jet rock to approximately 29 GPa in the middle of the Jet Rock Member.

The dynamic Poisson's ratio shows a gradual decrease from approximately 0.22 at the base of the Jet Rock Member to approximately 0.15 at the top of the Jet Rock Member (Figure 3.5b). There is limited variation in values of the dynamic Poisson's ratio in the lower half of the Jet Rock Member. The dynamic Poisson's ratio is lower than the static Poisson's ratio throughout the section. The trends in dynamic and static Poisson's ratio with section height are different. The values of the static Poisson's ratio increase from 0.24 to approximately 0.30 in the vicinity of the Whale Stones. Above the Whale Stones, the values decrease again from approximately 0.40 to 0.28 towards the top of the Jet Rock Member. The dynamic and static Young's modulus and Poisson's ratio vary for different samples taken from the same sample block. This shows that there is a variation in elastic properties

---

[2] The rock-mechanical properties were obtained from dry mudstone core plugs, without knowing the degree of saturation and could only be compared if the degree of saturation is similar for all core plugs. All samples were stored in a room (no humidity or temperature control) for the same period of time. However, similarities in the degree of saturation were not verified. The degree of water saturation highly affects the mechanical properties of clay-rich rocks, which is addressed in chapter 5.

on centimetre scale laterally and meter scale vertically. The uniaxial compressive strength (UCS) ranges between 58 and 75 MPa (Figure 3.5c).

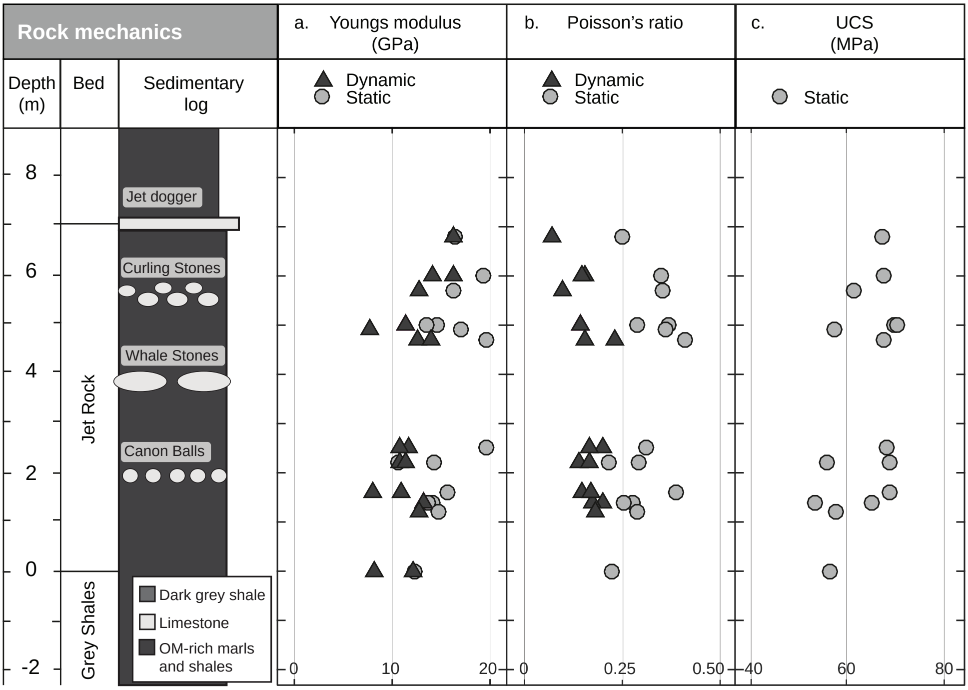

Figure 3.5: *Dynamic and static rock-mechanical properties of the Whitby Mudstone samples throughout the stratigraphic section. a. Dynamic and static Young's modulus versus section height. b. Dynamic and static Poisson's ratio versus section height. c. Uniaxial compressive strength versus section height.*

The elastic properties are plotted against the amount of clay content for each Whitby Mudstone sample (Figure 3.6). This study shows that there is a moderate correlation between the clay content and the static Young's modulus (R^2 ~0.5) and a weak correlation between clay content and a dynamic Young's modulus (R^2 ~0.3) (Figure 3.6a). The R^2 quantifies the quality of a fitting curve through the experimental data points. The Young's modulus seems to decrease with an increase in clay content. For pure clay minerals, smectites are the weakest, kaolinites the strongest, and illites in between [e.g., *Mitchell*, 1993]. Clay minerals are geomechanically weaker (less rigid) than quartz, feldspar, and dolomite [*Dewhurst et al.*, 2015]. There is no obvious correlation between the clay content and Poisson's ratio, but in general there is an increase in dynamic Poisson's ratio with increasing clay content (Figure 3.6b).

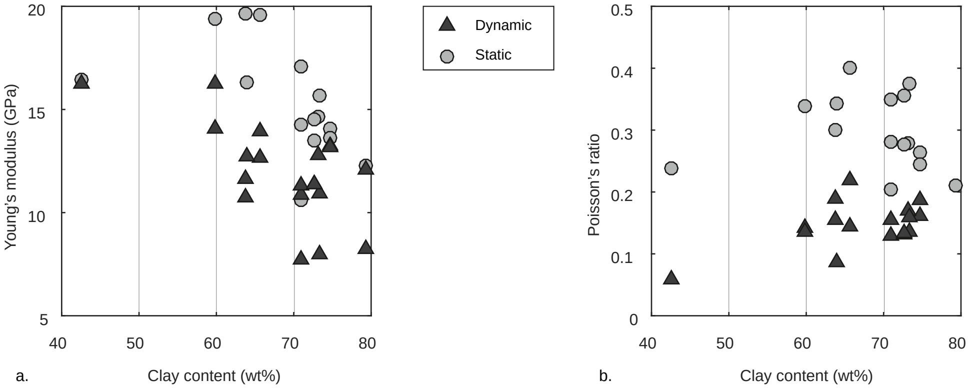

Figure 3.6: *Correlation between clay content and elastic properties of the Whitby Mudstone samples. a. Clay content versus Young's modulus. b. Clay content versus Poisson's ratio.*

■ 3.3.4 Brittleness

Different rock characteristics, including mineral composition data, ultrasonic measurements and rock mechanics were used to predict the brittle deformation behaviour of the WMF throughout the stratigraphic section.

B_1 defines the brittleness as relative quartz content of the shale. The brittleness is low (0.07 – 0.25) throughout the stratigraphic section, due to the relatively high clay content of the WMF (40 – 75 wt%) (Figure 3.7a). The most favourable conditions (varying from 0.54 up to 0.92) for brittle deformation are predicted by using the relation between elastic strain and total strain at failure (B_2) (Figure 3.7b). Predicting the brittleness based on P- and S-wave data deducted from laboratory experiments (B_3) gives a wide variation in brittleness throughout the section. In the lower half of the section the brittleness index is about 0.5 and increases in the upper half to about 0.85 (Figure 3.7c). B_4 is obtained from the normalised dynamic Young's Modulus and Poisson's ratio [*Jin et al.*, 2014; *Rickman et al.*, 2008] and based on the minimum and maximum Young's modulus and Poisson's ratio for the stratigraphic section. The brittleness index increases with an increasing dynamic Young's modulus (E) and decreasing dynamic Poisson's ratio (ν). An average brittleness index of about 0.50 with limited variation throughout the section is predicted (Figure 3.7d).

Significant heterogeneity is observed in the brittle deformation behaviour throughout the stratigraphic section of the WMF, even though a single method was used to quantify the brittleness. Additionally, the different methods used to quantify the brittleness show different values, because each brittleness index is based on different rock characteristics. The method used to quantify the brittleness influences therefore the prediction of the brittle deformation behaviour of the WMF. This discrepancy calls for a better prediction of the brittle deformation behaviour as is also stimulated by, for example, *Holt et al.* [2015]; *Rybacki et al.* [2016].

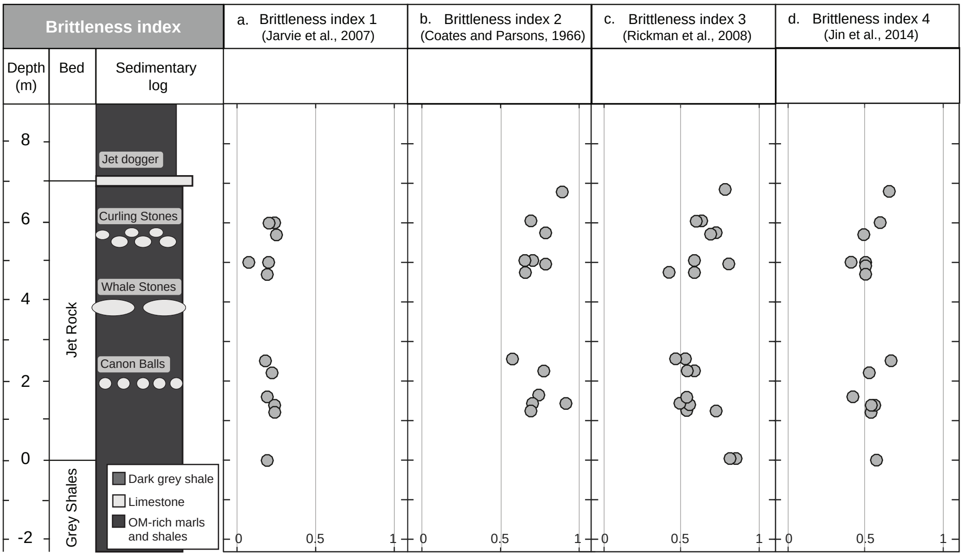

Figure 3.7: *Predictions on the brittle deformation behaviour of the WMF throughout the stratigraphic section calculated a. from the relative quartz content (B_1) [Jarvie et al., 2007], b. relation between elastic strain and total strain at failure (B_2) [Coates and Parsons, 1966], c. relation between dynamic Young's modulus and Poisson's ratio (B_3) [Rickman et al., 2008], d. and the relation between the minimum and maximum Young's modulus and Poisson's ratio (B_4) [Jin et al., 2014].*

3.4 Comparison with other mudstones and gas shales

3.4.1 Mineralogy and petrophysical properties comparison

The mineralogical composition of the WMF is compared to other Posidonia shales [*Chesapeake*, 2010; *Kanitpanyacharoen et al.*, 2012; *Gasparik et al.*, 2014; *Ghanizadeh et al.*, 2014; *Rexer et al.*, 2014; *Klaver et al.*, 2012, 2015, 2016; *Houben et al.*, 2016a,b;

Mathia et al., 2016; *Rybacki et al.*, 2016] and prospective US shales, including the Barnett, Haynesville, Eagle Ford, and Fort St. John [*Sone and Zoback*, 2013; *Gasparik et al.*, 2014; *Klaver et al.*, 2015] (Figure 3.8). Both the Posidonia Shale in the Netherlands and the WMF are relatively rich in sheet silicates. The Posidonia Shale from Germany, however, shows a higher carbonate content and a lower sheet silicate content compared to the WMF, whereas the silicate content is similar [e.g., *Houben et al.*, 2016a]. The prospective US gas shales have in common that they are relatively low in sheet silicate minerals (<60%) and show a large scatter in the carbonate and silicate content (Figure 3.8) [*Houben et al.*, 2016b]. This suggests that there is significant variation in mineral composition between shales from different basins.

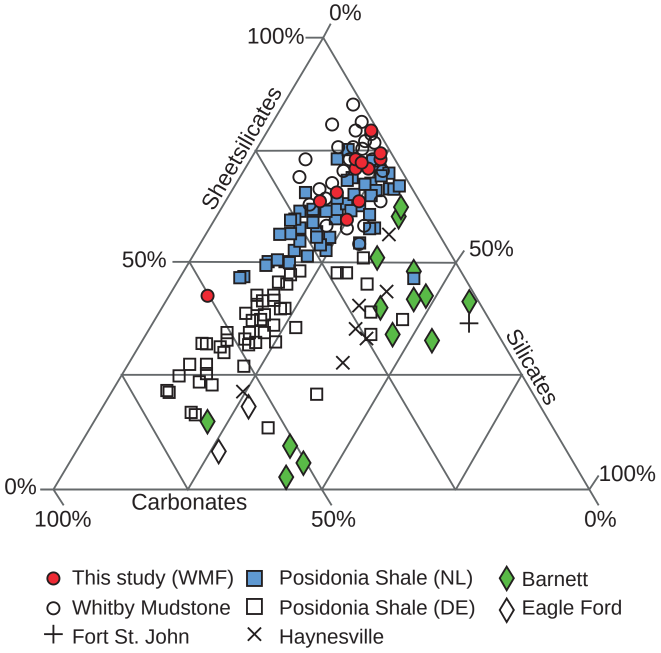

Figure 3.8: *Mineralogy of the WMF compared to other Posidonia Shales [Chesapeake, 2010; Kanitpanyacharoen et al., 2012; Gasparik et al., 2014; Ghanizadeh et al., 2014; Rexer et al., 2014; Klaver et al., 2012, 2015, 2016; Houben et al., 2016a,b; Mathia et al., 2016; Rybacki et al., 2016] and prospective US shales [Sone and Zoback, 2013; Gasparik et al., 2014; Klaver et al., 2015].*

■ 3.4.2 Ultrasonic velocity comparison

Sone and Zoback [2013] observed a positive correlation between the clay and kerogen content and the elastic anisotropy of US shales from different basins (Figure 3.9). An increase in clay content generally increases the elastic anisotropy, due to the preferred orientation of clay minerals. However, this study does not adhere to the general trend of *Sone and Zoback* [2013]. The *P*- and *S*-wave anisotropy is lower for the Whitby Mudstone than expected from *Sone and Zoback* [2013]. The variation in properties within one set of samples taken from the same depositional basin (Whitby Mudstone), does not show any correlation between clay content and elastic anisotropy. Note that the ultrasonic velocity results from *Sone and Zoback* [2013] were obtained under triaxial stress conditions. In this study, however, the velocities were measured on the benchtop (i.e., no confining pressure). Applying a confining pressure to the mudstone core plugs allows (micro) fractures to close, which highly impacts the velocities, hence elastic ansitropy of shales (see chapter 4). Therefore, care should be taken when comparing velocities and elastic anisotropy data obtained at ambient conditions (no confining pressure) to such data obtained from core plugs subjected to a confining pressure.

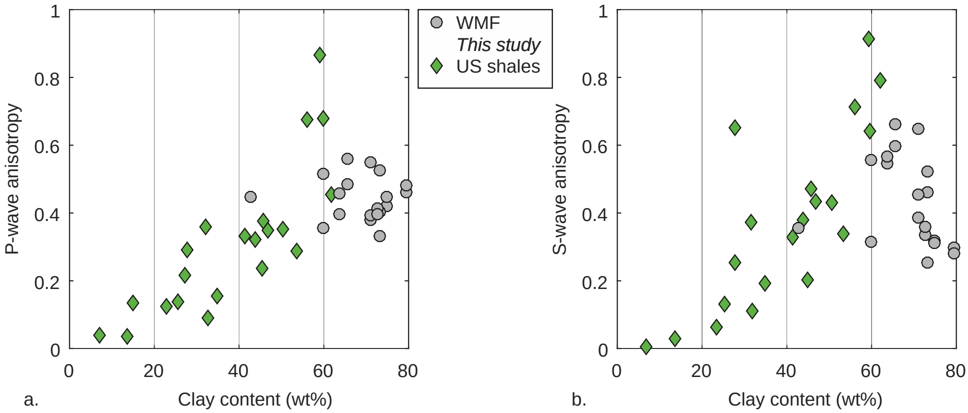

Figure 3.9: *Correlation between clay content and P-wave and S-wave anisotropy for the WMF compared to US shales from different basins [Sone and Zoback, 2013]. a. Clay content versus P-wave anisotropy (ε). b. Clay content versus S-wave anisotropy (γ).*

Trends in the degree of elastic anisotropy as a function of vertical velocities in US shales from different basins were reported by, for example, *Vernik and Liu* [1997]; *Sone and Zoback* [2013] (Figure 3.10). These authors measured the ultrasonic velocities on core plugs subjected to a confining pressure. This study on the WMF does not observe a correlation between the degree of elastic anisotropy and vertical velocities. This is consistent with the observations of *Vernik and Liu* [1997] on shales from different basins with a wide range of lithologies and maturity levels.

Fundamentally, there is no reason why the elastic anisotropy should correlate with the vertical velocity, since the elastic anisotropy is determined by using P- or S-wave velocities in both the vertical and the horizontal directions. An increase in P-wave anisotropy with increasing S-wave anisotropy is observed in this study, which is consistent with previous studies [e.g., *Sone and Zoback*, 2013; *Vernik and Liu*, 1997] (Figure 3.10c).

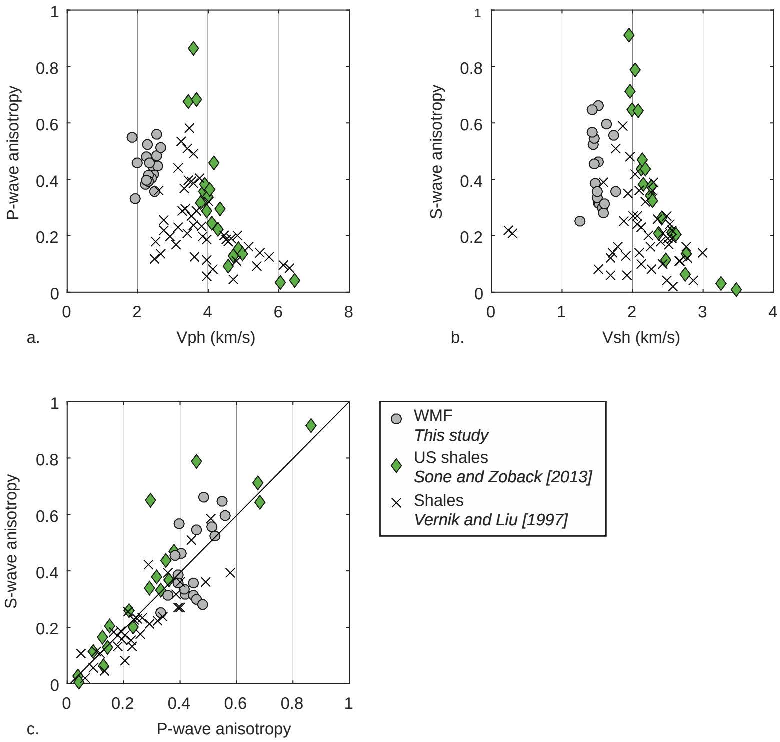

Figure 3.10: *Correlation between a. horizontal P-wave velocity (V_{ph}) and P-wave anisotropy (ε), b. horizontal S-wave velocity (V_{sh} and S-wave anisotropy (γ), c. P-wave anisotropy (ε) and S-wave anisotropy (γ) of the WMF compared with shales from different basins [Vernik and Liu, 1997; Sone and Zoback, 2013].*

■ 3.4.3 Rock-mechanical properties comparison

The results of this study show a weak negative correlation between the clay content and static Young's modulus on the outcrop scale (Figure 3.6a). When comparing these parameters with samples of US shales from different basins [*Sone and Zoback*, 2013], the Young's modulus values obtained in this study are relatively low (10 – 20 GPa) and the clay content is high (60 – 80%). These values may fit the trend of decreasing Young's modulus with increasing clay and kerogen content as shown by *Sone and Zoback* [2013] (Figure 3.11a). Note that the experiments performed on dry shale samples by *Sone and Zoback* [2013] were conducted under confined pressure conditions, which is likely to affect the deformation behaviour of shales [chapter 4; e.g., *Josh et al.*, 2012; *Rybacki et al.*, 2015]. Overall, literature studies [*Rybacki et al.*, 2015; *Sone and Zoback*, 2013] show a relatively low Young's modulus for a high clay content material, such as the Posidonia shales in Northwest Europe. No correlation was observed between shale composition and Poisson's ratio which is consistent with previous studies [e.g., *Sone and Zoback*, 2013] (Figure 3.11b).

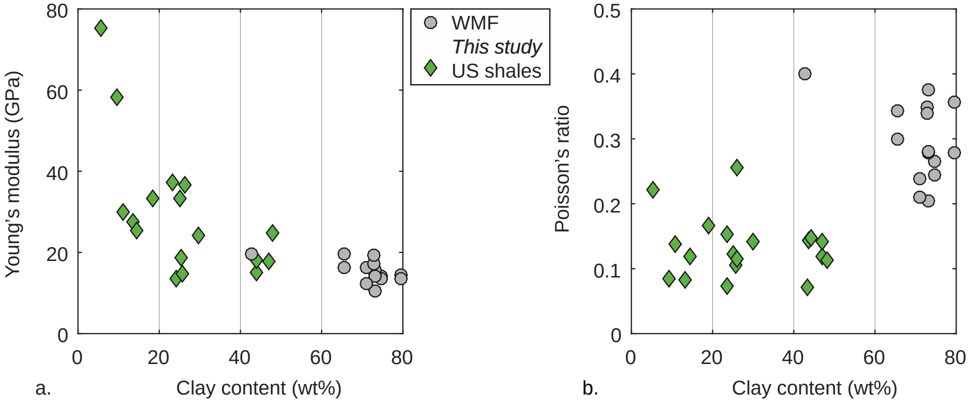

Figure 3.11: *Correlation between clay content and a. static Young's modulus, b. static Poisson's ratio of the WMF compared to US shales from different basins [Sone and Zoback, 2013].*

■ 3.4.4 Brittleness comparison

Predictions of the brittle deformation behaviour of the WMF were based on different rock characteristics (mineralogy, elastic parameters, and the relation between elastic strain and total strain at failure), therefore showing significant variations throughout the stratigraphic section and between the different methods used to quantify the brittle deformation behaviour. A more uniform method of determining the brittleness index is necessary so that predictions do not depend on the used method.

The brittle deformation behaviour of the WMF is compared to prospective gas shales including the Barnett, Haynesville, Eagle Ford and Forth St. John shales [*Sone and Zoback*, 2013; *Gasparik et al.*, 2014; *Klaver et al.*, 2015; *Rybacki et al.*, 2015]. When comparing the brittleness index calculated as a function of relative quartz content (B_1) of the WMF to prospective US shales, the brittleness of the WMF is relatively low (Figure 3.12). The low brittleness value is due to the relatively low quartz content in the WMF. This suggests that the WMF is less prone to mechanically fracturing compared to producing US shales. Comparing the brittleness, based on rock mechanical data (B_2, B_3, and B_4) of the WMF, to producing US shales is complicated. The experimental conditions used in this study and previous studies (e.g., confining pressure, temperature, water saturation) on brittle deformation behaviour differ from each other [*Jarvie et al.*, 2007; *Rickman et al.*, 2008; *Holt et al.*, 2011, 2015; *Yang et al.*, 2013; *Rybacki et al.*, 2016]. Since confining pressure and temperature impact the rock mechanical properties and, hence, the brittle behaviour of clay-rich rocks [*Josh et al.*, 2012; *Rybacki et al.*, 2015; *Yang et al.*, 2013], no comparison of brittleness was made based on the ultrasonic measurements and rock mechanical data.

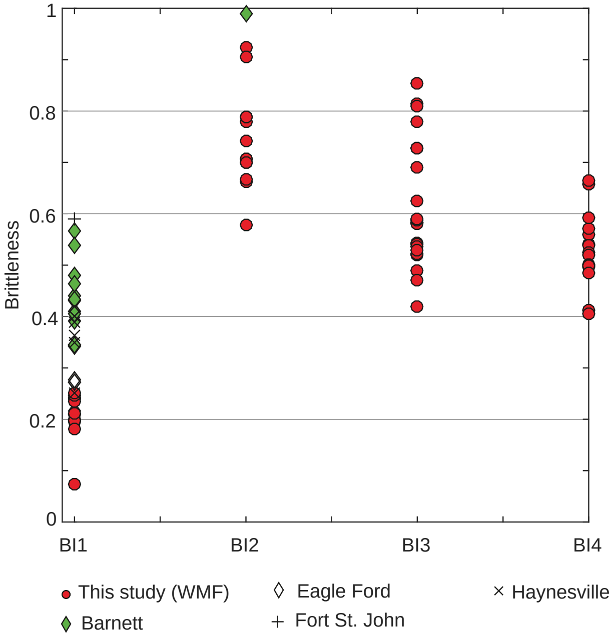

Figure 3.12: *Brittleness indices based on different rock characteristics of the WMF compared with US shales from different basins [Gasparik et al., 2014; Klaver et al., 2015; Rybacki et al., 2016; Sone and Zoback, 2013].*

3.5 Validity of generic trends

3.5.1 Heterogeneity on different scales

Shale gas reservoirs consist of multiple depositional units, which create significant variation in lithology, petrophysical properties, elastic anisotropy, and rock-mechanical behaviour [*Passey et al.*, 2010; *Sone and Zoback*, 2013]. This heterogeneity may impact the fluid-flow pathways, brittleness, fracture response, and ultimately oil or gas recovery efficiency. Furthermore, it may complicate to predict the deformation behaviour of shales [*Suarez-Rivera et al.*, 2006; *Ambrose et al.*, 2008; *Maxwell and Cipolla*, 2011].

Houben et al. [2016a,b] observed significant variation in mineralogical and petrophysical properties in the Whitby Mudstone samples on the millimetre scale based on Scanning Electron Microscope (SEM) mosaics. Porosity varies with measuring method [*Busch*, 2016; *Houben et al.*, 2016b] due to the fact that different methods measure porosity at different resolutions and the lateral and vertical variation naturally present in the rock. The WMF samples show that the highest percentage of pores are present in the clay matrix as intergranular pores, where highest matrix porosity coincides with a low overall matrix content [*Houben et al.*, 2016a]. All analyses in this study were performed on centimetre-scale Whitby Mudstone samples. All centimetre-scale samples show preferred bedding orientation and mineralogically different layers. Organic matter is oriented mainly parallel to the bedding [*Houben et al.*, 2016a,b]. At the cm-scale, microstructures consist of mineral floating within a fine-grained clay matrix with the presence of some cracks [*Houben et al.*, 2016a,b].

This study shows that significant heterogeneity in mineralogy, petrophysical properties, elastic anisotropy, and rock-mechanical behaviour is observed on an outcrop scale. A significant heterogeneity is also present in the US shales reported by *Sone and Zoback* [2013] within a narrow range in clay content (Figure 3.9a; clay content 20 – 40 wt%; P-wave anisotropy between 0.1 and 0.4). The heterogeneity in mineralogy and petrophysical properties may be caused by depositional fluctuations. When comparing the heterogeneities in mineralogy and petrophysical properties on an outcrop scale with shales from different basins, the heterogeneity on an outcrop scale is more confined, but is still significant. The presence of significant variation in rock properties on various scales, and the different methods used to quantify the brittle deformation of shales complicates predictions on brittle deformation behaviour throughout a reservoir.

3.5.2 Fit to existing trend

Finding generic trends in mechanical and physical rock properties is important to be able to make predictions on, for example, the fracture response, which is crucial for successful production from shale/mudstone reservoirs.

This study shows no obvious correlation within the Whitby Mudstone between: (1) clay content and elastic anisotropy, (2) vertical velocity and elastic anisotropy, and (3) clay content and elastic parameters. Only a weak to moderate correlation between the clay content and Young's modulus is present on an outcrop scale. The weak correlation observed on an outcrop scale implies that not only clay content controls the stiffness of the shales. A simple generic trend in mechanical and physical properties does not exist on an outcrop scale within the Whitby Mudstone due to the complexity of mudstones. When comparing US gas shales from different basins, however, a correlation between the clay content and Young's modulus is present (Figure 3.11). An overall decrease in Young's modulus with increasing clay content reflects a larger amount of compliant materials (clay and organics) and a smaller amount of stiff minerals (quartz and carbonates) [*Sone and Zoback*, 2013].

Sone and Zoback [2013] compared US gas shales from different basins and observed an increase in elastic anisotropy with increasing clay and kerogen content. This correlation may be the result of the anisotropic behaviour of the clay minerals itself and the anisotropic fabric created by the preferred orientation of clay minerals [*Johnston and Christensen*, 1996; *Vernik and Liu*, 1997; *Vernik and Nur*, 1992]. *Sone and Zoback* [2013] suggested that the high degree of anisotropy is also related to the high maturity exhibited in the shale samples, influencing the kerogen distribution and microcrack alignment [*Vanorio et al.*, 2008]. However, the study of *Sone and Zoback* [2013] also observed a low degree of anisotropy (i.e., <0.2) in some samples, even though all the analysed samples are mature (Figure 3.9). This implies that also other parameters than maturity cause the trend as observed by *Sone and Zoback* [2013]. Additionally, they suggested that the observed confined trends between the degree of anisotropy and vertical velocities may be caused by the narrow range in maturity exhibited in the US gas shales from different basins. Microfabric observations showed that the kerogen is oriented parallel to the bedding in mature shales, whereas the kerogen becomes finely scattered in post-mature shales. However, this trend was not observed in this study, even though all the analysed Whitby Mudstone samples were early mature and the organic matter is oriented mainly parallel to the bedding [*Houben et al.*, 2016b]. The absence of a correlation between vertical velocities and elastic anisotropy is consistent with the observations of *Vernik and Liu* [1997], who analysed organic-rich samples of shales from different basins that exhibit a wide range of maturation levels (immature to post mature).

The results suggest that there is no single parameter alone which influences the elastic anisotropy and, hence, the correlation between the vertical velocity and elastic anisotropy in shales, such as maturity or clay and kerogen content. *Sondergeld and Rai* [2011] suggest that there are multiple causes of anisotropy in shales, including alignment of clay platelets, organic matter, stresses, and fractures. *Hornby* [1998] suggested that compaction resulted in increased clay particle alignment, which causes an increase in anisotropy. The presence of bedding planes and microcracks oriented parallel to the bedding enhance the anisotropy [*Vernik and Nur*, 1992]. *Sayers* [2008] suggests that the shape and orientation of the pore space influences the anisotropy and may be different for clay-rich and quartz-rich shales. Pores are mainly oriented parallel to the bedding in clay-rich shales [*Houben et al.*, 2016a,b], whereas pores are more randomly orientated when the amount of quartz increases [*Houben et al.*, 2014]. The wide range of causes for shale anisotropy complicate the interpretation of anisotropy calculations and, hence, correlations made on shales on an outcrop scale.

A generic trend is present when the average of the samples from a single formation based on composition is taken and this trend for WMF fits to the trends of shales from different basins of *Sone and Zoback* [2013]. However, this trend is not visible on an outcrop scale. This study shows that on an outcrop scale variation in one parameter cannot automatically be translated to variation in another parameter. Parameters other than mineralogy also contribute to the behaviour of these complex shales; these parameters include the above-mentioned alignment of clay platelets, presence of bedding, organic matter, stresses, and fractures. This complexity of shales may cause significant spread in the parameters at a narrow range in clay content, and thus the absence of clear correlations. Further examination on microstructures and pore characteristics in shales is required to understand which parameters cause the absence of trends on an outcrop scale.

The presence of a trend when comparing shales from different basins may be caused by the large variation in properties. The variation in clay content for the WMF is lower (60 – 80%) than that of shale samples from different basins. Shales with a relative low clay content (<20%) will often have a lower anisotropy or higher Young's modulus than shales with a very high clay content (∼80%). The influence of parameters other than mineralogy might become less prominent when comparing shales from different basins. The trends observed by *Sone and Zoback* [2013] can thus be used when comparing different basins, but they are not necessarily applicable to outcrop scale or well log scales.

3.6 Conclusions

A significant variability in mineralogical, petrophysical, anisotropy, and rock mechanical properties were found on an outcrop scale in the Whitby Mudstone. Heterogeneity in mineral composition is more confined when the Whitby Mudstone is compared to shales consisting of a wide range of lithologies and from different basins. There are no obvious correlations between mineral composition and elastic properties in the Whitby Mudstone (outcrop scale), whereas the elastic properties seem to be a function of composition when a wider range of lithologies from different basins is included in the analysis. The elastic anisotropy, described by Thomsen parameters, does not correlate with mineral content on an outcrop scale. The generic trends used to describe the anisotropy and rock-mechanical properties defined by other studies, cannot always be applied to all types of gas shales at any scale. Multiple parameters will contribute to the behaviour of shales. The complexity in shales makes it difficult to find generic trends on an outcrop scale. Comparison with shales from different basins show, however, generic trends in rock-mechanical and rock-physical properties. The significant higher variation in lithology, hence rock-mechanical properties, between shales from different basins causes that the influence of parameters other than mineralogy become less prominent on a basin scale.

4

Impact of water saturation on the elastic anisotropy of the Whitby Mudstone, United Kingdom

Abstract The mineralogy and rock-physical properties of the Whitby Mudstone Formation are heterogeneous at an outcrop scale (chapter 3). The variation in mineralogy on the millimetre-scale of mudstones leads to highly anisotropic rocks. This high anisotropy complicates depth conversion in seismic exploration, and monitoring subsurface reservoirs during injection or production. In addition, the physical and mechanical properties of mudstones are highly sensitive to their water content. However, in laboratory studies, the saturation state of the tested mudstones is often not reported, if known at all. Although the impact of dehydration on the bulk properties of mudstones has been studied and reported in the literature, the effect of water saturation on the elastic anisotropy has attracted far less attention. This chapter examines the impact of water saturation on the elastic anisotropy of the Whitby Mudstone, during (1) isotropic stress loading up to the simulated *in situ* conditions (25 MPa); and during (2) differential stress loading. Firstly, the experimental protocols for testing fully-saturated and partially-saturated mudstones in the laboratory are explained in detail. Secondly, the results obtained from the laboratory experiments are presented. Finally, the causes of the changes in elastic anisotropy due to dehydration are discussed. The work raises awareness about the importance of preserving clay-rich rocks and carrying out their testing adequately in order to minimize the risk of reporting ambiguous laboratory results in the future.

Published as: Douma, L.A.N.R., J. Dautriat, J. Sarout, D.N. Dewhurst, and A. Barnhoorn (2019), Impact of water saturation on the elastic anisotropy of the Whitby Mudstone, United Kingdom, *Geophysics*, *85(1)*, 1-82
Note that minor changes have been introduced to make the text consistent with the other chapters.

4.1 Introduction

Mudstones are the most abundant rock formations worldwide [e.g., *Garrels and Mackenzie*, 1969] and play an important role in the oil and gas industry. These clay-rich rocks are characterized by a fine-grained tight matrix, making them relatively impermeable with respect to gas flow unless natural fractures develop [*Aplin and Macquaker*, 2011]. This makes mudstones an important seal for conventional petroleum reservoirs, as they are able to trap large volumes of hydrocarbons [*Dewhurst et al.*, 2011].

For successful exploration and production of conventional reservoirs, knowledge of the elastic anisotropy (i.e., variation in elastic properties with direction) of mudstones is necessary. These clay-rich rocks are often highly anisotropic [e.g., *Vernik and Liu*, 1997], due to the alignment of anisotropic clay particles, minerals, fractures, inter-layering of lithologies, and low-aspect ratio pores [*Hudson*, 1981; *Vernik and Liu*, 1997; *Sayers*, 2013]. This high anisotropy causes significant uncertainties for geophysical interpretation, such as depth conversion in seismic exploration, or monitoring subsurface reservoirs during production.

Although mudstones are important for the hydrocarbon industry, the elastic anisotropy of these clay-rich rocks is not well understood. The difficulties in understanding the elastic anisotropy of mudstones are mainly due to (1) their complex nature, and (2) the lack of experiments performed on well-preserved samples. A majority of the published laboratory studies report experiments with no pore pressure control and/or on unsaturated (unpreserved) clay-rich rocks without knowing the degree of saturation [e.g., *Vernik and Zoback*, 1992; *Sone and Zoback*, 2013; *Zhubayev et al.*, 2016; *Jin et al.*, 2018]. Only a few studies [*Dewhurst and Siggins*, 2006; *Delle Piane et al.*, 2011; *Sarout et al.*, 2014, 2015] performed experiments on well-preserved and saturated mudstones.

Preservation of mudstones at atmospheric conditions can lead to a loss of pore fluid by evaporation, altering their elastic properties, and creating desiccation fractures [*Erling et al.*, 2008; *Ewy*, 2015]. Desiccation also affects significantly the mechanical parameters of clay-rich rocks, such as rock strength and stiffness [*Vales et al.*, 2004; *Ramos da Silva et al.*, 2008; *Ghorbani et al.*, 2009]. Although the impact of dehydration on the bulk (elastic) properties (e.g., Young's modulus, ultimate strength, bulk modulus, shear modulus) of mudstones has been studied and reported in the literature, the effect of water saturation on the elastic anisotropy has attracted far less attention.

This study examines the impact of water saturation on the elastic anisotropy of the Whitby Mudstone, United Kingdom (UK), during (1) isotropic stress loading up to the simulated *in situ* conditions (25 MPa), and (2) differential stress loading. Mudstone core plugs with different water saturations were tested ultrasonically in undrained conditions in the laboratory. The evolution of P- and S-wave velocities was monitored along multiple ray paths to obtain the elastic anisotropy of the Whitby Mudstone. This study raises awareness about the importance of preserving clay-rich rocks and carrying out their testing adequately in order to minimize the risk of reporting ambiguous laboratory results in the future. The presented results provide insight into the evolution of elastic anisotropy due to changes in water saturation and could help to improve geophysical interpretation for hydrocarbon exploration and production.

4.2 Rock material and laboratory methods

■ 4.2.1 Rock material, sampling, and preparation

The tested mudstone specimens originate from a wave-cut platform of the WMF in the UK (Figure 4.1). This platform is subjected to seawater daily, due to the tidal cycle. Mudstone blocks were collected from the same horizon in this outcrop (lower base Jet Rock Unit) to minimize the heterogeneity between specimens (Figure 4.1). The bulk density of core plugs originating from the Jet Rock Unit is ~2.5 $g.cm^{-3}$ [chapter 3; *Douma et al.*, 2017], the porosity, obtained from the wet and dry mass of a mudstone core, is ~13%, the matrix permeability is in the range of 10^{-23} – 10^{-18} m^2, and pore diameters are between 72 – 300 nm [*Houben et al.*, 2016b].

Figure 4.2 shows two thin sections of mudstone samples taken from the base of the Mulgrave member [*Ten Veen et al.*, 2014]. The fine-grained matrix of the mudstone is essentially composed of clay minerals. Pelagic carbonate, organic matter, fine-grained quartz particles, and pyrite are also present (Figure 4.2a). Figure 4.2b shows the heterogeneity of the mudstones at submillimeter scale, where sharp-based siltstone laminae are grading upward into clay-rich laminae.

The collected mudstone blocks were stored in seawater from the moment of recovery to prevent loss of *in situ* pore fluids, assuming seawater has equilibrated with the clays present in the mudstone blocks over geological time scales, preventing them from shrinking or swelling upon re-saturation with this fluid in the laboratory. Four cylindrical plugs, ~38 mm in diameter and ~80 mm in length, were cored from the same block normal to the horizontal bedding (vertical plugs), using seawater as a cooling fluid. Three core plugs were equilibrated for two months at room temperature within desiccators maintained at a constant relative humidity (85%, 75%, or 35%, respectively). The required relative humidity values were achieved using different over-saturated saline solutions as described in detail by *Laloui et al.* [2013]. Under these relative humidity conditions, the final water saturations of the specimens at equilibrium were 70% ±10%, 58% ±10%, and 28% ±10%, respectively. One preserved sample was stored in seawater and had a water saturation of 92% ±10%. Appendix A details the method used to determine these final saturation states.

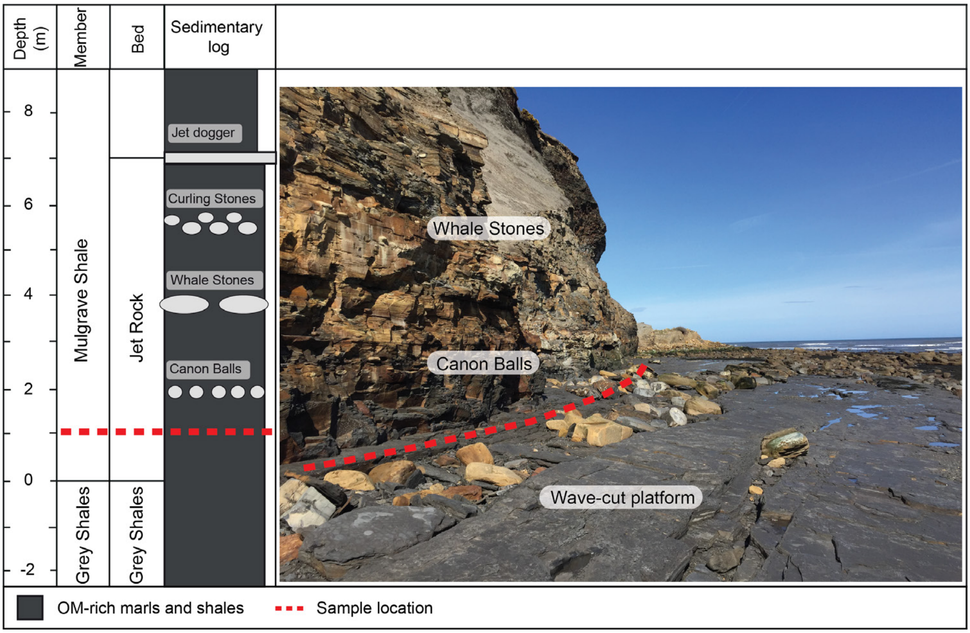

Figure 4.1: *Left: the mudstone core plugs were collected from the same horizon in the stratigraphic log of the WMF modified after Hesselbo et al. [2000]; Zijp et al. [2015]; Houben et al. [2016b]. Right: Mudstone blocks were collected from a wave-cut platform which is subjected to seawater on a daily basis due to tidal cycles.*

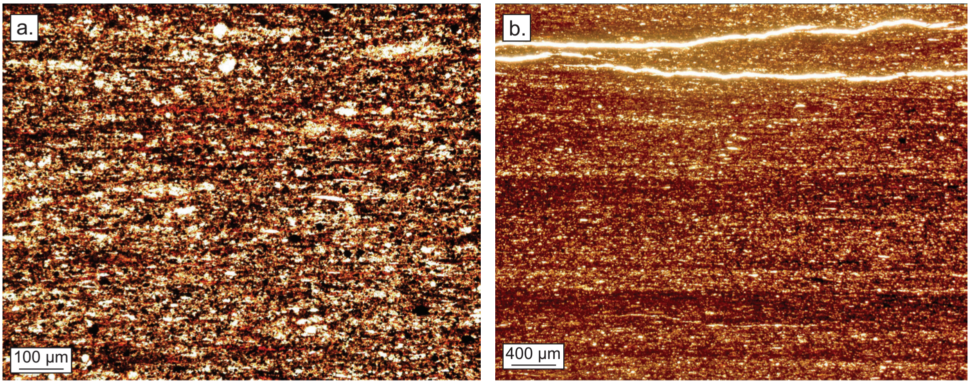

Figure 4.2: *The fine-grained matrix of the Whitby Mudstone mainly consists of clay-minerals (low-chroma, light and dark brown elliptical particles) (a). The intrinsic layering at submillimeter scale where sharp-based siltstone laminae is grading upward into clay-rich laminae is strongly present in these mudstones (b).*

■ 4.2.2 Preliminary characterization

The core plugs with a water saturation (S_w) of 92%, 70%, and 58% were subjected to preliminary Nuclear Magnetic Resonance (NMR) spectroscopy at 2 MHz (Oxford-GIT GeoSpec 2 MHz NMR spectrometer) to determine the water distribution profile along their axis. This technique measures the net magnetization of hydrogen atoms in the presence of an external magnetic field, where the amplitude of the signal corresponds indirectly to the water content of the core plug [*Dillinger and Esteban*, 2014]. The specimens were wrapped in cling film during the NMR measurements to minimize undesired loss of pore fluids. A total of 256 scans were carried out along the sample length. No NMR measurements were performed on the core plug with 28% S_w, because the risk of damaging this specimen was too high due to its fragility, which could have rendered the core plug unsuitable for subsequent mechanical testing.

The pre-deformation internal structure of the mudstone plugs was imaged using an X-ray Computed Tomography (XRCT) scanner. This technique uses X-rays to create a three-dimensional dataset of a sample by stacking cross-sectional two-dimensional X-ray attenuation projections. The loss of pore water from the specimens during the scanning was minimized by carefully wrapping them in cling film and completing a full scan within about five minutes. The created data set has a voxel size of $100\times100\times400$ μm and was visualized using *Avizo 9.5.0* software from ThermoScientific Ltd to assess the homogeneity of the core plugs, and to derive a density profile along the sample length.

■ 4.2.3 Experimental methodology

The equipment used for the mechanical and ultrasonic testing includes a triaxial stress vessel, a multichannel ultrasonic monitoring system, and ultrasonic P- and S-wave transducers [Figure 4.3; *Nadri et al.*, 2012; *Sarout et al.*, 2014, 2015, 2017]. Each core plug was placed in a Viton sleeve to protect it from the surrounding confining oil, and was mounted between top and base steel platens equipped with pore fluid lines. Additional S-wave transducers were also embedded in these platens. Two aluminum spacers with a diameter of 38 mm and thickness of 1 mm where placed at both ends of the partially-saturated core plugs to achieve macroscopically undrained conditions during testing. For the preserved plug, no steel spacers were used to allow the monitoring of the pore pressure during the experiment in macroscopically undrained conditions. The axial displacement between the top and base platens was monitored with two diametrically-opposed linear variable differential transformers (LVDTs) (Figure 4.3a). This dataset was used to calculate the average axial strain of the plug during the experiment. The local circumferential strain was directly measured with a strain gauge-based cantilever mounted through the Viton sleeve on the lateral surface of the core plug.

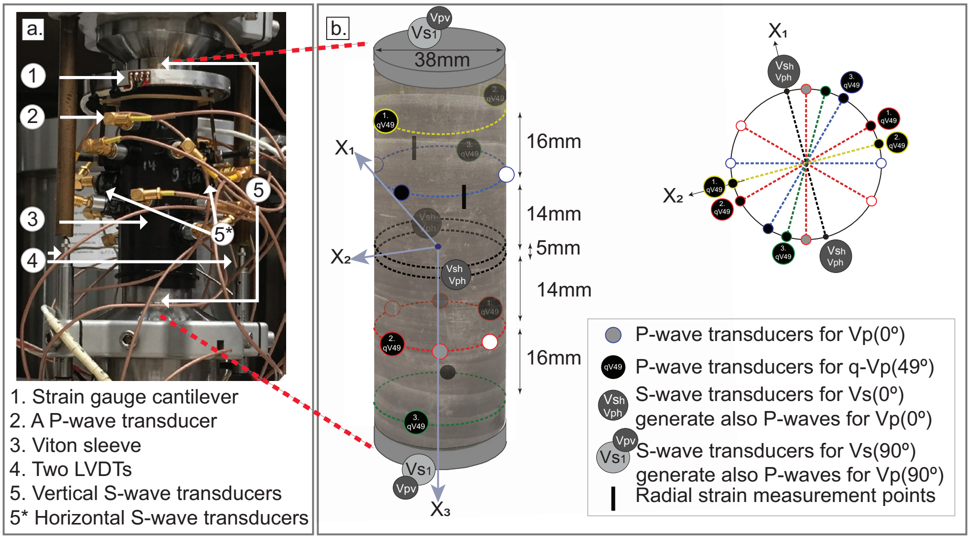

Figure 4.3: *a. Experimental setup in the laboratory. b. Schematic drawing illustrating the position of the ultrasonic P- and S-wave transducers on the horizontally layered, cylindrical mudstone specimen. The measured velocities include: P- and S-wave velocities (1) along the symmetry axis (V_{pv}, V_{sv}), (2) across the core diameter (V_{ph}, V_{sh}), and (3) the P-wave velocity at ~49° to the horizontal bedding plane ($qV_{p(49^{o})}$).*

The testing procedure is different for triaxial testing of the preserved and partially-saturated core plugs. The triaxial testing of the preserved mudstone sample included the following steps (Figure 4.4a):

[1] The preserved core plug (92% S_w) was saturated with brine and the pore pressure was controlled at 0.7 MPa once a confining pressure of 2 MPa was established at a temperature of 40°C ±0.5°C. A temperature of 40°C was selected to minimize the effect of temperature fluctuations during this long-term experiment. The chemical composition of the brine was the same as the composition of the natural seawater, assuming that the pore fluid composition within the WMF reached equilibrium with the surrounding seawater over geological time scales.

[2] The confining pressure was increased at 0.5 MPa.min^{-1} to 27 MPa and the pore pressure controlled at 2 MPa, resulting in an effective stress ($\sigma_i^{'}$) of 25 MPa.

[3] The core plug was consolidated for six weeks at constant isotropic stress conditions ($\sigma_1^{'} = \sigma_2^{'} = \sigma_3^{'} = 25$ MPa) controlling the pore pressure at 2 MPa until extremely low consolidation rates (~0.4 μm.day^{-1}) were reached. At the end of this consolidation stage, the pore network valves were closed to examine whether the pore pressure remained at ~2 MPa, indicating full saturation (100% S_w) and equilibrated pore pressure within the core plug. The extremely low consolidation rates observed in the tests, in combination with the stable pore pressure reached, indicated that the core plug equilibrated and reached full saturation.

[4] A vertical differential stress was applied orthogonal to the bedding ($\sigma_1 > \sigma_2 = \sigma_3$) on the saturated sample in macroscopically undrained conditions (i.e., pore network valves closed, with pore pressure monitoring, but no active pore pressure control), allowing the pore pressure to increase during loading. The core plug was deformed with a constant axial displacement rate (strain rate of 10^{-7} s^{-1}) until failure. A low strain rate was selected, so that the pore fluid has time to equilibrate within the volume of the low permeability plug during deformation. Failure occurred after two days.

In contrast, the three partially-saturated core plugs were tested with top and base aluminum spacers under macroscopically undrained conditions (i.e., no pore pressure control or monitoring, and no fluid allowed to exit the partially saturated plug). The key testing steps were as follows (Figure 4.4b):

[1] The confining pressure was increased to 25 MPa at 0.5 MPa.min^{-1}.

[2] The core plug consolidated for three days under constant isotropic stress conditions ($\sigma_1^{'} = \sigma_2^{'} = \sigma_3^{'} = 25$ MPa) and room temperature conditions (22°C ±1.5°C). Consolidation rates of ~40 $\mu\text{m.day}^{-1}$ were reached after three days of consolidation. It is assumed that the pore pressure in the partially-saturated core plugs remains zero during deformation.

[3] A vertical differential stress was applied orthogonal to the bedding ($\sigma_1 > \sigma_2 = \sigma_3$) on the partially-saturated core plugs. Each core plug was deformed with a constant axial displacement rate (strain rate of 10^{-7} s^{-1}) until failure. Failure occurred after 3 - 4 days.

Ultrasonic-wave velocity measurements were conducted along multiple propagation ray paths on a single core plug to calculate the full elastic tensor, assuming a vertical transversely isotropic (VTI) elastic medium. Four *S*-wave transducers (diameter 12 mm) and fourteen *P*-wave transducers (diameter 8 mm and dominant resonant frequency ~0.5 MHz) were directly attached to the core plug through the Viton sleeve to obtain the *P*- and *S*-wave velocities (1) along the symmetry axis (V_{pv}, V_{sv}), (2) across the core diameter (V_{ph}, V_{sh}), and the *P*-wave velocity (3) at ~49° to the horizontal bedding plane ($qV_{p(49°)}$) (Figure 4.3b). The *S*-wave transducers generated both *P*- and *S*-waves. A complete set of five *P*- and *S*-wave velocity measurements carried out at any specific stage of the experiment is referred to as a velocity survey. In fact, multiple velocity surveys were carried out during the three key stages of the experiment, i.e., during (1) the isotropic stress (confining pressure) loading to reach the simulated *in situ* conditions, (2) the consolidation ($\sigma_1^{'} = \sigma_2^{'} = \sigma_3^{'} = 25$ MPa), and (3) the differential stress loading up to failure ($\sigma_1 > \sigma_2 = \sigma_3$). A velocity survey was performed every two minutes during the confining pressure loading, every six hours during the consolidation stage, and every hour during the differential stress loading stage (Figure 4.4). Each survey consists of 18 consecutive shots fired by each transducer acting as a source. During each shot, the remaining 17 transducers act as receivers and the transmitted signals (waveforms) were recorded with a sampling rate of 10 MHz (sampling period of 0.1 μs).

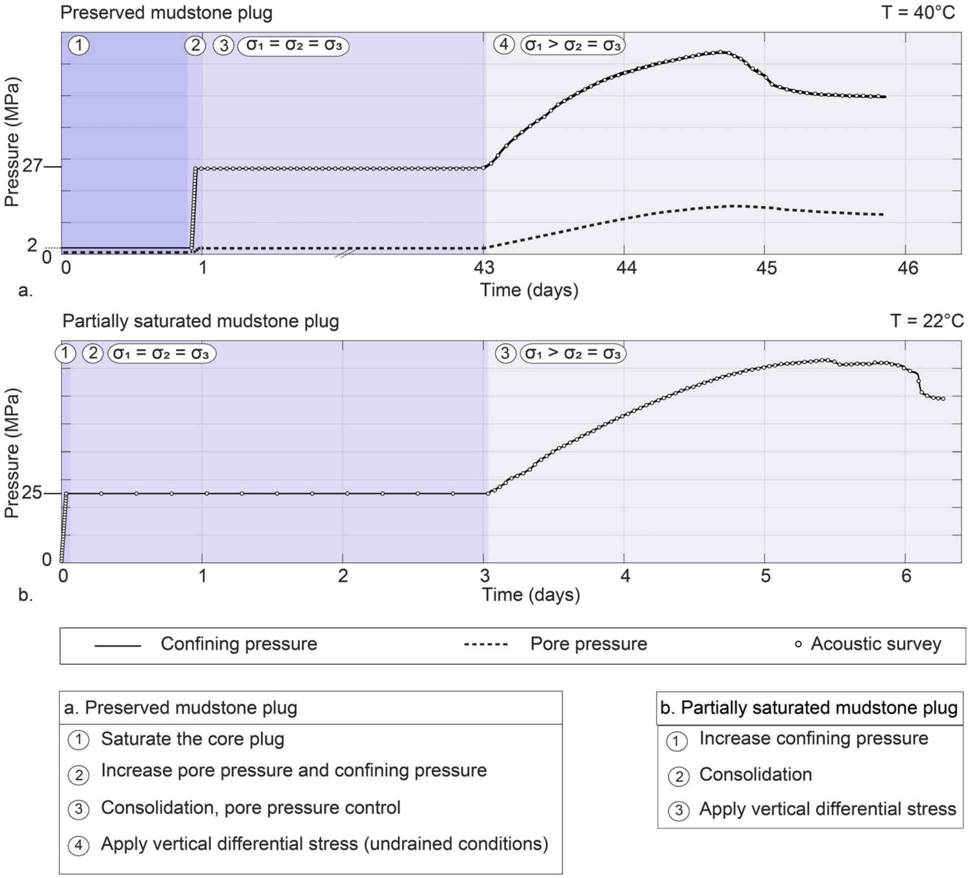

Figure 4.4: *Schematic diagrams of the experimental protocols for the a. preserved, and b. partially-saturated mudstone plugs. Three stages can be differentiated, including (1) increase in effective confining pressure up to 25 MPa, (2) consolidation at isobaric stress conditions, and (3) differential stress loading (anisotropic stress conditions). Note that testing the preserved mudstone plug is very time consuming due to the extra saturation stage.*

For illustration purposes, Figure 4.5 shows typical waveforms recorded during the consolidation stage of two partially-saturated core plugs (70% and 28%, respectively). P-wave arrival times were picked at the first break on the zero crossing. Uncertainties for the P-wave arrival times are ± 0.2 μs. S-wave arrival times were picked on the break of the wave on the zero crossing, when a significant change in shape of the waveform was observed (e.g., sudden increase in amplitude, see Figure 4.5c, d). S-wave picking was sometimes challenging (see e.g., Figure 4.5a, b). The quality of the waveforms was the highest during the consolidation stage. Therefore, S-waves were picked during this stage, and followed during the differential stress loading (cross correlation), so that the S-wave picking was consistent throughout the experiment. An attempt was made to improve S-wave picking by filtering out the high and low frequency components (i.e., band pass [5 kHz, 1.5 MHz]) in the recorded waveforms to no avail. Also, surface waves (e.g., Rayleigh waves with high amplitude) were picked (Figure 4.5b). Since the Rayleigh wave velocity is often lower than the S-wave velocity, the S-wave velocity could be estimated [see: *Wapenaar*, 1989]. As an additional guidance for the S-wave picking, the obtained V_p/V_s ratios were compared with V_p/V_s ratios of clay-rich shales available in the literature [*Dewhurst and Siggins*, 2006]. Finally, the dynamic Poisson's ratio (ν_{31}), obtained from the P- and S-wave velocities, was used to check consistency with the expected parameters bounds obtained for the WMF [e.g., *Zhubayev et al.*, 2016]. Uncertainties for S-wave arrival times are in the range ± 7 μs to ± 9 μs for the vertical S-waves (V_{sv}), and about ± 1 μs for the horizontal S-waves (V_{sh}).

4.2.4 Ultrasonic data reduction

The elastic coefficients C_{ij} of the rock are related to the phase velocity of elastic waves propagating along different directions with respect to the symmetry axes of the assumed vertical transversely isotropic (VTI) rock:

$$C_{11} = \rho V_{ph}^2(0^\circ) \tag{4.2.1}$$

$$C_{33} = \rho V_{pv}^2(90^\circ) \tag{4.2.2}$$

$$C_{44} = \rho V_{sv}^2(90^\circ) \tag{4.2.3}$$

$$C_{66} = \rho V_{sh}^2(0^\circ) \tag{4.2.4}$$

where ρ is the bulk density, and the angles represent the direction of propagation with respect to the bedding plane. The average value of the phase velocities measured along multiple ray paths having the same propagation direction with respect to the bedding plane were used in the above equations. The quasi-P-wave phase velocity ($qV_{p\theta}$) and its corresponding phase angle (θ) are related to M, from which C_{13} can be obtained [*Mavko et al.*, 2009]:

$$qV_{p\theta} = (C_{11}sin^2\theta + C_{33}cos^2\theta + C_{44} + \sqrt{M})^{\frac{1}{2}}(2\rho)^{-\frac{1}{2}} \tag{4.2.5}$$

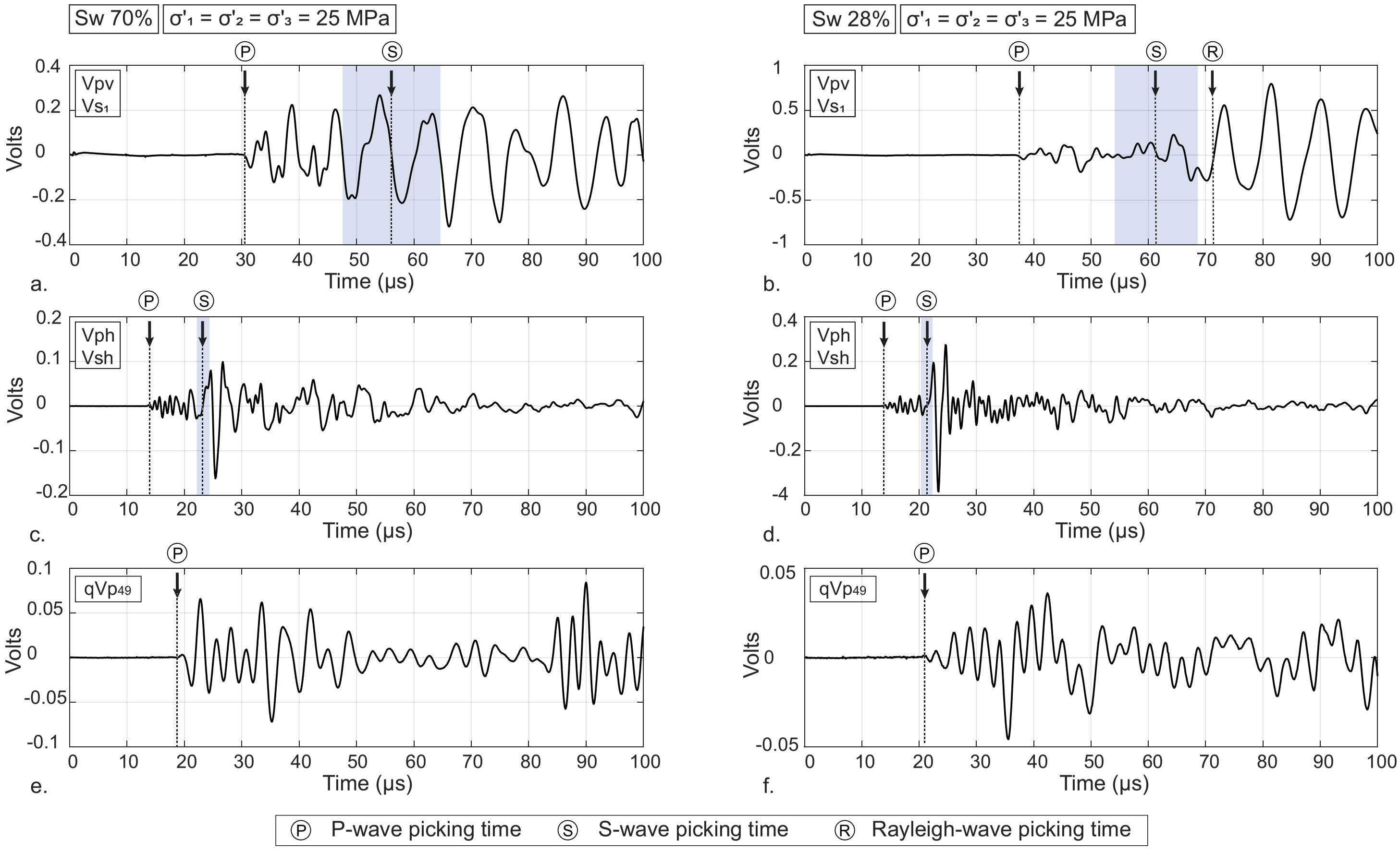

Figure 4.5: *Examples of waveforms at isotropic stress conditions ($\sigma_1^{'} = \sigma_2^{'} = \sigma_3^{'} = 25$ MPa). The quality of the waveforms vary significantly with water saturation and orientation, resulting in large picking uncertainties (highlighted in blue) for the S-waves (a, b). As a guideline, the S-waves were picked when significant change in shape of the waveform was observed. To check the reliability of the picked S-waves, the V_p/V_s ratio and dynamic Poisson's ratio were calculated.*

Where M is defined as:

$$M = [(C_{11} - C_{44})sin^2\theta - (C_{33} - C_{44})cos^2\theta]^2 + (C_{13} + C_{44})^2 sin^2 2\theta \qquad (4.2.6)$$

Finally, the anisotropy parameters ε, γ, and δ are also related to the elastic coefficients (and therefore to the phase velocities) as follows [*Thomsen*, 1986]:

$$\varepsilon = \frac{C_{11} - C_{33}}{2C_{33}} \qquad (4.2.7)$$

$$\gamma = \frac{C_{66} - C_{44}}{2C_{44}} \qquad (4.2.8)$$

$$\delta = \frac{(C_{13} + C_{44})^2 - (C_{33} - C_{44})^2}{2C_{33}(C_{33} - C_{44})} \qquad (4.2.9)$$

During the laboratory tests, arrival times were measured on a single core plug to obtain the full elastic tensor (Figure 4.3). For wave propagation along the symmetry axes of the VTI rock, group (ray) and phase velocity are equal. However, for the off-axes $qV_{p\theta}$, phase and group velocities can differ significantly, depending on the overall magnitude of the anisotropy. In our experimental configuration, the quasi-P-wave flight time picked in a given waveform, and the corresponding travel distance yield a group velocity [*Dewhurst and Siggins*, 2006; *Sarout et al.*, 2015; *Kovalyshen et al.*, 2018]. The ray path angle ϕ with respect to the bedding (symmetry) plane is about 49°. To obtain the elastic constant C_{13}, and hence the anisotropy parameter δ, this ray angle and velocity are first converted to phase angle θ and velocity $qV_{p\theta}$, using the method as described in detail by *Dewhurst and Siggins* [2006]. The ray path length was corrected for changes induced by axial- and radial deformation during testing. Uncertainties for the velocities, elastic constants, and anisotropy parameters were calculated with the method of error propagation assuming Gaussian (random) errors.

4.3 Results

4.3.1 Petrophysical properties

The core plugs with different water saturations, their density and water content profiles are shown in Figure 4.6. The XRCT images show that the core plugs are thinly layered, with a horizontal bedding supported mainly by local fluctuation of clay minerals content. The lighter layers correspond to relatively high-density minerals, representing carbonate-rich layers, while the darker layers represent incipient fractures resulting from clay dehydration (Figure 4.6b, c, d). No fractures were observed in the preserved core plug (Figure 4.6a). This suggests that coring resulted in limited damage visible at the resolution of the XRCT images. Local high-density spots (bright spots) were observed in Figure 4.6a, b, d, which suggests the presence of pyrite or fossils in the form of (pyritized) ammonites, often reported in shales and in the WMF in particular [*Powell*, 2010].

The corresponding density- and water content profiles were derived from the intensity (grey levels) of the XRCT images, and from the NMR spectroscopy, respectively. An overall density increase from the sample top to bottom was observed for all the core plugs (Figure 4.6). This observation supports the assumption of similarity of the structure of the different core plugs originating from the same horizon within the outcrop. Thus, differences in physical properties between the plugs can more reliably be attributed to their difference in water content or saturation. The average bulk density for the core plugs is ±2.45 $g.cm^{-3}$ (92% S_w), ±2.47 $g.cm^{-3}$ (70% S_w), ±2.46 $g.cm^{-3}$ (58% S_w), and ±2.45 $g.cm^{-3}$ (28% S_w) (Table 4.1). The average water content is 0.073 mL (92% S_w), 0.051 mL (70% S_w), and 0.041 mL (58% S_w) (Table 4.1), and correlates positively with the average saturation of the core plugs (Figure 4.6a, b, c). The water content is not uniform along the core plugs, and significant drops were observed in the vicinity of the horizontal incipient fractures in the partially-saturated samples (Figure 4.6a, b, c).

Table 4.1: *Experimental conditions, petrophysical and mechanical properties of the Whitby Mudstone core plugs (WMF-92, WMF-70, WMF-58, WMF-28).*

		WMF-92	**WMF-70**	**WMF-58**	**WMF-28**
Sample properties					
Length	mm	90.45 ± 0.1	77.86 ± 0.1	90.60 ± 0.1	85.42 ± 0.1
Diameter	mm	37.66 ± 0.1	37.56 ± 0.1	37.98 ± 0.1	37.73 ± 0.1
Experimental conditions					
Confining pressure	MPa	27	25	25	25
Pore pressure	MPa	2	-	-	-
Temperature	°C	40 ± 0.5	22 ± 1.5	22 ± 1.5	22 ± 1.5
Deformation rate	$mm.hr^{-1}$	0.0326	0.0280	0.0326	0.0308
Petrophysical properties					
Initial water saturation	%	92 ± 10	70 ± 10	58 ± 10	28 ± 10
Avg. bulk density	$g.cm^{-3}$	2.452 ± 0.006	2.466 ± 0.006	2.464 ± 0.006	2.456 ± 0.006
Avg. water content	mL	0.073 ± 0.004	0.051 ± 0.005	0.041 ± 0.004	-
Mechanical properties					
Peak stress	MPa	27 ± 0.7	41 ± 1	47 ± 1.2	55 ± 1.4
Static Young's modulus (E_3)	GPa	1.2 ± 0.2	2.9 ± 0.2	3.8 ± 0.2	4.7 ± 0.2
Static Poisson's ratio (ν_{31})	-	0.36 ± 0.02	0.21 ± 0.02	-	0.17 ± 0.01

4.3.2 Geomechanical properties

Figure 4.7 reports the mean effective stress-strain curves recorded during the axial loading of the preserved/re-saturated and partially-saturated core plugs at 25 MPa of initial effective pressure. Plotting the stress data as mean effective stress

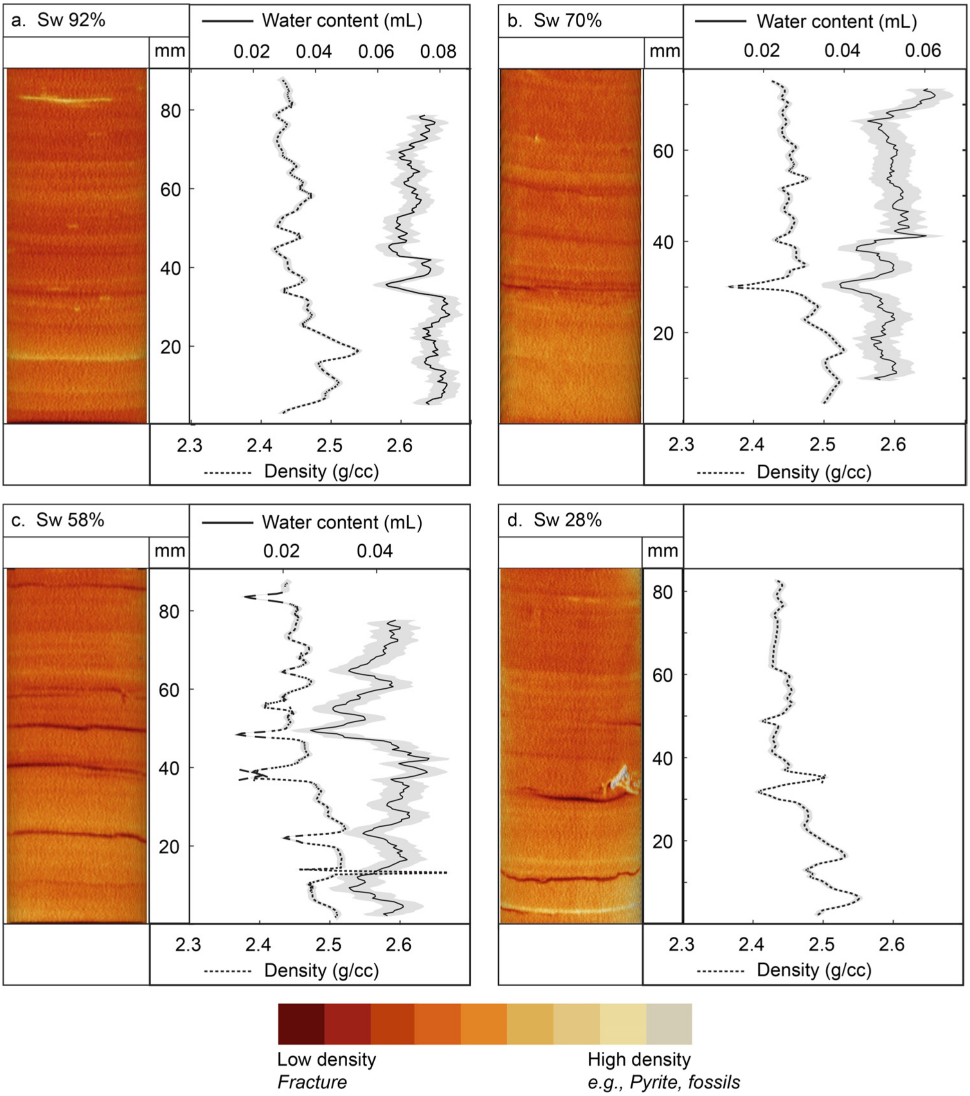

Figure 4.6: *XRCT images, and their corresponding density profile obtained from the images for the Whitby Mudstone core plugs at a. preserved and b., c., d. partially-saturated conditions. The grey area indicates the uncertainty. The water distribution along the core axis is obtained from NMR spectroscopy. NMR spectroscopy has not been performed on the sample with 28%* S_w *due to the low cohesion of this core plug. Bedding-parallel fractures develop due to dehydration.*

($\sigma'_m = \frac{\sigma'_1\sigma'_2+\sigma'_3}{3}$) incorporates the pore pressure evolution during loading. The reader is referred to Figures 5.3 and 5.4c in chapter 5 for the pore pressure evolution during axial loading and the differential stress-strain curves, respectively. Note that a pore pressure of 0 MPa is assumed for the partially-saturated core plugs. This assumption might be incorrect, since dehydration of low-permeability and clay-rich rocks can lead to a negative pore pressure (i.e., suction) [*Onaisi et al.*, 1994]. However, to our knowledge, there is no established relationship between the amount of suction and the stress applied on clay-rich rocks, which limits an accurate estimation of the applied mean effective stress.

Water saturation has a significant impact on the Young's modulus and peak strength of the Whitby Mudstone (Figure 4.7 and Table 4.1). A higher peak stress is recorded with the decrease in water saturation (Figure 4.7a). The peak stress for the plug with 58% S_w could only be extrapolated from the incomplete stress-strain data set, because the maximum LVDT displacement was reached slightly before sample failure. Overall, higher axial and radial strains are accommodated by the core plugs before failure with decreasing water saturation. The core plug with 28% S_w exhibits a sudden drop of the mean effective stress after the peak, which is not observed in the higher water saturation cases (Figure 4.7a). This might highlight a transition from a brittle failure to a more ductile yield [*Nygård et al.*, 2006] at the applied stress conditions, induced by the increasing water content.

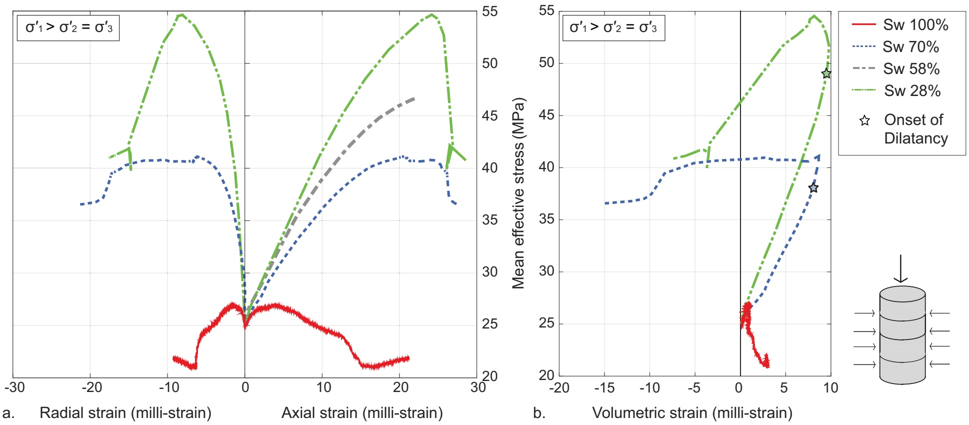

Figure 4.7: *a. Mean effective stress-strain behavior of the Whitby Mudstone samples at different saturations during axial loading. The water saturation (S_w) has a significant impact on the mechanical behavior of these clay-rich rocks. b. The partially-saturated samples become dilatant (decrease in volumetric strain), whereas the re-saturated/preserved sample remains compactive (increase in volumetric strain) during axial loading.*

The static Young's modulus (E_3) and Poisson's ratio (ν_{31}) were calculated from the linear part of the axial stress-axial strain and axial stress-radial strain curves and are reported in Table 4.1. The subscript of E refers to the loading direction (vertical direction, here defined as x_3) and for ν to the elastic strain in the horizontal direction (here x_1) to the stress applied in the x_3 direction, so that the measured Young's modulus and Poisson's ratio can be written as E_3 and ν_{31}, respectively. Note that Poisson's ratio of the core plug with 58% S_w could not be inferred due to a loss of the radial strain measurement during the test. With the water saturation decreasing from 100% to 28%, Young's modulus increases from 1.2 to 4.7 GPa and Poisson's ratio decreases from 0.36 to 0.17, respectively. Figure 4.7b shows the volumetric deformation of the saturated and partially-saturated mudstone plugs during loading. The total volumetric strain at a given differential stress is higher for a lower water saturation. For the partially-saturated mudstone plugs, the volumetric strain increases up to a mean effective stress of ~38 MPa for 70% S_w, or ~49 MPa for 28% S_w. A subsequent decrease of the volumetric strain, denoting the onset of dilation, is observed after these points. In contrast, no dilatancy point is recorded for the resaturated mudstone (100% S_w) plug for which the volumetric deformation remains compressive (positive) even after yield.

■ 4.3.3 Elastic properties

Ultrasonic wave velocity surveys were analyzed during three specific stages of the experiments, i.e., (1) hydrostatic loading, (2) consolidation at constant mean effective pressure, and (3) differential stress loading.

Hydrostatic loading

Figure 4.8 shows the evolution V_{ph} and V_{pv} for the preserved core plug and the three partially-saturated core plugs when increasing the confining pressure. For all the saturation states, the magnitude of V_{ph} is larger compared to V_{pv}, since waves propagate faster along the bedding or the fractures than across them [e.g., *Jones and Wang*, 1981]. No significant change in V_{ph} and V_{pv} is observed for the preserved sample (Figure 4.8a). In contrast, the partially-saturated samples show a significant sensitivity of V_{ph} and V_{pv} to the mean effective pressure and exhibit a non-linear trend (Figure 4.8b, c, d). This trend was also observed in previous studies [e.g., *Jones and Wang*, 1981; *Vernik and Landis*, 1996; *Pervukhina et al.*, 2008; *Dewhurst et al.*, 2011]. The largest increase in V_{pv} is observed at the first increment of effective pressure. Beyond ~17 MPa effective pressure, V_{pv} is virtually constant at 70% S_w and 58% S_w (Figure 4.8b, c) and beyond ~10 MPa effective pressure at 28% S_w (Figure 4.8d). The increase in V_{ph} is noticeable, but remains significantly less pronounced than the stress sensitivity in the vertical direction. The non-linear increase in velocity with increasing effective pressure in the partially saturated plugs is most likely related to fracture closure [*Kuila et al.*, 2011], and possibly the changes in water saturation within these fractures associated with a reduction in their volume. The linear trend observed for the preserved plug suggests that if such mechanisms are at play, their impact on V_{pv} and V_{ph} is relatively insignificant. The limited velocity change in the preserved mudstone plug could be due to (1) the absence of fractures (Figure 4.6) or (2) if smaller fractures are present (below resolution of the XRCT-image), they could be water saturated and thus incompressible. Another explanation is that, although the pore pressure is controlled at both ends of the core plug, the change in effective stress might be limited due to the increase in pore pressure within the sample during hydrostatic loading.

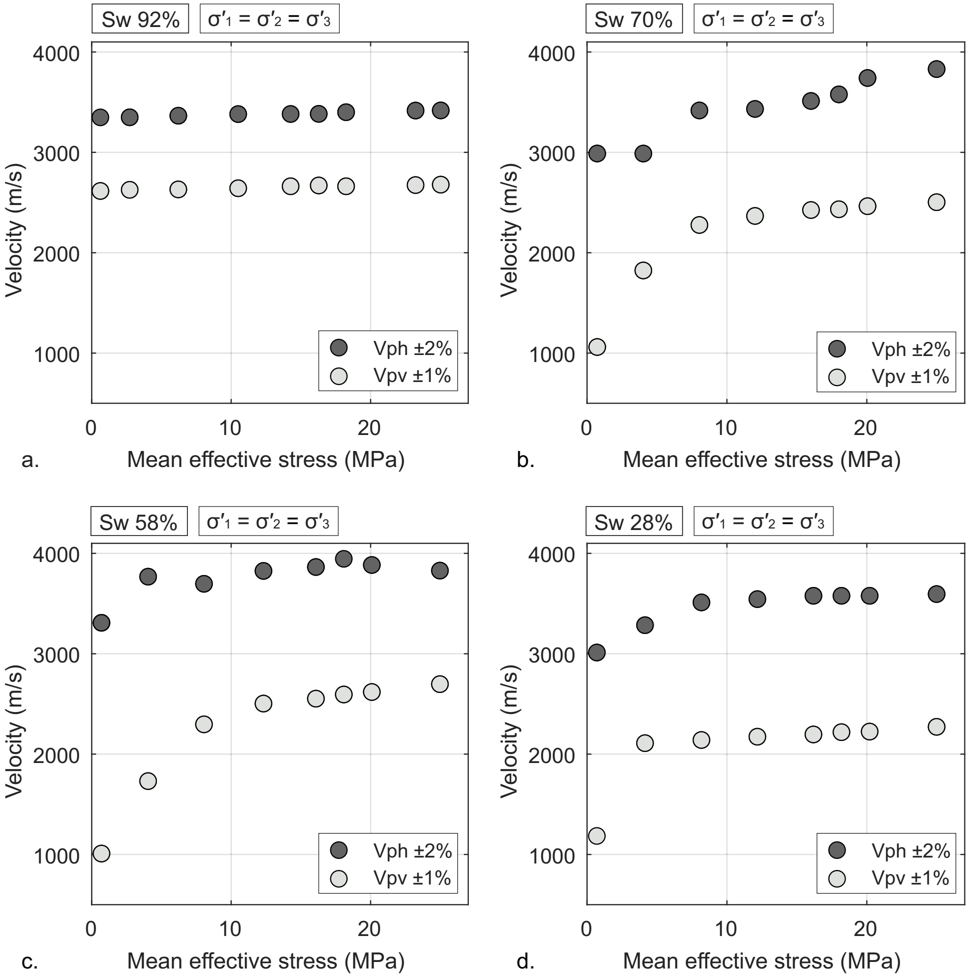

Figure 4.8: *Relationship between P-wave velocity and mean effective pressure for the mudstone samples at water saturations (S_w) of a. 100%, b. 70%, c. 58% and, d. 28%. For the saturated core plug, there is no significant change in V_{ph} and V_{pv} when increasing the mean effective pressure, whereas these velocities increase in the partially-saturated core plug due to the closure of bedding parallel fractures.*

Consolidation at constant effective pressure

The impact of water saturation on the group velocities obtained at three different stages during consolidation ($\sigma_1^{'} = \sigma_2^{'} = \sigma_3^{'} = 25$ MPa) is shown in Figure 4.9. The recorded wave velocities remain relatively unaffected by consolidation, although they are sensitive to the saturation state. The V_{ph} decreases from ~4000 m/s to ~3800 m/s with decreasing water saturation from 100% to 28%. The most significant velocity changes with decreasing water saturation are observed for $qV_{p(49^\circ)}$ decreasing from ~3420 m/s to ~3060 m/s (i.e., a 10.5% reduction), and for V_{pv} decreasing from ~3130 m/s to ~2620 m/s (i.e., a 16.3% reduction). For the same decrease in saturation, the V_{sh} increases from ~2300 m/s to ~2520 m/s (i.e., a 9.6% increase); whereas the change in V_{sv} is less significant, decreasing from ~1700 m/s to 1590 m/s (i.e., a 6.5% reduction), which is within experimental uncertainty. As reported in Figure 4.10, V_{ph}/V_{sh} decreases from ~1.71 to ~1.51 with decreasing water saturation. A similar trend is observed for V_{pv}/V_{sv}, decreasing from ~1.84 to ~1.66 (Figure 4.10).

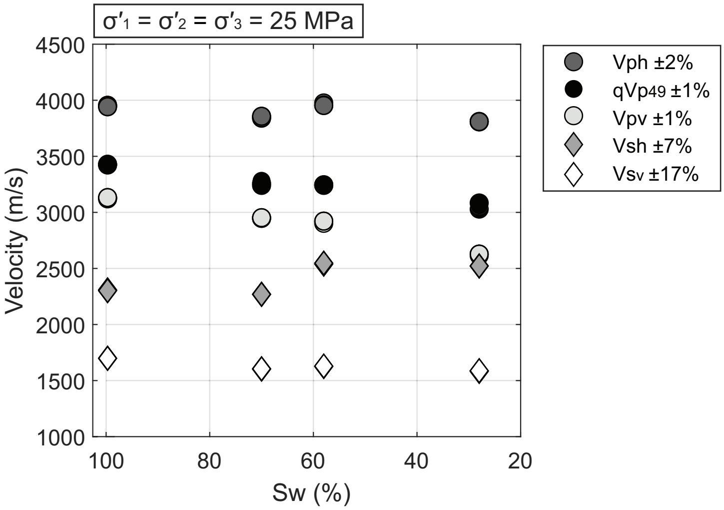

Figure 4.9: *Impact of water saturation (S_w) on the group velocities during consolidation ($\sigma_1^{'} = \sigma_2^{'} = \sigma_3^{'} = 25$ MPa). V_{pv} and qV_{p49} are affected the most by the degree of water saturation.*

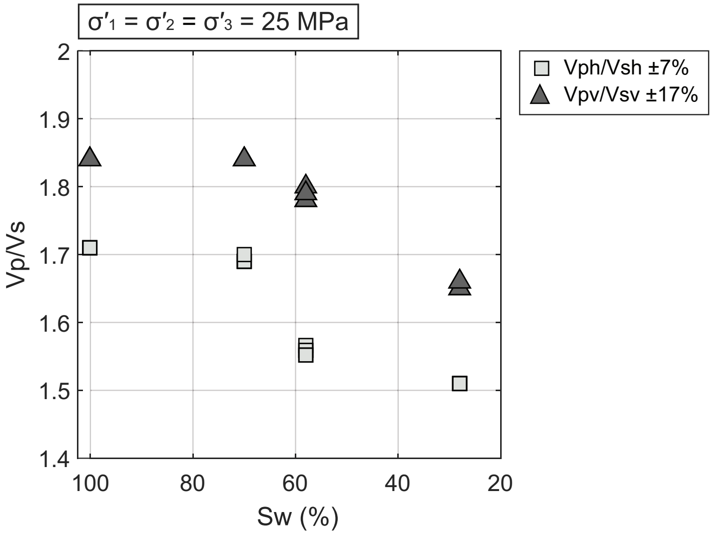

Figure 4.10: *Impact of water saturation (S_w) on the V_p/V_s ratios during consolidation. Both horizontal and vertical V_p/V_s ratio's decreases with dehydration.*

The evolution of the elastic coefficients (C_{11}, C_{33}, C_{44}, C_{66}, C_{13}) with water saturation during consolidation is shown in Figure 4.11. C_{11} and C_{44} slightly decrease with decreasing S$_w$ from 100% to 28%. However, this change remains limited and within experimental uncertainty. For the same saturation reduction, (1) the elastic coefficient C_{33} decreases from ~24 GPa to ~17 GPa, (2) C_{13} drops from ~10 GPa to ~6 GPa, although the uncertainty on this specific coefficient is significant (±53%), and (3) C_{66} increases from ~13 to ~16 GPa.

Figure 4.12 shows the anisotropy parameters (ε, γ, δ) obtained at three different stages during consolidation ($\sigma_1^{'} = \sigma_2^{'} = \sigma_3^{'} = 25$ MPa) for water saturations of 100%, 70%, 58%, and 28%. Consolidation has no significant impact on the anisotropy parameters. However, a clear trend is observed for the P-wave anisotropy parameter ε, which increases from ~0.30 to ~0.55 with S$_w$ decreasing from 100% to 28% (Figure 4.12a). A similar trend is observed in this saturation range for the S-wave anisotropy parameter γ, which increases from ~0.42 to ~0.76 (Figure 4.12b). The high values for ε and γ are consistent with results obtained in chapter 3 on the 'dry' core plugs tested on the benchtop. Note that the results obtained in this chapter cannot be compared one to one to the results presented in chapter 3, since the degree of saturation of the core plugs in chapter 3 is not known and the samples were not subjected to a confining pressure. No significant changes are observed for the elastic anisotropy parameter δ at water saturations ranging from 100% - 58% (Figure 4.12c), but increases from ~0 to 0.15 for S$_w$=28%. Note that the uncertainty for δ is extremely large (±0.5), making the value of this parameter either positive or negative.

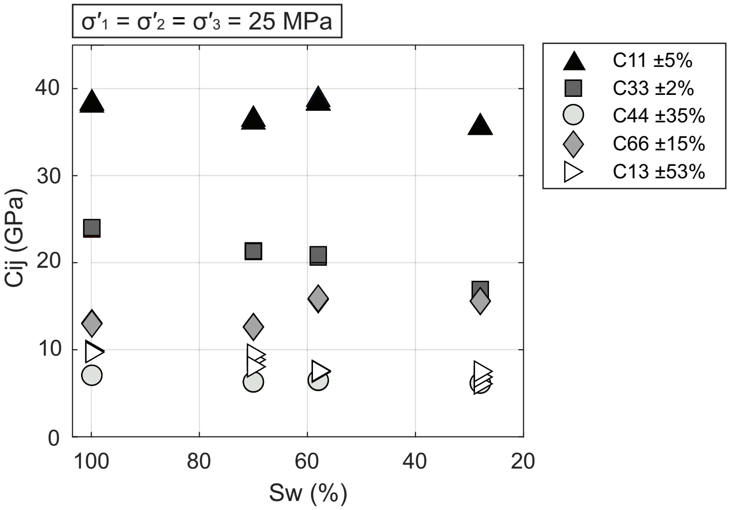

Figure 4.11: *The response of the elastic coefficients to water saturation (S_w) at three different stages during consolidation. A change in saturation has the highest impact on C_{33} and C_{66}. Note that the error for C_{13} is large.*

Differential stress loading

Figure 4.13 shows the mean effective stress-velocity plots for the Whitby Mudstone samples with varying water saturations. No significant velocity change is observed for the fully-saturated Whitby Mudstone core plug during deformation (Figure 4.13a). At S_w = 70%, V_{ph} is relatively constant and slightly decreases at the onset of dilatancy (Figure 4.13b). $qV_{p(49^\circ)}$ and V_{pv} increase from 3260 m/s to 3535 m/s and 2950 m/s to 3215 m/s, respectively. Only three data points were successfully recorded for Vsv due to a poor S-wave signal during the loading. At S_w = 58%, V_{ph} is relatively constant when the mean effective stress is between ~25 MPa and ~38 MPa, and decreases from ~3950 m/s to ~3760 m/s after this point. An overall increase in $qV_{p(49^\circ)}$, V_{pv}, and V_{sv} is observed during differential stress loading: $qV_{p(49^\circ)}$ increases from ~3240 m/s to ~3545 m/s, V_{pv} increases from ~2920 m/s to ~3214, and V_{sv} increases from ~1625 m/s to ~1870 m/s. No significant change is observed for V_{sh}. At S_w=28%, V_{ph} increases slightly from ~3800 m/s to ~3870 m/s when the mean effective stress increases up to the onset of dilatancy, and decreases to ~3820 m/s after this point (Figure 4.13d). An increase in $qV_{p(49^\circ)}$, V_{pv}, and V_{sv} with increasing differential stress is noticeable: $qV_{p(49^\circ)}$ increases from ~3030 m/s to ~3460 m/s, V_{pv} increases from ~2920 m/s to ~3215 m/s, and V_{sv}

increases from ~1580 m/s to ~1670 m/s. No significant change is observed for V_{sh}.

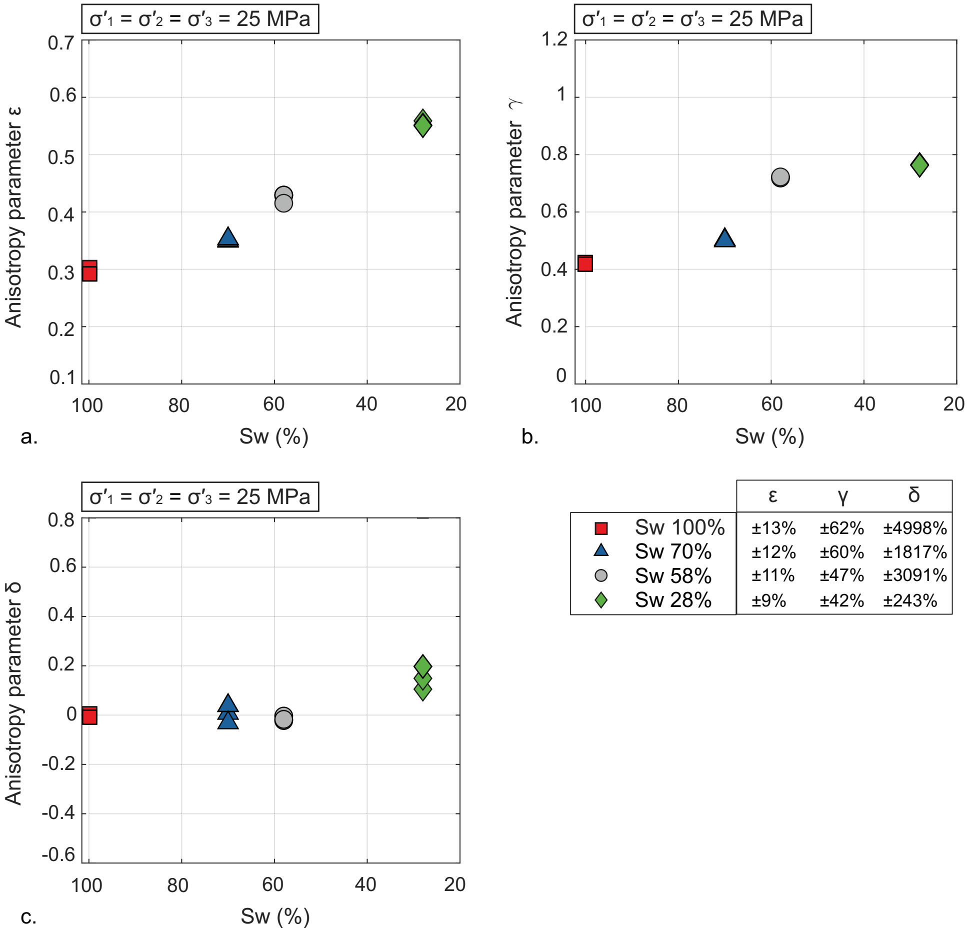

		ε	γ	δ
🟥	Sw 100%	±13%	±62%	±4998%
▲	Sw 70%	±12%	±60%	±1817%
●	Sw 58%	±11%	±47%	±3091%
◆	Sw 28%	±9%	±42%	±243%

Figure 4.12: *P- (ε) and S-wave (γ) anisotropy increases with decreasing water saturation (S_w) (a, b). There is no clear change in wave front geometry governed by Thomsen's δ parameter with dehydration (c). Note that the uncertainty for δ is extremely large. The anisotropy parameters do not evolve significantly during consolidation but are significantly affected by the state of water saturation.*

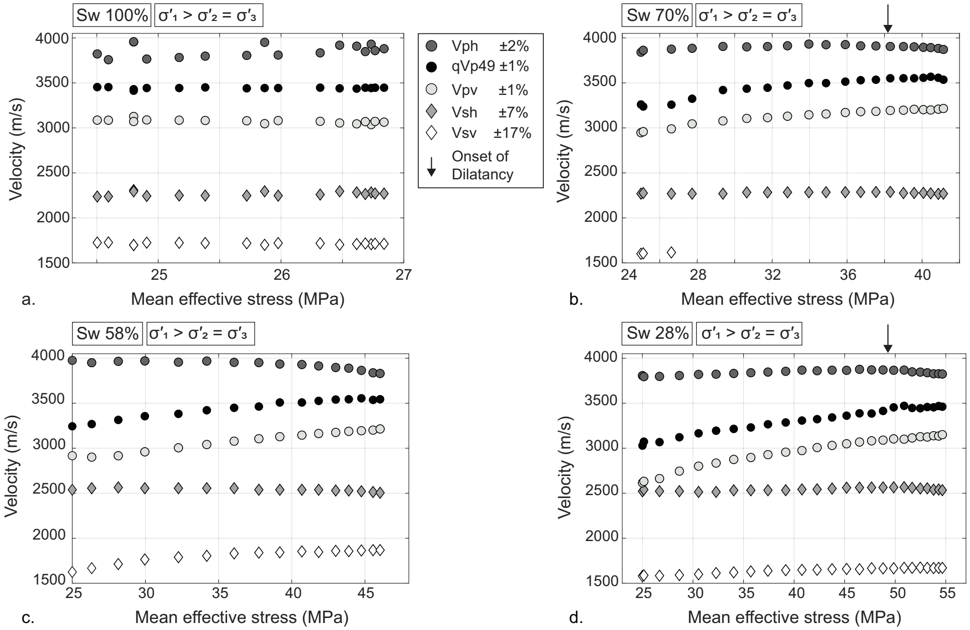

Figure 4.13: *Mean effective stress-velocity plots for the Whitby Mudstone. Note that the velocities are relatively constant with increasing mean effective stress for the saturated core plug (a). For the partially-saturated ones,* $qV_{p(49^\circ)}$ *and* V_{pv} *are the most sensitive to an increase in mean effective stress.*

The impact of the mean effective stress on the elastic coefficients is reported in Figure 4.14. For the fully-saturated Whitby Mudstone sample, no significant change in the elastic coefficients is observed (Figure 4.14a). At $S_w = 70\%$, C_{11} and C_{66} remain relatively constant, whereas C_{33} increases from $\sim$21 GPa to $\sim$25 GPa during loading (Figure 4.14b). At $S_w = 58\%$, C_{11} is relatively constant ($\sim$39 GPa) up to a mean effective stress of $\sim$38 MPa, and decreases to $\sim$36 GPa afterwards (Figure 4.14c), while C_{44} and C_{66} are not significantly affected. C_{33} and C_{13} are most affected by the mean effective stress, with recorded increases from $\sim$21 GPa to $\sim$26 GPa, and from $\sim$10 GPa to $\sim$14 MPa, respectively. Similar trends are observed for the partially-saturated sample at $S_w = 28\%$ (Figure 4.14d). C_{11} is relatively constant ($\sim$35 GPa) up to the onset of dilatancy, and decreases slightly after this point, while C_{44} and C_{66} remain constant. The most significant stress sensitivity is observed for C_{33} and C_{13}, increasing from $\sim$15 GPa to $\sim$25 GPa, and from $\sim$6 GPa to $\sim$15 GPa, respectively.

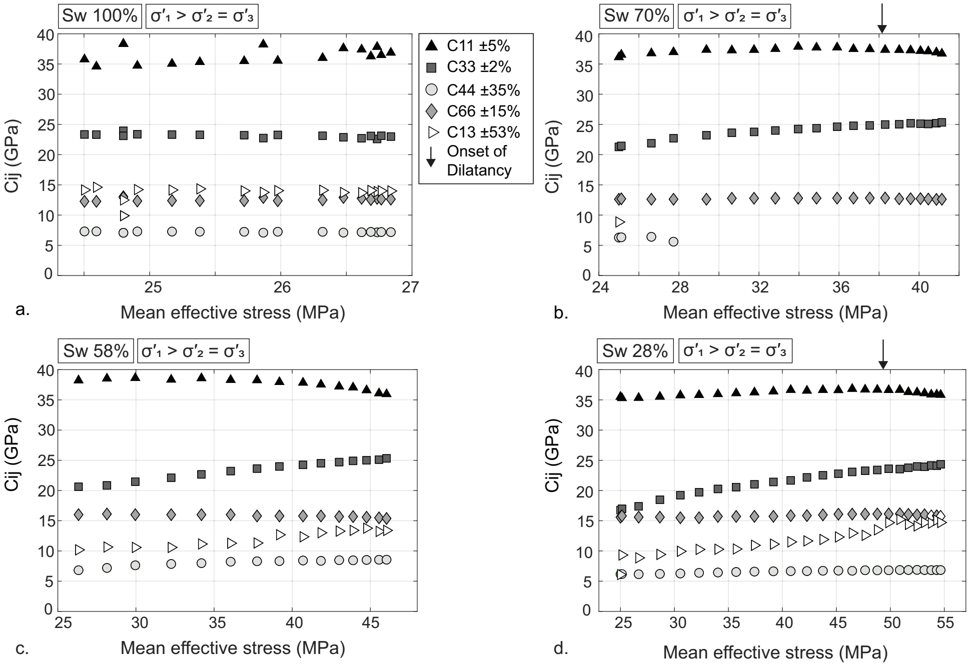

Figure 4.14: *Mean effective stress-C_{ij} plots for the Whitby Mudstone during axial loading. An increase in mean effective stress does not significantly change the elastic coefficients of the saturated core plug (a). For the partially-saturated ones, C_{33} and C_{13} are most sensitive to an increase in mean effective stress (b, c, d).*

The effect of mean effective stress on the calculated elastic anisotropy parameters is reported in Figure 4.15. The anisotropy parameters ε, γ, and δ are strongly dependent on the mean effective stress. ε and γ decrease with increasing mean effective stress, irrespective of the water saturation state (Figure 4.15a, b). The trend for the 100% S_w core plug is different compared to the partially-saturated ones, since the pore pressure (only monitored for the saturated core plug) increases with loading, affecting the mean effective stress. The value of δ (quantifies the departure of the wave front geometry from an ellipsoid) for the fully-saturated mudstone sample fluctuates between 0.26 and 0.30 (Figure 4.15c). At lower water saturations (58% S_w and 28% S_w), and in contrast with ε and γ, the evolution of δ with mean effective stress is non-monotonic, although the uncertainty in the determination of δ is high.

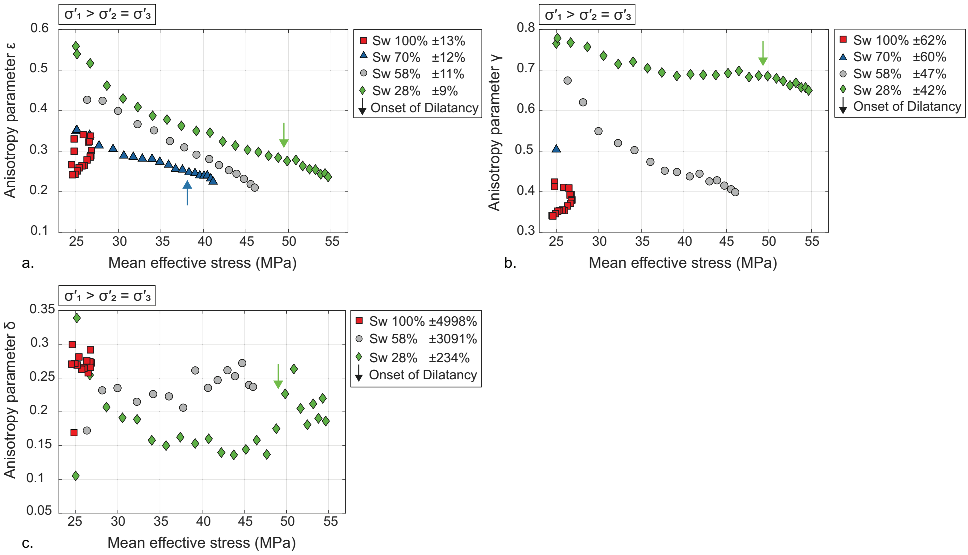

Figure 4.15: *The anisotropy parameters ε and γ decreases with an increase in mean effective stress (a, b). δ does not change significantly for the saturated core plug. The relationship between δ and mean effective stress is non-monotonic for the partially-saturated samples. Note that the errors for δ are extremely high.*

4.4 Discussion

4.4.1 Impact of water saturation on the mechanical properties (strength)

The mechanical properties of the Whitby Mudstone samples are highly affected by the degree of water saturation. With decreasing water saturation, the mudstone plugs become mechanically stronger and elastically stiffer (i.e., increase in Young's Modulus E_3), and Poisson's ratio ν_{31} decreases (Table 4.1), which is attributed to capillary suction [*Erling et al.*, 2008; *Ramos da Silva et al.*, 2008]. When a mudstone dehydrates, air can enter the pores/cracks, leading to a higher tensile stress (negative pressure) in the water phase which acts in maintaining pore/fracture walls together, and resulting in additional mechanical strength [e.g., *Onaisi et al.*, 1994; *Forsans and Schmitt*, 1994; *Ewy*, 2014]. Overall, the new experimental results presented here on the Whitby Mudstone are consistent with the findings reported in previous studies [e.g., *Vales et al.*, 2004; *Ramos da Silva et al.*, 2008; *Ghorbani et al.*, 2009].

As reported previously on other clay-rich rocks, the deformation behavior of the Whitby Mudstone samples is also governed by their state of water saturation. The partially-saturated samples compact at the early stages of differential loading and become dilatant before failure, whereas the fully-saturated sample remains compactant during deformation (Figure 4.7b). The absence of dilatation of the fully-saturated mudstone may indicate ductile deformation and plastic yield, whereas the partially-saturated samples deform and fail in a brittle manner [*Wong et al.*, 1997]. Other explanations for the absence of dilatant behavior in the fully-saturated sample are that, (1) the circumferential strain was measured across a more competent layer (heterogeneity), or (2) the circumferential strain was only measured in one direction relative to the fracture plane, therefore the maximum increase in radial strain was not captured.

■ 4.4.2 Impact of water saturation on the physical properties (stiffness)

The degree of water saturation has a significant effect on wave velocities in the Whitby Mudstone at isobaric stress conditions (Figure 4.9). The largest velocity changes are observed for the P-wave velocities. The pores of the fully-saturated mudstone plug are filled solely with brine, whereas the pores of the partially-saturated plugs are filled with both brine and air. Whether it is pure brine or a mixture of brine and air, the pore fluid has a higher density than air, which can lead to faster P-wave propagation [e.g., *Vales et al.*, 2004]. In addition, the bulk modulus (incompressibility/stiffness) of a rock saturated with pure brine or a mixture of brine and air, has a higher effective modulus than one saturated with air alone. Fracture formation due to dehydration enhances the decrease of P-wave velocities. Even though a majority of the fractures tend to close when increasing the confining pressure, the process might not be complete, and fracture closure and compaction might still occur during differential stress loading [*Kuila et al.*, 2011]. In addition, the water content in the vicinity of the major fractures in the partially-saturated samples seems extremely low (Figure 4.6), which might enhance P-wave velocity reduction.

In contrast to the P-wave velocity, the V_{sh} increases with dehydration, resulting in an increase in the horizontal shear modulus (C_{66}). This observation is consistent with the results presented by *Yurikov et al.* [2018] on the clay-rich Opalinus shale, where the shear modulus (C_{66}) gradually increases with dehydration. This suggests that other mechanisms rather than the presence of pore fluid might also affect the S-wave velocity. The increased shear stiffness (i.e., C_{66}) of the mudstones with decreasing water saturation can be explained by a dehydration-driven stiffening of the clay aggregates. The dehydration of clay minerals leads to an increase in capillary forces acting at the pore/fracture scale, an overall shrinking of the rock, a porosity reduction, and a thinning of the water film at the contact between clay particles, hence an overall stiffening of clay aggregates and rock frame [*Osipov et al.*, 2004; *Ferrari et al.*, 2014; *Yurikov et al.*, 2018].

The ε and γ of the Whitby Mudstone are high at isotropic stress conditions ($\sim$0.3 and $\sim$0.4, respectively). These high values of elastic anisotropy are consistent with previous work on 'dry' core plugs of this rock [chapter 3; *Zhubayev et al.*, 2016;

Douma et al., 2017] and other clay-rich shales [e.g., *Dewhurst and Siggins*, 2006]. The Whitby Mudstone consists mainly of anisotropic clay particles, organic material, and is highly laminated on a scale (∼0.5 mm) much finer than the propagating ultrasonic wavelength (∼4 - 8 mm) (Figures 4.2 and 4.6), resulting in a high intrinsic anisotropy [e.g., *Vernik and Nur*, 1992; *Sayers*, 1994; *Dewhurst and Siggins*, 2006; *Kuila et al.*, 2011]. In addition, cracks, fractures, and an increase in crack density are notorious for enhancing ultrasonic anisotropy [*Sayers*, 1994; *Sayers and Kachanov*, 1995; *Dewhurst and Siggins*, 2006; *Sarout and Guéguen*, 2008a]. The Whitby Mudstone samples originate from an outcrop, and therefore it is possible that (fluid-filled) microfractures are present in the core plugs due to tectonic uplift. However, there is no clear evidence for the presence of such fractures in the preserved mudstone samples (resolution of the XRCT-image; Figure 4.6a), although they are visible in the partially-saturated core plugs (Figure 4.6b, c, d).

Both ε and γ increase with decreasing water saturation (Figure 4.12a, b). As mentioned above, competing mechanisms contribute to the observed velocity changes, hence anisotropy changes, with dehydration. On one hand, clay particles shrink during dehydration, resulting in the formation of desiccation fractures, which tend to soften the material [*Ghorbani et al.*, 2009]. On the other hand, the stiffness of the rock frame increases due to dehydration. The combination of both mechanisms leads to a faster (1) decrease in V_{pv} than V_{ph}, enhancing ε, and (2) increase of V_{sh} relative to V_{sv}, hence increasing γ. An increase in ε and γ with dehydration is consistent with the modeling results of *Sarout and Guéguen* [2008a]; *Ougier-Simonin et al.* [2009]. In the experimental study of *Yurikov et al.* [2018], ε also increases with dehydration, whereas these authors show an opposite trend for γ. This can be due to the different composition of the shale, or the absence of bedding-parallel fractures in the clay-rich rocks tested by *Yurikov et al.* [2018].

■ 4.4.3 Impact of mean effective stress

When applying a differential stress parallel to the symmetry axis, discontinuities along the bedding planes (e.g., bedding-parallel fractures) tend to close and enhance compaction [*Dewhurst and Siggins*, 2006; *Sarout and Guéguen*, 2008b; *Dewhurst et al.*, 2011; *Kuila et al.*, 2011], which results in a velocity increase along the symmetry axis. In the fully saturated core plug, an increase in mean effective stress does not affect the P- and S-wave velocities significantly (max. 5%), most likely due to the water filling, the cracks increasing their elastic stiffness at ultrasonic frequencies (Figure 4.16a). For the partially-saturated core plugs, however, P- and S-wave velocities increase measurably with differential stress increase (Figure 4.16b, c). The vertical velocities, and quasi-P-wave velocity are more stress sensitive than the horizontal velocities as the volumetric strain increases (i.e., compactive). The velocity change can be due to closure of bedding-parallel fractures, enhanced by the presence of air in the pore space. Applying a differential stress in a direction orthogonal to the bedding is probably more efficient in closing the remaining fractures. As a result of compaction, the degree of saturation may increase locally (in the most compliant pores/cracks) in the core plug, enhancing the ultrasonic velocity change.

Entering the inelastic (post-elastic) deformation region, it is expected that new sub-vertical microfractures are formed parallel to the maximum principal compressive stress. These newly-formed microfractures do not affect bedding-orthogonal velocities, whereas they slightly reduce bedding-parallel velocities (Figure 4.16b, c), which is consistent with the findings of, for example, *Barnhoorn et al.* [2018]. In fact, the partially-saturated mudstones are still compactive, resulting in a further increase in V_{pv}, $qV_{p(49^{\circ})}$, and V_{sv} (Figure 4.16b, c).

As the differential stress (and the mean effective stress) increases, the volumetric strain suddenly departs from linearity (i.e., onset of dilatancy), then decreases (volume increase). From this point onwards, the fractures formed parallel to the maximum principal stress grow and coalescence into a macroscopic shear fracture (failure) [*Kuila et al.*, 2011]. Here, the rate at which the ultrasonic velocities increase slows down, the velocities decrease (i.e., negative velocity change), or they remain constant (Figure 4.16b, c), which is attributed to the development of stress-induced fractures. This observation is consistent with previous experimental work where velocities are reduced or remain constant before failure is reached [e.g., *Sarout and Guéguen*, 2008a; *Bonnelye et al.*, 2017]. Whether the velocities are sensitive enough to detect the formation of the new micro-fractures depends on several parameters, including crack density, fracture orientation with respect to the ultrasonic waves, fracture aperture, and microstructural characteristics of the rock [*Barnhoorn et al.*, 2018; *Zotz-Wilson et al.*, 2019].

Figure 4.17 shows the relative change in anisotropy parameter versus mean effective stress during the differential stress loading. ε and γ decrease with increasing mean effective stress (Figure 4.17a, b), which is consistent with previously published findings [e.g., *Sarout and Guéguen*, 2008a; *Kuila et al.*, 2011]. The decrease in ε and γ with increasing mean effective stress can be explained by the factors mentioned earlier in the discussion, including (1) closure of bedding-parallel fractures during compaction, where V_{pv} or V_{sv} increase faster than V_{ph} or V_{sh}, respectively, resulting eventually in a reduced anisotropy, and (2) the formation of sub-vertical stress-induced fractures, reducing V_{ph} and V_{sh}, and thus reducing elastic anisotropy [*Dewhurst and Siggins*, 2006; *Kuila et al.*, 2011]. The highest rate of change in ε and γ in the partially-saturated core plugs seems to occur at the onset of dilatancy (Figure 4.17a, b). For these core plugs, the dependence of δ (factor governing the departure of the wave front geometry from an ellipsoid) on the mean effective stress is non-monotonic (Figure 4.17c). Moreover, δ seems to decrease in the elastic region, then increase in the post-elastic (inelastic) region, when micro-fractures nucleate, propagate (inelastic region), and coalesce (Figure 4.17c). There is no clear trend for the fully-saturated core plug.

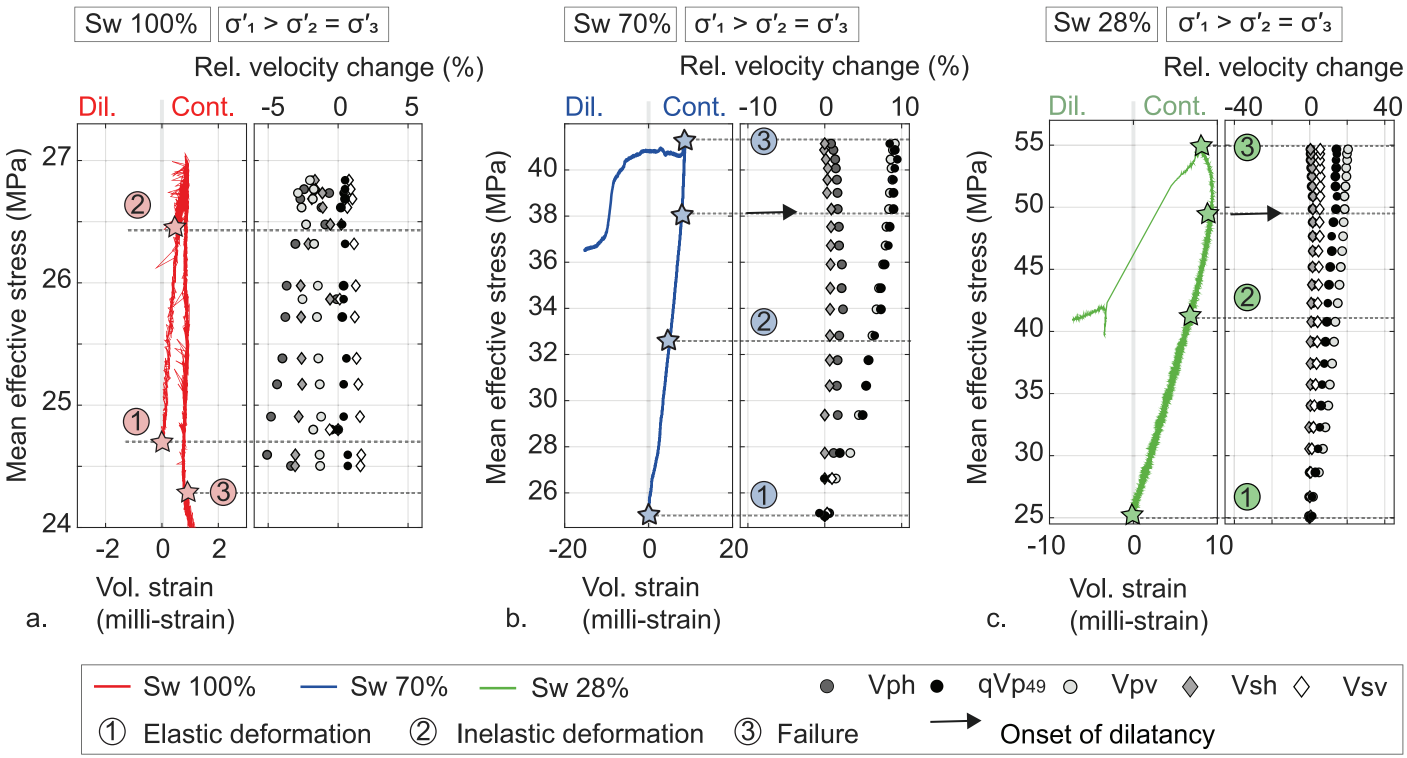

Figure 4.16: *Comparison between the mean effective stress-volumetric strain and relative velocity change (%) for three different water saturations. The total velocity change increases with dehydration. Note that for the partially-saturated core plugs (b, c), the velocities increases (positive change) until the onset of dilatancy.*

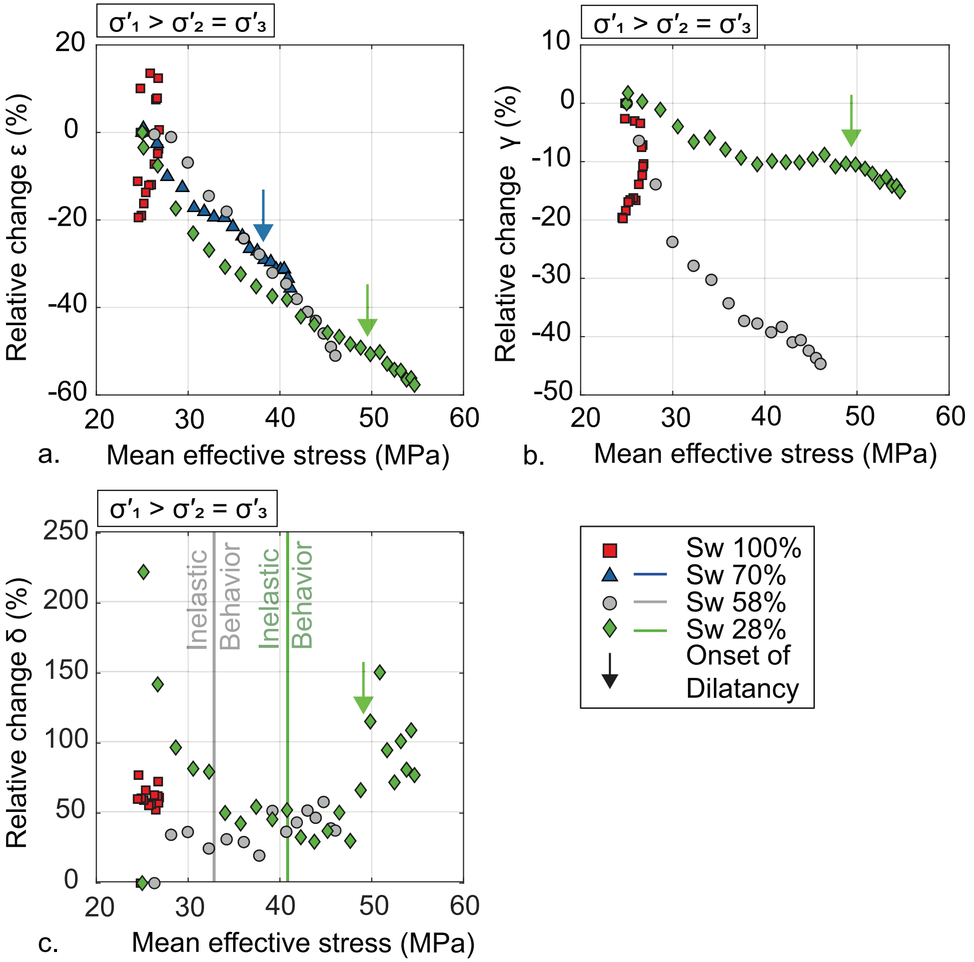

Figure 4.17: *Relative change (%) in anisotropy parameters* ε, γ, *and* δ. *The highest rate of change for* ε *and* γ *occurs at the onset of dilatancy (a, b). The non-monotonic response of* δ *can be related to the onset of inelastic behaviour.*

4.5 Conclusions

This study investigates the impact of water saturation on the elastic anisotropy of the Whitby Mudstone (UK). Mudstone core plugs with different water saturations were tested ultrasonically at undrained conditions and varying mean effective stresses in the laboratory. The intrinsic anisotropy of the Whitby Mudstone is high due to its composition and the presence of lamination. The results show that the water content highly affects the elastic anisotropy of mudstones. A decrease in water content increases the elastic anisotropy even further. There are three competing mechanisms that play a key role in the velocity changes, hence anisotropy changes, due to dehydration. First, when the water content decreases, the pore fluid is replaced by air, resulting in a P-wave velocity decrease (density differences). Second, dehydration results in the formation of mainly bedding-parallel fractures which tend to weaken the rock and reduce the P-wave velocities. Third, dehydration leads to frame stiffening, resulting in an increase in rock strength, Young's modulus, and S-wave velocity. Increasing mean effective stress reduces the elastic anisotropy parameters ε and γ due to (1) closure of imperfections, and (2) formation of stress-induced fractures. This study shows that the degree of saturation highly influences the elastic anisotropy of layered mudstones. The degree of water saturation should always be reported when performing experiments on mudstones. In addition, care should be taken when extrapolating the elastic properties obtained from the partially-saturated samples to *in situ* conditions.

5

The deformation behaviour of the Whitby Mudstone with variable water saturations

Abstract Understanding the mechanical and failure properties of mudstones is crucial to make predictions on their deformation behaviour, which is important for the development of these low-permeability reservoirs. The loss of *in situ* pore fluids from these clay-rich rocks has a significant effect on their bulk properties, as well as on the elastic anisotropy (chapter 4). Despite the enormous effect on these properties, experiments are still performed on poorly-preserved samples without any pore pressure control. The results obtained during these tests do not represent the *in situ* conditions of mudstones, leading to ambiguities in the interpretation of deformation behaviour of mudstones. This chapter shows the impact of water saturation on the mechanical behaviour of the Whitby Mudstone. The same experimental procedure as presented in chapter 4 was used. The mechanical properties and fracture behaviour of this mudstone are discussed in detail. The work emphasizes the importance of preserving clay-rich rocks and shows that the mechanical properties obtained through partially-saturated rocks should be treated with care when extrapolating them to *in situ* conditions.

Submitted as: Douma, L.A.N.R., J. Dautriat, J. Sarout, L. Esteban, D.N. Dewhurst, and A. Barnhoorn, The deformation behaviour of the Whitby Mudstone with variable water saturations. *Under review*
Note that minor changes have been introduced to make the text consistent with the other chapters.

5.1 Introduction

Mudstones are clay-rich rocks and are characterized by their sensitivity to contacting fluids and low permeability [*Best and Katsube*, 1995; *Horsrud et al.*, 1998]. Since mudstones are relatively impermeable with respect to fluid flow, they are an important natural seal for conventional petroleum reservoirs. Under the right conditions, these clay-rich rocks can also act as reservoirs for oil and gas as well as source rocks. Besides their important role in the petroleum industry, they are also recognized as potential host rocks for nuclear waste disposal [*Bossart et al.*, 2002] and as natural seals for long-term CO_2 storage in the subsurface [*Busch et al.*, 2008].

Understanding the deformation behaviour of mudstones is important for oil and gas trapping and production in terms of fracture initiation, propagation, and reopening [*Britt and Schoeffler*, 2009]. It is most likely that fractures initiate and propagate in a brittle manner when the mudstone is relatively strong, whereas self-sealing is often observed in weaker, more ductile mudstones [*Josh et al.*, 2012]. The elastic and failure properties, such as Young's modulus, Poisson's ratio, ultimate strength, and friction coefficient, are important parameters to predict the fracture/deformation behaviour of mudstones, but also for seal integrity evaluation, as input parameters for geomechanical models, and for the safety assessment of underground repositories.

Obtaining realistic elastic and failure properties of clay-rich rocks by geomechanical testing is challenging, due to their fragility, their extremely low permeability, their high capillary suction, and various interactions with brine [*Ewy*, 2018]. Realistic geomechanical properties of clay-rich rocks can only be defined in the laboratory if these rocks are preserved immediately after recovery and if the pore pressure is measured throughout the sample [*Ewy*, 2015, 2018]. Clay-rich rocks always have a negative pore pressure when they are not under stress, even though they are fully saturated [*Ewy*, 2018]. Therefore, the pore pressure should always be brought to a positive, measurable value prior to deformation if the samples are close to full water saturation [*Ewy*, 2018; *Giger et al.*, 2018]. Furthermore, applying inappropriate deformation rates during undrained axial loading affects their deformation behaviour [*Giger et al.*, 2018]. *Giger et al.* [2018] show that the clay-rich Opalinus Clay becomes mechanically stronger and behaves in a contractive manner when the applied deformation rate is too high, whereas it is dilatant at lower strain rates.

Poor preservation of clay-rich rocks leads to dehydration, which results in substantial modification of the microstructure [*Griffiths and Joshi*, 1990]. The significant amount of clay present in mudstones in combination with native pore fluid loss can result in cracking, porosity reduction, closure of macropores and increase in the micropore space, and shrinkage of samples [*Montes et al.*, 2004; *Romera et al.*, 2011; *Ferrari et al.*, 2014]. In addition, when dehydration occurs, air can enter the pores resulting in a tensional state of pore water and the emergence of strong capillary forces (suction) that can cause crack formation as the material shrinks. The magnitude of these forces is governed by the size of the smallest pores (micro-pores) often encountered in clay-rich rocks [*Ferrari et al.*, 2014; *Ewy*, 2015].

Despite the significant effect of dehydration on the microstructure and tensional state of pore water, rock-mechanical experiments are still performed on poorly-preserved samples without pore pressure control, or without even stating the initial degree of water saturation, if known at all. The loss of pore water highly affects the compressive strength and elastic properties of clay-rich rocks. Dehydration makes these rocks mechanically stronger and stiffer [*Minaeian et al.*, 2017; *Dewhurst et al.*, 2019]. *Su et al.* [2004] showed that the uniaxial compressive strength increases by a factor of three to four when the relative humidity decreases from 100% to 60%, whereas the Young's modulus is multiplied by a factor five. Compressive and shear velocities are also sensitive to the presence of water, resulting in an increase in elastic anisotropy when dehydration occurs [*Vales et al.*, 2004; *Pervukhina et al.*, 2015; *Yurikov et al.*, 2018; *Douma et al.*, 2019a]. Although it has been shown that the degree of water saturation and testing protocol impacts the elastic properties of mudstones, the effect of water saturation on strength/failure properties (e.g., friction coefficient, cohesion, ultimate compressive strength) and deformation behaviour (brittle versus ductile) has attracted far less attention.

This study shows the impact of water saturation in the Whitby Mudstone on its failure properties, deformation behaviour, and static elastic properties. Undrained triaxial compression experiments were performed on mudstone samples with different water saturations (92%, 70%, 58%, 28%), deformed at a wide range of confining pressures (5 MPa, 15 MPa, 25 MPa, 40 MPa). This study emphasizes the importance of preserving clay-rich rocks at the location of origin (e.g., well site or outcrop), immediately after recovery, and prior to sampling and testing in the laboratory, as well as stating the degree of water saturation to minimize the risk of inconsistent results.

5.2 Materials and methodology

■ 5.2.1 Sample material and preparation

The mudstone samples originate from the outcropping Whitby Mudstone Formation (WMF) from the northeast of England. This formation is recognised as an analogue for the time and depositional equivalent Posidonia Shale Formation (PSF), which is the main shale-gas prospect in the Netherlands. However, the PSF does not outcrop in the Netherlands, while well data and preserved samples of this formation are lacking [*Zijp et al.*, 2015].

Two mudstone blocks were collected from the same stratigraphic horizon (lower base Mulgrave Member (Jet Rock unit); see chapter 4 and *Douma et al.* [2017] for the stratigraphic column) to minimize heterogeneity between the samples. The basal Jet Rock unit comprises the lower ~5 m of the Mulgrave Member and is very similar to the PSF in the Dutch subsurface with respect to age, overall thickness, depositional environment (palaeowater depth 20 – 100 m), TOC distribution, and mineralogy. The Jet Rock unit consists of fissile, bituminous, dark-grey mudstones with abundant ammonites [*Houben et al.*, 2016b]. X-ray powder diffraction (XRD) analysis and Rock-Eval pyrolysis show that the unit is relatively rich in clays (50 – 70% sheet silicates) and is particularly enriched in organic matter (average TOC = 6%) [*Zijp et al.*, 2015], often interlayered within the matrix [*Houben et al.*, 2016b]. Based on the Kozeny-Carman equation, relating matrix permeability to the gas absorption porosity and average matrix grain size (100 nm – 2 μm) of the Whitby Mudstone, the Jet Rock Unit covers a large range of matrix permeability from 10^{-23} to 10^{-18} m^2 [*Houben et al.*, 2016b]. The SEM porosity (pore diameter >100 nm) is in the order of 0.5 - 2.5% and the gas adsorption (N_2, Ar, He) porosity (pore diameters $\geq$2 nm) is 0.3 - 7% [*Houben et al.*, 2016b]. The Whitby Mudstone core plugs used in this study have a minimum porosity of ~13%, estimated from the dry bulk density (~2.35 $g.cm^{-3}$) and the average grain density (~2.69 $g.cm^{-3}$), which were measured in the laboratory. The bulk density was obtained from the volume and dry mass of the core plug, which was dried in the oven at 105°C until its mass stabilized. The grain density was measured with a pycnometer and averaged using five different material powders collected at random locations in the sample block. There was some variation in measured grain density between the different powders, with a minimum of 2.65 $g.cm^{-3}$ and maximum of 2.72 $g.cm^{-3}$.

The two mudstone blocks were stored in seawater immediately after collection them from a wave-cut platform to prevent initial pore water loss. This wave-cut platform is submerged by seawater twice-daily due to the tidal cycle. Therefore, the assumption is made that the seawater has become in chemical equilibrium with the interstitial pore fluid of the outcropping mudstone over geological time scales. A total of 16 cylindrical samples with a length/diameter ratio of 2:1 were cored normal to the horizontal bedding out of two larger sample blocks. The two mudstone blocks were relatively homogeneous, based on visual observation and petrophysical measurements, which are described later. Seawater was used as cooling and lubricating fluid during coring to prevent swelling and/or shrinkage of the clays present in the mudstones.

The initial water saturation (i.e., natural saturation) was determined from a core plug, vacuum dried at 105°C until its mass stabilized, one vacuum dried core plug, by measuring the pore volume and brine volume. This latter parameter was obtained from the amount of water loss during drying and the pore fluid density. Uncertainties for water saturation were calculated with the method of error propagation assuming Gaussian (random) errors. Four core plugs with an initial water saturation (S_w) of 92% ±10% were stored in seawater. The remaining plugs were equilibrated for two months at room temperature in three desiccators (four core plugs in each desiccator). Each desiccator maintained a constant relative humidity of 85%, 75%, or 33%, which was achieved by using different over-saturated saline solutions as described in detail by *Laloui et al.* [2013]. Knowing the initial saturation, the final saturation state of the equilibrated mudstones was estimated by measuring their mass compared to the fully-dried core and preserved core plugs. More details on the methods used to determine the saturation at equilibrium can be found in Appendix A. Under these relative humidity conditions, the final water saturations of the specimens at equilibrium were 70% ±10%, 58% ±10%, and 28% ±10%, respectively. The 16 equilibrated core plugs were used for the laboratory deformation tests reported below.

5.2.2 Rock characterization at various saturations

The pre- and post-deformation mudstone plugs were imaged using a Siemens SOMATOM definition AS medical X-ray Computed Tomography (XRCT) scanner (helical image acquisition at 140kV and 500 mAs with the smallest field of view of 4 cm). The reconstructed 3D XRCT image data have a voxel size of $\sim 100\times100\times400$ μm. The pre-deformation core plugs were wrapped in cling film to minimize undesired pore fluid loss during scanning. The post-deformation core plugs were scanned in a Viton sleeve immediately after a mechanical deformation test was terminated. The internal structure was visualized using Avizo 9.5.0 software from ThermoScientific Ltd. The homogeneity and structural integrity of the equilibrated pre-deformation plugs is assessed prior to the test. The macroscopic deformation patterns of the post-test plugs are analysed in term of fracture orientation. The fractures are segmented from a unique threshold of the CT-attenuation corresponding to the created open porosity.

An Oxford-GIT GeoSpec 2 MHz Nuclear Magnetic Resonance spectrometer (NMR) was used on the core samples with S_w of 92%, 70%, and 58% to analyse the saturation profile along the core axis, the sample water content and the water-filled pore size distribution. The core plugs were wrapped in cling film during the NMR measurements to minimize the loss of pore fluids. Note that the plugs with a low S_w of 28% appeared very fragile due to the development of incipient dehydration fractures along the bedding planes. To minimise further sample handling, potential desiccation and loss of the sample cohesion, these low S_w plugs were not subjected to XRCT imaging and NMR spectroscopy.

The NMR-technique measures the net magnetization of hydrogen atoms (H^+ ions) in the presence of an external magnetic field, where the amplitude of the signal corresponds indirectly to the water content of the core plug and the relaxation time decay (transversal T_2 or longitudinal T_1) is related to the rock-fluid interactions [*Rabi et al.*, 1938; *Dunn et al.*, 2002]. The proton relaxation time T_2 distribution is determined by a Laplace inversion of the measured NMR relaxation decay curve and can be approximated to the pore size distribution of water-filling pores [*Dunn et al.*, 2002; *Dillinger and Esteban*, 2014]. The relaxation time T_2 is also used to differentiate water kinetics, where short T_2 values indicate irreducible water, due to the restriction of molecular motion in the small pores and interactions at the mineral surface, and long T_2 values indicate mobile water [*Kleinberg et al.*, 1994; *Dunn et al.*, 2002; *Dillinger and Esteban*, 2014]. A Carr-Purcell-Meiboom-Gill (CPMG) spin-echo pulse sequence was acquired on the samples to measure the water content and its distribution in the pore network using the shortest echo-spacing (50 μs) to resolve as much as possible the smallest pore sizes, a receiver delay of 5 s and an appropriate number of scans to reach an acceptable signal-to-noise ratio (>100). The CPMG was followed by a T_2 profile that measures the water content every ~0.3 mm (i.e., 256 slices along an 8 cm field of view) along the core plugs.

5.2.3 Rock mechanical testing

Triaxial compression tests were performed on the mudstone core plugs with saturation conditions S_w of 92%, 70%, 58%, and 28% and effective confining pressures of 5 MPa, 15 MPa, 25 MPa, and 40 MPa. The experimental conditions are displayed in Table 5.1. The same experimental protocols as described in chapter 4 were used (Figure 4.4). Each core plug was placed in a Viton sleeve to prevent the surrounding confining oil from invading the sample's pore space and placed between top and base steel platens equipped with pore fluid lines. Two aluminium spacers with a thickness of 1 mm were placed on the top and bottom of the partially-saturated core plugs (i.e., 70% S_w, 58% S_w, and 28% S_w) to achieve macroscopically undrained conditions during testing. No spacers were used for the preserved core plugs (i.e., initial S_w = 92%). Instead, the samples were re-saturated at a nominal pore pressure of 2 MPa and the pore pressure build-up was monitored during the undrained triaxial deformation experiment. Axial strain was inferred from monitoring the displacement between the top and base platens using two linear variable differential transformers (LVDTs). The radial strain was obtained from a strain gauge-based cantilever mounted through the Viton sleeve at mid-height of the sample (see also Figure 4.3a).

The testing procedure for the preserved/re-saturated core plugs and for the partially-saturated ones are different (see Figure 4.4). The preserved mudstone core plugs were re-saturated close to full saturation (~100% S_w). During re-saturation, the core plugs were isotropically consolidated at consolidation pressures of 12, 17, 27, and 42 MPa, keeping the pore pressure constant (2 MPa) at a temperature of 40°C ±0.5°C for a period of about 30 - 40 days until low consolidation rates (strain rate of $\sim 10^{-10}$ s^{-1}) were reached. The temperature was controlled above ambient to avoid diurnal temperature fluctuations in the laboratory. The pore network valves were closed prior to deformation to verify that the pore pressure remained at ~2 MPa, which was the case for all the resaturated core plug. The extremely low consolidation rates and the stable pore pressure were used as a guideline to assume full saturation of the core plug. The re-saturated core plugs were deformed up to failure at constant axial displacement rate (strain rate of $\sim 10^{-7}$ s^{-1}) under undrained conditions keeping the confining pressure constant. Note that the preserved core plugs (i.e., natural saturation) are referred to 92% S_w, and to 100% S_w after re-saturating the preserved core plugs in the deformation cell until full saturation was reached.

Table 5.1: *Sample properties, experimental conditions, and mechanical parameters of the tested preserved and partially-saturated Whitby Mudstone core plugs.*

			WMF-92				**WMF-70**				**WMF-58**				**WMF-28**			
	Units	Uncertainty	1	2	3	4	5	6	7	8	9	10	11	12	13	14	15	16
Initial water saturation	%	10	92				70				58				28			
Experimental conditions																		
Confining pressure	MPa		12	17	27	42	5	15	25	40	5	15	25	40	5	15	25	40
Pore pressure	MPa	0.1	2				-				-				-			
Temperature	$^{\circ}C	0.5/1.5	40 ± 0.5				22 ± 1.5				22 ± 1.5				22 ± 1.5			
Deformation rate	mm.hr^{-1}	-	0.0288	0.0308	0.0326	0.0203	0.0263	0.0292	0.0280	0.0151	0.0273	0.0291	0.0326	0.0177	0.0276	0.0309	0.0308	0.0178
Mechanical properties		(%)																
Peak stress	MPa	3	27.3	28.4	36.9	48.3	25.6	37.7	47.7	55.1	42.0	51.1	65.5	66.5	66.8	75.3	88.6	107.5
Static E_3	GPa	5	2.5	3.1	4.5	2.5	2.4	2.9	2.9	3.4	2.7	3.2	3.5	3.6	3.7	4.1	4.7	4.6
Static ν_{31}	-	4	-	0.39	0.44	0.24	-	0.20	0.21	0.31	0.22	0.25	-	0.30	0.22	0.21	0.17	0.14
Calculated UCS	MPa		24.2				23.8				40.7				59.3			
Cohesive strength (S_0)	MPa		9.13				8.77				15.45				20.0			
Friction angle	°		16.0				17.1				15.6				22.0			
Coefficient of internal friction (μ)	-		0.29				0.31				0.28				0.40			
Other properties																		
Skempton B coefficient	-		0.89	0.43	0.83	0.41	-	-	-	-	-	-	-	-	-	-	-	-
Peak P_p	MPa	0.1	8.3	6.4	15.4	10.3	-	-	-	-	-	-	-	-	-	-	-	-
P_p at failure	MPa	0.1	8.3	6.1	15.2	10.2	-	-	-	-	-	-	-	-	-	-	-	-

The partially-saturated core plugs were tested in macroscopically undrained conditions (i.e., no pore pressure control or monitoring), where no fluids could exit the partially-saturated core plug thanks to the top and bottom spacers. The core plugs were isotropically consolidated for three days at consolidation pressures of 5, 15, 25, and 40 MPa at room temperature conditions (22°C ±1.5°C). Since low consolidation rates (strain rate $<10^{-9}$ s^{-1}) were reached after three days, it was assumed that these rates would not impact the deformation behaviour, and the mudstone samples were axially loaded at constant strain rate of 10^{-7} s^{-1} until failure, keeping the confining pressure constant. The experimental protocols of the preserved and partially-saturated core plugs are detailed in chapter 4.

5.3 Results

■ 5.3.1 Characterization of the Whitby Mudstone at various saturation states

Figure 5.1 shows (1) an XRCT slice of the core plug, and (2) the water content profile derived from NMR for equilibrated mudstone core plugs with a water saturation of 92%, 70%, and 58% prior to the deformation experiment. The mudstone samples exhibit horizontal bedding supported by finely-layered (millimetre-scale) alternating high-density minerals (e.g., carbonate-rich) and relatively moderate/low-density minerals, (e.g., wet clays and organic matter). The dark lineation visible in the partially-saturated core plugs highlight incipient fractures resulting from clay dehydration (Figure 5.1; see also *Douma et al.* [2019a]), while local, high-density spots indicate the presence of pyrite or (fragmented) fossils.

The water content profiles were derived from the NMR spectroscopy and are all normalized to the maximum value of the water content obtained from one preserved core plug. The average normalized water saturation value decreases from ~0.85 to ~0.45 with dehydration (Figure 5.1). The water content is unequally distributed along each sample, but overall the profiles remains similar between samples at similar S_w. This observation suggests that heterogeneity between the different core plugs obtained from the same horizon of the outcrop is minimal. The water content is not equally distributed throughout the core plugs, due to the presence of alternating layers with different mineralogy highlighted on XRCT images. The notable drops in water content observed in the partially-saturated core plugs are well correlated to the horizontal dehydration fractures (Figure 5.1b, c).

Figure 5.2 shows the T_2 distribution curves of the equilibrated samples with a water saturation of 92%, 70%, and 58%. The NMR signal amplitude describing the matrix of the Whitby Mudstone varies between ~0.80 $g.cm^{-3}$ and ~0.85 $g.cm^{-3}$ of water for the preserved mudstone plugs and decreases to a minimum value of ~0.5 $g.cm^{-3}$ with dehydration. The overall T_2 values are relatively low, due to the small pore size of the Whitby Mudstone. The preserved core plugs (92% S_w) show

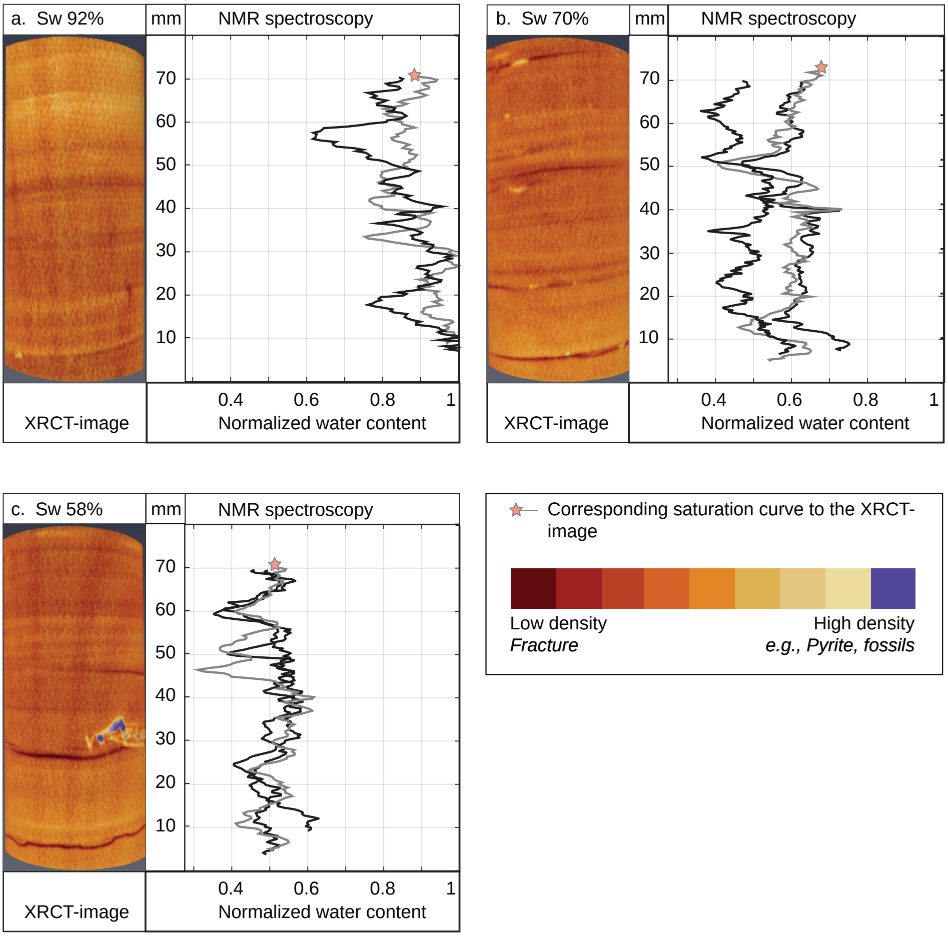

Figure 5.1: *XRCT-images and normalized water content (obtained from the NMR spectroscopy) of the mudstone core plugs at water saturations (S_w) of a. 92% (initial state), b. 70%, and c. 58% (Modified from Douma et al. [2019a]). The water content profiles depicted in grey with a star correspond to the presented XRCT-slice. The black ones correspond to other core plugs used for triaxial testing. Note that not all the core plugs were subjected to NMR. The Whitby Mudstone samples are finely layered (clay and carbonate rich layers) with localized (fragmented) fossils and pyrite. The presence of layering (i.e., differences in mineralogy, porosity) result in a water content profile which is not equally distributed along the core plug. The water content is normalized to the highest value of the mudstone sample with 92% S_w, and decreases with dehydration. Dehydration results in the formation of bedding-parallel fractures.*

a tri-modal distribution composed of (i) long T_2 (T_{2L}) around 60 milli-seconds (ms) ascribed to mobile water in fractures; (ii) intermediate T_2 (T_{2i}) distribution centred around 2 ms ascribed to the inter-grains pores and (iii) short T_2 (T_{2s}) centred around 0.1 ms ascribed to the clay-bound water (Figure 5.2). Only the T_{2i} shifts toward shorter T_2 proportionally with the increase of the dehydration intensity along with the signal amplitude (i.e., water content decreases). T_{2L} disappeared at 58% S_w suggesting that all the larger pores/fractures dried out at low saturation. At $S_w \leq$ 70%, T_{2s} and T_{2i} cannot be de-coupled as the partial saturation of the T_{2i} pore size becomes too close of T_{2s} pore size leading to a single population centred between T_{2i} and T_{2s}.

5.3.2 Triaxial test results

Stress-strain relationship

The geomechanical test results are reported by referring to the effective stress $\sigma_i^{'}$ and the differential stress σ_{diff} defined as:

$$\sigma_i^{'} = \sigma_i - \alpha P_p \tag{5.3.1}$$

$$\sigma_{diff} = \sigma_1^{'} - \sigma_3^{'} \tag{5.3.2}$$

where α is the dimensionless Biot-Willis coefficient [*Biot*, 1941]. It is commonly assumed that this parameter has a value close to one in water-saturated shales *Dewhurst and Siggins* [2006], the test results are hence reported under this assumption. In conventional (axi-symmetric) triaxial deformation experiments $\sigma_1^{'}$ and $\sigma_3^{'}$ represent the axial stress and the confining pressure applied on the rock sample respectively, and σ_2=σ_3. $\sigma_1^{'}$ and $\sigma_3^{'}$ are the maximum and minimum effective stresses, respectively. In the following, positive strains denote compaction, while extension is counted negatively. The volumetric strain ε_v (i.e., unit change in volume) are written as:

$$\varepsilon_v = \varepsilon_a + 2\varepsilon_r \tag{5.3.3}$$

where ε_v, ε_a, and ε_r represent the volumetric, axial, and radial strains respectively. Young's modulus E_3 and Poisson's ratio ν_{31} are obtained from the linear stress-strain response.

Figure 5.3 presents the pore pressure response induced by undrained axial load of the fully re-saturated samples (assuming S_w = 100%) at initial effective confining pressure 10, 15, 25 and 40 MPa. The re-saturated core plug was not tested at an effective confining pressure of 5 MPa, because the pore pressure increase during loading might have resulted in a negative effective minimum pressure and the loss of jacket sealing. Instead, a re-saturated core plug was tested at a confining pressure of 12 MPa (Figure 5.3a).

For all the re-saturated samples, the increase in differential stress induces a pore pressure build-up, primarily due to porosity reduction. The overall stress-strain response is typical of the brittle behaviour characterised by a differential pressure peak, associated with a pore pressure peak induced by macroscopic failure and pore

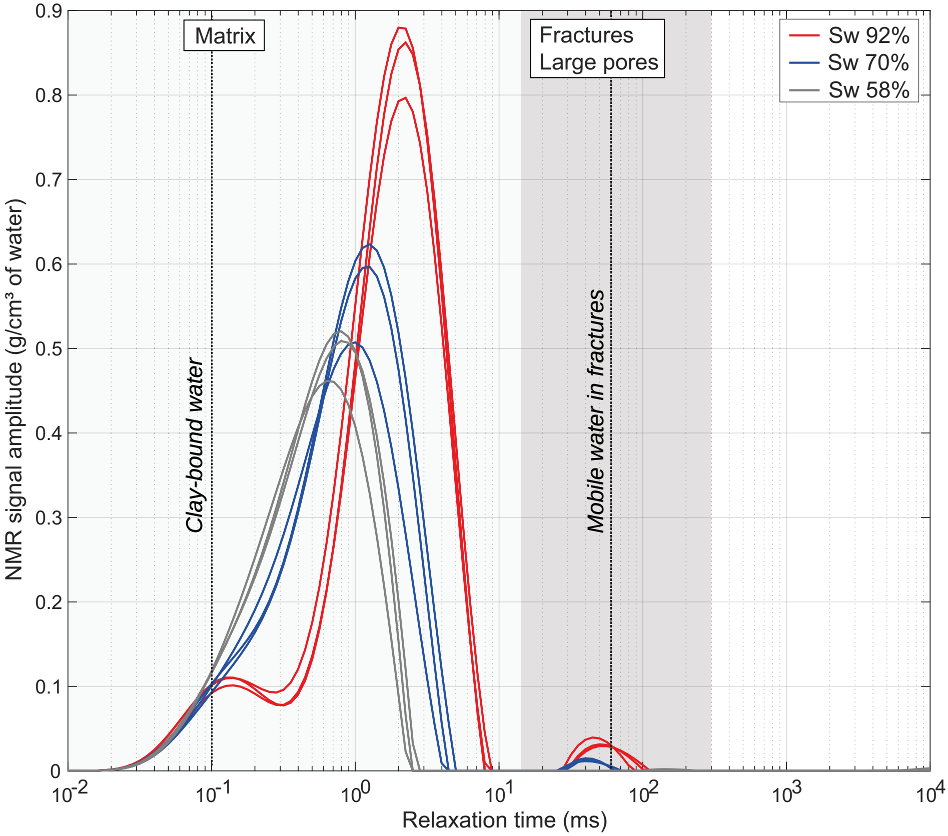

Figure 5.2: *NMR T_2 distribution of the Whitby mudstone plugs collection at three hydration states (S_w = 92%, 70 and 58%). The T_2 distribution curves shift to the left when the mudstone core plugs dehydrate, indicating loss of mobile water mostly in the largest pores including inter-grains matrix (T_2 ~1 ms) and fractures (T_2 >10 ms) [Kleinberg et al., 1994; Dunn et al., 2002; Dillinger and Esteban, 2014]. The amount of water present in the sample matrix decreases with dehydration (decrease in signal amplitude), with the large T_2 disappearing showing full dehydration at 58% S_w (i.e., T_2 >10 ms disappeared).*

pressure dissipation. The linear elastic-deformation evolution of the stress-strain curve is limited or not observed; this might be primarily due to the evolution of the minimum effective stress while loading under undrained conditions. The peak stress and following residual stress, show a positive dependency to the initial effective confining pressure. However, the amplitude of pore pressure build-up is not correlated to the initial effective confining pressure or the amount of axial shortening experienced by the sample prior to failure.

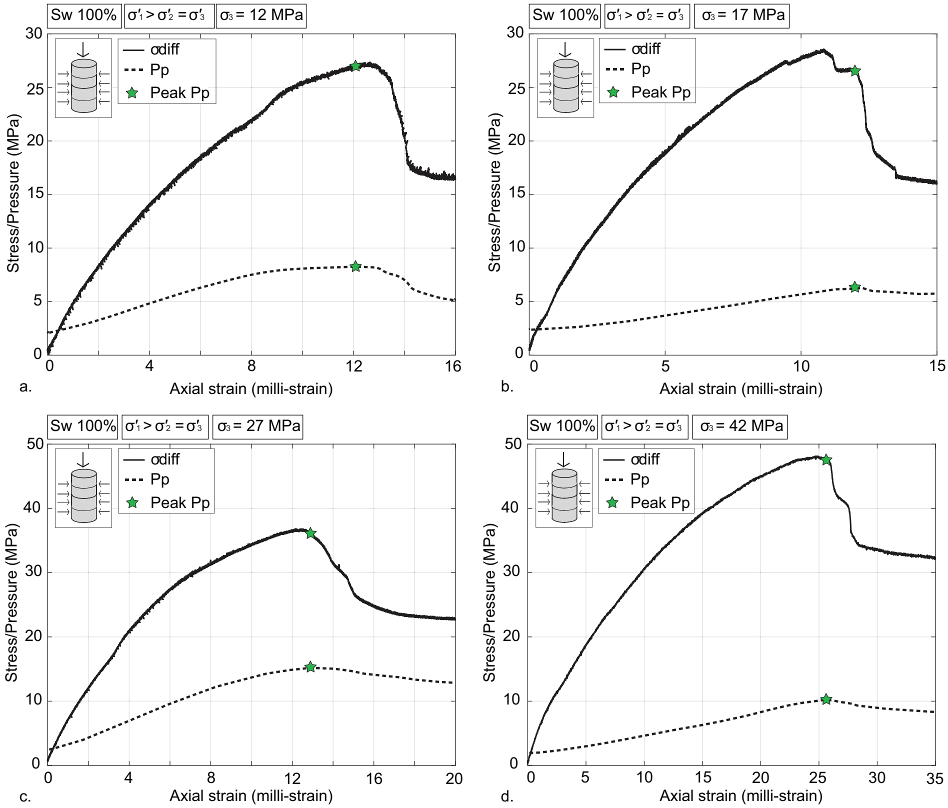

Figure 5.3: *The pore pressure (P_p) of the re-saturated mudstone core plugs increases during axial loading under undrained conditions. Note that the pore pressure was only controlled during isotropic compression of the re-saturated core plugs at confining pressures (σ_3) of a. 12 MPa, b. 17 MPa, c. 27 MPa, and d. 42 MPa. The preserved mudstone core plugs (S_w = 92%) were re-saturated (close to full saturation) prior to axial loading. These samples are referred to as re-saturated core plugs, where S_w is assumed to be 100%.*

Figure 5.4 shows the differential stress – strain curves recorded during axial loading of the re-saturated and partially-saturated mudstone core plugs at (initial) effective confining pressure conditions of 5, 15, 25, and 40 MPa. As reported previously, the re-saturated mudstone has not been tested at $\sigma_3^{'} = 5$ MPa. At $\sigma_3^{'} =$ 5 MPa and $\sigma_3^{'} = 25$ MPa for the partially-saturated samples $S_w = 70\%$ and $S_w =$ 58%, the radial strains were not recorded due to a loss of the radial strain signal during the test (Figure 5.4a, c). Therefore, volumetric deformation could not be calculated. Most of the tested samples present stress-strain curves typical of brittle behaviour with a peak stress followed by strain softening and macroscopic failure propagation. The volumetric strains originally increase linearly under elastic porosity reduction, but at a critical stress, usually denoted $C^{'}$, volumetric strains show dilatancy. This onset of dilatancy is usually associated with micro-crack development and porosity increase. The degree of dilatancy observed before failure differs from sample to sample, while fully saturated samples tested at $\sigma_3^{'} = 25$ MPa and $\sigma_3^{'} = 40$ MPa show only compactive strains prior to failure.

At a given saturation S_w, both onset of dilatancy $C^{'}$ and peak stress C^* values increase with the initial effective confining pressure increase. At a given initial effective confining pressure, $C^{'}$ and C^* values systematically increase with the decrease in saturation S_w.

The stress-strain data for the re-saturated Whitby Mudstone samples can also be represented on a differential stress - mean effective stress plot ($q - p^{'}$ plot) as shown in Figure 5.5. The effective mean stress $p^{'}$ and mean differential stress q are defined as:

$$p^{'} = \frac{\sigma_1^{'} + \sigma_3^{'}}{2} \tag{5.3.4}$$

$$q = \frac{\sigma_1 - \sigma_3}{2} \tag{5.3.5}$$

The $q - p^{'}$ plots can be used to assess (1) the compaction state of the shale before testing [*Dewhurst and Hennig*, 2003], and (2) whether the mudstone is dilative or contractive [*Ingram and Urai*, 1999; *Nygård et al.*, 2006]. These plots are only obtained for the re-saturated core plugs, since the pore pressure was not monitored for the partially-saturated ones. The $q - p^{'}$ plots for the re-saturated Whitby Mudstone are right-sloping (i.e., $p^{'}$ increases with increasing q) at low shear stress, suggesting that this mudstone is overconsolidated at the stress levels used in these tests. The right-sloping plots indicate that the mechanical stress applied is increasing at a higher rate than the pore pressure.

The $q - p^{'}$ plots can also be used to assess whether the Whitby Mudstone behaves in a dilative or contractive manner during deformation. At low confining pressure ($\sigma_3^{'}$= 12 MPa), the re-saturated Whitby Mudstone dilated as shown by the tendency of the stress path to lean to the right as the shear stress q increases [*Nygård et al.*, 2006]. The peak pore pressure and peak q coincide. At higher confining pressures ($\sigma_3 \leq 17$ MPa), the curvature prior to peak q is to the left, indicating that failure is associated with contraction [*Nygård et al.*, 2006]. The average pore fluid pressure (average of the measured top and bottom pore fluid pressure) is still increasing at this stage, and also after peak q was reached (Figure 5.5). The stress path of the re-saturated core plug deformed under $\sigma_3 = 27$ MPa has the largest pore pressure rise and therefore curves more to the left at an earlier stage compared to the other re-saturated ones. Note that the pore pressure response for the plotted $q - p^{'}$ plots 2 and 4 was relatively low (see Figure 5.3b, c), and therefore these plots need to be interpreted with caution.

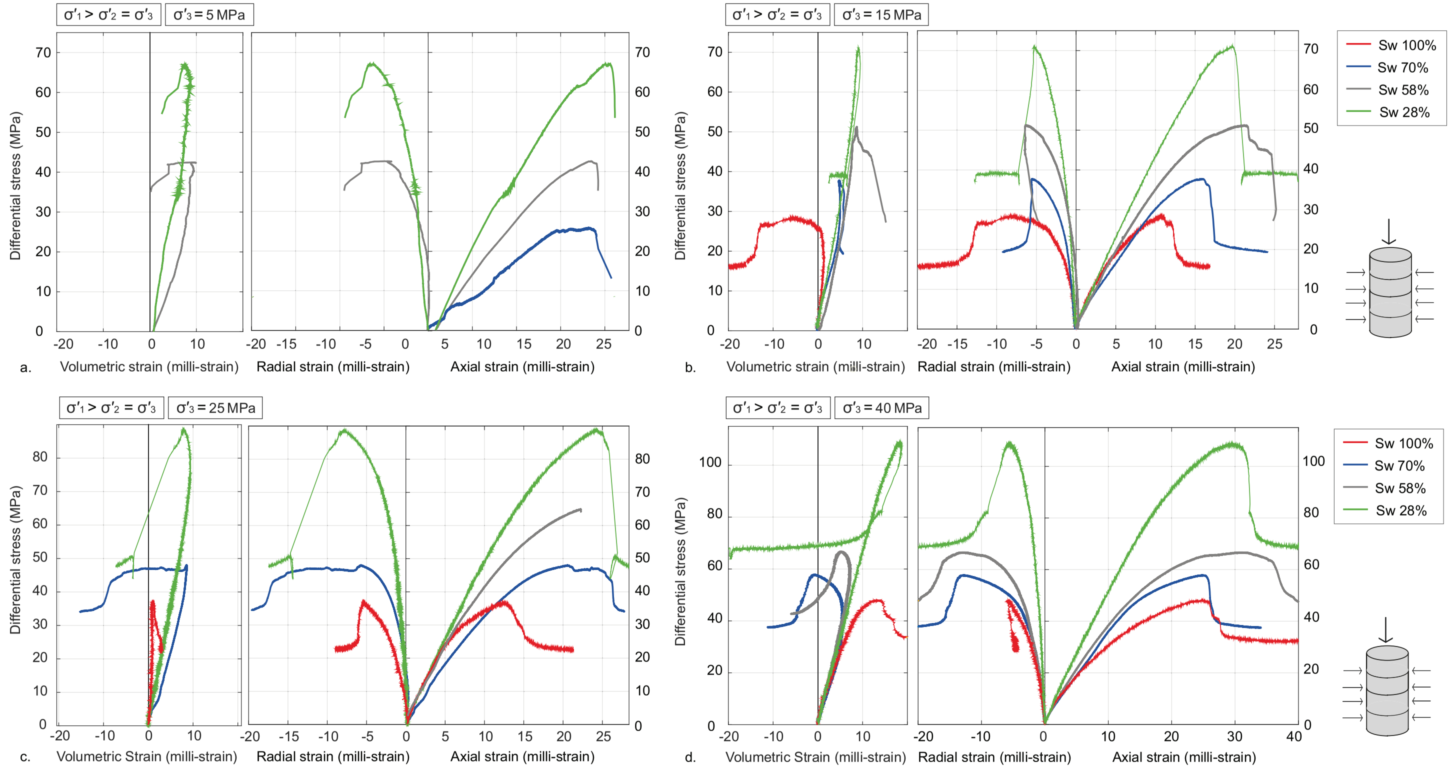

Figure 5.4: *Recorded stress - strain curves for the re-saturated and partially-saturated core plugs at effective confining pressure conditions of a. 5 MPa, b. 15 MPa, c. 25 MPa, and d. 40 MPa. The stress-strain curve of the re-saturated core plug (100%* S_w*) at* $\sigma_3^{'} = 5$ *MPa is absent, since it was not tested at these conditions. Peak stress increases with decreasing water saturation. The peak stress at* $S_w = 58\%$ *and* $\sigma_3^{'} = 25$ *MPa was obtained by extrapolation of the incomplete stress-strain curve. The partially-saturated core plugs are dilative, whereas the re-saturated ones are dilative when* $\sigma_3^{'} = 15$ *MPa, but remain contractive at higher confining pressures.*

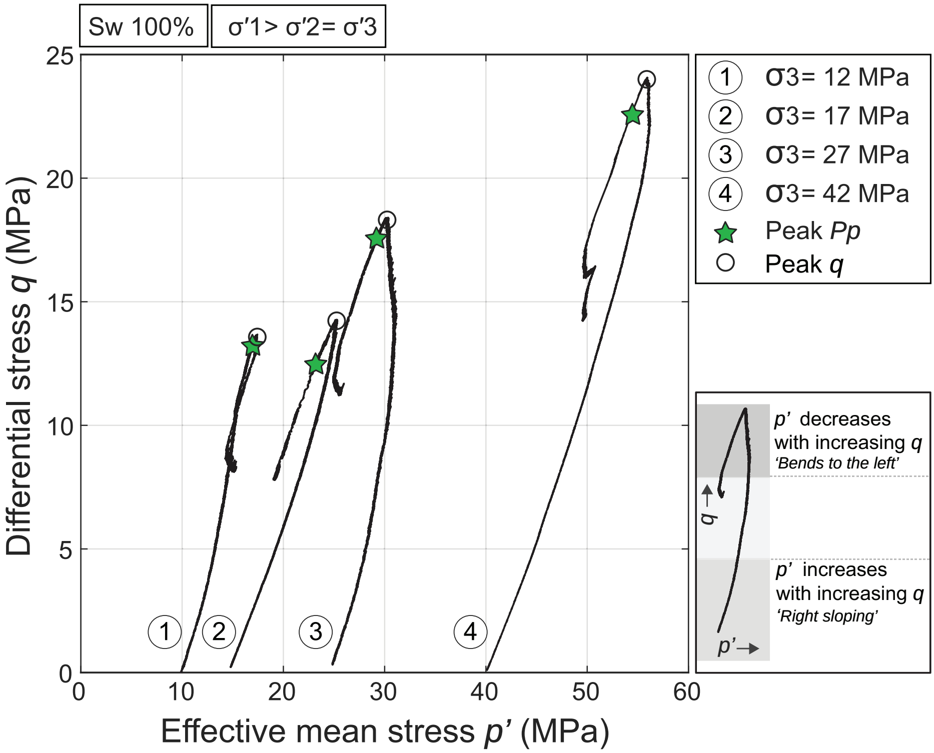

Figure 5.5: *The effective stress paths for the re-saturated mudstone plugs deformed at different confining pressures (σ_3). At low confining pressure, the core plug dilates whereas the core plugs contracted at higher confining pressures ($\sigma_3 \geq 17$ MPa).*

Elastic properties of the Whitby Mudstone

The strength and elastic properties were obtained from the stress - strain curves in Figure 5.4 and are reported in Figure 5.6 and summarised in Table 5.1. At a given water saturation, the sample strengths are increasing with the increase in confining pressure. Peak stress increases by more than a factor two from S_w = 92% to S_w = 28% for all the applied confining pressures (Figure 5.6a and Table 5.1).

The degree of water saturation has also a significant impact on both Young's modulus and Poisson's ratio. Overall, Young's modulus (E_3) increases with dehydration and increasing confining pressure (Figure 5.6b). There is no clear relation between Poisson's ratio ν_{31} and water saturation, although except for one outlying point, a general decrease with decreasing saturation is observed (Figure 5.6c).

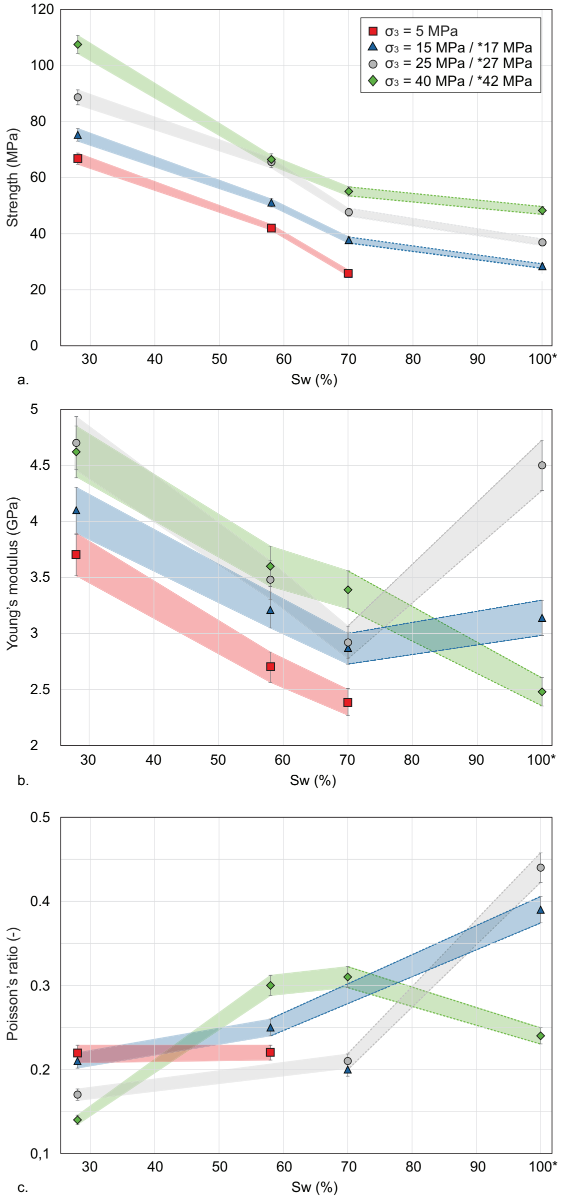

Figure 5.6: *The rock strength and Young's modulus of the mudstones increase with dehydration (a, b). There is no clear relation between the Poisson's ratio and water saturation, although except for one outlying point, a general decrease with decreasing saturation is observed (c). Note that the properties for the partially-saturated mudstones and saturated ones are taken under different effective stress conditions.*

Mohr-Coulomb failure criterion

The strength results of the mudstone core plugs, tested under a wide range of confining pressures, can also be plotted in the form of Mohr diagrams representing the state of stress within the sample at the failure point (Figure 5.7). The failure criterion can be expressed as:

$$\tau = S_0 + \sigma_n \mu_i \tag{5.3.6}$$

where S_0, σ_n, and μ_i are the cohesive strength, normal stress, and coefficient of internal friction, respectively.

For the partially-saturated core plugs, the pore pressure is assumed negligible. This might be seen as a strong assumption, since dehydration of clay-rich rocks can lead to a high negative pore pressure [*Onaisi et al.*, 1994]. However, to the authors knowledge, as yet there is no well-established correlation between the amount of suction/negative pore pressure and effective stress for clay-rich materials. For the re-saturated core plugs, the average pore pressure reached at the failure point is considered to derive the effective stresses $\sigma_1^{'}$ and $\sigma_3^{'}$. This average pore pressure is displayed in Table 5.1.

The parameters calculated from the triaxial testing results are reported in Table 5.1. The coefficient of internal friction μ does not change significantly at (initial) water saturations of 92%, 70%, and 58% (~0.29), but increases to ~0.40 when $S_w =$ 28%. The calculated unconfined compressive strength (UCS) and cohesive strength (S_0) increase with approximately a factor of three and a factor of two, respectively, as the water saturation decreases from 92% to 28%. The UCS and S_0 values for the re-saturated sample and the 70% S_w sample are similar.

Post deformation fractures

Figure 5.8 shows the post-deformation XRCT-images for the mudstone core plugs at saturation conditions of 92%, 70%, 58%, and 28% deformed at a confining pressure of 40 MPa. At failure, the re-saturated and partially-saturated samples exhibit a brittle response with a distinct, localized shear fracture typical of brittle deformation behaviour. The fractures propagate at an angle of ~45° from the axial load direction when re-saturated (Figure 5.8a). The angle decreases, relative to the axial load direction, at lower water saturations (~30°). Similar shear fractures were observed in all the core plugs deformed at confining pressure conditions of 5, 15, and 25 MPa. The horizontal fractures observed in the partially-saturated samples with S_w = 58% and S_w = 28% (Figure 5.8c, d) are not directly associated with the axial load, but are thought to be either the result of desiccation prior to deformation, or due to the stress and pressure release at the end of each deformation experiment.

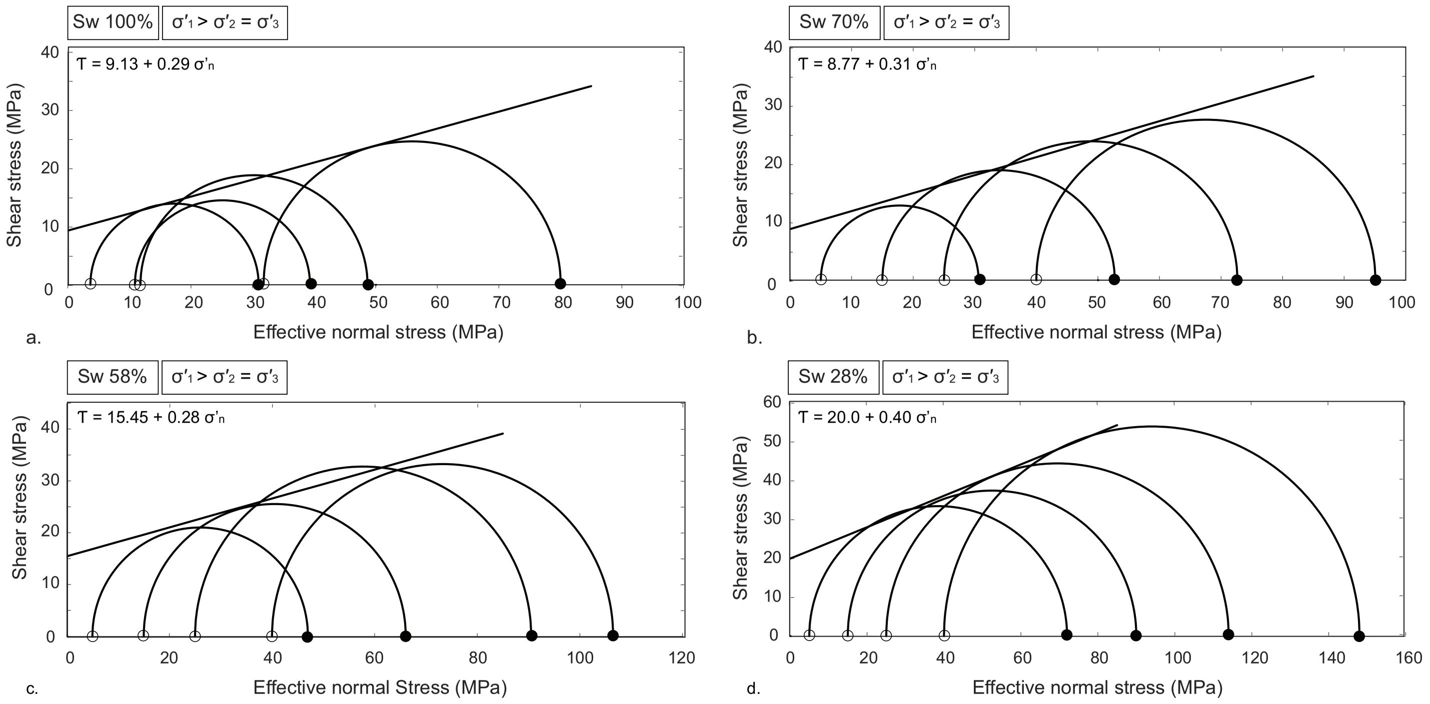

Figure 5.7: *Failure envelope for the Whitby Mudstone at water saturation conditions of a. 100%, b. 70%, c. 58%, and d. 28%. The calculated* S_0 *(the y-axis intercept) is affected the most by a decrease in water saturation. The peak effective stress* $\sigma_1^{'}$ *and the effective confining pressure* $\sigma_3^{'}$ *obtained from the deformation experiments are indicated by the closed and open circles, respectively.*

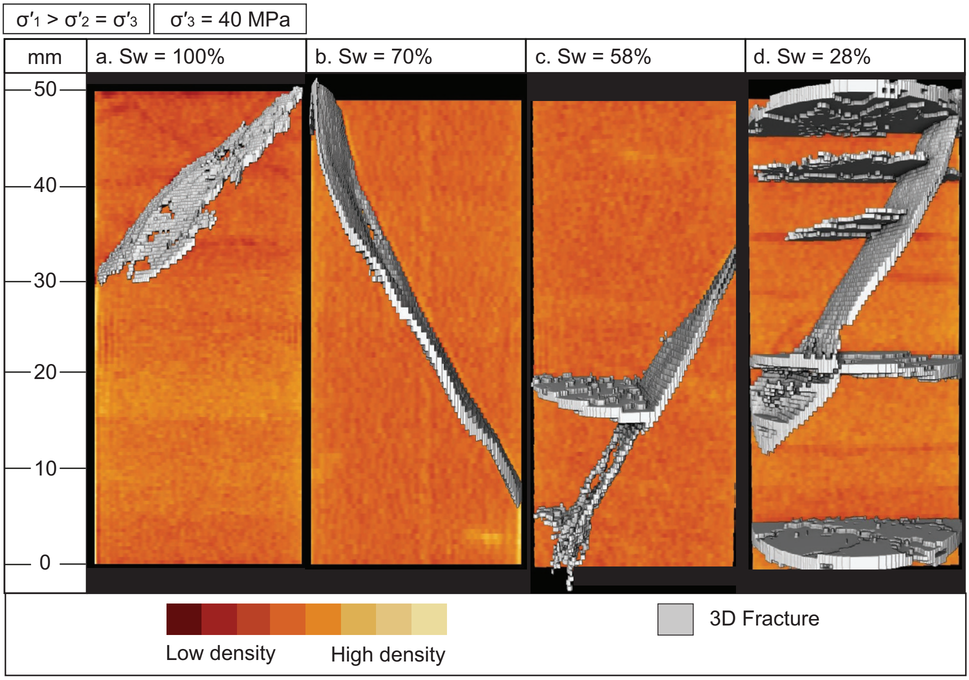

Figure 5.8: *Localized, macroscopic shear fractures are developed in the Whitby Mudstone after axial deformation and typical for brittle deformation behaviour. The horizontal fractures in the partially-saturated core plugs are likely the result of desiccation prior to deformation or stress release of a combination of both (c., d.). All images are from the sample effective confining pressure level of 40 MPa. The 28% S_w sample is the most heavily fractured.*

5.4 Discussion

5.4.1 Pore-fluid pressure response of the re-saturated Whitby Mudstone

Discrepancies have been systematically observed between the amplitude of pore and confining pressure increases recorded for the re-saturated mudstones, contrary to the observations of, for example, *Dewhurst and Hennig* [2003]. These discrepancies might be related to (i) local sample heterogeneities or (ii) a lack of saturation.

Unequal water distribution throughout the core plugs was revealed on the NMR profiles (Figure 5.1) and is mainly related to the presence of alternating layers with different mineralogy, porosity and permeability. This might result in local heterogeneity of the pore pressure response during undrained loading, such as over-pressure in the vicinity of low porosity layers, which are not captured by the pressure transducers located at the sample ends.

The low pore fluid pressure response can be induced by a lack of saturation even after 30 − 40 days of consolidation. In this case, some of the pore fluid pressure might be dissipated by pore water re-distribution into locally unsaturated pores, resulting in a lower pore pressure response than expected. Skempton's B coefficient provide usually a good proxy to the level of saturation of clay-rich rocks [*Giger et al.*, 2018] and is estimated from the pore pressure response (ΔP_p) under an undrained isotropic loading [*Skempton*, 1954]:

$$\Delta P_p = AB\Delta\sigma_1 \tag{5.4.1}$$

For completely elastic behaviour, $A = \frac{1}{3}$ [*Biot*, 1941]. Since the change in mean total stress ($\Delta\sigma_m$) is equal to $\frac{1}{3}\Delta\sigma_1$, the undrained pore pressure relation can be rewritten as:

$$\Delta P_p = B\Delta\sigma_m \tag{5.4.2}$$

ΔP_p and $\Delta\sigma_m$ were obtained relative to a fixed reference point, selected from the most linear part (elastic behaviour) of the $\sigma_m - \varepsilon_a$ plot and corresponding pore pressure change. While Skempton-B tests were not specifically performed for these samples, we tried to estimate this parameter to understand the results that were obtained.

The B-value is expected to be close to, but lower than, 1 for a fully-saturated clay-rich rock [*Gutierrez et al.*, 2015; *Favero et al.*, 2018; *Giger et al.*, 2018]. High porosity-shales are more deformable and have higher B values (∼0.9), whereas more highly-compacted and stiffer shales have lower B values (∼0.75) [*Ewy*, 2018]. The estimated B-coefficient of the re-saturated Whitby Mudstone samples has a value between ∼0.8 − 0.9 at confining pressures of 12 MPa and 27 MPa, but is far below the expected value at confining pressures of 17 MPa and 42 MPa (0.43 and 0.41, respectively). Note that these B coefficients obtained during undrained axial loading are only an estimated values, since A is not often exactly $\frac{1}{3}$ for shales [*Skempton*, 1954; *Wang*, 1997; *Giger et al.*, 2018].

As suggested by *Ewy* [2018], the pore pressure should increase at a consistent rate from the moment the axial load is applied. Even if a systematic increase of the pore pressure is observed for all the test, the increase rate appears slightly lower at the beginning of the axial loading stage and diverged from the stress-strain curve trends for the plugs with an apparent low B-coefficient.This might be due to (1) yield and pore collapse, but it can also indicate (2) a lack of full saturation of the core plugs at the initiation of the axial load or (3) the presence of residual dissolved air in the saturating brine. *Ewy* (personal communication) recommends the application of a minimum pore pressure of 3 MPa to ensure the dissolution of air bubbles potentially trapped in the brine. Below this value, for example 2 MPa used in this study, pore fluid can still be highly compressible resulting in a low B-coefficient value.

Finally, the pore pressure response can be significantly affected by the applied loading rate [*Ewy*, 2018; *Giger et al.*, 2018]. Due to the low permeability and the drainage conditions limited to the sample ends, porosity reduction induced by the axial load can lead to an excess pore pressure within the sample, which cannot be measured or known [*Head*, 1998; *Ewy*, 2018]. In this case, the pore pressure measured at the sample ends differs from the internal sample pore pressure, resulting in misleading effective stress values [*Ewy et al.*, 2001; *Giger et al.*, 2018]. The allowable loading rate in triaxial testing is controlled by the capacity of the mudstone to equilibrate pore fluid pressure within the core plug [*Head*, 1998; *Ewy et al.*, 2001; *Ewy*, 2018; *Giger et al.*, 2018]. *Head* [1998] (section 19.6.2 in *Head* [1998]) and *Ewy et al.* [2001] defined expressions of the allowable loading rate depending on the sample dimensions (length and diameter) of the mudstone plugs, the consolidation coefficient (c_v), and the axial strain at failure. As no consolidation coefficient are reported in the literature for the Whitby mudstone and c_v was not measured during this study, c_v was estimated from a compilation of measurements performed by *Ewy* [2018] on shales covering large ranges of void ratio and permeability. The void ratio of the Whitby Mudstone core plugs is approximately 0.14, therefore a c_v between $1 - 5$ mm^2.hr^{-1} was chosen (see Table 2 in *Ewy* [2018]) to estimate the allowable strain rate. Assuming a c_v between 1 - 5mm^2.hr^{-1}, knowing the dimensions of the core plugs, the axial strain at failure ($\sim$1%) and the drainage configuration (limited to the sample ends), the maximum allowable strain rate to allow dissipation of pore pressure excess of the Whitby Mudstone under drained conditions would be of $\sim 2.5\times 10^{-8}$ s^{-1}. The strain rate applied during this study is in the order of 10^{-7} s^{-1}, which is mainly imposed by the limit to drive the hydraulic pump controlling the actuator at very low displacement rates. Hence, the pore pressure measured at the sample ends is only apparent and probably under-estimates the “true” internal pore pressure.

5.4.2 Impact of water saturation on the mechanical and elastic properties

The mechanical and elastic properties of the Whitby Mudstone are highly affected by the degree of water saturation. Note that the amplitude of the pore pressure build-up is not correlated to the initial effective confining pressure, which significantly affects the failure envelopes, and thus the calculated friction coefficient and cohesive strength. The friction coefficient of the Whitby Mudstone is low compared to most sedimentary rocks at high water saturations, but increases with dehydration (Figure 5.9). The low value of the friction coefficient is in agreement with previous studies on saturated, clay-rich rocks [e.g., *Dewhurst and Hennig*, 2003; *Nygård et al.*, 2006; *Dewhurst et al.*, 2015]. The cohesive strength increases significantly with decreasing water saturation (Figure 5.9). In addition, the Whitby Mudstone becomes mechanically stronger and elastically stiffer with dehydration. For the partially-saturated mudstones, the correlation between water saturation and strength/stiffness seems linear. However, no empirical relationship was established due to the limited amount of data points and thus the lack of evidence that these parameters should be related linearly. Heterogeneities within the sample could explain the absence of a clear correlation between water saturation and Poisson’s ratio. After all, the radial strain is measured across a weaker layer, providing a high radial strain, or attached within a stiff layer, providing an abnormally low radial strain.

The increase in rock strength and stiffness is in agreement with previous studies on the elastic properties of clay-bearing rocks [*Vales et al.*, 2004; *Ramos da Silva et al.*, 2008; *Ghorbani et al.*, 2009; *Minaeian et al.*, 2017; *Dewhurst et al.*, 2019]. The increase in cohesive strength, rock strength, and stiffness with dehydration is attributed to strong capillary suction within the pores of clay-rich rocks (matric suction) as well as the solute/osmotic suction resulting in a total suction effect throughout the material [e.g., *Ferrari et al.*, 2014]. Suction is thus related to the pores' spatial distribution within the rock and to the pore size distribution, but also to the presence of clays [*Laloui*, 2013]. The effect of capillary forces is larger when the pore size/radius becomes smaller. At low water saturations, water forms curved menisci at the small pores between grains [*Laloui*, 2013]. This causes a surface tension at the contact of the water and air in the neighbouring pores, resulting in frictional forces pulling the individual grains together [*Minaeian et al.*, 2017]. This negative pore pressure leads to an additional mechanical strength, stiffness and cohesion. At close to fully saturated conditions, the capillary bonds are lessened, resulting in lower cohesion. Besides the suction phenomenon, dehydration of clay-bearing rocks stiffens (1) the individual clay particles [*Ebrahimi et al.*, 2012], 2012), and (2) the rock frame [*Douma et al.*, 2019a]. When dehydration occurs, the water film between clay particles becomes thinner, enhancing the stiffness of the contacts between clay particles [*Osipov et al.*, 2004].

■ 5.4.3 Deformation behaviour of the Whitby Mudstone

The homogeneity of the strain field (localized or distributed deformation) and the deformation mechanisms are fundamental to describe the way a rock deforms [*Rutter*, 1986]. Here, the homogeneity of deformation is determined at the macroscopic scale (core samples), so that macroscopic brittle deformation is characterized by strain localization into a deformation band (e.g., shear fracture), and macroscopic ductile deformation by non-localized strain. Based on the homogeneity of deformation alone, it is unknown which fundamental deformation mechanism is operating. The deformation mechanisms acting at the microscopic scale (grain scale/microstructure) can be classified into those involving contraction/dilatancy and those not involving volume change [*Rutter*, 1986]. Both deformation mechanisms can result in either localized or distributed deformation at the macroscopic scale. Note that existing definitions for brittle and ductile clay-rich rocks based on the presence or absence of dilatancy and permeability changes alone [e.g., *Ingram and Urai*, 1999] are mechanism-dependent and might be incomplete. The scale at which a rock deformation is described should always be stated.

The stress - strain curves show that the partially-saturated Whitby Mudstone samples fail in the brittle domain at all confining pressures tested here (Figure 5.4). Shear failure of the partially-saturated mudstones result in the formation of dilative fracture planes (Figures 5.4, 5.8), which are likely to allow fracture permeability to develop [*Ingram and Urai*, 1999; *Nygård et al.*, 2006]. According to *Rutter* [1986],

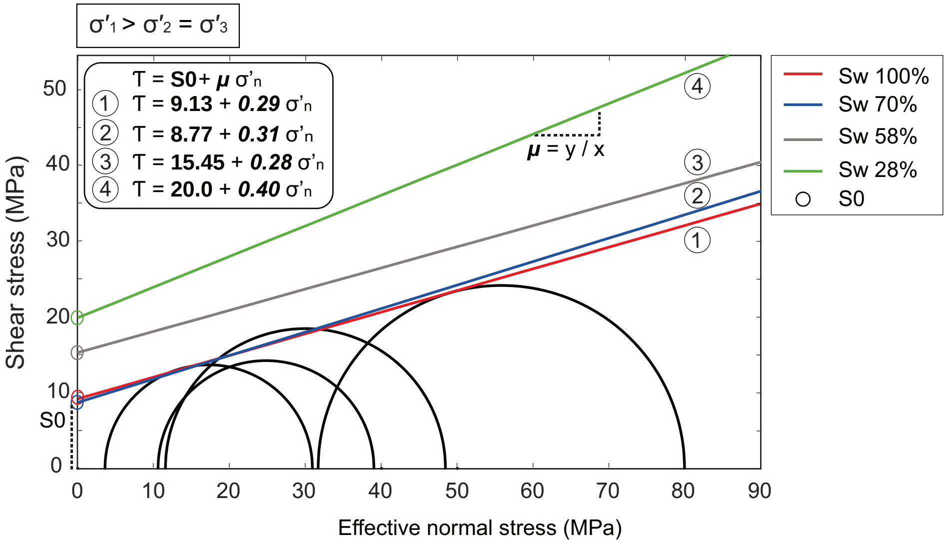

Figure 5.9: *The coefficient of internal friction (slope of the failure envelope) does not change significantly when $S_w \geq 58\%$, but increases at a lower saturation. The cohesive strength S_0 is affected the most by the degree of water saturation (S_w).*

the dilative character of the partially-saturated mudstones suggests that cataclastic deformation mechanisms are operating, in which (groups of) grains become cracked and may exhibit sliding with respect to one-another, while the overall crystal structure remains undistorted. In general, deformation mechanisms can be identified at the grain scale a posteriori using microscopy on thin sections. However, due to the small grain size of mudstones and the dependency of the micro-structures to the hydration level, the identification of deformation mechanisms on these rocks becomes extremely challenging. Identifying these mechanisms is outside the scope of this study, so only the deformation behaviour at the macroscopic scale is discussed.

The attainment of peak stress differs for re-saturated and partially-saturated Whitby Mudstone samples (Figure 5.4). The contractive behaviour of the re-saturated Whitby Mudstone at high confining pressure is essentially brittle as indicated by the formation of a localized shear fracture (Figure 5.8d). However, the classification of *Rutter* [1986] suggests that ductile deformation mechanisms are also operating under these conditions [*Rutter*, 1986; *Nygård et al.*, 2006]. The contractive behaviour of the re-saturated Whitby Mudstone at failure will probably prevent the creation of fracture permeability [*Ingram and Urai*, 1999]. The formation of a shear fracture in saturated mudstones in combination with broadening of the peak of the stress-strain curves at high confining pressures is consistent with the findings of *Dewhurst and Hennig* [2003], who performed experiments on saturated, relatively stiff

Muderong shale samples. These authors classified this behaviour as transitional, where the samples underwent larger increments of strain at constant differential stress, but eventually showed a stress drop due to the formation of a localised shear fracture at failure.

While the data suggest that the degree of water saturation affects the deformation behaviour (contractive/dilative) of the Whitby Mudstone, *Giger et al.* [2018] showed that inappropriate loading rates can also affect the stress paths of a saturated, clay-rich rock significantly. These authors performed triaxial undrained tests on the Opalinus Clay applying various strain rates. When loading the Opalinus Clay too fast, the curvature of the stress path ($q - p'$ space) prior to reaching its peak is to the left, indicating contraction, whereas it curves to the right at the maximum appropriate strain rate, indicating dilation. In addition, the peak stress and maximum pore fluid pressure coincide at fast loading rates, whereas the maximum pore fluid pressure is reached well before the maximum q at appropriate loading rate. For the Whitby Mudstone, the pore fluid pressure coincides with the maximum q at low confining pressures and increases after the maximum q at high confining pressures. As discussed earlier, the loading rate used in this study are slightly too fast for the permeability and the drainage conditions of the Whitby mudstone and could therefore contribute to the change in stress path. Additionally, the mean effective stress paths are affected by the average pore pressure, and the assumption is made that the pore pressure measured at the top and bottom of the sample represents the pore pressure within the sample. The low pore pressure build-up affects the stress path significantly. The key limitation in determining the contractive/dilatant behaviour from the strain data is that the measured radial strain does not represent the average strain field over the whole volume of the specimen.

The Whitby Mudstone samples deformed triaxially showed in all cases macroscopic shear fractures. Shear fractures were also reported in the literature for partially-dry [e.g., *McGinnis et al.*, 2017; *Sarout et al.*, 2017] and fully-saturated [e.g., *Nygård et al.*, 2006] clay-bearing rocks. The fracture angle of the shear fracture steepens (relative to the axial loading direction) when the Whitby Mudstone dehydrates. This is supported by previous findings reported by *McGinnis et al.* [2017]; *Vales et al.* [2004].

The Mohr-Coulomb failure envelopes for the re-saturated and partially-saturated Whitby Mudstone are linear over the range of confining pressures used in these tests (Figure 5.6), indicating a macroscopic brittle deformation behaviour [*Petley*, 1999; *Dewhurst and Hennig*, 2003]. *Dewhurst and Hennig* [2003] obtained similar results for the Muderong Shale, whereas *Petley* [1999] observed non-linear Mohr-Coulomb failure envelopes at similar confining pressure conditions as tested here. However, there is a great variation in the properties of mudrocks, such as mineralogy (clay type), pore size and distribution, degree of consolidation, cementation, and interparticle bonding, which affect the deformation behaviour of mudstones [*Marsden et al.*, 1992; *Petley*, 1999; *Nygård et al.*, 2006].

For clay-rich rocks, as well as other sedimentary rocks, its is proven that physical conditions, such as temperature and confining pressure, highly affect the deformation behaviour [*Rutter*, 1986; *Horsrud et al.*, 1994, 1998]. Compared to a sandstone, the mechanical response of shales is more dependent on temperature and less dependent on pressure [*Johnston*, 1987; *Horsrud et al.*, 1994]. Increasing the temperature will improve the resaturation of a clay-rich rock, reducing the capillary effects which contributes to a decrease in strength and stiffness [*Schmitt et al.*, 1994; *Papamichos et al.*, 1997; *Horsrud et al.*, 1998]. It is likely that at higher confining pressures and temperatures, the saturated Whitby Mudstone will show non-linear behaviour, with eventually curved failure envelopes (as shown by *Petley* [1999]) indicating macroscopic ductile deformation. The experiments presented here did not account for temperature changes, which is necessary when determining the deformation behaviour of the Whitby Mudstone at depth (actual reservoir conditions).

5.5 Conclusions

This study investigates the impact of water saturation of the Whitby Mudstone on its failure properties, deformation behaviour, and static elastic properties. Mudstone core plugs with different water saturations were deformed under undrained conditions at a wide range of confining pressures. The results show that the water content highly affects the mechanical properties and deformation behaviour of the Whitby Mudstone. The low friction coefficient of the Whitby Mudstone as well as the cohesive strength increases with decreasing water saturation. In addition, the Whitby Mudstone becomes mechanically stronger and stiffer with dehydration, due to increasing capillary suction within the pores of clay-rich rocks. The Whitby Mudstone shows macroscopic brittle deformation at all hydration states. Failure of the partially-saturated Whitby Mudstone results in the development of dilative shear fractures, whereas the fully-saturated Whitby Mudstone develops contractive shear fractures except at low confining pressures. Although the macroscopic deformation is similar for the partially-saturated and fully-saturated Whitby Mudstone, the nature of brittle deformation (dilative/contractive) differs with saturation state, especially at higher confining pressures. This study shows that the degree of water saturation highly impacts the rock-mechanical behaviour of clay-rich rocks. Preservation of mudstones is important and the degree of water saturation should always be reported to minimize the risk of reporting ambiguous laboratory results in the future.

6

The elastic anisotropy and mechanical properties of the partially-saturated Whitby Mudstone at elevated temperatures

Abstract The elastic anisotropy and mechanical properties of the Whitby Mudstone were obtained at room temperature conditions (chapters 4 and 5), which do not represent subsurface conditions. In the subsurface, mudstones are often buried at a few kilometres depth, where the temperature and pressure increases with depth. These parameters are known to affect the mechanical properties of mudstones. This chapter examines the effect of temperature on the elastic anisotropy and mechanical properties of the partially-saturated Whitby Mudstone. Firstly, the experimental set up and protocol are explained in detail. Secondly, the mechanical results obtained from the laboratory experiments are presented, followed by the ultrasonic velocities and elastic anisotropy, obtained at isotropic stress conditions. Finally, the causes of the changes in elastic anisotropy and mechanical properties are discussed. This work helps to get more insight into the elastic anisotropy and deformation behaviour of the partially-saturated Whitby Mudstone towards reservoir conditions.

6.1 Introduction

Mudstones play an important role in various industries. These clay-rich rocks can act as a source rock for conventional petroleum reservoirs, but also as an unconventional reservoir. In addition, due to their low permeability, they can act as a natural seal for conventional reservoirs, as well as for geo-sequestration projects [*Busch et al.*, 2008; *Dewhurst et al.*, 2019].

The role a mudstone plays in the subsurface is highly dependent on the properties of the rock, including its mineralogy, porosity, permeability, and maturity, as well as its mechanical and petrophysical properties. Top seals/mudstone caprocks are important to provide trapping mechanisms keeping the hydrocarbons in the reservoir or the injected CO_2 in the subsurface and are, for example, characterized in terms of thickness, areal extent, seal capacity (pore-scale capillary properties), and seal integrity (mechanical properties) [*Dewhurst et al.*, 2019]. Although the role of a caprock is to trap fluids in the subsurface, unconventional mudstone reservoirs need to be brittle enough to create open fractures allowing hydrocarbons to flow.

Irrespective to the role a mudstone plays in the subsurface, it is necessary to know their elastic anisotropy (i.e., variation of elastic properties with direction) and their deformation behaviour for successful exploration and production, as well as for assessing caprock integrity. The highly anisotropic character of mudstones [e.g., *Vernik and Nur*, 1992; *Vernik and Liu*, 1997; *Dewhurst and Siggins*, 2006] causes significant issues in depth conversion in seismic exploration, and in monitoring subsurface reservoirs during injection or production. The high elastic anisotropy of mudstones are mainly due to the preferred orientation of anisotropic clay particles, fractures, inter-layering of lithology, and low-aspect ratio pores [*Hudson*, 1981; *Vernik and Nur*, 1992; *Vernik and Liu*, 1997; *Sayers*, 2013]. Due to the low permeability of mudstones, reservoirs often require hydraulic fracturing. Fractures initiate and propagate in a brittle manner when the rock is relatively strong, whereas self-sealing often occurs in weaker, more ductile mudstones [*Josh et al.*, 2012].

The elastic anisotropy and deformation behaviour of mudstones is often determined at low temperature conditions. These conditions do not represent subsurface conditions, since the temperature and pressure increase with depth. Previous studies showed that the ultrasonic P-wave velocities in shales decrease with increasing temperature [*Johnston*, 1987; *Horsrud et al.*, 1998], due to the changes in pore fluid properties and weakening of the rock. Temperature has also a significant effect on the deformation behaviour of clay-rich rocks. They become more ductile and mechanically weaker with increasing temperature [e.g., *Lempp et al.*, 1994; *Horsrud et al.*, 1998; *Masri et al.*, 2014; *Rybacki et al.*, 2015]. This thermally-induced weakening can be due to re-saturation, reducing capillary pressures [*Horsrud et al.*, 1998], due to a reduction in effective stress caused by thermally-induced pore pressure increase [*Zhang*, 2018], or due to increasing contributions of more ductile deformation mechanisms. Although the P-wave velocities are affected by temperature changes, there is not much reported on the effect of temperature on the elastic anisotropy of clay-rich rocks.

This study investigates the effect of temperature on the elastic anisotropy and mechanical properties of the Whitby Mudstone. The evolution of P-wave velocities were measured along multiple ray path angles under isotropic stress loading at different temperature conditions. A method of P-wave inversion [*Kovalyshen et al.*, 2017] was used to obtain the elastic anisotropy parameters ε and δ, and symmetry axis of the Whitby Mudstone. The advantage of this method compared to the conventional way to measure elastic parameters of a TI medium (chapter 4) is that the orientation of the symmetry axis is obtained by the algorithm, so the orientation of the symmetry axis is not inferred from the visual inspection of the bedding orientation on the rock specimen [*Kovalyshen et al.*, 2017]. In addition, the error for δ is significantly smaller. The mechanical properties of the Whitby Mudstone were obtained at 150°C for a wide range of confining pressures. The presented results give insight into the effect of temperature on the elastic anisotropy and mechanical behaviour of partially-saturated mudstones.

6.2 Materials and methodology

6.2.1 Sample material, preparation, and characterization

The tested mudstone specimens originate from the base of the Mulgrave Shale Member. Thin sections taken from the base of the Mulgrave Member show that the mudstone is heterogeneous at the submillimetre scale, and essentially composed of sheet silicates ($50-70\%$, interlayered illite/smectite, illite, and kaolinite) [chapter 4; *Ten Veen et al.*, 2014; *Houben et al.*, 2016b; *Douma et al.*, 2019a]. Rock-Eval pyrolysis show that this member is particularly enriched in organic matter (average TOC = 6%) [*Zijp et al.*, 2015], often interlayered within the matrix [*Houben et al.*, 2016b]. The porosity, estimated from the dry bulk density and grain density, of mudstone core plugs originating from the Mulgrave Shale Member is ∼13% [*Douma et al.*, 2019a].

Sample blocks were collected from a wave-cut platform, which is submerged by seawater daily due to the tidal cycle. The sampled mudstone blocks were stored in seawater after sampling them to prevent initial pore water loss. The assumption is made that the pore fluid of the mudstone samples became in chemical equilibrium with the seawater. Four cylindrical core plugs with a ∼80 mm length and ∼38 mm diameter were cored normal to the bedding out of one sample block to minimize the heterogeneity between them. Seawater was used as cooling fluid during coring to prevent swelling or shrinkage of the clays present in the mudstone.

The cylindrical core plugs were placed in a desiccator with a constant relative humidity atmosphere of ∼75% at room temperature until their mass stabilized, indicating that there was no water loss and equilibrium was reached (Figure 6.1). The relative humidity atmosphere of ∼75% was achieved by using an over-saturated NaCl solution [*Laloui et al.*, 2013]. Under this relative humidity, the final water saturation of the core plugs was ∼58% ±10%. Appendix A details the method of estimating the water saturation.

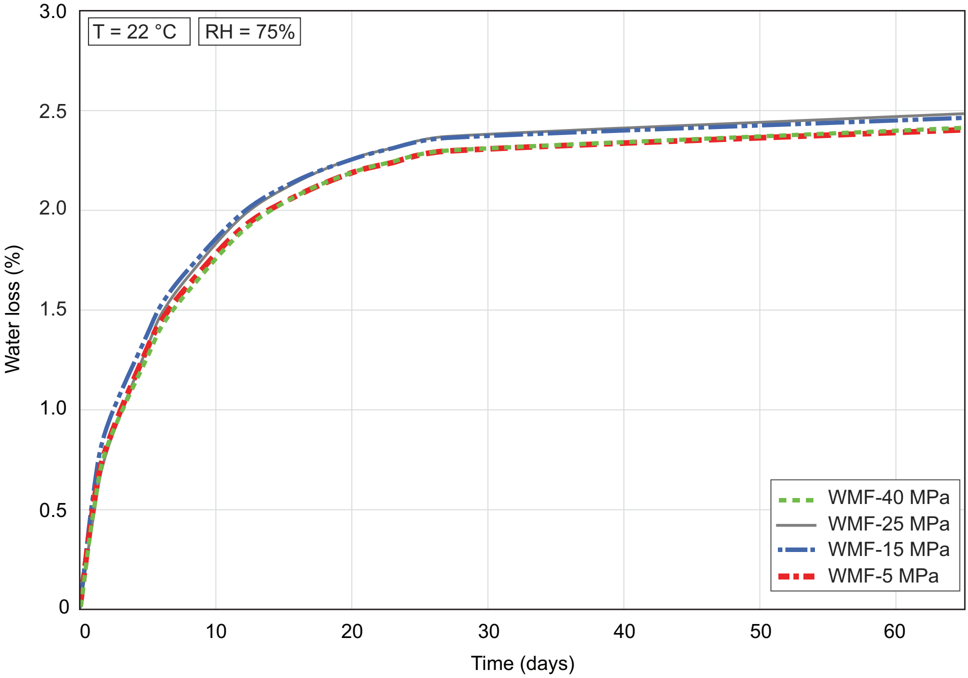

Figure 6.1: *Four cylindrical core plugs were placed in a desiccator with a constant relative humidity atmosphere of 75% until mass stabilization. Equilibrium was reached after ∼60 days.*

After stabilization, grey scale attenuation maps were obtained from the core plugs, which were imaged using a Siemens SOMATOM definition AS medical X-ray Computed Tomography (XRCT) scanner (helical image acquisition at 140kV and 500 mAs with the smallest field of view of 4 cm). The reconstructed 3D XRCT image data have a voxel size of ∼100×100×400 μm. The core plugs imaged prior to deformation were wrapped in cling film to minimize pore fluid loss during scanning. The mudstone cores were scanned in a Viton sleeve immediately after mechanically testing them in the laboratory. Grey scale attenuation maps (i.e., density maps) were obtained from the scans using Avizo 9.5.0 software to identify heterogeneities in mineralogy (density) between the different core plugs.

The saturation profile along the core axis, the water content and water-filled pore size distribution in the pore network were measured using an Oxford-GIT GeoSpec 2 MHz Nuclear Magnetic Resonance spectrometer (NMR). The core plugs were wrapped in cling film when subjected to NMR, to minimize pore water loss. During NMR, a Carr-Purcell-Meiboom-Gill (CPMG) spin-echo pulse sequence was acquired on the mudstone core plugs to measure the water content and its distribution in the pore network. The shortest echo-spacing (50 μs) was used to resolve the smallest pore sizes possible, a receiver delay of 5 s, and an appropriate number of scans to reach a signal-to-noise ratio >100. The CPMG was followed by a T_2 profile measuring the water content every ~0.3 mm (i.e., 256 slices along a 80 mm field of view) along the core plugs. The water loss of the core plugs after measuring the dimensions, CT-scanning, and NMR measurements was ~0.1%.

6.2.2 Experimental setup and protocol

The experimental setup used for the mechanical and ultrasonic testing includes (1) a *Sanchez Technologies* axisymmetric triaxial stress vessel where an axial and radial stress can be applied independently on the cylindrical mudstone plug, and (2) an ultrasonic monitoring system with ultrasonic P-wave transducers attached directly to the core sample (Figure 6.2) [see also: *Sarout et al.*, 2017].

The core plug was placed in a *Viton* sleeve to protect it from the surrounding oil which was present in the triaxial deformation vessel (Figure 6.2a). Aluminium spacers with a thickness of 1 mm and diameter of 38 mm were placed on top and bottom of the sample to achieve macroscopically undrained conditions. The pore pressure was not monitored during the experiment, since the core plugs were partially-saturated. The axial displacement was measured with three linear variable differential transformers (LVDTs), which were located outside the triaxial stress vessel (Figure 6.2a). The average of the three LVDTs was taken to calculate the axial deformation of the mudstone sample during the experiment. The local circumferential strain was directly measured with a strain gauge-based cantilever, which was attached through the *Viton* sleeve on the lateral surface of the mudstone sample. 18 P-wave transducers were attached directly to the core plug through sealable holes in the flexible *Viton* sleeve (Figure 6.2). The P-wave transducers are 6 mm in diameter and made of piezo-ceramic material with a central resonant frequency of ~0.5 MHz.

The experimental protocol of the mudstone core plugs included the following steps (Figure 6.3):

[1] The axial stress (σ_1) and radial stress ($\sigma_2 = \sigma_3$) were increased at 0.5 MPa/min at room temperature conditions (22°C ±1.5°C) until the desired stress conditions (5 MPa/ 15 MPa/ 25 MPa/ 40 MPa) were reached. For safety reasons, the axial stress was kept ~0.5 MPa higher than the radial stress. Note that this is defined in this chapter as *isotropic stress conditions*, where $\sigma_1 = \sigma_2 = \sigma_3$, even though σ_1 was slightly higher than the radial stress (σ_2 and σ_3).

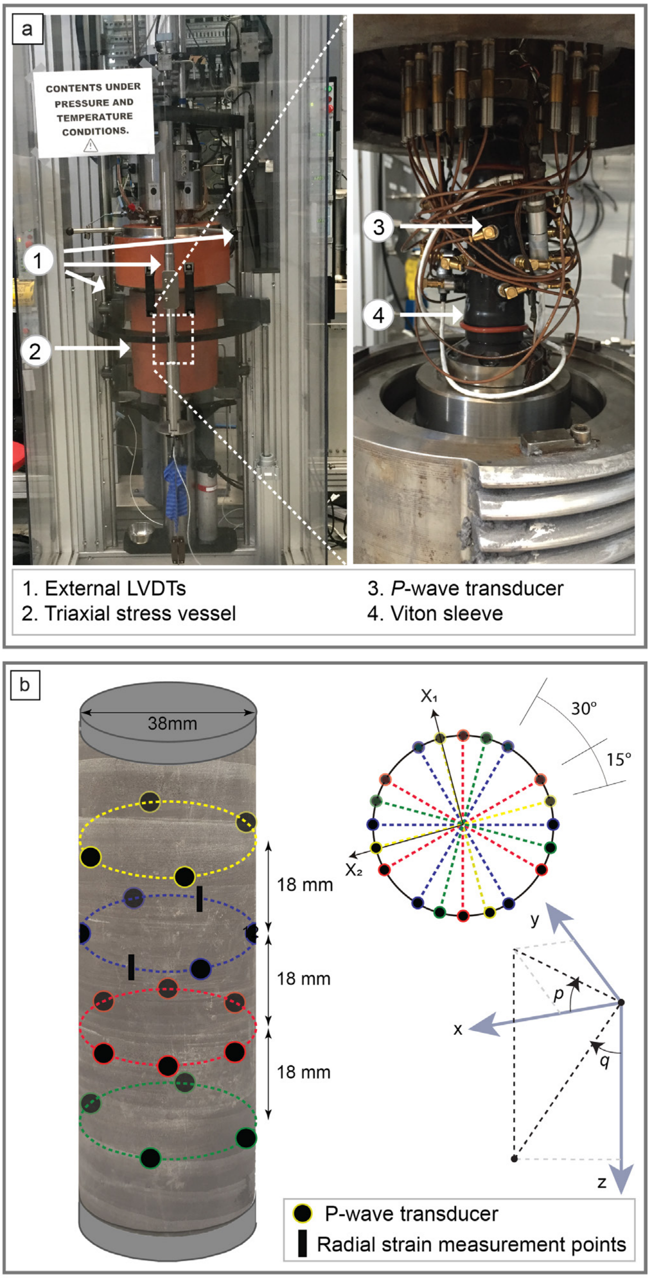

Figure 6.2: *a. Experimental Setup in the laboratory. b. Schematic drawing illustrating the position of the ultrasonic P-wave transducers. This configuration makes it possible to measure P-wave velocities along multiple ray paths.*

[2] The temperature was increased stepwise from 22°C ±1.5°C to 150°C ±0.5°C holding the stress conditions constant (isotropic stress, where $\sigma_1 = \sigma_2 = \sigma_3$). The core plugs equilibrated for 2-3 days at a constant temperature before the next temperature step.

[3] A vertical differential stress was applied orthogonal to the bedding ($\sigma_1 > \sigma_2 = \sigma_3$). Each core plugs was deformed until failure with a constant axial displacement rate (strain rate of 10^{-07} s^{-1}). Failure occurred after ~3 days.

Ultrasonic-wave velocities were obtained along multiple propagation ray paths on a single core plug. A velocity survey was performed every six hours at isotropic stress conditions (step 2). This survey includes a complete set of 18 P-wave velocity measurements carried out at a specific stage of the experiment. Each survey consists of 18 consecutive shots fired by each transducer acting as a source. During each shot, the remaining 17 transducers act as receivers. The waveforms were recorded with a sampling rate of 10 MHz (i.e., sampling period of 0.1 μs).

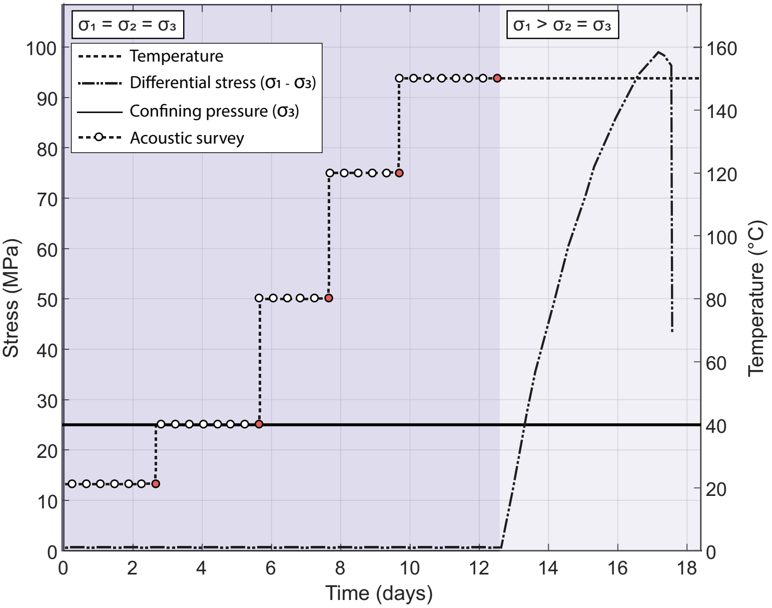

Figure 6.3: *Example of the experimental protocol at confining pressure conditions of 25 MPa. Two stages could be differentiated, including (1) isotropic stress conditions ($\sigma_1 = \sigma_2 = \sigma_3$) where the temperature was increased stepwise (21° C, 40° C, 80° C, 120° C, 150° C), and (2) differential stress loading at 150° C until failure of the mudstone core plug. A velocity survey was performed every ~6 hours at isotropic stress conditions. The velocity surveys performed at the end of stabilization at a constant temperature (red circles) were analysed in this study.*

6.2.3 Obtaining the elastic anisotropy parameters

Thomsen [1986] shows that the longitudinal phase velocity v of a P-wave propagating through a transversely isotropic (TI) media can be described by

$$v^2(\theta) = \alpha_0^2[1 + \varepsilon sin^2\theta + D^*(\theta)], \tag{6.2.1}$$

where θ is the phase angle between the symmetry axis and the propagation direction of the plane wave D^*, which can be expressed by [*Kovalyshen et al.*, 2017]

$$D^*(\theta) = \frac{1}{2}(1 - \frac{\beta_0^2}{\alpha_0^2})\left\{\left[1 + 4\frac{2\delta - \varepsilon}{1 - \beta_0^2/\alpha_0^2}sin^2\theta + 4\frac{2(\varepsilon - \delta)(1 - \beta_0^2/\alpha_0^2) + \varepsilon^2)}{(1 - \beta_0^2/\alpha_0^2)^2}sin^4\theta\right]^{1/2} - 1\right\} \tag{6.2.2}$$

where α_0^2 and β_0^2 are the P- and S-wave phase velocities along the symmetry axis, respectively. ε and δ and Thomsen's anisotropy parameters.

Kovalyshen et al. [2017] proposed a simple mathematical approximation of Thomsen's parameterization of the TI elastic anisotropy, using the group velocity (V) for a given angle (ϕ), following:

$$V = \left[\left(\frac{sin\phi}{a}\right)^k + \left(\frac{cos\phi^k}{c}\right)\right]^{-1/k} \tag{6.2.3}$$

where k is dimensionless, and a and c correspond to the P-wave velocity perpendicular and along the symmetry axis, respectively. In terms of Thomsen's parameters, $a = \alpha_0\sqrt{1 + 2\varepsilon}$ and $c = \alpha_0$.

The numerical inversion algorithm presented by *Kovalyshen et al.* [2017] uses Thomsen's model (Equations 6.2.1; 6.2.2) and the simple mathematic approximation (Equation 6.2.3) to determine the symmetry axis and Thomsen's parameters, assuming only transverse isotropy (TI). The orientation of the symmetry axis is not set as a priori. This algorithm is used to determine the azimuth of the symmetry axis p and dip angle q and Thomsen's parameters [*Thomsen*, 1986], including (1) the P-wave phase velocity along the symmetry axis α_0, (2) the P-wave anisotropy parameter ε, and (3) the wave front geometry δ.

The P-wave velocities measured along 180 ray paths were used as input files for the numerical inversion algorithm. The arrival times were picked manually at the first break of the zero crossing. The uncertainty for the P-wave arrival times is ± 0.2 μs. The velocities were obtained from the arrival times and corresponding travel distance. Note that in our experimental configuration, the velocities yield a group velocity with ray path angle ϕ [*Dewhurst and Siggins*, 2006; *Sarout et al.*, 2015; *Kovalyshen et al.*, 2018]. For illustration purposes, Figure 6.4 shows typical waveforms at two different angles (ϕ) with respect to the vertical axis, recorded after ~2 days of stabilization at 80°C.

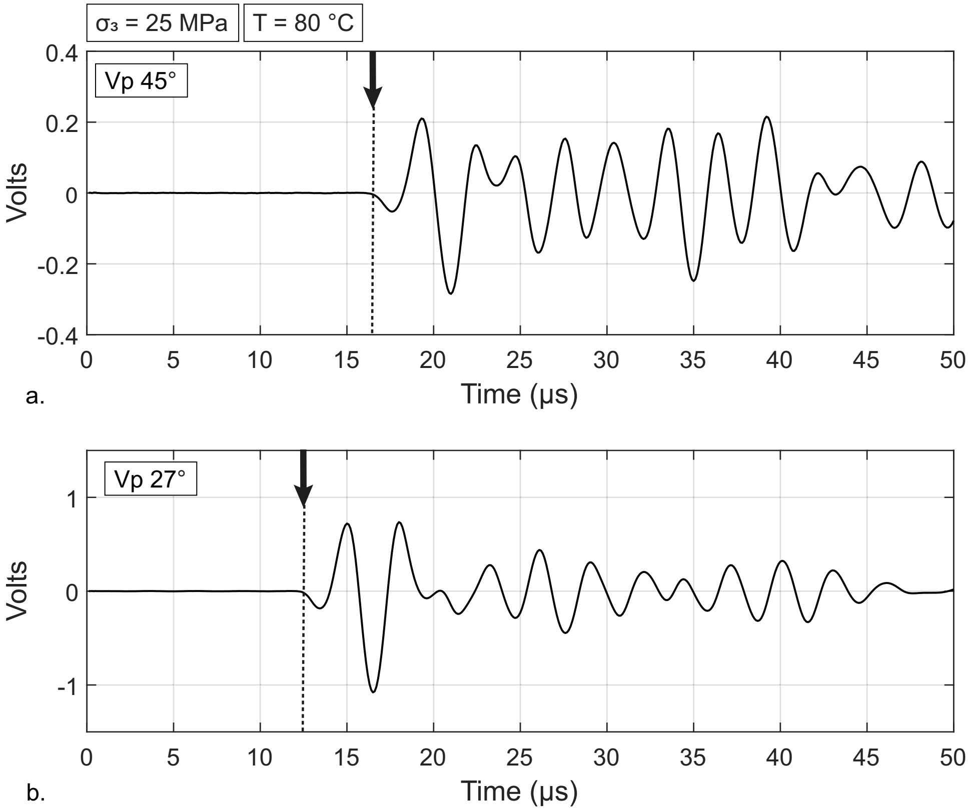

Figure 6.4: *Example waveforms of the Whitby Mudstone at confining pressures of 25 MPa and 80° C with ray path angles of a. 45° and b. 27° with respect to the vertical axis. P-wave arrival times were picked manually on the first break of the zero crossing.*

Knowing the P-wave velocities at different ray path angles, the algorithm first solves the correlation between the velocities and the elastic anisotropy parameters by fitting the measured P-wave velocities to the model presented in Equation 6.2.3, using a robust least-squares regression [*Holland and Welsch*, 1977]. This gives a first approximation of the azimuth of the symmetry axis p and dip angle q and Thomsen's parameters. A robust fit algorithm removes outliers from the input P-wave arrival time dataset. Second, Thomsen's model (Equations 6.2.1; 6.2.2) is fitted to the data set using the robust least-squares regression to give a more precise value of these properties. Note that Thomsen's model is based on phase velocities, and therefore the algorithm solves the correlation between group and phase velocity [*Tsvankin*, 2012]. For the inversion of the P-wave ultrasonic survey, a value of 0.55 is taken for β_0/α_0. This is based on the measurements performed by *Douma et al.* [2019a] (see also chapter 4) on Whitby Mudstone core plugs sampled from the same horizon in the outcrop, and having the same water saturation ($\sim$58%) as the ones tested here.

The algorithm inverts for the orientation of the symmetry axis and plots the velocity on the axis calculated by the algorithm. In other words, the group velocity vector is plotted on the reference frame (axis of symmetry) calculated by the algorithm, and thus representing the shape of the wave front. An example of the inferred Thomsen model fitted to the P-wave velocity dataset of a Whitby Mudstone core plug is shown in Figure 6.5.

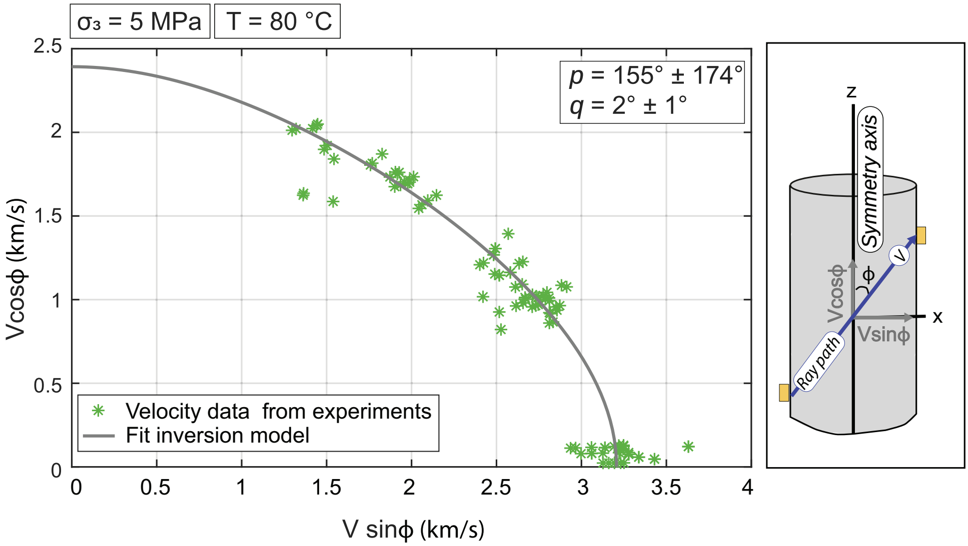

Figure 6.5: *The model described by Kovalyshen et al. [2017] is fitted to the P-wave velocities at different ray path angles measured on the Whitby Mudstone. The group velocity vector is plotted on the axis of symmetry calculated by the algorithm, representing the shape of the wave front. The numerical inversion algorithm uses P-wave velocities to determine the azimuth of the symmetry axis p and dip angle q as well as Thomsen's parameters.*

6.3 Results

■ 6.3.1 Characterizing the Whitby Mudstone core plugs

The density profile of the four different core plugs was derived from the intensity (grey levels) of the XRCT-scans and presented in Figure 6.6. The density profiles are relatively similar for the different mudstone samples, supporting the assumption that the core plugs, originating from the same horizon in the outcrop, are relatively similar in density (mineralogy). The bulk density is not homogeneous along the core axis and ranges in general between 2.35 – 2.40 $g.cm^{-3}$, with some density drops (2.35 – 2.22 g/cm^{-3}). These drops are related to bedding parallel fractures, which are likely to be formed due to dehydration when equilibrated in the desiccator [*Douma et al.*, 2019a].

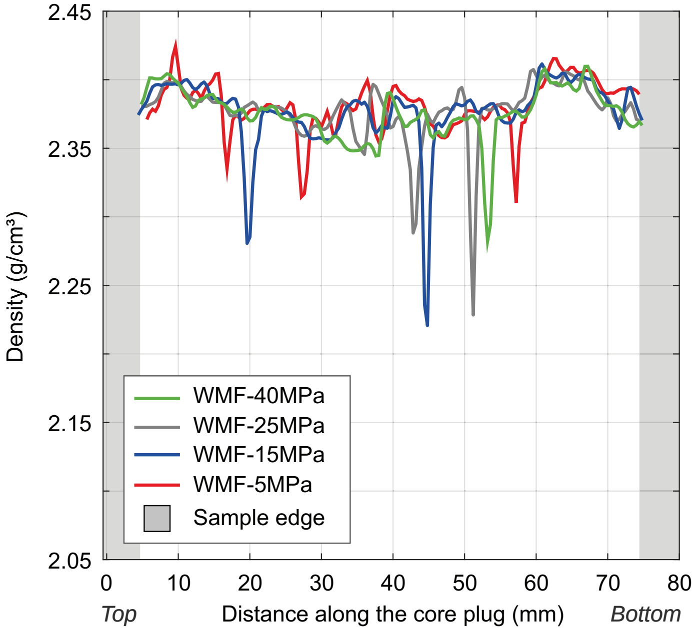

Figure 6.6: *The four core plugs used for the experiments show similar density profiles along their axis (top to bottom), suggesting that the heterogeneity in density (mineralogy) between the core plugs is minimal. The large drops in density represent the formation of dehydration fractures formed during equilibration in the desiccator.*

Figure 6.7 shows the normalized water content profile along the core axis and the T_2 distribution curves for the four mudstone core plugs derived from the NMR spectroscopy. The water content is normalized against the maximum value of core plug WMF-25MPa (Figure 6.7a). The normalized water content is not equally distributed along the core axis of each sample. This can be due to the presence of alternating layers with different mineralogy and porosity, which is consistent with the observations from the density profiles. Layers consisting of mainly clay particles are likely to have a large amount of water (free and bound water). In addition, layers having a relatively high porosity are likely to have a higher water content compared to the ones having a low porosity.

The T_2 distribution curves indicate that the water kinetics are similar for the four core plugs (Figure 6.7b), such that the water is mainly present in the inter-grain pores and bound to the clays. It is likely that the water evaporated from the larger pores and fractures when drying/equilibrating in the desiccator with a relative humidity atmosphere of ~75%. The overall T_2 values are relatively low (<20 ms), due to the small pore size of the Whitby Mudstone. The NMR signal amplitude describes the matrix of the Whitby Mudstone and has a similar intensity for all the core plugs (~0.52 g/cm^{-3} of water).

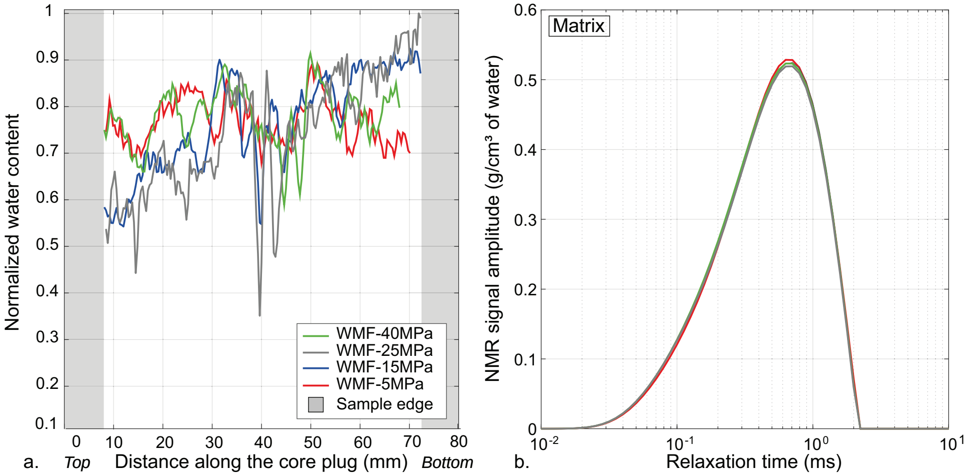

Figure 6.7: *a. The normalized water content was derived from the NMR spectroscopy and is not distributed equally along the core axis of the Whitby Mudstone due to alternating layers with different mineralogy and porosity. The data in the grey area was removed, since this did not represent the actual water content due to the edge effect of the core plug. b. The NMR signal amplitude has the same intensity for all the four mudstone core plugs.*

■ 6.3.2 Deformation behaviour of the Whitby Mudstone

Axial deformation at isotropic stress conditions

Figure 8 shows the axial strain of Whitby Mudstone core plugs over time at different temperature steps. Corrections were applied to the axial strain data during consolidation and at the time step of temperature increase, since the LVDTs were very sensitive to temperature changes. When consolidating at a constant temperature, the temperature changes due to daily temperature variations (day/night) were recorded. When increasing the temperature with ~20°C, the average expansion of the LVDTs is ~0.1 mm. The amount of expansion was extracted from the axial strain data.

The axial strain increases over time and with increasing temperature. After three days of consolidation at 22°C, the axial strain is ~0.5 milli-strain at stress conditions of 5, 15, and 25 MPa, and ~2 milli-strain at 40 MPa, after only two days of consolidation. The axial strain increases with increasing temperature, especially when T≥80°C. The largest increase in axial strain is at 150°C (up to 5 milli-strain).

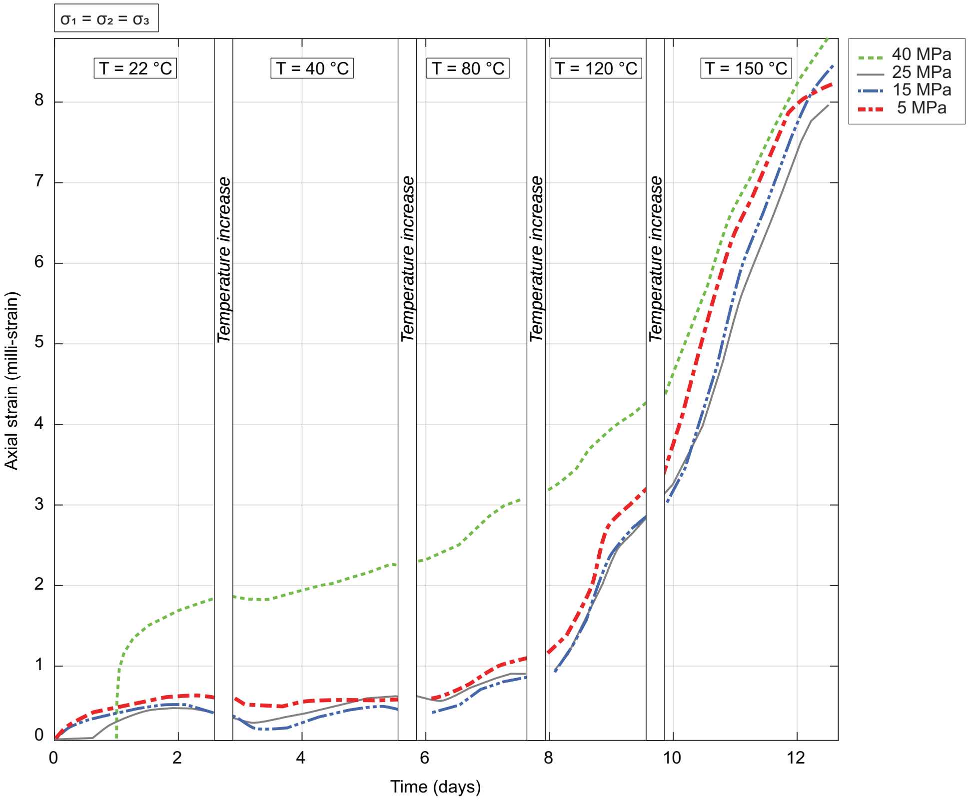

Figure 6.8: *The axial strain increases for the Whitby Mudstone, especially at higher temperatures (T≥80° C). An increase in axial strain indicates shortening of the core plug in the vertical direction. Corrections were applied to the axial strain data at isotropic stress conditions and at the temperature steps, since the external deformation arms were very sensitive to the temperature changes.*

Rock-mechanical properties and failure criterion (differential stress conditions)

Figure 6.9a shows the differential stress – axial strain curves for the Whitby Mudstone deformed at different confining pressures at a temperature of 150°C ±0.5°C. The differential stress is defined as the difference between the axial load (σ_1) and the confining pressure (σ_3) applied on the core plug. The Whitby Mudstone shows initially linear-elastic deformation, followed by non-linear deformation, peak differential stress (peak strength), and a sudden reduction in differential stress (Figure 6.9a). The peak stress increases with confining pressure. Rock-mechanical properties, including Young's Modulus E_3 and Poisson's ratio ν_{31}, were obtained from the linear part of the stress- strain curve, between 40% – 60% of the peak stress. E_3 does not change significantly with confining pressure (remains ~2.6±0.3 GPa). ν_{31} is relatively low (~0.14) at a confining pressure of 5 MPa, but increases at higher confining pressures (~0.21). Values of the peak differential stress and the rock-mechanical properties obtained from the differential stress – axial strain curves are displayed in Table 6.1.

The differential stress – volumetric strain curves of the Whitby Mudstone are displayed in Figure 6.9b. The volumetric strain (ε_v) is defined in chapter 5 (see Equation 5.3.3). Under all tested confining pressure conditions, the volumetric strain first increases, indicating volumetric compaction. At the onset of dilatancy, the volumetric strain decreases with ongoing axial loading for the core plugs tested at confining pressures of 15 MPa, 25 MPa, and 40 MPa. This is less significant for the core plug deformed at a lower confining pressure (5 MPa).

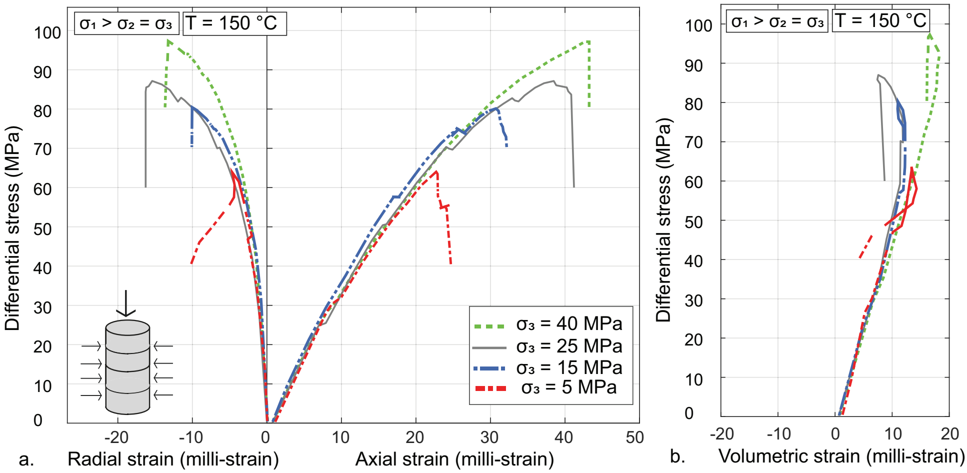

Figure 6.9: *a. The stress – strain curves show typical brittle behaviour, with a well-defined peak strength. The peak differential stress increases with increasing confining pressure (σ_3). b. First, the volumetric strain increases with axial loading (compaction), whereas it decreases at the onset of dilatancy.*

Table 6.1: *Sample properties, experimental conditions, and mechanical properties of the Whitby Mudstone.*

		WMF-5MPa	**WMF-15MPa**	**WMF-25MPa**	**WMF-40MPa**
Sample properties					
Length	mm	76.28 ± 0.1	76.37 ± 0.1	75.76 ± 0.1	75.65 ± 0.1
Diameter	mm	37.81 ± 0.1	37.65 ± 0.1	37.59 ± 0.1	37.66 ± 0.1
Initial water saturation	%	58 ± 10	58 ± 10	58 ± 10	58 ± 10
Experimental conditions					
Confining pressure	MPa	5	15	25	40
T at failure	°C	150 ± 0.5	150 ± 0.5	150 ± 0.5	150 ± 0.5
Deformation rate	mm.hr^{-1}	0.0275	0.0275	0.0273	0.0272
Mechanical properties at 150° C					
Peak differential stress	MPa	64 ± 2	80 ± 2	87 ± 2	97 ± 2
Static E_3	GPa	2.6 ± 0.3	3.3 ± 0.8	2.6 ± 0.3	2.6 ± 0.3
Static ν_{31}	-	0.14 ± 0.01	0.23 ± 0.01	0.21 ± 0.01	0.20 ± 0.01
Calculate UCS	MPa	63			
Cohesive strength (S_0)	MPa	22.7			
Friction angle	°	18.1			
Coefficient of internal friction (μ)	-	0.22			

The stress – strain data of the Whitby Mudstone obtained at a wide range of confining pressures at 150°C can also be displayed in the form of a Mohr diagram (Figure 6.10). The failure criterion could be established from the results of the triaxial deformation experiments (see Equation 5.3.6. The Whitby Mudstone has a cohesive strength of ∼23, a friction coefficient of 0.33 and a friction angle of ∼18°. The friction coefficient and angle is relatively low compared to most sedimentary rocks, but in agreement with values found for clay-rich rocks [chapter 5 and *Dewhurst and Hennig*, 2003]. The failure envelope is linear over the tested confining pressures. The mechanical properties are displayed in Table 6.1. Note that for the partially-saturated Whitby mudstone core plugs a pore pressure (P_p) of 0 MPa was assumed to obtain the effective normal stress ($\sigma_i - P_p$). This assumption might be incorrect, since previous studies [e.g., *Onaisi et al.*, 1994; *Ferrari et al.*, 2014] showed that dehydration of clay-rich rocks can lead to negative pore pressures. However, to the authors knowledge, there is no well-established correlation for clay-rich rocks between the amount of negative pore pressure and the effective stress.

■ 6.3.3 Ultrasonic *P*-wave velocities at isotropic stress conditions

Figure 6.11 shows average ultrasonic *P*-wave velocities (group velocities) at different ray path angles measured at isotropic stress conditions at different temperatures (22°C, 40°C, 80°C, 120°C, 150°C). The average *P*-wave velocity was obtained by averaging all the picked *P*-wave velocities obtained from different source – receiver pairs having the same ray path angle. Note that the ray path angle represents the angle with respect to the symmetry axis assuming that the bedding is horizontal (VTI medium).

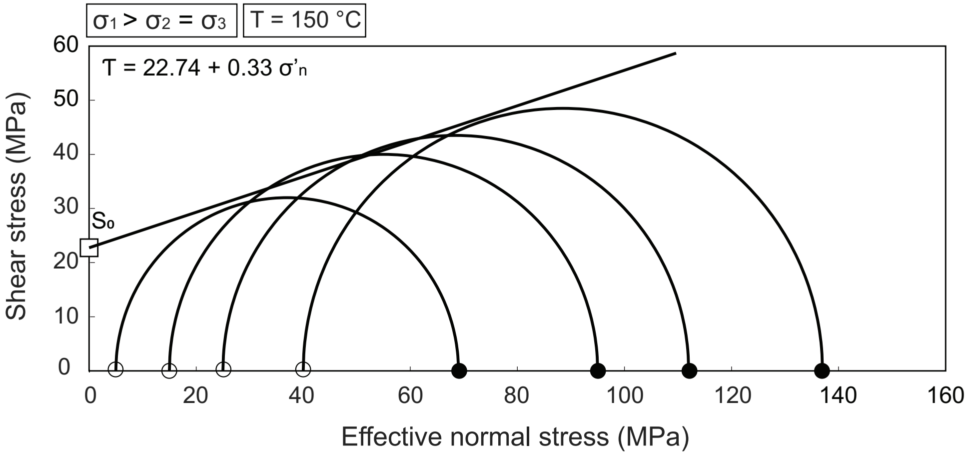

Figure 6.10: *The failure envelope of the Whitby Mudstone at 150 °C obtained from the triaxial deformation experiments. The peak stress (σ_1) and confining pressure (σ_3) are indicated by the closed and open circles, respectively. The square indicates the cohesive strength (y-axis intercept).*

All P-wave velocities increase with confining pressure and decrease with decreasing ray path angle (Figure 6.11). In general, an increase in temperature leads to a decrease in ultrasonic P-wave velocity. However, the horizontal velocity (V_{p90°) first decreases, and increases again at ~120°C (Figure 6.11a). The largest change in V_{p90° was observed at low isotropic stress (5 MPa), where it decreases from ~4000 m/s to ~3650 m/s (~9%) (22°C to 120°C) and increases again to ~3800 m/s (150°C). The change in horizontal P-wave velocity due to temperature changes becomes less significant when the confining pressure increases.

A similar trend was observed at a ray path angle of 65°, where the P-wave velocity decreases when the temperature increases from 22°C to 120°C and increases again at 150°C (Figure 6.11b). The velocity drop is the largest at 15 MPa, decreasing from ~3550 m/s to ~3400 m/s (~4%) (22°C to 120°C) and increasing again at 150°C to ~3500 m/s. At 5 MPa, the P-wave velocity remains around ~3200 m/s up to 120°C but increases to ~3300 m/s at 150°C (~3%).

The P-wave velocity does not change significantly when the ray path angle is 45°, and decreases a maximum of ~50 m/s with increasing temperature at isotropic stress of 5 MPa, 15 MPa, and 25 MPa (Figure 6.11c). At higher isotropic stress conditions (40 MPa), the P-wave velocity decrease from ~3400 m/s to 3250 m/s (~5%) when the temperature increases from 21°C to 150°C.

A similar trend is observed at a ray path angle of 34°, where the P-wave velocity decreases from ~2900 m/s to 2800 m/s (~4%) (15 MPa), ~3200 m/s to ~3150 m/s

(~2%) (25 MPa), and 3500 m/s to 3200 m/s (~8%) (40 MPa) when the temperature increases from 22°C to 150°C (Figure 6.11d). The trend is less clear at 5 MPa confining pressure, where the velocity ranges between ~2550 m/s and ~2650 m/s.

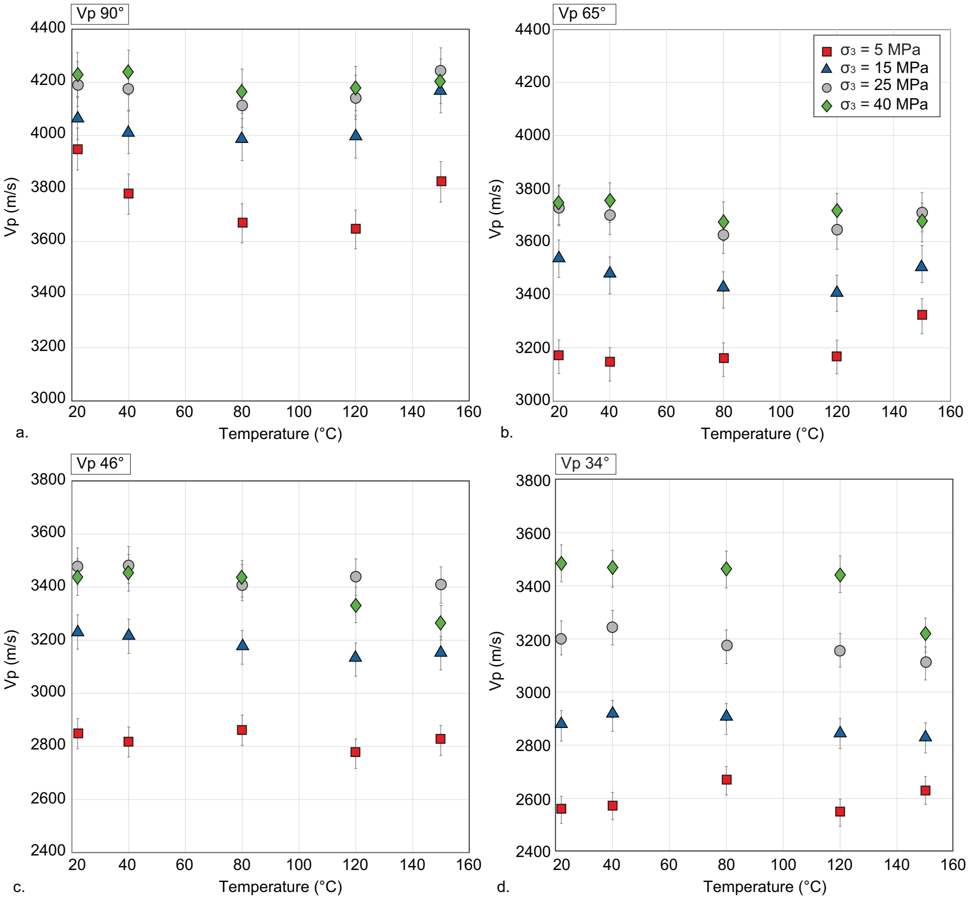

Figure 6.11: *Averaged ultrasonic P-wave velocities (group velocities) at four different ray path angles. In general, P-wave velocities decrease with increasing temperature. At an angle of 90° (a) and 65° (b), the velocity first decreases, and increase again at 150° C. The P-wave velocity increases with confining pressure.*

■ 6.3.4 The symmetry axis and elastic anisotropy of the Whitby Mudstone

The group velocities picked from the recorded waveforms were used as input parameters for the inversion algorithm presented by *Kovalyshen et al.* [2017] to obtain the orientation of the symmetry axis and the elastic anisotropy parameters.

Figure 6.12 shows an example of the ultrasonic P-wave velocities plotted relative to the symmetry axis calculated by the algorithm [*Kovalyshen et al.*, 2017], and the model fitted to the experimental data for different temperatures at 15 MPa (isotropic stress conditions). The experimental data and fitted model show that P-wave velocity decreases with decreasing ray path angle, so that the P-wave velocity along the symmetry axis (angle = 0° ; $V sin\phi = 0$ km/s) is lower than the velocity perpendicular to the symmetry axis (angle = 90° ; $V cos\phi = 0$ km/s). Some of the velocity points are off the trend, which can be due to inappropriate velocity picking, due to the relatively large size of the transducers, or the assumption that the signal travels from the centre of the source of the transducer to the centre of the receiver [*Kovalyshen et al.*, 2017]. Additionally, the variation in P-wave velocities obtained from ray paths with the same angle relative to the symmetry axis can indicate that there are heterogeneities in the mudstone core plug locally, such as fossil (fragments), affecting the velocities along different ray paths even though the ray path angle does not change. The robust fitting minimized the effect of outliers affecting the inversion [*Kovalyshen et al.*, 2017].

The symmetry axis of the core plugs at isotropic stress condition was calculated at the different temperature steps. The azimuth p and dip q of the symmetry axis of all the core plugs is shown in Table 6.2. The dip of the symmetry axis is between 1° and 3° for all the tested mudstone core plugs at all temperatures, which is supported by the visual inspection of a (near) horizontal bedding plane. It is not likely that the temperature changes the symmetry axis of the core plug. However, there is a large variation in p calculated for a single core plug at different temperature steps. For example, at an isotropic stress of 15 MPa, p varies between 2° and 47° with uncertainties up to 63°. The value for p is difficult to determine by the algorithm, since the dip is near zero. When the dip of the symmetry axis is near zero, it means that it does not clearly dip in any direction, resulting in a large uncertainty in p. *Kovalyshen et al.* [2017] also indicate that the quality of the inversion depends on the orientation of the symmetry axis with respect to the transducer array. The algorithm works best if the symmetry axis is inclined, preferably >17°.

Figure 6.13 shows the elastic anisotropy parameters α_0, ε, and δ, for the Whitby Mudstone at varying isotropic stress conditions and temperatures. The P-wave velocity along the symmetry axis increases with isotropic stress (Figure 6.13a). In general, α_0 decreases with increasing temperature (Figure 6.13a). At 40 MPa, α_0 remains relatively constant (~3000 m/s) when increasing the temperature up to 120°C, and drops to ~2800 m/s at 150°C. At stress conditions (25 MPa; 15 MPa), α_0 decreases from ~2740 m/s to ~2660 m/s (~3%) and ~2470 m/s to ~2370 m/s (4%), respectively, when the temperature increases from 22°C to 150°C. Contrary to the core plugs, the mudstone sample tested at 5 MPa increases from ~2150 m/s to ~2400 m/s (11%) when heating from 22°C to 80°C and decreases again to ~2250 m/s at 150°C.

The P-wave anisotropy parameter ε is relatively high at 5 MPa (~0.7), and de-

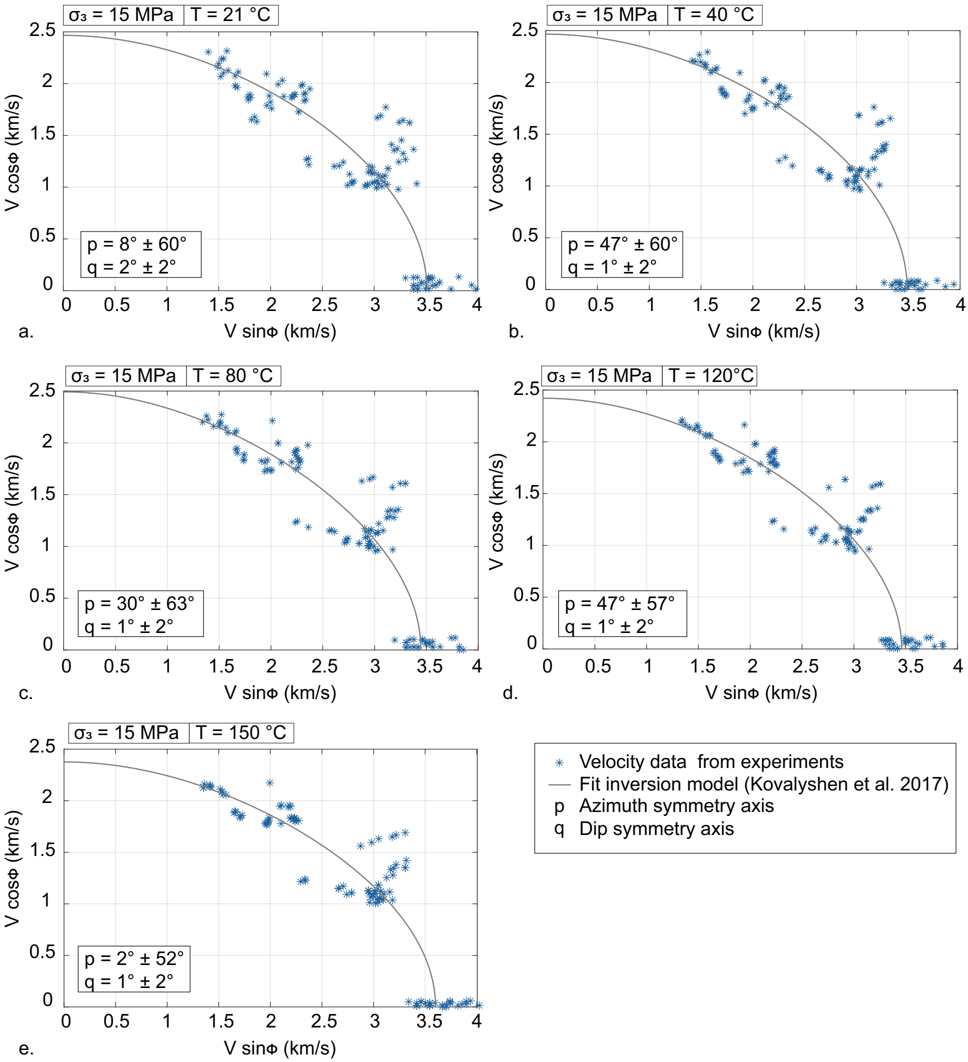

Figure 6.12: *The inferred Thomsen model was fitted to the experimental data obtained from the same core plugs tested at isotropic stress conditions ($\sigma_1 = \sigma_2 = \sigma_3 = 15MPa$) for different temperatures: a. 21°C, b. 40°C, c. 80°C, d. 120°C, e. 150°C. Velocities are plotted relative to the calculated symmetry axis, representing the shape of the wave front. The dip of the symmetry axis is ~1° (i.e., symmetry axis perpendicular to the horizontal bedding), and therefore the axis does not clearly dip in any direction, resulting in a wide variation in azimuth and an extremely large uncertainty.*

Table 6.2: *Symmetry axis of the core plugs at different temperature conditions calculated by the algorithm. The dip angle is near zero, resulting in a large uncertainty for the azimuth.*

		Temperature (°C)				
		22	40	80	120	150
WMF-5MPa						
Azimuth p	°	19 ± 234	3 ± 280	154 ± 174	114 ± 163	160 ± 209
Dip q	°	3 ± 1	1 ± 1	2 ± 1	2 ± 1	2 ± 1
WMF-15MPa						
Azimuth p	°	8 ± 61	47 ± 59	30 ± 63	41 ± 57	2 ± 52
Dip q	°	2 ± 3	1 ± 3	1 ± 3	1 ± 3	1 ± 2
WMF-25MPa						
Azimuth p	°	3 ± 78	2 ± 76	3 ± 70	3 ± 67	2 ± 67
Dip q	°	3 ± 2	3 ± 2	3 ± 2	3 ± 2	3 ± 2
WMF-40MPa						
Azimuth p	°	174 ± 50	183 ± 42	171 ± 56	166 ± 48	130 ± 35
Dip q	°	2 ± 1	3 ± 1	3 ± 2	1 ± 1	1 ± 1

creases with isotropic stress (∼0.25 at 40 MPa) (Figure 6.13b). ε does not change significantly when the temperature increases from 21°C to 80°C, except at low stress (5 MPa) where ε decreases from ∼0.7 to ∼0.4 (57%). ε increases significantly at higher temperatures (120°C to 150°C) at all confining pressure conditions.

There is no clear correlation between the temperature and wave front geometry δ (Figure 6.13c). δ varies between ∼0 and ∼0.4 at confining pressures up to 25 MPa, and is negative at higher confining pressure (40 MPa). Note that the uncertainty for δ is significant.

6.4 Discussion

6.4.1 The mechanical behaviour of the partially-saturated Whitby Mudstone at 150°C

The peak strength increases with confining pressure, which is in agreement with previous studies [*Petley*, 1999; *Dewhurst and Hennig*, 2003; *Rybacki et al.*, 2015]. Based on the shape of the stress – strain curves, the Whitby Mudstone shows typical brittle deformation behaviour at 150°C under all the tested confining pressures [*Petley*, 1999].

Brittle deformation behaviour was also observed for the Whitby Mudstone core plug, originating from the same stratigraphic horizon as the ones presented in this study and having a similar water saturation ($S_w \sim 58\%$), deformed at a lower tem-

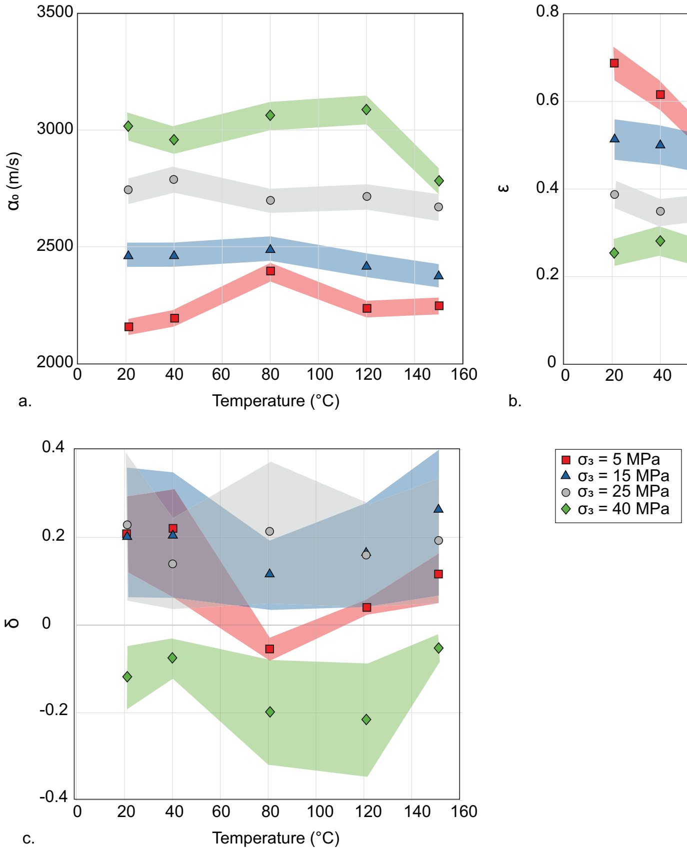

Figure 6.13: *Elastic anisotropy parameters for the Whitby Mudstone at different temperature and confining pressure conditions. The coloured area indicates the uncertainty. a. In general, the P-wave velocity perpendicular to the symmetry axis (α_0) decreases with increasing temperature, except at low confining pressure. The velocity increases with increasing confining pressure. b. P-wave anisotropy ε increases with increases at high temperatures and decreases with increasing confining pressure. c. No clear trend was observed for the wave front geometry δ. Note that the uncertainty for δ is large.*

perature (~21°C) (chapter 5). Comparing the deformation results from this study with the data presented in chapter 5 [see also: *Douma et al.*, 2019b] indicate that the mechanical (failure) properties are dependent on temperature (Figure 6.14). At a temperature of 150°C, the rock strength increases, as well as the cohesive strength of the Whitby Mudstone. The change in friction coefficient is less significant. This could be related to coupling effects between the fluid and the solid phase [*Horsrud et al.*, 1998]. Most of the pore water in a mudstone is not in a 'free' state [*Horsrud et al.*, 1998], but often adsorbed on the external surfaces of the clay particles, as well as within the sheet structures of these particles, due to the small pore sizes and the electric nature of the mineral surface [*Horsrud et al.*, 1998; *Zhang*, 2018]. This is supported by the NMR data obtained for the Whitby Mudstone samples (Figure 6.7). Heating a mudstone can lead to thermal expansion of brine around the clay particles and inside clay laminae, release of water to the pore space, and reduced inter laminar spacing [*Horsrud et al.*, 1998]. In particular in partially-saturated cores, where the majority of the 'free' water is already evaporated [*Douma et al.*, 2019b], heating causes the release of adsorbed water, leading to more solid-solid type contacts between particles, enhancing the cohesion and friction resistance between solid particles, which strengthen the mudstone [*Zhang*, 2018]. In addition, although the core plug is at macroscopically undrained conditions, heating may dry the mudstone, resulting in higher capillary pressures and stiffening of the rock frame, which may resulting in a higher rock strength and cohesive strength [*Douma et al.*, 2019a,b].

The thermal response is likely to be different when clay-rich rocks are (near) full saturation. *Horsrud et al.* [1998] shows a decrease in strength and stiffness for preserved North Sea shales when increasing the temperature from room temperature to 80°C. *Schmitt et al.* [1994]; *Papamichos et al.* [1997]; *Horsrud et al.* [1998] suggest that an increase in temperature improves the re-saturation, which reduces the capillary effects in clay-rich rocks significantly. *Zhang* [2018] suggests that fully-saturated mudstones weaken when the temperature increases from 20°C to 116°C, due to thermally-induced pore pressure, resulting in a decrease in mean effective stress, as well as by thermally-induced reduction of cohesion and friction resistance of the bound water films between solid particles.

6.4.2 Impact of temperature on the ultrasonic velocities and elastic anisotropy

In general, the P-wave velocities of the Whitby Mudstone decreases with increasing temperature. A reduction in P-wave velocity is in agreement with the findings of, for example, *Johnston* [1987] showing a decrease in P-wave velocity of ~10% when heating the saturated North Sea Kimmeridge Clay up to 100°C, and *Horsrud et al.* [1994], showing a reduction in P-wave velocity of ~5% with increasing temperature (20°C to 80°C). The velocity reduction of 5% and 10% as found by *Johnston* [1987] and *Horsrud et al.* [1994] are in agreement with the amount of velocity reduction found in this study. *Johnston* [1987] suggests that the P-wave velocity dependence on temperature in a rock is mostly controlled by the properties of the pore fluid. An increase in temperature reduces the density and viscosity of the brine, as well as its compressibility, which results in a lower P-wave velocity.

At higher temperatures ($T \geq 120$°C), the P-wave velocity at an angle of 90° and 65° increases, which is especially the case at lower confining pressures. In clay-rich rocks, the changes in fluid properties may compete with the clay effects, since most of the pore fluid is bound to the grains. On one hand, the density and compressibility of the brine decreases with temperature [*Sharqawy et al.*, 2010], resulting in lower P-wave velocities. On the other hand, heating leads to release of bound water [*Sun et al.*, 2016; *Zhang*, 2018], and therefore, the loss of interlayer water

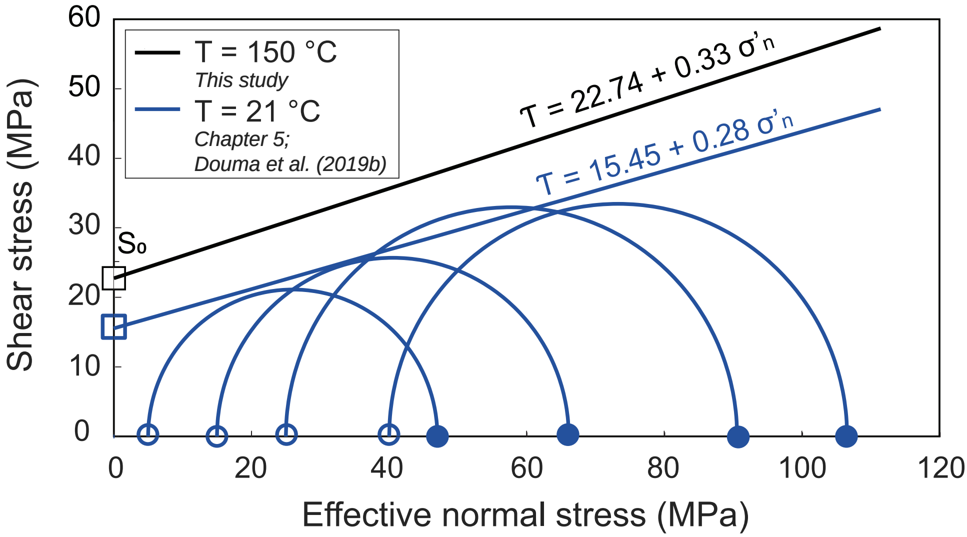

Figure 6.14: *The rock strength, the cohesive strength, and the coefficient of internal friction obtained for the Whitby Mudstone with a water saturation of ∼58% increases at higher temperatures. The open and closed circles represent the confining pressure and peak strength of the Whitby Mudstone deformed at 21° C by Douma et al. [2019b] (chapter 5), respectively.*

from the mineral structure might result in grain contact stiffening [*Dewhurst and Siggins*, 2006]. *Sun et al.* [2016] showed that adsorbed and interlayer water can evaporated at temperatures between 100°C amd 250°C, whereas structural water at temperatures >300°C. Stiffening of the aggregate can lead to an increase in *P*-wave velocity [*Dewhurst and Siggins*, 2006]. Even though the mudstone core plugs are under macroscopically undrained conditions, the results suggest that the bound water can still migrate to the empty pore space when heated.

The idea of grain contact stiffening is supported by the mechanical data, showing that the Whitby Mudstone becomes elastically stiffer at 150°C. The effect of the grain stiffening is larger than the effect of change in fluid properties, simply because the amount of grains present in the bulk volume is much larger. In addition, the axial strain data at isotropic stress conditions shows that the axial strain increases significantly when T ≥120°C. The significant increase in axial strain may suggest that there is temperature dependent axial compaction, which is likely to result in a denser material, increasing *P*-wave velocities. *Dewhurst and Siggins* [2006] suggest that it is difficult to mechanically compact a clay-rich rock with very small pores (pore throat of ∼20 nm) [*Dewhurst et al.*, 2002] and a porosity <20% [*Dewhurst et al.*, 1998] even at high stress levels. However, the (micro) fractures present in the Whitby Mudstone due to drying and/or tectonic uplift (stress relief micro fractures) are likely to close at isotropic stress conditions, especially because σ_1 is slightly higher than σ_2 and σ_3 and acts perpendicular to the fracture orientation. The closure of (micro) fractures result in higher P-wave velocities [*Holt et al.*, 1997; *Dewhurst and Siggins*, 2006].

The ε of the Whitby Mudstone at isotropic stress conditions is high, and decreases with increasing stress. It is expected that the finest-grained clay materials have the highest anisotropies in physical properties [*Clennell et al.*, 1999]. The high ε is consistent with previous work on the Whitby Mudstone having the same degree of saturation tested at room temperature [*Douma et al.*, 2019a] and other clay-rich shales [e.g., *Dewhurst and Siggins*, 2006]. The presence of anisotropic clay particles, organic material, laminations, and fractures in the Whitby Mudstone result in a high intrinsic anisotropy [*Vernik and Nur*, 1992; *Sayers*, 1994; *Dewhurst and Siggins*, 2006; *Kuila et al.*, 2011; *Douma et al.*, 2019a]. The change in ε under isotropic stress conditions can be related to changing particle alignment and/or porosity decrease [*Hornby*, 1998]. However, it is not likely that particles rearrange under isotropic stress conditions or that the porosity is reduced significantly, since the Whitby Mudstone is a compacted mudstone with small pores. It is more likely that ε decreases with increasing isotropic stress, due to the closure of imperfections, such as bedding parallel fractures, which is in agreement with other studies [*Jakobsen and Johansen*, 2000; *Dewhurst and Siggins*, 2006]. Note that at higher temperatures (T>300°C), structural water can escape, significantly damaging the chrystal lattice [*Sun et al.*, 2016], which is likely to change the elastic anisotropy. Additionally, when T>300°C, organic matters in the clay structure can undergo oxidation and decomposition reactions [*Sun et al.*, 2016], which may affect the ultrasonic velocities. *Vernik and Nur* [1992] showed that the elastic anisotropy can be enhanced by the effect of temperature due to more liquified state of kerogen when heated [*Vernik and Nur*, 1992]. However, *Vernik and Landis* [1996] showed that the intrinsic elastic anisotropy of tight black shales is practically independent of their maturity rank and primarily affected by the organic richness.

The increase in ε at high temperatures (T≥120°C) is a result of the changes in P-wave velocity with temperature. The significant change in the horizontal P-wave velocity relative to the velocities in the other directions results in an increase in ε at 150°C. The values for δ are higher compared to the values found on other Whitby Mudstone samples (chapter 4;*Douma et al.* [2019a]). There is no clear trend between temperature and δ, and note that the uncertainty for δ is still significant.

The effect of temperature on the ultrasonic velocities, hence elastic anisotropy, are likely to be different when obtained for fully-saturated core plugs. At saturated conditions, it is less likely that the bound water will migrate when heated, since pore water is filling the pores [*Zhang*, 2018]. Rock frame weakening due to temperature increase [e.g., *Schmitt et al.*, 1994; *Horsrud et al.*, 1998] in combination with pore fluid expansion [*Zhang*, 2018] and a decrease in pore fluid density [*Johnston*, 1987] reduces the bulk modulus. This is likely to lower the ultrasonic velocities [*Johnston*, 1987; *Horsrud et al.*, 1994]. In the subsurface, mudstones can have water saturations around 80%-95% [*Moritz*, 1995], and therefore, the elastic anisotropy of the Whitby Mudstone might be different at depth (elevated temperature), when saturated.

6.5 Conclusions

This study investigates the effect of temperature on the mechanical properties and elastic anisotropy of the partially-saturated Whitby Mudstone. Mudstone core plugs with a water saturation of 58% were tested ultrasonically under macroscopically undrained conditions at different temperatures. Additionally, the mudstone core plugs were brought to failure at a wide range of confining pressures at 150°C. The partially-saturated Whitby Mudstone behaves in a brittle manner at 150°C. At isotropic stress conditions, the elastic anisotropy of the Whitby Mudstone is high, due to its composition, the presence of laminations and dehydration fractures. The results show that ε increases at high temperatures. There are two key mechanisms which play an important role in velocity changes, hence anisotropy changes, of the partially-saturated mudstone at elevated temperatures. First of all, an increase in temperature reduces the density and compressibility of the pore fluid resulting in a P-wave velocity decrease. Second, the increase in temperature leads to migration of adsorbed water, resulting in grain contact stiffening, hence increase in rock strength and cohesion, leading to an increase in P-wave velocity. No clear trend was observed for δ with increasing temperature. This study shows that elevated temperatures can change the elastic anisotropy of partially-saturated mudstones. The results may not represent the subsurface conditions and are likely to deviate when heating fully-saturated core plugs.

7

The mechanical contrast between layers controls fracture containment in layered rocks

Abstract The deposition process of unconventional reservoirs (such as mudstone reservoirs) is rarely constant, resulting in heterogeneities in mineralogy on various scales (chapter 3), resulting in many lithological layers (chapters 4, 5) with significant variation in mechanical properties within the rock succession (chapter 3). This heterogeneity affects fracture nucleation and containment, which makes it difficult to predict whether fractures propagate through multiple layers or stay within one layer. A consequence of fracture containment in individual layers is that the fractures are not effectively connecting the individual high-permeability layers in a bedded reservoir sequence, thereby limiting the reservoir potential significantly. In contrast, fracture propagation through layer boundaries may result in loss of cap rock integrity and potentially create unwanted reservoir leakage pathways. Although both fracture propagation and containment in layered sedimentary rocks is widely recognized in the field, the mechanisms which control fracture propagation over fracture containment are not fully understood. This chapter examines the control of mechanical contrast on the fracture containment in layered rocks. First, the experimental setup is presented, followed by the results obtained through rock-mechanical experiments on fracture containment and orientation. The effect of mechanical contrast on fracture containment is discussed and predictions are made on which subsurface conditions fractures are contained in one layer or propagate across layers. This work makes it possible to better predict fluid flow paths in a reservoir, as well as to unravel the tectonic history of a rock succession.

Published as: Douma, L.A.N.R., J. A. Regelink, G. Bertotti, Q.D. Boersma, A. Barnhoorn (2019), The mechanical contrast between layers controls fracture containment in layered rocks, *Journal of Structural Geology*, 127, 103856
Note that minor changes have been introduced to make the text consistent with the other chapters.

7.1 Introduction

As the global demand for energy is increasing, societies turn to so-called unconventional resources to meet the energy supply requirements. The production from unconventional petroleum reservoirs is challenging, because of the low permeability of the rocks forming these reservoirs. Naturally fractured reservoirs have a large potential for increased recovery, since open fractures allow fluids to flow [*Newhouse*, 1942], and are an important source for connectivity. Natural fractures can form anywhere throughout the reservoir when stresses exceed the local ultimate strength of the rock [*Handin*, 1969]. With ongoing deformation, fractures propagate through the rock succession and provide well-connected pathways [*Cooke and Underwood*, 2001], allowing fluids to flow.

The deposition process of these reservoir lithologies is rarely constant over the geological time scale, resulting in many lithological units with significant variation in mechanical properties within the rock succession [e.g., *Passey et al.*, 2010]. This heterogeneity affects nucleation and propagation of natural fractures [*Roche et al.*, 2013; *Anders et al.*, 2014]. Variations in stress state, due to the complex interplay of layer thickness and mechanical properties, makes it difficult to predict whether fractures propagate through multiple layers or are contained within one layer. In this chapter, fractures are defined as propagating fractures when crossing the layer boundary and are contained when they do not cross the layer boundary. These contained fractures can be compared to a *top-bounded* height distribution according to the classification presented by *Hooker et al.* [2013]. A consequence of fracture containment in individual layers is that the fractures are not effectively connecting the individual high-permeability layers in a bedded reservoir sequence, thereby limiting the reservoir potential significantly. In contrast, when fractures are not contained within one bed, fractures propagate through layer boundaries, which may result in loss of cap rock integrity and potentially create unwanted reservoir leakage pathways.

Due to the importance of fracture propagation and containment in layered reservoirs, this complex phenomenon is extensively studied by numerical modelling [*Simonson et al.*, 1978; *van Eekelen*, 1982; *Bai et al.*, 2000; *Schöpfer et al.*, 2006; *Guo et al.*, 2017; *Wang et al.*, 2018; *Yue et al.*, 2018], by laboratory tests [*Daneshy*, 1978; *Warpinski et al.*, 1981; *Teufel and Clark*, 1984; *Warpinski and Teufel*, 1987; *Schöpfer et al.*, 2011; *AlTammar et al.*, 2019] and in outcrops [*Helgeson and Aydin*, 1991; *Brenner and Gudmundsson*, 2002, 2004; *Ferrill and Morris*, 2008; *Hooker et al.*, 2013; *Cilona et al.*, 2016; *Laubach et al.*, 2018]. Previous studies have shown that the properties of the lithological unit, often referred to as mechanical stratigraphy, control the deformation style, fracture type, its frequency, intensity, and fracture height in a layered sedimentary system [e.g., *Teufel and Clark*, 1984; *Narr and Suppe*, 1991; *Gross*, 1995; *Rijken and Cooke*, 2001; *Lorenz et al.*, 2002; *Underwood et al.*, 2003]. The mechanical stratigraphy comprises the (1) mechanical properties (e.g., rigidity, brittleness, elastic moduli) of each lithological unit; (2) layer thickness; and (3) nature of the layer interface [e.g., *Ferrill and Morris*, 2003;

Laubach et al., 2009; *Ferrill et al.*, 2014; *McGinnis et al.*, 2017]. Mechanical properties, such as stiffness, are affected by variations in mineralogy, depositional texture, porosity, and the degree of cementation [*Engelder et al.*, 2009; *Ferrill et al.*, 2014]. Joints often initiate within stiff layers showing brittle deformation behaviour and arrest at the interface with softer layers that deform in a ductile manner, because these layers tend to blunt the fracture tip [e.g., *Gudmundsson*, 2002, 2003; *Yue et al.*, 2018]. Differences in stiffness (Young's modulus) on either side of the layer interface result in an *in situ* stress contrast between the layers and are dominating in fracture containment of fluid-driven fractures [*Warpinski et al.*, 1981; *Teufel and Clark*, 1984; *Jeffrey and Bunger*, 2009]. Layer thickness is a key parameter used in fracture models to predict fracture growth and fracture development [*Pollard*, 1987; *Bai et al.*, 2000; *Olson*, 2004]. The shear stress of the interface between different layers increases with applied normal stress (depth), friction coefficient, and interface cohesion [*Anderson*, 1981; *Teufel and Clark*, 1984]. Fluid-driven fractures tend to arrest at interfaces with relatively low shear strengths and interfacial slip can alter the growth of these fractures [*Gu et al.*, 2008]. When layers are strongly bonded, hydraulic fractures propagate through the layer interface, despite the differences in mechanical properties between the adjacent layers [*Daneshy*, 1978]. It is important to note that the mechanical stratigraphy observed nowadays may not represent the fracture stratigraphy *Laubach et al.* [e.g., 2009]; *Lavenu and Lamarche* [e.g., 2018]. For example, the mechanical properties of rocks change with diagenesis [*Dvorkin et al.*, 1994; *Rijken et al.*, 2002; *Shackleton et al.*, 2005; *Laubach et al.*, 2009], which can highly affect the fracture height [*Hooker et al.*, 2013]. Therefore, the present-day measurements of the rock mechanical properties may not be the properties under which fracturing occurs [*Laubach et al.*, 2009].

The majority of these studies on fracture containment reported the stratigraphic controls on tensile, (man-made) fluid-driven fractures/joints in brittle-ductile sequences. However, normal faulting (shear fractures) in layered brittle-brittle sequences is also recognized in the field [*Ferrill et al.*, 2014]. This study adapts the effect of mechanical stratigraphy on natural, stress-driven shear fractures, providing insight into processes governing fracture containment in layered sequences, where all layers deform in a brittle manner. The importance of rock strength between adjacent layers is highlighted, rather than the stiffness contrast, a parameter used in modelling studies [e.g., *Daneshy*, 1978; *Simonson et al.*, 1978; *Brenner and Gudmundsson*, 2004; *Yue et al.*, 2018]. The impact of strength differences between adjacent layers (i.e., mechanical contrast) on the fracture containment is quantified in the laboratory. Compression tests are performed in the laboratory on layered samples with a range of mechanical contrasts at different confining pressures to determine at which subsurface conditions (i.e., stress conditions) fractures are contained in one layer or propagate across layers. The fractures formed in this study are stress-driven shear fractures, referring to natural, normal faults formed in the subsurface, where in the field, σ_1 is the vertical and maximum principal stress. In addition, numerical, finite element modelling is compared to the laboratory results to determine the stress magnitude, distribution, and its orientation within a layered sequence. The results contribute to get insight into the fracture stratigraphy to predict containment of shear fractures in layered reservoirs, deforming in a brittle manner at shallow depths (first couple of kilometres) in the subsurface.

7.2 Materials and methodology

7.2.1 Sample material and preparation

Laboratory experiments were performed on cylindrical core plugs consisting of one lithology and on composite three-layered samples. The cylindrical core plugs consisting of one lithology have a 29 mm diameter and 60 mm length and were used to obtain the unconfined compressive strength (UCS) of the individual lithologies. A Length diameter ratio of 2:1 was used, since the UCS is often over-estimated when $L/D < 2$ [*Paterson and Wong*, 2005]. The individual components of the layered samples have a 29 mm diameter and 20 mm length. Their end phases were ground parallel to each other. The layered samples were created by stacking three individual components up to a sample length of $\sim$60 mm. The top and bottom of the composite sample have the same unconfined compressive strength (UCS), but the middle layer has a different UCS (Figure 7.1). The position of the strongest and weakest component varies under the different composite samples. This did not influence the fracture behaviour. The ratio in UCS between the strongest and weakest layer is defined as mechanical contrast (MC). The layer interfaces are polished with a 125 μm abrasive to create the same surface roughness. The samples were dried in the oven at 90°C for 24 hours prior to rock-mechanical testing in the laboratory.

The components were obtained from six different lithologies with varying strengths (Figure 7.1). The lithologies originate from different outcrops, are silica-rich, and show brittle deformation behaviour. The helium porosity and matrix density were measured in the laboratory. The majority of the lithologies are described in the literature [*Hettema et al.*, 1991; *Hettema and Pater*, 1998; *Klein et al.*, 2001]. Table 7.1 summarizes the rock description and petrophysical properties of the lithologies used in this study. A wide range of mechanical contrasts ($MC = 1.1 - 17.0$) was created by varying the composition of the three-layered sample (Figure 7.1). Mechanical contrasts in between 7.1 and 17 are absent, because there was no sample material available to create mechanical contrasts falling within this range. The three-layered sample where $MC = 17$ was created to mimic an extreme strength contrast, but note that the range of realistic mechanical contrasts in the subsurface is ≤ 5.

7.2.2 Experimental procedure

Unconfined compression tests were performed on oven-dried lithologies to obtain the UCS of the individual rock samples (cylindrical samples, length = 60mm; diameter = 30 mm). The value of peak stress was obtained from the stress-strain curve and represents the UCS of the sample. Confined compression tests (0 – 50 MPa) were performed on various dry, composite three-layered samples to investigate the control of the mechanical contrast on the fracture containment at different depths in the subsurface (reservoir conditions). Fractures are contained when they do not propagate through the layer interface between the weak and strong components. When one or more fractures propagate into the adjacent layer, they are not contained anymore. Cylindrical samples were placed in the pressure bench with a 500 kN load frame and deformed until failure to create stress-driven fractures. The experiment was stopped when a constant stress was achieved after failure. In the laboratory experiments, the vertical stress (σ_1) applied on the cylindrical samples represents the largest principal stress. The applied confining pressure is the horizontal stress, where $\sigma_2 = \sigma_3$. These horizontal stresses were applied using the triaxial Hoek cell [*Hoek and Franklin*, 1968]. The axial strain was recorded by linear variable differential transformers (LVDTs). Displacement rates of 0.006 mm.s^{-1} (equivalent strain rate of $\sim 10^{-4}$ s^{-1}) were used. The experiments were conducted under room temperature conditions (20°C) and low confining pressures (<50 MPa). At these conditions, the used lithologies were susceptible to brittle failure. No pore pressure was applied during the compression tests in the laboratory on the dry rock samples.

Three-layered sample	Sample A	Sample B	Sample C	Sample D	Sample E	Sample F	Sample G
Mechanical contrast (MC) *MC = Strong / Weak*	1.1	1.4	2.9	4.8	5.2	7.1	17.0
UCS layered sample *(MPa)*	176	24	39	39	44	51	17
L1	AI	FEL	BNT	AI	BNT	FEL	SLT
UCS (MPa)	205 ± 12	31 ± 4	43 ± 1	205 ± 12	43 ± 1	31 ± 4	13
L2	GRA	BNT	BER	BNT	GRA	GRA	GRA
UCS (MPa)	222 ± 20	43 ± 1	125 ± 15	43 ± 1	222 ± 20	222 ± 20	222 ± 20
L3	AI	FEL	BNT	AI	BNT	FEL	SLT
UCS (MPa)	205 ± 12	31 ± 4	43 ± 1	205 ± 12	43 ± 1	31 ± 4	13

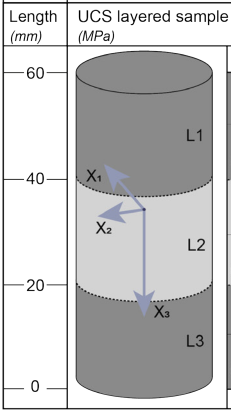

Figure 7.1: *Three-layered samples with different mechanical contrasts (MC) used for the laboratory experiments. The unconfined compressive strength (UCS) of (1) the individual layers (L1-L3) (obtained from core plugs of 60 mm length and 30 mm diameter) and (2) the layered samples (A-G) is displayed. Lithologies include AI – Ainsa Sandstone, BER – Beringen Sandstone, BNT – Bentheim Sandstone, FEL – Red Felser, SLT – siltstone, GRA – Benin Granite.*

7.2.3 Fracture analysis

The stress-driven fractures were visualized using the Nanotom X-ray micro computed tomography (micro-CT) scan (resolution 30 μm). This technique uses X-rays to create a three-dimensional dataset of a sample by stacking cross-sectional two-dimensional images [*Wellington and Vinegar*, 1987]. The created dataset was visualized using *Avizo Fire* software to characterize the fracture containment.

Table 7.1: *Petrophysical properties and description of the different lithologies used in this study. The He-porosity and matrix density were measured in the laboratory. AI – Ainsa Sandstone, BER – Beringen Sandstone, BNT – Bentheim Sandstone, FEL – Red Felser, SLT – siltstone, GRA – Benin Granite.*

Lithology	**He porosity (%)**	**Matrix density (kg/m^3)**	**Outcrop/ quarry**	**Rock description**
SLT	-	-	Spain	Poorly consolidated siltstone
FEL	21	2.656	Germany	Relatively homogeneous sandstone with a large variety of silicate minerals, including clays
BNT	25	2.664	Germany	Homogeneous, relatively quartz-rich sandstone
BER	9	2.690	Belgium	Laminated grey sandstone consisting of mainly quartz and feldspar grains
AI	17	2.704	Spain	Relatively quartz-rich, calcite cemented sandstone
GRA	0	2.641	Benin	Quartz-rich granite, with some microline, plagioclase, and biotite

7.2.4 Modelling stress distribution, magnitude, and orientation

The stress distribution, magnitude, and orientation within the three-layered samples were modelled in two dimensions using ABAQUS finite element software. The model setup consists of three homogeneous layers, where the individual layers have the same dimensions as the ones in the laboratory experiments, namely 29 mm length and 20 mm height. The model domain has a linear elastic rock matrix following Hooke's law for two-dimensional plane strain materials and has an isotropic Young's modulus E and Poisson's ratio ν. The values for these parameters were calculated from the stress-strain curve, obtained during deformation experiments on the individual components (large core plugs: 60 mm length; 30 mm diameter) in the laboratory (Table 7.2). The Young's modulus E_3 and Poisson's ratio ν_{31} were calculated from the stress-strain data between 40% and 60% of the peak stress. The subscript of E_3 indicates that the core plug was loaded in the vertical direction (x_3) and the ν_{31} refers to the elastic strain in the horizontal direction (x_1) as a response to the stress applied in the x_3-direction. In the presented models, E_3 and ν_{31} were varied to determine the stress distribution, magnitude, and orientation within the layered medium.

Friction along the interfaces of the different layers has not been taken into account in the model (i.e., all layers are coupled and no interfacial slip was allowed). Following the Coulomb friction law ($\tau_s = \mu\sigma_n$, see also *Cooke and Underwood* [2001]), decoupling of layers at their interfaces can only occur at low interfacial friction coefficients (μ <0.2), and/or under relatively low normal stresses, which is in this study the applied σ_1. Due to the relatively high friction coefficient, high normal stresses and the relatively low local tensile stresses present in the rock sample, it is not likely that decoupling of the layers will occur. Therefore, coupling the three individual layers without friction along the interfaces is interpreted to be a valid assumption at the imposed laboratory boundary conditions.

The applied model boundary conditions are based on the laboratory set up as described above. The bottom layer is fixed in all directions (i.e., x = 0, y = 0). The top layer is fixed in the horizontal direction (i.e., x = 0) and is free to move in the vertical direction. All other locations inside the rectangular sample are free to move in both horizontal and vertical directions in response to the applied stress field. In the model, the layers are coupled.

The vertical stress σ_1 was applied instantaneously and corresponds to the maximum rock strength (peak stress) of the three-layered rock sample obtained from the deformation experiments as presented in Figure 7.1. Horizontal stresses ($\sigma_2 = \sigma_3$) of 0, 10, 15, and 30 MPa were applied, and no pore pressure was assumed. The presented results follow the geological convention where compression is positive and tension is negative.

Table 7.2: *Static Young's Modulus, Poisson's ratio for the individual components of the layered sample. Lithologies include AI – Ainsa Sandstone, Ber – Beringen Sandstone, BNT – Bentheim Sandstone, FEL – Red Felser, SLT – siltstone, GRA – Benin Granite. The elastic properties were used as input parameters for the finite-element modelling to estimate the stress distribution within the layered samples.*

Lithology	**Young's modulus (E_3) (GPa)**				**Poisson's ratio (ν_{31}) (-)**
	σ_3= 0 MPa	**σ_3= 10 MPa**	**σ_3= 15 MPa**	**σ_3= 30 MPa**	**σ_3= 0 MPa**
SLT	2.74	-	-	-	0.053
FEL	7.2	12.6	13.8	15.2	0.13
BNT	9.1	-	-	-	0.21
BER	20.0	19.4	19.5	-	0.11
AI	29.5	23.1	-	24.3	0.15
GRA	30.8	-	-	-	0.18

7.3 Results

7.3.1 Rock-mechanical properties

Figure 7.2 reports the stress-strain relationships recorded under unconfined conditions during axial loading of (1) the three-layered samples with different mechanical contrasts and (2) the individual components. The results show that the three-layered sample always fails close to the ultimate strength of the weakest layer, irrespective of the mechanical contrast (Figure 7.2). The UCS values of the individual lithologies and the layered samples with different mechanical contrasts are reported in Figure 7.1. The UCS values of the individual lithologies, as well as the UCS of the layered ones were obtained from cylindrical samples with a length:diameter ratio of 2:1. Note that the UCS values of the individual components in the layered samples (length:diameter ratio < 1) are likely to differ from the UCS values of the individual lithologies (length:diameter ratio $= 2$). It is well-known that the brittle failure strength increases as the length:diameter ratio decreases [*Paterson and Wong*, 2005].

The elastic properties, including the static Young's Modulus E_3 and Poisson's ratio 31, were obtained from the axial stress – axial strain and the axial stress – radial strain curves between 40% and 60% of the peak stress for the individual lithologies and are reported in Table 7.2. The Poisson's ratio was calculated only at unconfined pressure conditions, since it was not possible to measure the circumferential strain with the experimental set up used to apply a confining pressure. The values of the elastic properties were used as input parameters for finite element modelling to estimate the stress distribution, magnitude, and direction within the layered samples.

7.3.2 Vertical fracture growth and containment

Layered samples deformed at unconfined pressure conditions with varying mechanical contrasts are shown in Figure 7.3. The results show that the UCS value of the layered sample is always close to the value of its weakest layer (Figure 7.2), suggesting that fractures initiate at the failure condition of the weakest layer, irrespective of the mechanical contrast and the position of the weak and strong component. Fractures propagate through the interface into stronger layers when the mechanical contrast is between 1.1 and 7.1 (Figure 7.3a, b, c). Fractures are only contained when the strength ratio between two layers is extremely high ($\sim$17, Figure 7.3d), for which there is only one example in this set of experiments.

The second set of experiments investigates the effect of increasing confining pressure (10 - 50 MPa) on fracture containment. Layered samples with the same mechanical contrast (MC $= 4.8$) deformed at different confining pressure conditions are shown in Figure 7.4. The fracture propagates from the weakest layer through the interface into the stronger layer at confining pressure conditions up to 15 MPa (Figure 7.4a, b, c). Fractures are contained when the confining pressure is 30 MPa

(Figure 7.4d).

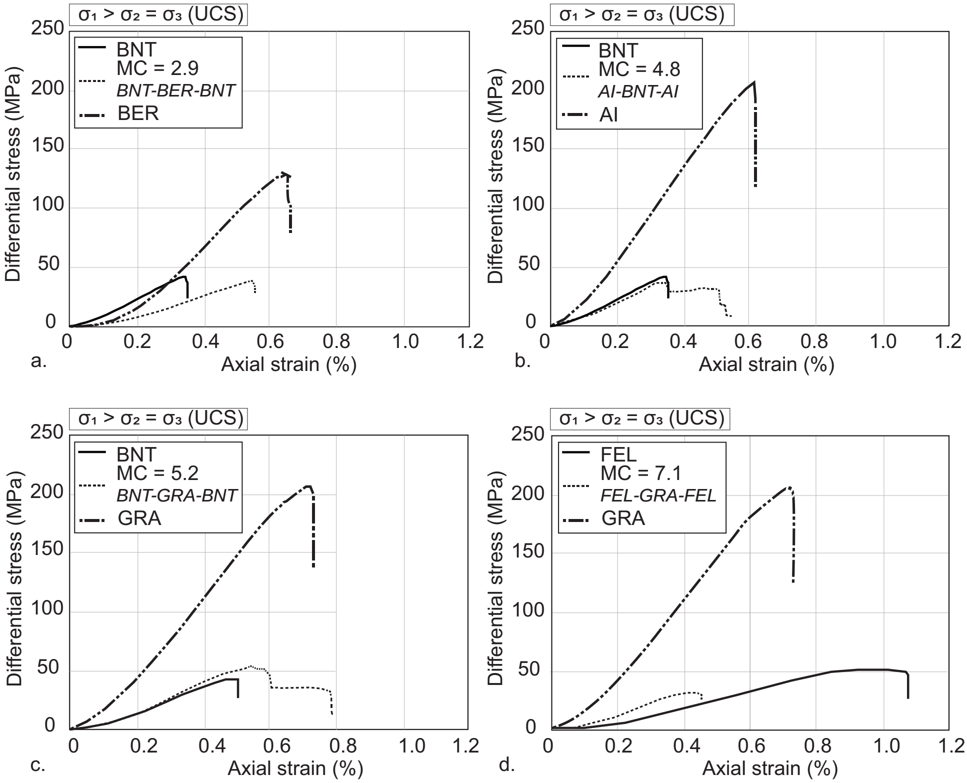

Figure 7.2: *Stress-strain relationship for the individual components and three-layered samples with a mechanical contrast (MC) of: a. 2.9, b. 4.8, c. 5.2, and d. 7.1 at unconfined conditions. The layered sample always fails close to the value of the unconfined compressive strength of the weakest layer, irrespective to the position of the weak and strong layer. The weaker layers are the outer layers in a, c, and d, whereas the weak layer represents the middle layer in the layered sample presented in b.*

Mechanical contrast and the applied confining pressure have a significant effect on fracture containment in layered rocks (Figure 7.5). Fractures always propagate from the weakest layer through the layer interface into stronger layers at low mechanical contrast, irrespective of the applied confining pressure. At high confining pressure conditions, the ability of fractures to cross the layer boundaries is controlled by the mechanical contrast.

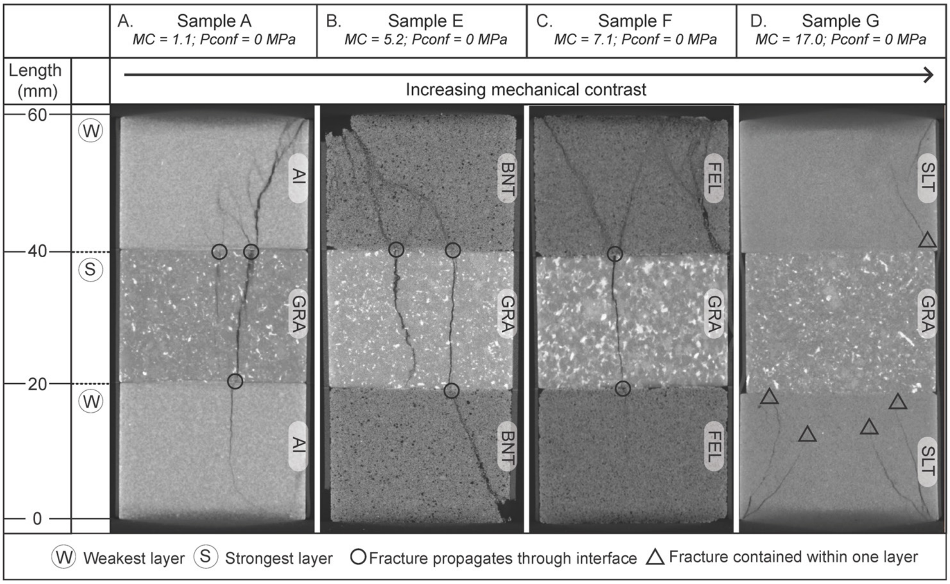

Figure 7.3: *Micro-CT scans after deformation at unconfined pressure conditions of the three-layered samples with mechanical contrasts (MC) of: a. 1.1, b. 5.2, c. 7.1, and d. 17.0. Fractures propagate through stronger layers when the mechanical contrast is ≤7.1. Fracture refraction between layers occurred when MC≥5.2. The loading direction is from the top.*

■ 7.3.3 Fracture dip

The fracture dip changes when crossing the interface at mechanical contrasts ≥2.9 (Figure 7.3b, c; Figure 7.4a). Fractures with an angle of ∼30° always form in the weakest layer, irrespective of the mechanical contrast and confining pressure applied to the sample. The fracture dip becomes steeper when propagating into the stronger layer. Conjugate sets of shear fractures form in the relatively weak sandstone layers when MC≥4.8. (Figure 7.3b, c; Figure 7.4a). Applying a confining pressure does not have a significant effect on the development of shear fractures and vertical fractures (Figure 7.3a, b, c). Similar observations were obtained in the field [e.g., *Ferrill and Morris*, 2003] and from the three-layered model by, for example, *Guo et al.* [2017].

■ 7.3.4 Stress distribution in layered media

The stress distribution, magnitude, and orientation were obtained through a 2D numerical modelling study. Figure 7.6 shows an example of the modelling results for the layered sample with a mechanical contrast of 5.2 under unconfined conditions, showing the (1) magnitude of the horizontal compressive and tensile stresses (Figure 7.6a), (2) the orientation and magnitude of the horizontal stresses (Figure 7.6b),

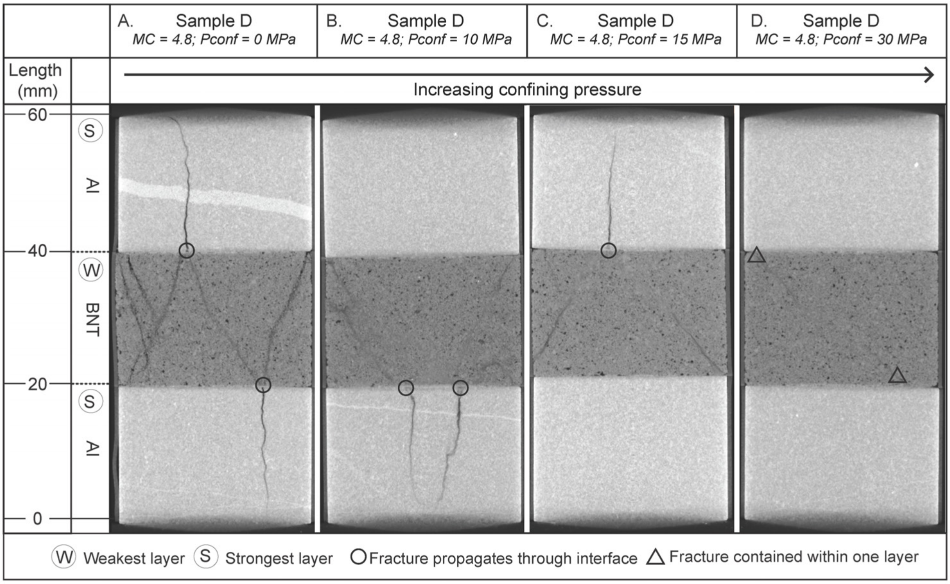

Figure 7.4: *Micro-CT scans after deformation of the three-layered samples with the same mechanical contrast (MC = 4.8) deformed at confining pressure conditions of: a. 0 MPa, b. 10 MPa, c. 15 MPa, and d. 30 MPa. Increasing the confining pressure eventually leads to fracture containment in layered rocks. The loading direction is from the top and the sides.*

and (3) the magnitude and direction of the horizontal strain (Figure 7.6c). The horizontal stresses are unequally distributed within the sample, with mainly horizontal oriented tensile stresses in the strong, middle layer (Figure 7.6a, b). Horizontal strains of approximately -0.5 are present in the relatively strong, middle layer (Figure 7.6c).

Figure 7.7 shows the tensile stress magnitude and distribution within the layered samples at unconfined conditions with increasing mechanical contrast obtained from the finite element modelling. The black area represents compressive stresses regions (σ_3 >0 MPa) within the layered sample. In the presented experiments, the orientation of the minimum compressive stresses is always horizontal (see for example Figure 7.6). Low tensile stresses (0 MPa – 4.5 MPa) and compressive stresses are present in the layered sample where MC = 1.1 (Figure 7.7a). At higher mechanical contrasts, the stresses in the weakest layer are mainly compressive, whereas tensile stresses are dominant in the strongest layer (Figure 7.7b, c, d). The magnitude of the tensile stresses in this layer decreases with increasing mechanical contrast. The maximum value reached in the strongest layer is ~14 MPa when MC = 5.2 (Figure 7.7b), ~9 MPa when MC = 7.1 (Figure 7.7c), and ~1 MPa is present when the MC = 17.0 (Figure 7.7d).

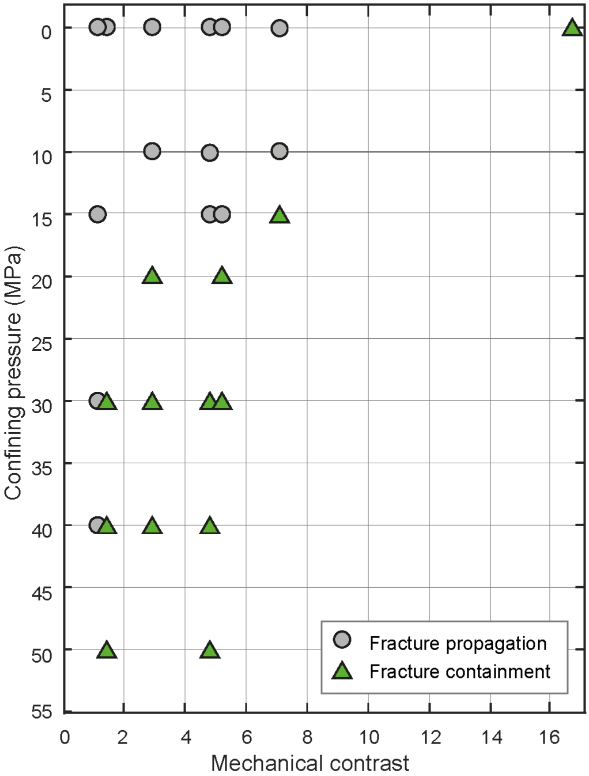

Figure 7.5: *Both the mechanical contrast and confining pressure impact the fracture containment in three-layered samples. The symbols (dot and triangle) represent the experimental data.*

The effect of confining pressure on the tensile stress magnitude and distribution is shown in Figure 7.8. Stresses are compressive (black area) in the weakest layers at confining pressures ranging from 0 MPa – 30 MPa when MC = 4.8 (Figure 7.8). The distribution and magnitude of the tensile stresses present in the strongest layer decreases from max. ∼11 MPa to max. ∼8 MPa when the confining pressure increases from 0 MPa to 15 MPa (Figure 7.8a, b, c). In addition, the total area comprising tensile stresses decreases with increasing confining pressure. No tensile stresses are present in the layered sample when the confining pressure is 30 MPa (Figure 7.8d).

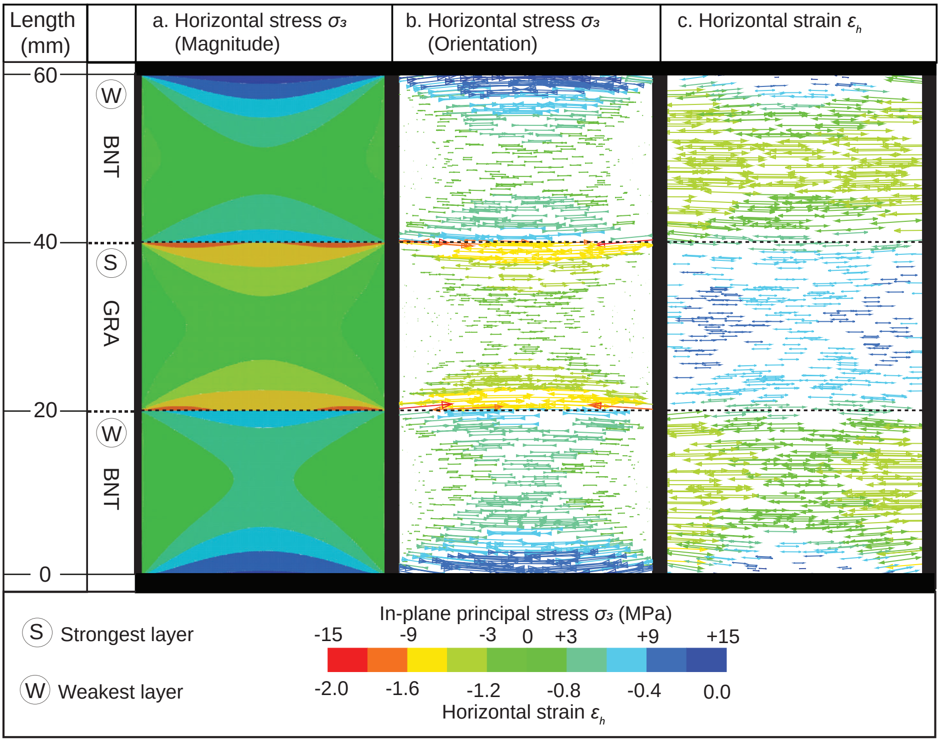

Figure 7.6: *An example of the finite-element modelling results of the layered sample with a mechanical contrast of 5.2 under unconfined conditions consisting of Bentheim Sandstone (BNT) and Benin Granite (GRA). The applied vertical stress* σ_1 *is equal to the ultimate strength of this sample, obtained through the deformation experiments in the laboratory. The magnitude of the horizontal stress distribution* σ_3 *(a), orientation (b) and horizontal strain (c) are unequally distributed throughout the rock specimen. Note that tensile stresses have negative values and compressive ones positive.*

7.4 Discussion

7.4.1 Fracture initiation in brittle, layered sequences

The stress-strain relationship shows that fractures initiate when the differential stress exceeds the ultimate strength of the weakest layer (Figure 7.2). This suggests that fractures form in the weakest layer. However, it is not easy to determine the relative timing and localization of fractures, since only the final stages could be visualized during the presented experiments. It is most likely that fractures initiate at the point of an interface, for example, the piston-rock interface or a lithological boundary [*Bai et al.*, 2000]. Therefore, in the experimental setup presented in this study, fracture initiation at the top or bottom of the cylindrical sample is most

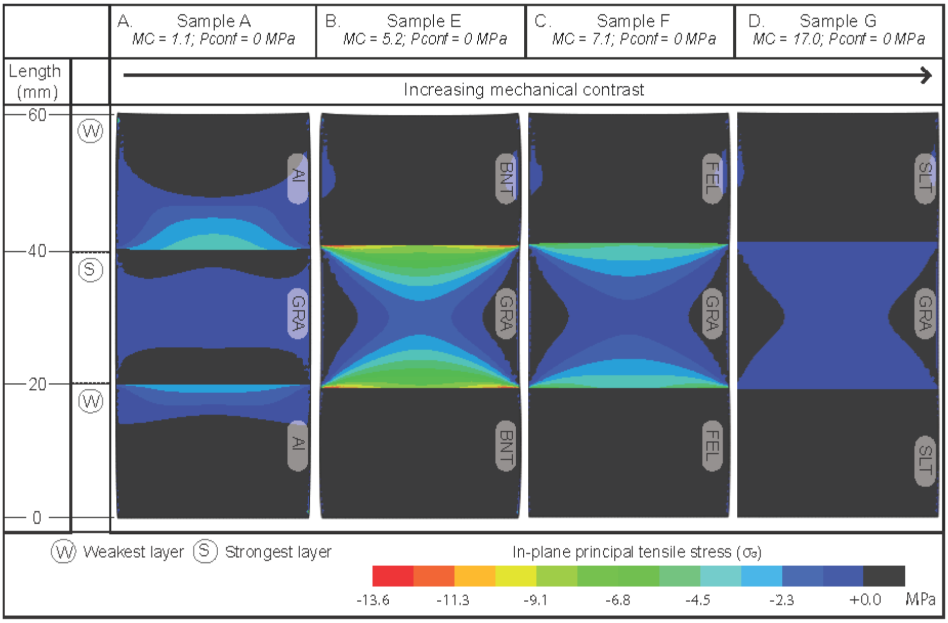

Figure 7.7: *Horizontal tensile stress distribution (negative value) and magnitude in layered samples with mechanical contrasts (MC) of: a. 1.1, b. 5.2, c. 7.1, and d. 17.0 at the peak strength of the specimen. The magnitude of the horizontal tensile stresses is sufficient to generate tensile fractures when the mechanical contrast is between 5.2 and 7.1.*

likely to occur, since the elastic stress distribution is not homogeneous throughout the cylindrical sample during UCS and triaxial compression tests [*Paterson and Wong*, 2005]. The areas at the platen/piston interface are most severely stressed.

Field investigations on alternating brittle and ductile layers show that faults nucleate in layers that are susceptible to brittle failure [*Eisenstadt and Paor*, 1987; *Gudmundsson*, 2002, 2003; *Ferrill and Morris*, 2003; *Ferrill et al.*, 2012, 2016]. This is consistent with experimental studies [e.g., *Donath*, 1970] showing that, as strain accumulates in a mechanically layered sedimentary section, brittle layers will fault first, whereas ductile layers accommodate greater strains before failure [*Donath*, 1970; *Ferrill and Morris*, 2008; *Welch et al.*, 2009; *Ferrill et al.*, 2012]. Field studies on alternating brittle layers with different competences of, for example, *Ferrill and Morris* [2003]; *Ferrill et al.* [2014] do not have geometrical features that might indicate whether the fracture initiated in the weak or strong layer.

In this study, all the lithologies deform in a macroscopically brittle manner. The stress-strain curves show a (1) linear-elastic initial deformation, followed by non-linear deformation, and (2) a well-defined peak strength, followed by a sudden

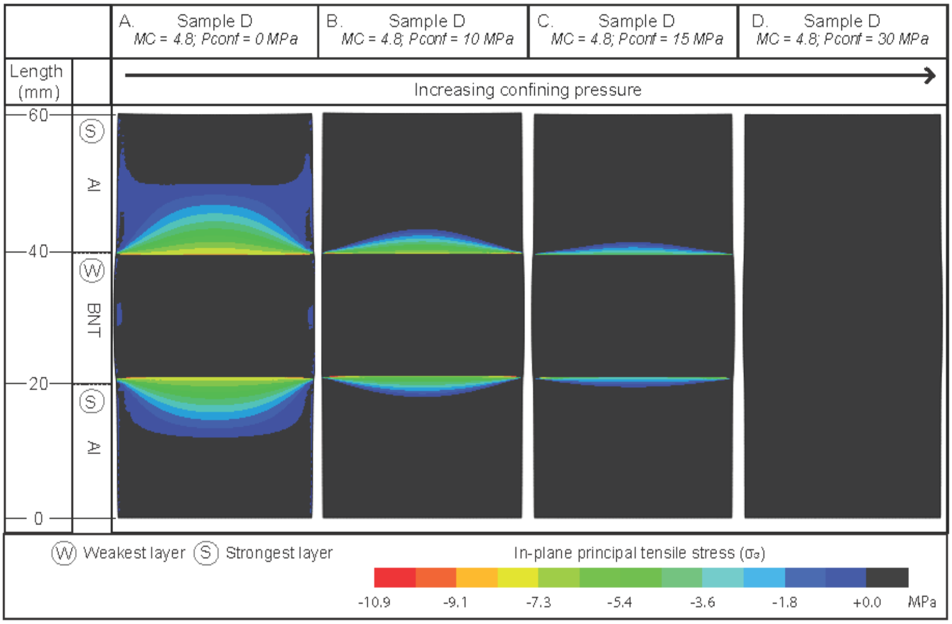

Figure 7.8: *Horizontal tensile stress (negative) distribution and magnitude at the peak strength of layered samples with the same mechanical contrast (MC = 4.8) at confining pressure conditions of: a. 0 MPa, b. 10 MPa, c. 15 MPa, and d. 30 MPa. The tensile stress distribution and magnitude decreases with increasing confining pressure.*

reduction in shear strength, typical for brittle deformation [*Byerlee*, 1968]. The total amount of axial strain experienced by the individual lithologies, as well as by the layered samples, is only $\leq 1\%$, where the amount of strain experienced by layers deforming at the same pressure and temperature conditions in a ductile fashion is much higher [*Donath*, 1970]. In addition, the deformed, individual core plugs showed in all cases macroscopic shear fractures, indicating strain localization into a deformation band, representing macroscopic brittle deformation behaviour [*Rutter*, 1986]. Moreover, the amount of stress, rather than the amount of strain accommodated by the layer, is the controlling factor for brittle deformation to occur. Shear fractures are formed when the stresses exceed the local ultimate strength of a rock [*Handin*, 1969]. In addition, the fracture orientation and modeling results suggest that the strong layers failed in tension, which must have happen after shear failure in the weakest layer. Otherwise, the rock strength in the strong layer would not be exceeded. Fore these reasons, it is most likely that fractures nucleate in the weakest lithology when all the layers are susceptible to brittle failure.

7.4.2 The effect of mechanical contrast on fracture containment

Fracture containment at low confining pressure

Numerical modelling, outcrop studies, and laboratory experiments [among others, *van Eekelen*, 1982; *Teufel and Clark*, 1984; *Warpinski and Teufel*, 1987; *Narr and Suppe*, 1991; *Rijken and Cooke*, 2001; *Ferrill et al.*, 2014; *Yue et al.*, 2018] show that properties of lithological units, such as mechanical properties (e.g., Young's modulus), thickness, and nature of the layer interface, control the deformation style, fracture type, frequency, intensity, and fracture height in layered sedimentary systems. This study focusses on the effect of mechanical properties, highlighting the stress contrast between adjacent layers. In numerical modelling and outcrop studies, the stiffness (Young's modulus) contrast is used as parameter to examine fracture containment in layered sequences [*Simonson et al.*, 1978; *Yue et al.*, 2018], since the actual rock strength is difficult to evaluate in the field or to obtain from well logs [*Ferrill and Morris*, 2008]. The results presented here will not change significantly when taking the stiffness contrast between adjacent layers instead (see Table 7.2 for the rock stiffness values).

In the laboratory, σ_1 is the maximum principal stress, applied normal to the bedding. σ_2 and σ_3 are the minimum, horizontal principal stresses ($\sigma_2 = \sigma_3$). This can be compared to the stress conditions in the field under which normal faults can develop, where σ_1 is vertical and the maximum principal stress. The results obtained from the unconfined compressive tests show that the mechanical contrast of a layered rock does not always act as a containment barrier. Failure occurs at the compressive strength of the weakest layer. It is not likely that a stronger layer fails at the same differential stress (σ_{diff}=σ_1–σ_3) as the weakest layer.

Paterson and Wong [2005] shows that the stress distribution is not equally distributed within a cylindrical sample during a UCS tests (Figure 12c in *Paterson and Wong* [2005]), due to (1) boundary effects at the contact with the platens, where frictional constraint being one of the most important factors, and (2) the length:diameter ratio, where the brittle fracture stress decreases as the length:diameter ratio increases [*Paterson and Wong*, 2005]. An acceptable l:d for rock-mechanical testing is $\geq$2. This is consistent with the modeling results, showing that the magnitude and orientation of the maximum vertical stress (σ_1) and the horizontal stress (σ_3) is discontinuous within the layered sample (Figures 7.7). Additionally, tensile stresses are present in the strongest layer at unconfined conditions even though the sample is in overall compression. The inhomogeneous stress field affects the *in situ* differential stress in the adjacent strong layers [*Peacock and Sanderson*, 1992; *Ferrill and Morris*, 2003; *Kettermann and Urai*, 2015].

The inhomogeneous *in situ* stress distribution within the weak and strong layers is also shown by the change in fracture orientation between two adjacent layers with a relatively large mechanical contrast. Fault refraction is namely due to different types of failure (extension vs. shear) of layers [*Schöpfer et al.*, 2006]. Studies on fluid-driven fractures suggest that the *in situ* stress contrast between layers is the most important factor controlling fracture containment [*Nolte and Smith*, 1979; *Warpinski et al.*, 1981, 1982; *Teufel and Clark*, 1984; *Jeffrey and Bunger*, 2009].

Heterogeneous *in situ* stress distribution in cylindrical core plugs, hence the variation in fracture dip, is controlled by the boundary effects and length:diameter ratio and can be enhanced by, among others, contrasting rock mechanical properties (e.g., Strength, Young's modulus, Poisson's ratio) of adjacent layers [e.g., *Peacock and Sanderson*, 1992; *Ferrill and Morris*, 2003; *van Gent et al.*, 2010; *Kettermann and Urai*, 2015]. During deformation, the weak layer elongates more than the strong layer, causing an additional extensional force in the strongest layer [*Bourne*, 2003] (Figure 7.7). At unconfined conditions, σ_3 is zero. The addition of an extensional force in the strongest layer decreases the horizontal stress ($\sigma_3 <0$) (Figure 7.7), resulting in an increase in differential stress. This allows the strongest layer to fail in hybrid or tensile mode, combining features from both tensile and shear failure (see for example Figure 4 in *Ferrill and Morris* [2003]). The weakest layers, however, fail in shear mode (Figures 7.3; 7.7). The granite layers, for example, have failed close to pure tension since the fracture orientation in almost vertical. Once the weak layers has failed in shear, the stress field in the strong layer is strongly extensional and thus, the granite has to overcome its tensile strength, which is 10-13 times lower than the UCS (see *Boersma et al.* [2020] for the tensile strength values of the used lithologies). The change in fracture orientation is therefore attributed to the different modes of fracturing within the different lithologies with contrasting strength at low confining pressures [*Gross*, 1995; *Childs et al.*, 1996; *Ferrill and Morris*, 2003; *Schöpfer et al.*, 2007; *Guo et al.*, 2017].

The fracture geometries observed in the deformed, layered core plugs are similar to the ones observed in the field and to the geometries created in other experimental studies where adjacent layers have a significant stiffness contrast [among others, *Peacock and Sanderson*, 1992, 1994; *Ferrill and Morris*, 2003; *Brenner and Gudmundsson*, 2004; *Ferrill et al.*, 2014]. For example, *Ferrill et al.* [2014] showed that fractures were formed in (1) shear mode in weaker, calcareous mudstone layers and in (2) hybrid mode in stronger, chalk layers. Fracture refraction is less significant at relatively low stiffness contrasts, as observed in the field by, for example, *Larsen and Gudmundsson* [2010].

Fracture containment at higher confining pressures

The inhomogeneous *in situ* stress distribution is the controlling factor on fracture containment in layered sequences [*Nolte and Smith*, 1979; *Warpinski et al.*, 1981, 1982]. Note that, in the brittle field, the boundary effects and length:diameter ratio is less significant during triaxial testing (i.e., confining pressure) compared to the UCS tests. The addition of confining pressure leads to a more nearly uniform stress distribution in cylindrical core samples, where a length:diameter ratio of 2 appears to be satisfactory [*Paterson and Wong*, 2005]. The presence of a mechanical contrast results in an additional extensional force experienced by the strongest layer. The magnitude of the tensional stress can be large enough to allow fracture propagation in layered samples with contrasting strength at low confining pressures [*Ferrill and Morris*, 2003; *Ferrill et al.*, 2014; *Kettermann and Urai*, 2015]. An increase in confining pressure will change the *in situ* stress distribution within the sample (Figure 7.8) and therefore affect fracture containment within one layer and propagation through layer boundaries (Figure 7.4). At confining pressure conditions where $\sigma_3 \geq 10$ MPa, the ability of fractures to cross the layer boundaries is inhibited, even at high mechanical contrasts (Figure 7.5). An increase in confining pressure (σ_3) prevents fractures from propagating through stronger layers, because the decrease in principal stress (σ_3) caused by the elongation of the weakest layer is not large enough to (1) create tensile stresses which are able to overcome the tensile strength of the strongest layer, or (2) create any tensile stresses, meaning that the strongest layer only experiences compressional stresses (σ_3 remains >0) (Figure 7.8). In the latter case, the differential stress is not large enough to overcome the shear strength of the strongest layer, resulting in fracture containment in the weakest, brittle layer. This is in agreement with *Kettermann and Urai* [2015], showing that tensile and hybrid fractures are formed at shallow depth (small overburden pressures) whereas only shear fractures are formed at higher pressures, as well as with *Schöpfer et al.* [2007], suggesting that fault refraction in multi-layered media is dependent on both strength contrast of the adjacent layers and confining pressure. The numerical modelling study of *Simonson et al.* [1978] on hydraulic fracture height growth supports the idea that stiffer layers (in this study the strongest ones) can act as a containment barrier, depending on the *in situ* stresses. The authors suggest that the stress intensity factor at the end of the crack tip approaches zero as the tip gets closer to the interface, and therefore the stiffer layer prevents fractures from penetration.

Predicting fracture containment in the subsurface

Outcrop studies generally provide the fracture geometry at the present-day mechanical stratigraphy [*Brenner and Gudmundsson*, 2004; *Larsen and Gudmundsson*, 2010; *Ferrill et al.*, 2014], which does not represent the fracture stratigraphy [*Laubach et al.*, 2009; *Lavenu and Lamarche*, 2018]. Mechanical properties measured in the field are expected to have been modified by, for example, diagenesis, unloading, erosion, and weathering of the outcrop [*Laubach et al.*, 2009; *McGinnis et al.*, 2017]. In addition, similar fracture network geometries can form under different stress conditions. For these reasons, it is difficult to predict the underlying mechanisms for fracture containment within a layered sequence based on outcrop studies alone.

The experimental laboratory results present in this chapter can help to predict at which stress conditions and mechanical contrasts fractures are contained within a layer in the subsurface. Note that this study only focusses on the containment of natural fractures in brittle sequences at shallow depth (first few kilometres) in the subsurface, where σ_1 is the vertical and maximum principal stress. The control of mechanical contrast and confining pressure on fracture containment can be implemented by correlating confining pressure to burial depth to predict fracture containment in layered rocks in the subsurface (Figure 7.9). At a normal faulting stress regime, where σ_1 represents the maximum, vertical principal stress, fracture propagation into an adjacent stronger layer is favourable at relatively shallow levels in the upper crust, where brittle deformation behaviour is favourable, whereas fracture containment is favourable at deeper levels. The range of realistic mechanical contrasts (MC$\leq$5) indicates that fracture propagation is only expected to occur in the first couple of kilometres in the upper crust.

Existing correlations between confining pressure and depth remain ambiguous. Confining pressure can only be related to burial depth when assuming a highly idealized state of stress in the crust [*Handin et al.*, 1963]. Three different models [*Anderson*, 1951; *Zoback*, 2007; *Fossen*, 2010] describing the changes in stress state through the crust are used to relate the confining pressure (σ_3) to burial depth, assuming rock density of 2.7 $g.cm^{-3}$. The different methods used to predict the stress state in the subsurface show different depth values (Figure 7.9), because each method is based on different assumptions. Therefore, the method used to quantify the depth influences the predictions on fracture containment in layered rocks in the subsurface.

The gradient used to estimate the stress increase with depth is a topic of debate, which will not be resolved [*Simonson et al.*, 1978], except by direct measurements [*Haimson and Fairhurst*, 1967]. The magnitudes of the horizontal stresses can be measured directly from borehole data [e.g., *Vernik and Zoback*, 1992]. These measurements are more accurate than the depth values estimated by the different models. Therefore, the usage of direct measurements of confining pressure is preferred over depth models to predict fracture containment in the subsurface.

The relationship between fracture containment in layered rocks, mechanical contrast, and confining pressure can also be used to constrain the mechanical contrast of individual layers in the field/outcrops when stress conditions are known. Furthermore, the fracture containment relationship can be added to fluid-flow models of fractured and layered media. When the mechanical properties of the individual layers are known, accurate predictions of fracture extent, style, and orientation can be added with other parameters, such as fracture aperture, fracture density, local stress field around larger faults, or layer thickness, which are needed to build a constrained discrete fracture network model [e.g., *Josnin et al.*, 2002; *Maerten et al.*, 2006, 2016; *Anders et al.*, 2014; *Guo et al.*, 2017].

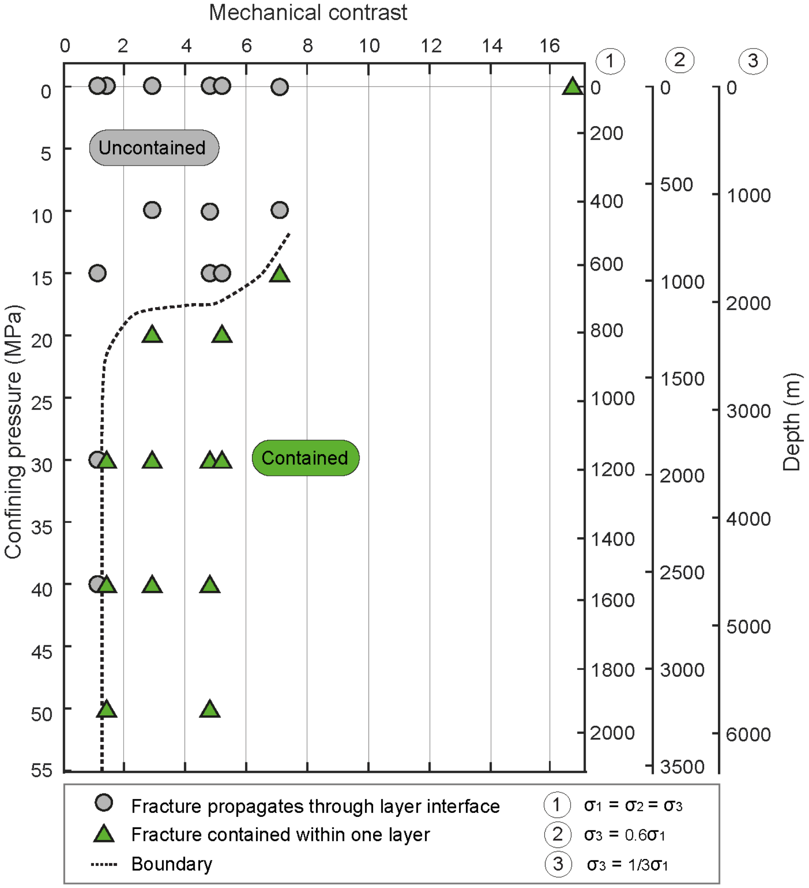

Figure 7.9: *Fractures propagate through the layer boundary at relatively shallow levels in the upper crust, whereas fracture containment is favourable at deeper levels. Three different models [Anderson, 1951; Zoback, 2007; Fossen, 2010] are used to relate the confining pressure and burial depth.*

7.5 Conclusions

This study investigates the impact of mechanical contrast on the fracture containment in layered rocks, deforming in a brittle fashion. Compression tests are performed on three-layered samples with varying mechanical contrast at different confining pressure conditions. The results show that stress-driven fractures always initiate at the failure point of the weakest layer and either propagate through the layer interface, or are contained within the weakest layer. The mechanical contrast within a layered rock does not always act as a containment barrier, due to low effective horizontal stresses, and differences in differential stress between the weak layer and strong layer. The combination of mechanical contrast and confining pressure does control the fracture containment in layered rocks. Applying a confining pressure increases the effective horizontal stress, resulting in fracture containment. This study contributes insights into the fracture stratigraphy to predict containment of shear fractures in layered reservoirs, deforming in a brittle manner at shallow depths (first couple of kilometres) in the subsurface. Mechanical contrast combined with the *in situ* stress conditions need to be considered when predicting natural, fluid flow paths, which is necessary for the successful development of low-permeability layered reservoirs.

8

Discussion and Conclusion

The aim of this study has been to investigate the elastic anisotropy and deformation behaviour of mudstones, and their evolution due to changes in water saturation. The main focus of this thesis is on hydrocarbon exploration and production in the Netherlands. Geomechanical experiments and ultrasonic velocity measurements were performed in the laboratory on the Whitby Mudstone. This clay-rich rock is used as an analogue for the Dutch Posidonia Shale, the main shale-gas prospect in the Netherlands. The findings of this study give insight into the elastic anisotropy and deformation behaviour of the Whitby Mudstone and highlight the importance of preserving clay-rich rocks and testing them adequately in the laboratory. The main findings of this thesis are briefly summarized, after which the relevance and limitations of the study are discussed, followed by an outlook of future work.

8.1 Synopsis

There is a significant variability in mineralogical and petrophysical properties between shales deposited in different basins, as well as within the same basin. This leads to a wide variation in elastic anisotropy and mechanical behaviour of shales at various scales (chapters 2, 3). *Shales* can be divided into *gas shales* and *mudstones*, where mudstones have a higher clay content than gas shales (chapter 2).

The Whitby Mudstone is a clay-rich mudstone (chapter 3). Its mineralogical composition in combination with the presence of lamination result in a high intrinsic (elastic) anisotropy (chapter 4). This clay-rich rock behaves macroscopically brittle, creating contractive shear fractures, and has a low friction coefficient when fully saturated (chapter 5). The elastic anisotropy and mechanical properties are highly affected by the degree of water saturation (chapters 4 and 5). A decrease in water saturation increases the elastic anisotropy even further, due to density differences in the pore space, formation of bedding-parallel fractures and stiffening of the rock frame (chapter 4). This latter property leads to a mechanically stiffer and stronger mudstone when dehydrated (chapter 5). In addition, the nature of brittle deformation (dilative/contractive) is affected by the saturation state. Due to the significant impact of water saturation on the elastic anisotropy and mechanical behaviour, the degree of saturation should always be reported when performing laboratory measurements on shales.

In the subsurface, the temperature and pressure increases with depth, which affect the elastic properties and deformation behaviour of rocks (chapters 5, 6 and 7). The Whitby Mudstone has a lower elastic anisotropy and becomes mechanically stiffer and stronger at higher pressures (chapters 5 and 6). Shear fractures formed at depth (normal faulting regime) are not likely to enhance the permeability of the saturated Whitby Mudstone due to their contractive character (chapter 5). Whether shear fractures remain in one lithological unit depends on the depth and the contrast in rock strength between adjacent layers (chapter 7). High temperatures result in a stronger rock and enhances the elastic anisotropy if the mudstone is partially-saturated (chapter 6). These saturation conditions might not represent actual reservoir conditions and are likely to deviate when mudstones are fully-saturated.

8.2 Perspective and limitations

The work presented here was conceived to evaluate the elastic anisotropy and mechanical behaviour of the Whitby Mudstone and their evolution due to changes in water saturation, with the main focus on hydrocarbon exploration and production in the Netherlands.

The findings presented in this thesis ensure that the elastic anisotropy and mechanical behaviour of the Whitby Mudstone are better understood at various temperature and pressure conditions. In addition to this, the understanding in the mechanisms responsible for the (changes in) elastic anisotropy and mechanical behaviour of clay-rich rocks at various saturation states is improved. Predictions on the nature of deformation, and whether fractures in clay-rich rocks are likely to be dilative or contractive can be made when the degree of water saturation and stress conditions are known.

Dilative fractures enhance the permeability, and form fluid-flow pathways when effectively connected. The presence of fluid flow paths increases the productivity in otherwise low-permeability mudstone reservoirs, but may form potential leaking pathways for CO_2 and radioactive waste when stored in the subsurface. The likelihood of such fluid-flow pathways to form at shallow depth in brittle, layered sequences is also predicted in this thesis.

Focussing on hydrocarbon exploration and production in the Netherlands, the elastic anisotropy and mechanical behaviour of the Whitby Mudstone were evaluated. The high anisotropy of the Whitby Mudstone needs to be considered for geophysical interpretation for hydrocarbon exploration and production. The values of the elastic anisotropy presented in this thesis were obtained from ultrasonic velocities measured in the laboratory at ultrasonic frequencies (MHz). In the field, however, velocities are often measured at seismic or sonic frequencies (seismic surveys: 1 - 100 Hz; sonic log measurements in wellbore: kHz range) [*Lozovyi et al.*, 2018]. The velocity is a function of material properties (e.g., matrix, pore fluid), external variables (e.g., pressure, temperature), and frequency. This latter property is referred to as dispersion and has been reported for shales [e.g., *Duranti et al.*, 2005; *Szewczyk et al.*, 2018a]. The elastic properties of shales are therefore not only anisotropic, but also frequency dependent [*Duranti et al.*, 2005; *Szewczyk et al.*, 2017, 2018b], meaning that the values measured in the laboratory are likely to be different from the ones measured in the wellbore or field. This needs to be taken into account when using the anisotropy values as input for geophysical models.

In terms of mechanical behaviour, proven shale plays tend to be brittle, with a Young's modulus higher than 24 GPa, and are mostly made of silica and carbonate material, having a few clay constituents (<40%) [*Britt and Schoeffler*, 2009]. The Whitby Mudstone has a significant lower Young's modulus, but behaves macroscopically brittle, forming localized shear fractures in a normal faulting regime. At shallow depth (first couple of kilometres) in the subsurface, the fractures formed in the partially-saturated Whitby Mudstone are dilative and increase the permeability of the rock, which is favourable for hydrocarbon recovery. However, when the Whitby Mudstone is saturated with brine, shear fractures are contractive at depths geq1 km (15 MPa confining pressure), so that the reservoir permeability is not enhanced by the formation of these fractures. When brine saturated, it is likely that the Whitby Mudstone becomes weaker and more ductile as the temperature increases, which is observed by other studies on clay-rich rocks [e.g., *Horsrud et al.*, 1994, 1998; *Petley*, 1999]. This will make the Whitby Mudstone a potential natural seal in terms of geomechanical properties, but less favourable for hydrocarbon production.

The elastic and mechanical properties of the Whitby Mudstone vary on an outcrop scale. Therefore, care should be taken when extrapolating these properties to the Dutch Posidonia Shale. It should also be noted that the rock samples used in this thesis originate from an outcropping wave-cut platform, and therefore do not represent the rock material at actual subsurface conditions. Pore fluids are altered and the water saturation state have changed over geological time and tectonic uplift might have damaged the core samples.

To understand the elastic anisotropy and mechanical behaviour of the mudstones in the subsurface, it is crucial to know their saturation state at *in situ* conditions. It is likely that mudstones are saturated (80% - 95% S_w; *Moritz* [1995]) with formation brine when acting as a (top) seal in the subsurface. For a shale gas reservoir, however, the pores are filled with both formation brine, as well as gas, indicating that these shales are in partial saturation *in situ* [*Ewy*, 2015]. The generation of gas has driven the water saturation of these shales down [*Ewy*, 2015]. The effect of natural gas-filled pores, instead of air-filled pores, on the mechanical and elastic properties of the Whitby Mudstone should be considered to characterize its reservoir properties, to further improve hydrocarbon exploration and production in the Netherlands.

8.3 Outlook and recommendations

Future work may focus towards performing geomechanical and geophysical experiments on mudstones having different pore fluids, tested at subsurface conditions (elevated pressure and temperature). This is not only important for hydrocarbon exploration and production, but also for CO_2 sequestration projects and nuclear waste disposal.

In addition to the results presented in this thesis, it is recommended to perform geomechanical and ultrasonic experiments at elevated temperature and pressure on saturated Whitby Mudstone/Posidonia Shale samples for further characterization at subsurface conditions. The Posidonia Shale is of interest as an overburden, natural seal, and hydrocarbon reservoir in the Dutch subsurface. However, it is not likely that shale-gas production gets off the ground in the Netherlands, since the Dutch government will not give out any permits for shale gas exploration.

Although, there will not be any commercial exploration or extraction of shale gas in the Netherlands in the coming years, shale gas exploration and production is still ongoing in other countries (e.g., USA, China, Canada, UK). Shale gas reservoirs are partially saturated in the subsurface. The results in this thesis show that the presence of air in the pores has a significant effect on the mechanical and elastic properties of mudstones. However, the pores of shale gas reservoirs are filled with formation brine and natural gas. Therefore, it is recommended to investigate the effect of natural gas on the mechanical and elastic properties of partially-saturated shales at reservoir conditions in the laboratory.

When testing partially-saturated shales in the laboratory, the assumption is made that the pore pressure is zero, which is not the case. Unstressed, partially-saturated shales (both mudstones and gas shales) have a negative pore pressure (suction). If not accounted for this negative pore pressure, mechanical properties such as rock strength, might be overestimated in the laboratory. A well-established correlation for clay-rich rocks between the amount of negative pore pressure and effective stress should be developed in the future.

Since the world is striving towards a lower carbon future, the interest in other energy resources than oil and gas (e.g., nuclear energy) and sequestration projects increases. Clay-rich rocks are potential host rocks for nuclear waste disposal. The results of this thesis could be used to predict the effect of dehydration due to ventilation in deep geological repositories, but additional research on the effect of temperature on the mechanical properties of clay-rich rocks is also useful for this application, since high-level radioactive waste generates heat. For CO_2 sequestration projects, mudstones can act as a natural seal. The effect of CO_2 on the mechanical properties of mudstones should be investigated to assess the seal integrity when CO_2 is injected in a reservoir.

Finally, it is recommended to link the microscale properties (plug scale) obtained in this thesis to the macroscale (reservoir scale), by using (or developing) geomechanical and rock-physical models for upscaling purposes. Upscaling is challenging, due to the multiscale heterogeneities in shales. But without upscaling, the lab-derived properties could not be used to provide input for modelling at the reservoir scale.

A

Estimating water saturation

A total of four mudstone disks with a ∼38 mm diameter and ∼12 mm length from the same Whitby Mudstone block were used to estimate the (1) initial water saturation, and (2) water saturation at different relative humidity. The estimated water saturations obtained from these mudstone blocks are assumed to be representative for the core plugs used in this study.

A.1 Porosity calculation

The minimum porosity (ϕ) of one Whitby Mudstone disk was calculated using the dry bulk density (ρ_{bulk}) and the grain density (ρ_{grain}), following:

$$\phi = 1 - \frac{\rho_{bulk}}{\rho_{grain}}. \tag{A.1.1}$$

Material originating from the same mudstone block was pulverized, vacuum dried for 24 hours at 105°C, and analyzed with a pycnometer to measure ρ_{grain}. The average grain density based on ten different runs was used for the calculations. ρ_{bulk} was calculated using the bulk volume ($V_{bulk} =^2 L$) and the dry mass (m_{dry}) of the mudstone disk, measured after drying under vacuum in the oven at 105°C until the mass stabilized, using:

$$\rho_{bulk} = \frac{m_{dry}}{V_{bulk}}. \tag{A.1.2}$$

Note that the assumption is made that the porosity obtained from the vacuum-dried disk represents the porosity used for all further calculations.

A.2 Water saturation

The initial water saturation ($S_{winitial}$) was obtained from the vacuum dried mudstone disk, using:

$$S_{winitial} = \frac{V_{brine}}{V_{pore}}. \tag{A.2.1}$$

Knowing ϕ and V_{bulk}, the total pore volume (V_{pore}) can be estimated. The volume of the brine (V_{brine}) can easily be obtained from the amount of water loss during drying ($m_{wet} - m_{dry}$) and the pore fluid density (ρ_{fluid}).

Three disks were placed in three different desiccators with relative humidity atmospheres of ~85%, ~75%, and ~35%. The corresponding water saturations (S_w) of these disks were estimated by:

$$S_w = S_{winitial} - \frac{V_{brineRH}}{V_{poreRH}}, \tag{A.2.2}$$

where V_{poreRH} and $V_{brineRH}$ correspond to the pore- and brine volume, respectively, obtained from the disk that was exposed to a particular relative humidity atmosphere.

Bibliography

AlTammar, M. J., S. Agrawal, and M. M. Sharma (2019), Effect of Geological Layer Properties on Hydraulic-Fracture Initiation and Propagation: An Experimental Study, *SPE Journal*, *24*(02), 757–794, doi:10.2118/184871-pa.

Ambrose, W. A., S. Lakshminarasimhan, M. H. Holtz, V. Nunez-Lopez, S. D. Hovorka, and I. Duncan (2008), Geologic factors controlling CO2 storage capacity and permanence: Case studies based on experience with heterogeneity in oil and gas reservoirs applied to CO2 storage, *Environmental Geology*, *54*(8), 1619–1633, doi:10.1007/s00254-007-0940-2.

Anders, M. H., S. E. Laubach, and C. H. Scholz (2014), Microfractures: A review, *Journal of Structural Geology*, *69*(PB), 377–394, doi:10.1016/j.jsg.2014.05.011.

Anderson, E. (1951), *The dynamics of faulting and dyke formation with applications to Britain.*, 2 ed., 12–13 pp., Oliver and Boyd, Edinburgh.

Anderson, G. D. (1981), Effects of Friction on Hydraulic Fracture Growth Near Unbonded Interfaces in Rocks, *Society of Petroleum Engineers Journal*, *21*(01), 21 – 29, doi:10.2118/8347-PA.

Aplin, A. C., and J. H. Macquaker (2011), Mudstone diversity: Origin and implications for source, seal, and reservoir properties in petroleum systems, *AAPG Bulletin*, *95*(12), 2031–2059, doi: 10.1306/03281110162.

Bai, T., D. Pollard, and H. Gao (2000), Explanation for fracture spacing in layered materials, *Nature*, *403*(6771), 753–6, doi:10.1038/35001550.

Barnhoorn, A., J. Verheij, M. Frehner, A. Zhubayev, and M. Houben (2018), Experimental identification of the transition from elasticity to inelasticity from ultrasonic attenuation analyses, *Geophysics*, *83*(4), MR221–MR229, doi:10.1190/geo2017-0534.1.

Best, M. E., and T. J. Katsube (1995), Shale permeability and its significance in hydrocarbon exploration, *The Leading Edge*, *14*(3), 165–170, doi:10.1190/1.1437104.

Biot, M. A. (1941), General theory of three-dimensional consolidation, *Journal of Applied Physics*, *12*(2), 155–164, doi:10.1063/1.1712886.

Boersma, Q. D., L. Douma, G. Bertotti, and A. Barnhoorn (2020), Mechanical controls on horizontal stresses and fracture behaviour in layered rocks: A numerical sensitivity analysis, *Journal of Structural Geology*, *130*(103907).

Boggs, S. (2006), *Principles of sedimentology and stratigraphy*, Upper Saddle River, New Jersey.

Bonnelye, A., A. Schubnel, C. David, P. Henry, Y. Guglielmi, C. Gout, A. L. Fauchille, and P. Dick (2017), Elastic wave velocity evolution of shales deformed underuppermost crustal conditions, *Journal of Geophysical Research: Solid Earth*, *122*(1), 130–141, doi:10.1002/2016JB013040.

Bossart, P., P. M. Meier, A. Moeri, T. Trick, and J. C. Mayor (2002), Geological and hydraulic characterisation of the excavation disturbed zone in the Opalinus Clay of the Mont Terri Rock Laboratory, *Engineering Geology*, *66*(1-2), 19–38, doi:10.1016/S0013-7952(01)00140-5.

Bourne, S. J. (2003), Contrast of elastic properties between rock layers as a mechanism for the initiation and orientation of tensile failure under uniform remote compression, *Journal of Geophysical Research*, *108*(B8), 2395, doi:10.1029/2001JB001725.

Brenner, S. L., and A. Gudmundsson (2002), Permeability development during hydrofracture propagation in layered reservoi rs, *Norges geologiske undersokelse Bulletin*, *439*, 71–77.

Brenner, S. L., and A. Gudmundsson (2004), Arrest and aperture variation of hydrofractures in layered reservoirs, *Geological Society, London, Special Publications*, *231*, 117–128, doi:10.1144/GSL.SP.2004.231.01.08.

Britt, L. K., and J. Schoeffler (2009), The Geomechanics Of A Shale Play: What Makes A Shale Prospective!, *SPE Eastern Regional Meeting*, (September), 23–25, doi:10.2118/125525-MS.

Busch, A. (2016), Shale porosity - what can we learn from different methods?, in *Fifth EAGE Shale Workshop*.

Busch, A., S. Alles, Y. Gensterblum, D. Prinz, D. N. Dewhurst, M. D. Raven, H. Stanjek, and B. M. Krooss (2008), Carbon dioxide storage potential of shales, *International Journal of Greenhouse Gas Control*, *2*(3), 297–308, doi:10.1016/j.ijggc.2008.03.003.

Byerlee, J. D. (1968), Brittle-ductile transition in rocks, *Journal of Geophysical Research*, *73*(14), 4741–4750, doi:10.1029/jb073i014p04741.

Campbell, C. V. (1967), Lamina, Laminaset, Bed and Bedset, *Sedimentology*, *8*(1), 7–26, doi:10.1111/j.1365-3091.1967.tb01301.x.

Chalmers, G. R. L., D. J. K. Ross, and R. M. Bustin (2012), Geological controls on matrix permeability of Devonian Gas Shales in the Horn River and Liard basins, northeastern Britisch Columbia, Canada, *International Journal of Coal Geology*, *103*, 120–131.

Chesapeake (2010), Posidonia cutting research.

Childs, C., A. Nicol, J. J. Walsh, and J. Watterson (1996), Growth of vertically segmented normal faults, *Journal of structural Geology*, *18*(12), 1389–1397, doi:https://doi.org/10.1016/S0191-8141(96)00060-0.

Cilona, A., A. Aydin, J. Likerman, B. Parker, and J. Cherry (2016), Structural and statistical characterization of joints and multi-scale faults in an alternating sandstone and shale turbidite sequence at the Santa Susana Field Laboratory: Implications for their effects on groundwater flow and contaminant transport, *Journal of Structural Geology*, *85*, 95–114, doi:10.1016/j.jsg.2016.02.003.

Clarkson, C. R., N. Solano, R. M. Bustin, A. M. M. Bustin, G. R. L. Chalmers, L. He, and T. P. Black (2013), Pore structure characterization of North American shale gas reservoirs using USANS/SANS, gas adsorption, and mercury intrusion, *Fuel*, *103*, 606–616.

Clennell, M. B., D. N. Dewhurst, K. M. Brown, and G. K. Westbrook (1999), Permeability anisotropy of consolidated clays, *Geological Society Special Publication*, *158*, 79–96, doi:10.1144/GSL.SP.1999.158.01.07.

Coates, D. F., and R. C. Parsons (1966), Experimental Criteria For Classification Of Rock Substances, *International Journal of Rock Mechanics and Mining Sciences*, *3*, 181–189, doi: 10.1016/0148-9062(66)90022-2.

Cooke, M. L., and C. A. Underwood (2001), Fracture termination and step-over at bedding interfaces due to frictional slip and interface opening, *Journal of Structural Geology*, *23*(2-3), 223–238, doi:10.1016/S0191-8141(00)00092-4.

Daneshy, A. (1978), Hydraulic Fracture Propagation in Layered Formations, *Society of Petroleum Engineers Journal*, *18*(01), 33–41, doi:10.2118/6088-pa.

Dayal, A. M., and D. Mani (2017), *Shale Gas: Exploration and Environmental and Economic Impacts*, Elsevier.

Delle Piane, C., D. N. Dewhurst, A. F. Siggins, and M. D. Raven (2011), Stress-induced anisotropy in brine saturated shale, *Geophysical Journal International*, *184*(2), 897–906, doi:10.1111/j.1365-246X.2010.04885.x.

Dewhurst, A. Siggins, U. Kuila, and M. B. Clennell (2008), Elastic Geomechanical and Petrophysical Properties of Shales, *U.S. Rock Mechanics Symposium*, pp. ARMA 08–208, doi: ARMA08-208.

Dewhurst, D. N., and A. L. Hennig (2003), Geomechanical properties related to top seal leakage in the Carnarvon Basin, Northwest Shelf, Australia, *Petroleum Geoscience*, *9*(3), 255–263, doi: 10.1144/1354-079302-557.

Dewhurst, D. N., and A. F. Siggins (2006), Impact of fabric, microcracks and stress field on shale anisotropy, *Geophysical Journal International*, *165*(1), 135–148, doi:10.1111/j.1365-246X.2006.02834.x.

Dewhurst, D. N., A. C. Aplin, J.-P. Sarda, and Y. Yang (1998), Compaction-driven evolution of porosity and permeability in natural mudstones: An experimental study, *Journal of Geophysical Research: Solid Earth*, *103*(B1), 651–661, doi:10.1029/97jb02540.

Dewhurst, D. N., R. M. Jones, and M. D. Raven (2002), Microstructural and petrophysical characterization of Muderong Shale: Application to top seal risking, *Petroleum Geoscience*, *8*(4), 371–383, doi:10.1144/petgeo.8.4.371.

Dewhurst, D. N., A. F. Siggins, J. Sarout, M. D. Raven, and H. M. Nordgard-Bolas (2011), Geomechanical and ultrasonic characterization of a Norwegian Sea shale, *Geophysics*, *76*(3), WA101–WA111, doi:10.1190/1.3569599.

Dewhurst, D. N., J. J. Sarout, C. Delle Piane, A. F. Siggins, and M. D. Raven (2015), Empirical strength prediction for preserved shales, *Marine and Petroleum Geology*, *67*(November), 512–525, doi:10.1016/j.marpetgeo.2015.06.004.

Dewhurst, D. N., C. D. Piane, L. Esteban, J. Sarout, M. Josh, M. Pervukhina, and B. M. Clennell (2019), Microstructural, Geomechanical, and Petrophysical Characterization of Shale Caprocks, in *Geological Carbon Storage: Subsurface Seals and Caprock Integrity*, edited by S. Vialle, J. Ajo-Franklin, and J. W. Carey, agu monogr ed., pp. 3–30, John Wiley & Sons.

Dillinger, A., and L. Esteban (2014), Experimental evaluation of reservoir quality in Mesozoic formations of the Perth Basin (Western Australia) by using a laboratory low field Nuclear Magnetic Resonance, *Marine and Petroleum Geology*, *57*, 455–469, doi:10.1016/j.marpetgeo.2014.06.010.

Donath, F. A. (1970), Some information squeezed out of a rock, *American Scientist*, *58*, 54–72.

Douma, L., M. Primarini, M. Houben, and A. Barnhoorn (2017), The validity of generic trends on multiple scales in rock-physical and rock-mechanical properties of the Whitby Mudstone, United Kingdom, *Marine and Petroleum Geology*, *84*, 135–147, doi:10.1016/j.marpetgeo.2017.03.028.

Douma, L. A. N. R., J. Dautriat, J. Sarout, D. N. Dewhurst, and A. Barnhoorn (2019a), Impact of water saturation on the elastic anisotropy of the Whitby Mudstone, United Kingdom, *Geophysics*, *85*(1), 1–82.

Douma, L. A. N. R., J. Dautriat, J. Sarout, L. Esteban, D. N. Dewhurst, and A. Barnhoorn (2019b), The deformation behaviour of the Whitby Mudstone with variable water saturations, *Submitted.*

Dunn, K. J., D. J. Bergman, and G. A. LaTorraca (2002), Nuclear magnetic resonance: Petrophysical and logging applications, *Elsevier*, *32*, 293.

Duranti, L., R. T. Ewy, and R. Hofmann (2005), Dispersive and attenuative nature of shales: Multiscale and multifrequency observations, in *SEG Technical Program Expanded Abstracts 2005*, pp. 1577–1580, Society of Exploration Geophysicists.

Dusseault, M. B. (2004), Coupled thermo-mechano-chemical processes in shales: The petroleum borehole, in *Elsevier Geo-Engineering Book Series*, pp. 573–580, Elsevier.

Dvorkin, J., A. Nur, and H. Yin (1994), Effective properties of cemented granular materials, *Mechanics of Materials*, *18*(4), 351–366, doi:10.1016/0167-6636(94)90044-2.

Ebrahimi, D., R. J. Pellenq, and A. J. Whittle (2012), Nanoscale elastic properties of montmorillonite upon water adsorption, *Langmuir*, *28*(49), 16,855–16,863, doi:10.1021/la302997g.

Eisenstadt, G., and D. G. D. Paor (1987), Alternative model of thrust-fault propagation, *Geology*, *15*(7), 630–633, doi:https://doi.org/10.1130/0091-7613(1987)15.

Engelder, T., G. G. Lash, and R. S. Uzcátegui (2009), Joint sets that enhance production from Middle and Upper Devonian gas shales of the Appalachian Basin, *AAPG Bulletin*, *93*(7), 857–889, doi:10.1306/03230908032.

Erling, F., R. Holt, A. M. Raaen, R. Risnes, and P. Horsrud (2008), *Petroleum related rock mechanics*, 2nd ed., 251 – 287 pp., Elsevier Sience.

Ewy, R., C. Bovberg, and R. Stankovic (2010), Strength anisotropy of mudstones and shales, *44th US Rock Mechanics Symposium and 5th US-Canada Rock Mechanics Symposium*, doi: 10.1017/CBO9781107415324.004.

Ewy, R. T. (2014), Mechanical Anisotropy of Gas Shales and Claystones, in *Fourth EAGE Shale Workshop*, April 2014.

Ewy, R. T. (2015), Shale/claystone response to air and liquid exposure, and implications for handling, sampling and testing, *International Journal of Rock Mechanics and Mining Sciences*, *80*, 388–401, doi:10.1016/j.ijrmms.2015.10.009.

Ewy, R. T. (2018), Practical approaches for addressing shale testing challenges associated with permeability, capillarity and brine interactions, *Geomechanics for Energy and the Environment*, *14*, 3–15, doi:10.1016/j.gete.2018.01.001.

Ewy, R. T., E. J. Daniels, and R. J. Stankovich (2001), Behavior of a reactive shale from 12000 feet depth, *DC Rocks 2001, The 38th U.S. Symposium on Rock Mechanics (USRMS), 7-10 July, Washington, D.C.*, pp. 77–84.

Favero, V., A. Ferrari, and L. Laloui (2018), Anisotropic Behaviour of Opalinus Clay Through Consolidated and Drained Triaxial Testing in Saturated Conditions, *Rock Mechanics and Rock Engineering*, *51*(5), 1305–1319, doi:10.1007/s00603-017-1398-5.

Ferrari, A., V. Favero, P. Marschall, and L. Laloui (2014), Experimental analysis of the water retention behaviour of shales, *International Journal of Rock Mechanics and Mining Sciences*, *72*, 61–70, doi:10.1016/j.ijrmms.2014.08.011.

Ferrill, D. A., and A. P. Morris (2003), Dilational normal faults, *Journal of Structural Geology*, *25*(5), 827, doi:10.1016/S0191-8141(02)00196-7.

Ferrill, D. A., and A. P. Morris (2008), Fault zone deformation controlled by carbonate mechanical stratigraphy, Balcones fault system, Texas, *AAPG Bulletin*, *92*(3), 359–380, doi: 10.1306/10290707066.

Ferrill, D. A., A. P. Morris, and R. N. McGinnis (2012), Extensional fault-propagation folding in mechanically layered rocks: The case against the frictional drag mechanism, *Tectonophysics*, *576-577*, 78–85, doi:10.1016/j.tecto.2012.05.023.

Ferrill, D. A., R. N. McGinnis, A. P. Morris, K. J. Smart, Z. T. Sickmann, M. Bentz, D. Lehrmann, and M. A. Evans (2014), Control of mechanical stratigraphy on bed-restricted jointing and normal faulting: Eagle Ford Formation, south-central Texas, *AAPG Bulletin*, *98*(11), 2477–2506, doi:10.1306/08191414053.

Ferrill, D. A., A. P. Morris, S. S. Wigginton, K. J. Smart, R. N. McGinnis, and D. Lehrmann (2016), Deciphering thrust fault nucleation and propagation and the importance of footwall synclines, *Journal of Structural Geology*, *85*, 1–11, doi:10.1016/j.jsg.2016.01.009.

Ferrill, D. A., A. P. Morris, R. N. McGinnis, K. J. Smart, S. S. Wigginton, and N. J. Hill (2017), Mechanical stratigraphy and normal faulting, *Journal of Structural Geology*, *94*, 275–302, doi: 10.1016/j.jsg.2016.11.010.

Fjær, E., and O. M. Nes (2014), The impact of heterogeneity on the anisotropic strength of an outcrop shale, *Rock Mechanics and Rock Engineering*, *47*(5), 1603–1611, doi:10.1007/s00603-014-0598-5.

Forsans, T., and L. Schmitt (1994), Capillary forces: The neglected factor in shale instability studies? Paper SPE 28029, *Proceedings of Rock Mechanics in Petroleum Engineering*, pp. 71–84, doi:10.2118/28029-MS.

Fossen, H. (2010), *Structural Geology*, 4 ed., 83–85 pp., Cambridge University Press.

Frimmel, A., W. Oschmann, and L. Schwark (2004), Chemostratigraphy of the Posidonia Black Shale , SW Germany I . Influence of sea-level variation on organic facies evolution, *Chemical Geology*, *206*(3), 199–230, doi:10.1016/j.chemgeo.2003.12.007.

Garrels, R. M., and F. T. Mackenzie (1969), Sedimentary rock types: Relative proportions as a function of geological time, *Science*, *163*(3867), 570–571, doi:10.1126/science.163.3867.570.

Gasparik, M., P. Bertier, Y. Gensterblum, A. Ghanizadeh, B. M. Krooss, and R. Littke (2014), Geological controls on the methane storage capacity in organic-rich shales, *International Journal of Coal Geology*, *123*, 34–51, doi:10.1016/j.coal.2013.06.010.

Ghadeer, S. G., and J. H. S. Macquaker (2012), The role of event beds in the preservation of organic carbon in fine-grained sediments: Analyses of the sedimentological processes operating during deposition of the Whitby Mudstone Formation (Toarcian, Lower Jurassic) preserved in northeast England, *Marine and Petroleum Geology*, *35*(1), 309–320, doi:10.1016/j.marpetgeo.2012.01.001.

Ghanizadeh, A., A. Amann-Hildenbrand, M. Gasparik, Y. Gensterblum, B. M. Krooss, and R. Littke (2014), Experimental study of fluid transport processes in the matrix system of the European organic-rich shales: II. Posidonia Shale (Lower Toarcian, northern Germany), *International Journal of Coal Geology*, *123*, 20–33, doi:10.1016/j.coal.2013.06.009.

Ghorbani, A., M. Zamora, and P. Cosenza (2009), Effects of desiccation on the elastic wave velocities of clay-rocks, *International Journal of Rock Mechanics and Mining Sciences*, *46*(8), 1267–1272, doi:10.1016/j.ijrmms.2009.01.009.

Giger, S. B., R. T. Ewy, V. Favero, R. Stankovic, and L. M. Keller (2018), Consolidated-undrained triaxial testing of Opalinus Clay : Results and method validation, *Geomechanics for Energy and the Environment*, *14*, 16–28, doi:10.1016/j.gete.2018.01.003.

Grainger, P. (1984), The classification of mudrocks for engineering purposes., *Quarterly Journal of Engineering Geology*, *17*(4), 381–387.

Griffiths, F. J., and R. C. Joshi (1990), Clay Fabric Response to Consolidation, *Applied Clay Science*, *5*(1), 37–66.

Gross, M. R. (1995), Fracture partitioning : Failure mode as a function of lithology in the Monterey Formation of coastal California, *GSA Bulletin*, *107*(7), 779–792, doi:https://doi.org/10.1130/0016-7606(1995)107.

Gu, H., E. Siebrits, and A. Sabourov (2008), Hydraulic Fracture Modeling With Bedding Plane Interfacial Slip, in *SPE Eastern Regional/AAPG Eastern Section Joint Meeting*, Society of Petroleum Engineers, doi:10.2118/117445-ms.

Gudmundsson, A. (2002), Emplacement and arrest of sheets and dykes in central volcanoes, *Journal of Volcanology and Geothermal Research*, *116*(3-4), 279–298, doi:10.1016/S0377-0273(02)00226-3.

Gudmundsson, A. (2003), Surface stresses associated with arrested dykes in rift zones, *Bulletin of Volcanology*, *65*(8), 606–619, doi:10.1007/s00445-003-0289-7.

Guo, L., J. P. Latham, and J. Xiang (2017), A numerical study of fracture spacing and through-going fracture formation in layered rocks, *International Journal of Solids and Structures*, *110-111*, 44–57, doi:10.1016/j.ijsolstr.2017.02.004.

Gutierrez, M., D. Katsuki, and A. Tutuncu (2015), Determination of the continuous stress-dependent permeability, compressibility and poroelasticity of shale, *Marine and Petroleum Geology*, *68*, 614–628, doi:10.1016/j.marpetgeo.2014.12.002.

Haimson, B., and C. Fairhurst (1967), Initiation and extension of hydraulic fractures in rocks, *Society of Petroleum Engineers Journal*, *7*(03).

Haldar, S. K., and J. Tisljar (2014), Shale and mudstone, in *Introduction to mineralogy and petrology*, Elsevier.

Handin, J. (1969), On the Coulomb-Mohr failure criterion, *Journal of Geophysical Research*, *74*(22), 5343–5348, doi:10.1029/jb074i022p05343.

Handin, J., R. V. Hager, M. Friedman, and J. N. Feathers (1963), Experimental Deformation of Sedimentary Rocks under Confining Pressure: Pore Pressure Tests, *Bulletin of the American Association of Petroleum geologists*, *47*(5), 717–755, doi:10.1126/science.51.1323.468.

Head, K. H. (1998), *Manual of Soil Laboratory Testing, Volume 3: Effective Stress Tests*, John Wiley & Sons, Chichester, U.K.

Helgeson, D. E., and A. Aydin (1991), Characteristics of joint propagation across layer interfaces in sedimentary rocks, *Journal of Structural Geology*, *13*(8), 897–911, doi:10.1016/0191-8141(91)90085-W.

Herber, R., and J. D. Jager (2010), Geoperspective Oil and Gas in the Netherlands – Is there a future ?, *Netherlands journal of geosciences*, *89*(02), 91–107, doi:10.1017/S001677460000072X.

Hesselbo, S. P., D. R. Grocke, H. C. Jenkyns, C. J. Bjerrum, P. Farrimond, H. S. M. Bell, and O. R. Green (2000), Massive dissociation of gas hydrate during a Jurassic oceanic anoxic event, *Nature*, *406*(6794), 392–395, doi:10.1038/35019044.

Hettema, M. H. H., and C. J. D. Pater (1998), The Poromechanical Behaviour of Felser Sandstone: Stress- and Temperature-Dependent, *Society of Petroleum Engineers - SPE/ISRM Rock Mechanics in Petroleum Engineering, Trondheim, Norway.*

Hettema, M. H. H., C. J. D. Pater, and K.-H. A. A. Wolf (1991), of temperature and pore water on creep of sandstone, in *The 32nd US Symposium on Rock Mechanics (USRMS)*, Amerian Rock Mechanics Association.

Hoek, E., and J. Franklin (1968), Simple triaxial cell for field or laboratory testing of rock, *Transactions of the Institution of Mining and Metallurgy*, *77*, 22–26.

Holland, P. W., and R. E. Welsch (1977), Robust regression using iteratively reweighted least-squares, *Communications in Statistics - Theory and Methods*, *6*(9), 813–827, doi:10.1080/03610927708827533.

Holt, R., E. Fjær, J. Stenebråten, and O.-M. Nes (2015), Brittleness of shales: Relevance to borehole collapse and hydraulic fracturing, *Journal of Petroleum Science and Engineering*, *131*(1), 200–209, doi:10.1016/j.petrol.2015.04.006.

Holt, R. M., A.-K. Furre, and P. Horsrud (1997), Stress Dependent Wave Velocities in Sedimentary Rock Cores : Why and Why Not ?, *Int. J. Rock Mech. & Min. Sci*, *34*(128), 3–4.

Holt, R. M., E. Fjær, O. M. Nes, and H. Alassi (2011), A shaly look at brittleness, *45th US Rock Mechanics Geomechanics Symposium*, pp. 1–10.

Hooker, J. N., S. E. Laubach, and R. Marrett (2013), Fracture-aperture sizedfrequency, spatial distribution, and growth processes in strata-bounded and non-strata-bounded fractures, cambrian mesón group, NW argentina, *Journal of Structural Geology*, *54*, 54–71, doi:10.1016/j.jsg.2013.06.011.

Hornby, B. E. (1998), Experimental laboratory determination of the dynamic elastic properties of wet, drained shales, *Journal of Geophysical Research*, *103*(97), 945–964.

Horsrud, P. (2001), Estimating mechanical properties of shale from empirical correlations, *SPE Drilling & Completion*, *16*(02), 68–73.

Horsrud, P., R. Holt, E. Sonstebo, G. Svano, and B. Bostrom (1994), Time dependent borehole stability: Laboratory studies and numerical simulation of different mechanisms in shale, in *Rock Mechanics in Petroleum Engineering*, Society of Petroleum Engineers, doi:10.2523/28060-ms.

Horsrud, P., E. Sonstebo, and R. Boe (1998), Mechanical and petrophysical properties of North Sea shales, *International Journal of Rock Mechanics and Mining Sciences*, *35*(8), 1009–1020, doi:10.1016/S0148-9062(98)00162-4.

Houben, M., A. Barnhoorn, L. Wasch, J. Trabucho-Alexandre, C. Peach, and M. Drury (2016a), Microstructures of Early Jurassic (Toarcian) shales of Northern Europe, *International Journal of Coal Geology*, *165*, 76–89, doi:10.1016/j.coal.2016.08.003.

Houben, M. E., G. Desbois, and J. L. Urai (2014), A comparative study of representative 2D microstructures in Shaly and Sandy facies of Opalinus Clay (Mont Terri, Switzerland) inferred form BIB-SEM and MIP methods, *Marine and Petroleum Geology*, *49*, 143–161, doi:10.1016/j.marpetgeo.2013.10.009.

Houben, M. E., A. Barnhoorn, J. Lie-A-Fat, T. Ravestein, C. J. Peach, and M. R. Drury (2016b), Microstructural characteristics of the Whitby Mudstone Formation (UK), *Marine and Petroleum Geology*, *70*, 185–200, doi:10.1016/j.marpetgeo.2015.11.011.

Hucka, V., and B. Das (1974), Brittleness determination of rocks by different methods, *International Journal of Rock Mechanics and Mining Sciences and*, *11*(10), 389–392, doi:10.1016/0148-9062(74)91109-7.

Hudson, J. A. (1981), Wave speeds and attenuation of elastic waves in material containing cracks, *Geophysical Journal of the Royal Astronomical Society*, *64*(1), 133–150, doi: 10.1111/j.1365-246X.1981.tb02662.x.

Ingram, G. M., and J. L. Urai (1999), Top-seal leakage through faults and fractures: the role of mudrock properties, *Geological Society, London, Special Publications*, *158*(1), 125–135, doi: 10.1144/GSL.SP.1999.158.01.10.

Ingram, R. L. (1953), Fissility of mudrocks, *Bulleting of the Geological Society of America*, *64*(August), 869–878.

Jakobsen, M., and T. A. Johansen (2000), Anisotropic approximations for mudrocks: A seismic laboratory study, *Geophysics*, *65*(6), 1711–1725, doi:10.1190/1.1444856.

Jarvie, D. M., R. J. Hill, T. E. Ruble, and R. M. Pollastro (2007), Unconventional shale-gas systems: The Mississippian Barnett Shale of north-central Texas as one model for thermogenic shale-gas assessment, *AAPG Bulletin*, *91*(4), 475–499, doi:10.1306/12190606068.

Jeffrey, R. G., and A. Bunger (2009), A Detailed Comparison of Experimental and Numerical Data on Hydraulic Fracture Height Growth Through Stress Contrasts, *SPE Journal*, *14*(03), 413–422, doi:10.2118/106030-pa.

Jin, X., S. N. Shah, J.-C. Roegiers, and B. Zhang (2014), Fracability evaluation in shale reservoirs-an integrated petrophysics and geomechanics approach, in *SPE Hydraulic Fracturing Technology Conference. Society of Petroleum Engineers*, pp. 1–14, doi:http://dx.doi.org/10.2118/168589-MS.

Jin, Z., W. Li, C. Jin, J. Hambleton, and G. Cusatis (2018), Anisotropic elastic, strength, and fracture properties of Marcellus shale, *International Journal of Rock Mechanics and Mining Sciences*, *109*(May), 124–137, doi:10.1016/j.ijrmms.2018.06.009.

Johnston, D. H. (1987), Physical properties of shale at temperature and pressure, *Geophysics*, *52*(10), 1391–1401, doi:10.1190/1.1442251.

Johnston, J. E., and N. I. Christensen (1996), Seismic anisotropy of shales, *International Journal of Rock Mechanics and Mining Sciences and Geomechanics Abstracts*, *33*, 72A–72A(1), doi: 10.1029/95JB00031.

Jones, L. E. A., and H. F. Wang (1981), Ultrasonic velocities in Cretaceous shales from the Williston basin, *Geophysics*, *46*(3), 288–297, doi:10.1190/1.1441199.

Josh, M., L. Esteban, C. D. Piane, J. Sarout, D. N. Dewhurst, and M. B. Clennell (2012), Laboratory characterisation of shale properties, *Journal of Petroleum Science and Engineering*, *88-89*, 107–124, doi:10.1016/j.petrol.2012.01.023.

Josnin, J.-Y., H. Jourde, P. Fénart, and P. Bidaux (2002), A three-dimensional model to simulate joint networks in layered rocks, *Canadian Journal of Earth Sciences*, *39*(10), 1443–1455, doi: 10.1139/e02-043.

Kanitpanyacharoen, W., F. B. Kets, H. R. Wenk, and R. Wirth (2012), Mineral preferred orientation and microstructure in the Posidonia Shale in relation to different degrees of thermal maturity, *Clays and Clay Minerals*, *60*(3), 315–329, doi:10.1346/CCMN.2012.0600308.

Kemp, S. J., R. J. Merriman, and J. E. Bouch (2005), Clay mineral reaction progress-the maturity and burial history of the Lias Group of England and Wales, *Clay minerals*, *40*(1), 43–61.

Kettermann, M., and J. L. Urai (2015), Changes in structural style of normal faults due to failure mode transition: First results from excavated scale models, *Journal of Structural Geology*, *74*, 105–116, doi:10.1016/j.jsg.2015.02.013.

Klaver, J., G. Desbois, J. L. Urai, and R. Littke (2012), BIB-SEM study of the pore space morphology in early mature Posidonia Shale from the Hils area, Germany, *International Journal of Coal Geology*, *103*, 12–25, doi:10.1016/j.coal.2012.06.012.

Klaver, J., G. Desbois, R. Littke, and J. L. Urai (2015), BIB-SEM characterization of pore space morphology and distribution in postmature to overmature samples from the Haynesville and Bossier Shales, *Marine and Petroleum Geology*, *59*, 451–466, doi:10.1016/j.marpetgeo.2014.09.020.

Klaver, J., G. Desbois, R. Littke, and J. L. Urai (2016), BIB-SEM pore characterization of mature and post mature Posidonia Shale samples from the Hils area, Germany, *International Journal of Coal Geology*, *158*, 78–89, doi:10.1016/j.coal.2016.03.003.

Klein, E., P. Baud, T. Reuschlé, and T. F. Wong (2001), Mechanical behaviour and failure mode of Bentheim sandstone under triaxial compression, *Physics and Chemistry of the Earth, Part A: Solid Earth and Geodesy*, *26*(1-2), 21–25, doi:10.1016/S1464-1895(01)00017-5.

Kleinberg, R. L., W. E. Kenyon, and P. P. Mitra (1994), Mechanism of NMR relaxation of fluids in rock, *Journal of Magnetic Resonance, Series A*, *108*(2), 206–214.

Kovalyshen, Y., J. Sarout, and J. Dautriat (2017), Inversion of ultrasonic data for transversely isotropic media, *Geophysics*, *82*(1), C1–C7, doi:10.1190/geo2016-0102.1.

Kovalyshen, Y., J. Sarout, and M. Lebedev (2018), On the interpretation of ultrasonic laboratory measurements in anisotropic media, *Geophysics*, *83*(4), C173–C178, doi:10.1190/geo2017-0634.1.

Kuila, U., D. N. Dewhurst, A. F. Siggins, and M. D. Raven (2011), Stress anisotropy and velocity anisotropy in low porosity shale, *Tectonophysics*, *503*(1-2), 34–44, doi:10.1016/j.tecto.2010.09.023.

Laloui, L. (2013), *Mechanics of unsaturated geomaterials*, John Wiley & Sons.

Laloui, L., S. Salager, and M. Rizzi (2013), Retention behaviour of natural clayey materials at different temperatures, *Acta Geotechnica*, *8*(5), 537–546, doi:10.1007/s11440-013-0255-2.

Larsen, B., and A. Gudmundsson (2010), Linking of fractures in layered rocks: Implications for permeability, *Tectonophysics*, *492*(1-4), 108–120, doi:10.1016/j.tecto.2010.05.022.

Laubach, S. E., J. E. Olson, and M. R. Cross (2009), Mechanical and fracture stratigraphy, *AAPG Bulletin*, *93*(11), 1413–1426, doi:10.1306/07270909094.

Laubach, S. E., J. Lamarche, B. D. Gauthier, W. M. Dunne, and D. J. Sanderson (2018), Spatial arrangement of faults and opening-mode fractures, *Journal of Structural Geology*, *108*, 2–15, doi:10.1016/j.jsg.2017.08.008.

Lavenu, A. P., and J. Lamarche (2018), What controls diffuse fractures in platform carbonates? Insights from Provence (France) and Apulia (Italy), *Journal of Structural Geology*, *108*, 94–107, doi:10.1016/j.jsg.2017.05.011.

Lempp, C., L. Felsmechanik, U. Karlsruhe, U. Bayer, G. Potsdam, D. H. Welte, O. Geochemistry, and F. J. Gmbh (1994), SPE 28039 The effect of temperature on rock mechanical properties and fracture mechanisms in source rocks - Experimental results L ’ effet de la temperature sur les proprietes mecaniques et les mecanismes de fissurage en cas de schiste bitumineux - Result.

Littke, R., D. Baker, D. Leythaeuser, and J. Rullkotter (1991), Keys to the depositional history of the Posidonia Shale (Toarcian) in the Hils Syncline, northern Germany, *Geological Society, London, Special Publications*, *58*(1), 311–333.

Lorenz, J. C., J. L. Sterling, D. S. Schechter, C. L. Whigham, J. L. Jensen, J. C. Lorenz, and J. L. Sterling (2002), basin , Texas : The effects of reservoir behavior, *3*(3), 505–524.

Lozovyi, S., A. Bauer, S. Giger, and S. Chakraborty (2018), Static vs. dynamic stiffness of shales: Frequency and stress effects, *52nd U.S. Rock Mechanics/Geomechanics Symposium*.

Maerten, L., P. Gillespie, and J. M. Daniel (2006), Three-dimensional geomechanical modeling for constraint of subseismic fault simulation, *AAPG Bulletin*, *90*(9), 1337–1358, doi:10.1306/03130605148.

Maerten, L., F. Maerten, M. Lejri, and P. Gillespie (2016), Geomechanical paleostress inversion using fracture data, *Journal of Structural Geology*, *89*, 197–213, doi:10.1016/j.jsg.2016.06.007.

Marsden, J., R. Holt, S. Nakken, and A. Raaen (1992), Mechanical and petrophysical characterization of highly stressed mudstones, in *Rock Characterization: ISRM Symposium, Eurock'92*, pp. 51–56, Chester, UK.

Masri, M., M. Sibai, J. Shao, and M. Mainguy (2014), Experimental investigation of the effect of temperature on the mechanical behavior of Tournemire shale, *International Journal of Rock Mechanics and Mining Sciences*, *70*, 185–191, doi:10.1016/j.ijrmms.2014.05.007.

Mathia, E. J., L. Bowen, K. M. Thomas, and A. C. Aplin (2016), Evolution of porosity and pore types in organic-rich, calcareous, Lower Toarcian Posidonia Shale, *Marine and Petroleum Geology*, *75*, 117–139, doi:10.1016/j.marpetgeo.2016.04.009.

Mavko, G., T. Mukerji, and J. Dvorkin (2003), *The rock physics handbook: tools for seismic analysis in porous media*, 17–50 pp., Cambridge University Press.

Mavko, G., T. Mukerji, and J. Dvorkin (2009), *The Rock Physics Handbook, Second Edition*, 654 pp., Cambridge University Press, doi:http://dx.doi.org/10.1017/CBO9780511626753.

Maxwell, S. C., and C. Cipolla (2011), What Does Microseismicity Tell Us About Hydraulic Fracturing?, *SPE Annual Technical Conference and Exhibition*, (November), SPE 146,932, doi:10.2118/146932-MS.

McGinnis, R. N., D. A. Ferrill, A. P. Morris, K. J. Smart, and D. Lehrmann (2017), Mechanical stratigraphic controls on natural fracture spacing and penetration, *Journal of Structural Geology*, *95*, 160–170, doi:10.1016/j.jsg.2017.01.001.

McKee, E. D., and G. W. Weir (1953), Terminology for stratification and cross-stratification in sedimentary rocks, *Geological Society Of America Bulletin*, *64*(4), 381–390.

Minaeian, V., D. N. Dewhurst, and V. Rasouli (2017), Deformational behaviour of a clay-rich shale with variable water saturation under true triaxial stress conditions, *Geomechanics for Energy and the Environment*, *11*, 1–13, doi:10.1016/j.gete.2017.04.001.

Mitchell, J. K. (1993), *Fundamentals of soil behaviour*, second ed., 437 pp., John Wiley & Sons.

Montes, H. G., J. Duplay, L. Martinez, S. Escoffier, and D. Rousset (2004), Structural modifications of Callovo-Oxfordian argillite under hydration/dehydration conditions, *Applied Clay Science*, *25*(3-4), 187–194, doi:10.1016/j.clay.2003.10.004.

Moritz, L. (1995), *Geotechnical properties of clay at elevated temperatures*.

Nadri, D., J. Sarout, A. Bóna, and D. Dewhurst (2012), Estimation of the anisotropy parameters of transversely isotropic shales with a tilted symmetry axis, *Geophysical Journal International*, *190*(2), 1197–1203, doi:10.1111/j.1365-246X.2012.05545.x.

Narr, W., and J. Suppe (1991), Joint spacing in sedimentary rocks, *Journal of Structural Geology*, *13*(9), 1037–1048, doi:10.1016/0191-8141(91)90055-N.

Newhouse, W. H. (1942), *Ore deposits as related to structural features*, Princeton University Press.

Nolte, K. G., and M. B. Smith (1979), Interpretation of Fracturing Pressures, in *SPE Annual Technical Conference and Exhibition, 23-26 September, Las Vegas, Nevada*, pp. 1–8, Society of Petroleum Engineers.

Nygård, R., M. Gutierrez, R. K. Bratli, and K. Høeg (2006), Brittle-ductile transition, shear failure and leakage in shales and mudrocks, *Marine and Petroleum Geology*, *23*(2), 201–212, doi:10.1016/j.marpetgeo.2005.10.001.

Olson, J. E. (2004), Predicting fracture swarms — the influence of subcritical crack growth and the crack-tip process zone on joint spacing in rock, *Geological Society, London, Special Publications*, *231*(1), 73–88, doi:10.1144/GSL.SP.2004.231.01.05.

Onaisi, A., C. Durand, A. Audibert, and R. Malmaison (1994), Role of Hydration State of Shales in Borehole Stability Studies, in *Rock mechanics in*, Society of Petroleum Engineers.

Osipov, V., V. Sokolov, and V. Eremeev (2004), *Clay Seals of Oil and Gas Deposits*, 284 pp., CRC press.

Ougier-Simonin, A., J. Sarout, and Y. Guéguen (2009), A simplified model of effective elasticity for anisotropic shales, *Geophysics*, *74*(3), D57–D63, doi:10.1190/1.3096616.

Papamichos, E., M. Brignoli, and F. J. Santarelli (1997), Experimental and theoretical study of a partially saturated collapsible rock, *Mechanics of Cohesive-Frictional Materials*, *2*(3), 251–278, doi:10.1002/(SICI)1099-1484(199707)2.

Passey, Q. R., K. M. Bohacs, W. L. Esch, R. Klimentidis, S. Sinha, and E. Upstream (2010), From Oil-Prone Source Rock to Gas-Producing Shale Reservoir – Geologic and Petrophysical Characterization of Unconventional Shale-Gas Reservoirs, in *International Oil & Gas Conference and Exhibition in China. Society of Petroleum Engineers*, pp. 1707–1735, doi: http://dx.doi.org/10.2118/131350-MS.

Paterson, M. S., and T.-F. Wong (2005), *Experimental rock deformation-the brittle field*, Springer Science & Business Media.

Peacock, D. C., and D. J. Sanderson (1992), Effects of layering and anisotropy on fault geometry, *Journal of the Geological Society*, *149*(5), 793–802, doi:10.1144/gsjgs.149.5.0793.

Peacock, D. C., and D. J. Sanderson (1994), Geometry and development of relay ramps in normal fault systems, *American Association of Petroleum Geologists Bulletin*, *78*(2), 147–165, doi: 10.1306/BDFF9046-1718-11D7-8645000102C1865D.

Pervukhina, M., D. Dewhurst, B. Gurevich, U. Kuila, T. Siggins, M. Raven, and H. M. N. Bolås (2008), Stress-dependent elastic properties of shales: Measurement and modeling, *The Leading Edge*, *27*(6), 772–779, doi:10.1190/1.2944162.

Pervukhina, M., B. Gurevich, D. N. Dewhurst, P. Golodoniuc, and M. Lebedev (2015), Rock physics analysis of shale reservoirs, in *Fundamentals of Gas Shale Reservoirs*, edited by R. Rezaee, chap. 9, pp. 186–200, Wiley Publishing.

Petley, D. N. (1999), Failure envelopes of mudrocks at high confining pressures, *Geological Society, London, Special Publications*, *158*(1), 61–71, doi:10.1144/GSL.SP.1999.158.01.05.

Picard, M. D. (1953), Marlstone - a Misnomer as Used in Uinta Basin, Utah, *AAPG Bulletin*, *37*(5), 1075–1077.

Pollard, D. D. (1987), Progress In Understanding Jointing Over The Past Century, *Geological Society Of America Bulletin*, *100*(8), 1181–1204, doi:https://doi.org/10.1130/0016-7606(1988)100.

Powell, J. H. (2010), Jurassic sedimentation in the Cleveland Basin: a review, *Proceedings of the Yorkshire Geological Society*, *58*(1), 21–72, doi:10.1144/pygs.58.1.278.

Pye, K. (1985), Electron microscope analysis of zoned dolomite rhombs in the Jet Rock Formation (Lower Toarcian) of the Whitby area, U.K., *Geological Magazine*, *122*(3), 279–286, doi:10.1017/S0016756800031496.

Rabi, I. I., J. Zacharias, S. Millman, and P. Kusch (1938), A new method of measuring nuclear magnetic moment, *Phys rev*, *53*(318), 137–144, doi:10.1016/S0031-8914(39)80004-0.

Ramos da Silva, M., C. Schroeder, and J. C. Verbrugge (2008), Unsaturated rock mechanics applied to a low-porosity shale, *Engineering Geology*, *97*(1-2), 42–52, doi:10.1016/j.enggeo.2007.12.003.

Rexer, T. F., E. J. Mathia, A. C. Aplin, and K. M. Thomas (2014), High-pressure methane adsorption and characterization of pores in posidonia shales and isolated kerogens, *Energy and Fuels*, *28*(5), 2886–2901, doi:10.1021/ef402466m.

Rickman, R., M. Mullen, E. Petre, B. Grieser, and D. Kundert (2008), A practical use of shale petrophysics for stimulation design optimization: All shale plays are not clones of the Barnett Shale, in *SPE Annual Technical Conference and Exhibition. Society of Petroleum Engineers*, Wang, pp. 1–11, doi:10.2118/115258-MS.

Rijken, Peggy, Holder, Jon, Olson, E. Jon, Laubach, and E. Stephen (2002), Predicting Fracture Attributes in the Travis Peak Formation Using Quantitative Mechanical Modeling and Structural Diagenesis, *52*, 837–847.

Rijken, P., and M. L. Cooke (2001), Role of shale thickness on vertical connectivity of fractures: Application of crack-bridging theory to the Austin Chalk, Texas, *Tectonophysics*, *337*(1-2), 117–133, doi:10.1016/S0040-1951(01)00107-X.

Roche, V., C. Homberg, and M. Rocher (2013), Fault nucleation, restriction, and aspect ratio in layered sections: Quantification of the strength and stiffness roles using numerical modeling, *Journal of Geophysical Research: Solid Earth*, *118*(8), 4446–4460, doi:10.1002/jgrb.50279.

Romera, E., G. Della Vecchia, and C. Jommi (2011), An insight into the water retention properties of compacted clayey soils, *Géotechnique*, *61*(4), 313–328, doi:10.1680/geot.2011.61.4.313.

Ross, D. J. K., and R. M. Bustin (2009), The importance of shale composition and pore structure upon gas storage potential of shale gas reservoirs, *Marine and Petroleum Geology*, *26*(6), 916–927.

Rutter, E. H. (1986), On the nomenclature of mode of failure transitions in rocks, *Tectonophysics*, *122*(3-4), 381–387, doi:10.1016/0040-1951(86)90153-8.

Rybacki, E., A. Reinicke, T. Meier, M. Makasi, and G. Dresen (2015), What controls the mechanical properties of shale rocks? - Part I: Strength and Young's modulus, *Journal of Petroleum Science and Engineering*, *135*, 702–722, doi:10.1016/j.petrol.2016.02.022.

Rybacki, E., T. Meier, and G. Dresen (2016), What controls the mechanical properties of shale rocks? - Part II: Brittleness, *Journal of Petroleum Science and Engineering*, *144*, 39–58, doi:10.1016/j.petrol.2016.02.022.

Sarout, J., and Y. Guéguen (2008a), Anisotropy of elastic wave velocities in deformed shales: Part 1 — Experimental results, *Geophysics*, *73*(5), D75–D89, doi:10.1190/1.2952745.

Sarout, J., and Y. Guéguen (2008b), Anisotropy of elastic wave velocities in deformed shales: Part 2 — Modeling results, *Geophysics*, *73*(5), D91–D103, doi:10.1190/1.2952745.

Sarout, J., L. Esteban, C. D. Piane, B. Maney, and D. N. Dewhurst (2014), Elastic anisotropy of Opalinus Clay under variable saturation and triaxial stress, *Geophysical Journal International*, *198*(3), 1662–1682, doi:10.1093/gji/ggu231.

Sarout, J., C. Delle Piane, D. Nadri, L. Esteban, and D. N. Dewhurst (2015), A robust experimental determination of Thomsen's δ parameter, *Geophysics*, *80*(1), A19–A24, doi: 10.1190/geo2014-0391.1.

Sarout, J., Y. Le Gonidec, A. Ougier-Simonin, A. Schubnel, Y. Gueguen, and D. N. Dewhurst (2017), Laboratory micro-seismic signature of shear faulting and fault slip in shale, *Physics of the Earth and Planetary Interiors*, *264*, 47–62, doi:10.1016/j.pepi.2016.11.005.

Sayers, C. (2013), The effect of anisotropy on the Young's moduli and Poisson's ratios of shales, *Geophysical Prospecting*, *61*(2), 416–426, doi:10.1111/j.1365-2478.2012.01130.x.

Sayers, C. M. (1994), The elastic anisotrophy of shales, *Journal of Geophysical Research*, *99*(B1), 767–774, doi:10.1029/93JB02579.

Sayers, C. M. (2008), The effect of low aspect ratio pores on the seismic anisotropy of shales, in *2008 SEG Annual Meeting. Society of Exploration Geophysicists.*, pp. 2750–2754, doi:10.1190/1.3063916.

Sayers, C. M., and M. Kachanov (1995), Microcrack-induced elastic wave anisotropy of brittle rocks, *Journal of Geophysical Research*, *100*(B3), 4149–4156.

Schmitt, L., T. Forsans, and F. J. Santarelli (1994), Shale testing and capillary phenomena, *International Journal of Rock Mechanics and Mining Sciences and*, *31*(5), 411–427, doi: 10.1016/0148-9062(94)90145-7.

Schöpfer, M., C. Childs, and J. Walsh (2007), Two-dimensional distinct element modeling of the structure and growth of normal faults in multilayer sequences: 1. Model calibration, boundary conditions, and selected results, *Journal of Geophysical Research: Solid Earth*, *112*(10), doi: 10.1029/2006JB004902.

Schöpfer, M. P., C. Childs, and J. J. Walsh (2006), Localisation of normal faults in multilayer sequences, *Journal of Structural Geology*, *28*(5), 816–833, doi:10.1016/j.jsg.2006.02.003.

Schöpfer, M. P., A. Arslan, J. J. Walsh, and C. Childs (2011), Reconciliation of contrasting theories for fracture spacing in layered rocks, *Journal of Structural Geology*, *33*(4), 551–565, doi:10.1016/j.jsg.2011.01.008.

Schwark, L., and A. Frimmel (2004), Chemostratigraphy of the Posidonia Black Shale, SW-Germany II. Assessment of extent and persistence of photic-zone anoxia using aryl isoprenoid distributions, *Chemical Geology*, *206*(3-4), 231–248, doi:10.1016/j.chemgeo.2003.12.008.

Shackleton, J. R., M. L. Cooke, and A. J. Sussman (2005), Evidence for temporally changing mechanical stratigraphy and effects on joint-network architecture, *Geology*, *33*(2), 101–104, doi: 10.1130/G20930.1.

Sharqawy, M. H., J. H. Lienhard V, and S. M. Zubair (2010), Thermophysical properties of seawater: A review of existing correlations and data, *Desalination and Water Treatment*, *16*(1-3), 354–380, doi:10.5004/dwt.2010.1079.

Shaw, D. B., and C. E. Weaver (1965), The mineralogical composition of shales, *Journal of Sedimentary Research*, *35*(1), 213–222.

Simonson, E., A. Abou-Sayed, and R. Clifton (1978), Containment of Massive Hydraulic Fractures, *Society of Petroleum Engineers Journal*, *18*(01), 27–32, doi:10.2118/6089-pa.

Skempton, A. W. (1954), the Pore-Pressure Coefficients A and B, *Geotechnique*, *4*(4), 143–147, doi:10.1680/sposm.02050.0010.

Sondergeld, C., and C. Rai (2011), Elastic anisotropy of shales, *The Leading Edge*, *30(3)*(30(3)), 324–331.

Sone, H., and M. D. Zoback (2013), Mechanical properties of shale-gas reservoir rocks - Part 1: Static and dynamic elastic properties and anisotropy, *Geophysics*, *78*(5), D381–D392, doi: 10.1190/geo2013-0050.1.

Song, J., R. Littke, P. Weniger, C. Ostertag-Henning, and S. Nelskamp (2015), Shale oil potential and thermal maturity of the Lower Toarcian Posidonia Shale in NW Europe, *International Journal of Coal Geology*, *150-151*, 127–153, doi:10.1016/j.coal.2015.08.011.

Su, K., N. Hoteit, and O. Ozanam (2004), Desiccation and Rehumidification Effects On The Thermohydromechanical Behaviour of the Callovo-Oxfordian Argillaceous Rock, *Elsevier Geo-Engineering Book Series*, *2*, 419–424, doi:10.1016/S1571-9960(04)80077-6.

Suarez-Rivera, R., S. Green, J. McLennan, and M. Bai (2006), Effect of Layered Heterogeneity on Fracture Initiation in Tight Gas Shales, in *SPE Annual Technical Conference and Exhibition. Society of Petroleum Engineers.*, doi:10.2118/103327-MS.

Sun, Q., W. Zhang, and H. Qian (2016), Effects of high temperature thermal treatment on the physical properties of clay, *Environmental Earth Sciences*, *75*(7), 1–8, doi:10.1007/s12665-016-5402-2.

Szewczyk, D., A. Bauer, and R. M. Holt (2017), Stress-dependent elastic properties of shales—laboratory experiments at seismic and ultrasonic frequencies, *Geophysics Journal International*, *212*(1), 189–210.

Szewczyk, D., R. Holt, and A. Bauer (2018a), The impact of saturation on seismic dispersion in shales—Laboratory measurements Dispersion in shales—Impact of saturation, *Geophysics*, *83*(1), MR15–MR34.

Szewczyk, D., R. Holt, and A. Bauer (2018b), Influence of subsurface injection on time-lapse seismic: laboratory studies at seismic and ultrasonic frequencies., *Geophysical Prospecting*, *66*(S1), 99–115.

Ten Veen, J., R. Verreussel, D. Ventra, M. Zijp, and T. Boxem (2014), TNO report R10265: Improved sweet spot identification and smart development using integrated reservoir characterization, *Tech. rep.*, TNO.

Ter Heege, J., M. Zijp, S. Nelskamp, L. Douma, R. Verreussel, J. Ten Veen, G. de Bruin, and R. Peters (2015), Sweet spot identification in underexplored shales using multidisciplinary reservoir characterization and key performance indicators: Example of the Posidonia Shale Formation in the Netherlands, *Journal of Natural Gas Science and Engineering*, *27*, 558–577, doi: 10.1016/j.jngse.2015.08.032.

Teufel, L., and J. Clark (1984), Hydraulic Fracture Propagation in Layered Rock: Experimental Studies of Fracture Containment, *Society of Petroleum Engineers Journal*, *24*(1), 19–32, doi: 10.2118/9878-PA.

Thomsen, L. (1986), Weak elastic anisotropy, *Geophysics*, *51(10)*(5), 1954–1966, doi:10.1190/1.1442051.

Trabucho-Alexandre, J. (2015), Organic Matter-Rich Shale Depositional Environments, *Fundamentals of Gas Shale Reservoirs*, pp. 21–45, doi:10.1002/9781119039228.ch2.

Trabucho-Alexandre, J., R. Dirkx, H. Veld, G. Klaver, and P. de Boer (2012), Toarcian black shales in the Dutch Central Graben: record of energetic, variable depositional conditions during an oceanic anoxic event, *Journal of Sedimentary Research*, *82*(4), 258–259.

Tsvankin, I. (2012), *Seismic signatures and analysis of reflection data in anisotropic media*, Society of Exploration Geophysicists.

Underwood, C. A., M. L. Cooke, J. A. Simo, M. A. Muldoon, C. A. Underwood, and M. L. Cooke (2003), Stratigraphic control on vertical fracture patterns in Silurian dolomite, NE Wisconsin, *American Association of Petroleum Geologist Bulletin*, *1*(1), 121–142, doi:10.1306/072902870121.

Vales, F., D. Nguyen Minh, H. Gharbi, and A. Rejeb (2004), Experimental study of the influence of the degree of saturation on physical and mechanical properties in Tournemire shale (France), *Applied Clay Science*, *26*(1-4 SPEC. ISS.), 197–207, doi:10.1016/j.clay.2003.12.032.

Van Bergen, F., M. Zijp, S. Nelskamp, and H. Kombrink (2013), Shale gas evaluation of the early Jurassic Posidonia Shale Formation and the carboniferous Epen Formation in the Netherlands, *AAPG memoir: Chritical assessment of shale resources plays*, (103), 1–24, doi:10.1306/134017221H53468.

van Eekelen, H. (1982), Hydraulic Fracture Geometry: Fracture Containment in Layered Formations, *Society of Petroleum Engineers Journal*, *22*(3), 341–349, doi:http://dx.doi.org/10.2118/9261-PA.

van Gent, H. W., M. Holland, J. L. Urai, and R. Loosveld (2010), Evolution of fault zones in carbonates with mechanical stratigraphy - Insights from scale models using layered cohesive powder, *Journal of Structural Geology*, *32*(9), 1375–1391, doi:10.1016/j.jsg.2009.05.006.

Vanorio, T., T. Mukerji, and G. Mavko (2008), Emerging methodologies to characterize the rock physics properties of organic-rich shales, *The Leading Edge*, *27(6)*(6), 780–787, doi:10.1190/1.2944165.

Vernik, L., and C. Landis (1996), Elastic anisotropy of source rocks: Implications for hydrocarbon generation and primary migration, *AAPG Bulletin*, *80*(4), 531–544.

Vernik, L., and X. Liu (1997), Velocity anisotropy in shales : A petrophysical study, *Geophysics*, *62(2)*(2), 521–532, doi:10.1190/1.1444162.

Vernik, L., and A. Nur (1992), Ultrasonic velocity and anisotropy of hydrocarbon source rocks, *Geophysics*, *57(5)*(5), 727–735, doi:10.1190/1.1443286.

Vernik, L., and M. D. Zoback (1992), Estimation of Maximum Horizontal Principal Stress Magnitude From Stress-Induced Well Bore Breakouts in the Cajon Pass Scientific Research Borehole, *Journal of Geophysical Research*, *97*(B4), 5109–5119, doi:10.1029/91JB01673.

Wang, H. F. (1997), Effects of deviatoric stress on undrained pore pressure response to fault slip, *Journal of Geophysical Research*, *102*(B8), 943–950.

Wang, W., J. E. Olson, M. Prodanović, and R. A. Schultz (2018), Interaction between cemented natural fractures and hydraulic fractures assessed by experiments and numerical simulations, *Journal of Petroleum Science and Engineering*, *167*(March), 506–516, doi:10.1016/j.petrol.2018.03.095.

Wapenaar, C. (1989), *Elastic Wave Field Extrapolation: Redatuming of Single and Multi-Component Seismic Data*, 1–468 pp., Elsevier B.V.

Warpinski, N. R., and L. W. Teufel (1987), Influence of Geologic Discontinuities on Hydraulic Fracture Propagation, *Journal of Petroleum Technology*, *39*(02), 209–220.

Warpinski, N. R., J. A. Clark, R. A. Schmidt, and C. W. Huddle (1981), Laboratory Investigation on the Effect of In Situ Stresses on Hydraulic Fracture Containment, in *SAND-80-2307C; CONF-81051805 Sandia National Labs., Albuquergue, NM (USA)*.

Warpinski, N. R., R. A. Schmidt, and D. A. Northrop (1982), In-Situ Stresses: The Predominant Influence on Hydraulic Fracture Containment, *Journal of Petroleum Technology*, *34*(03), 653–664, doi:10.2118/8932-pa.

Weaver, C. E. (1989), *Clays, muds, and shales*, Elsevier.

Welch, M. J., R. K. Davies, R. J. Knipe, and C. Tueckmantel (2009), A dynamic model for fault nucleation and propagation in a mechanically layered section, *Tectonophysics*, *474*(3-4), 473–492, doi:10.1016/j.tecto.2009.04.025.

Wellington, S. L., and H. J. Vinegar (1987), X-Ray Computerized Tomography, *Journal of Petroleum Technology*, *39*(08), 885–898.

Wentworth, C. K. (1922), A Scale of Grade and Class Terms for Clastic Sediments, *The Journal of Geology*, *30*(5), 377–392, doi:10.1086/622910.

Wong, T. F., C. David, and W. Zhu (1997), The transition from brittle faulting to cataclasic flow in porous sandstones:Mechanical deformation, *Journal of Geophysical Research*, *102*(B2), 3009–3025, doi:10.1029/96JB03282.

Yang, Y., H. Sone, A. Hows, and M. D. Zoback (2013), Comparison of brittleness indices in organic-rich shale formations, in *47th US Rock Mechanics/ Geomechanics Symposium. American Rock Mechanics Association.*, vol. 2, pp. 1398–1404.

Yue, K., J. E. Olson, and R. A. Schultz (2018), Layered Modulus Effect on Fracture Modeling and Height Containment, pp. 1–20, doi:10.15530/urtec-2018-2898691.

Yurikov, A., M. Lebedev, and M. Pervukhina (2018), Water retention effects on the elastic properties of Opalinus shale, *Geophysical propspecting*, *67*(4), 984–996, doi:10.1111/1365-2478.12673.

Zhang, C. L. (2018), Thermo-hydro-mechanical behavior of clay rock for deep geological disposal of high-level radioactive waste, *Journal of Rock Mechanics and Geotechnical Engineering*, *10*(5), 992–1008, doi:10.1016/j.jrmge.2018.03.006.

Zhubayev, A., M. E. Houben, D. M. J. Smeulders, and A. Barnhoorn (2016), Ultrasonic velocity and attenuation anisotropy of shales, Whitby, United Kingdom, *Geophysics*, *81(1)*(1), D45–D56, doi:10.1190/geo2015-0211.1.

Zijp, M., J. Ten Veen, R. Verreussel, J. T. Heege, D. Ventra, and J. Martin (2015), Shale gas formation research: From well logs to outcrop - And back again, *First Break*, *33(2)*(2), 99–106.

Zoback, M. D. (2007), *Reservoir Geomechanics*, 131–134 pp., Cambridge University Press.

Zotz-Wilson, R., T. Boerrigter, and A. Barnhoorn (2019), Coda-Wave Monitoring of Continuously Evolving Material Properties and the Precursory Detection of Yielding, *The Journal of Acoustical Society of America*, *1060*(145), doi:10.1121/1.5091012.

Acknowledgements

This thesis is funded by the Dutch Upstream Gas Top-sector Initiative (project no. TKIG01020) and industry partners Energie Beheer Nederland (EBN), Neptune Energy Netherlands, and Wintershall Noordzee. The project has greatly profited from the involvement of Jan Lutgert, Leo van Borren, and Fred Kluin.

Without the support of Auke Barnhoorn, this thesis would have never existed. I am grateful for your trust, companionship and, above all, thank you for giving me all the freedom I needed to design my own research. Kees Wapenaar, thank you for reading the entire thesis in detail, even though this is not your research area.

The support by David Dewhurst is greatly appreciated. You made it possible that we could perform experiments in CSIRO's Geomechanics and Geophysics laboratory. I am grateful for your guidance during the last two years of my Ph.D. Others from CSIRO Energy have also contributed greatly, in particular Jeremie Dautriat, who have taught me to work with shales in the laboratory, always figured out a new solution when a precious core plug was damaged again, and taught me the most useful French words; Joel Sarout, who explained the theory behind the rock-physical measurements, and reviewed the manuscripts in such detail; and Lionel Esteban who explained the NMR measurements and had his barbecue and pool available at all times. David Nguyen, Shane Kager, and Stephen Firns it was a pleasure, and sometimes challenging, to work with you in the laboratory. Helene Velcin and Camille Cialec, thank you for making my stay in Perth an unforgettable experience. It was a pleasure to work with all of you and I doubt whether I would have been motivated enough to finish my PhD without my stay at CSIRO.

This thesis has benefited greatly from several additional contributions. Part of the results presented in this thesis was obtained by a group of B.Sc. and M.Sc. students at the TU Delft: Jaap Regelink, Faroek Janmahomed, Mutia Primarini, and

Siavash Honardar. Performing laboratory work at the TU Delft would not have been possible without the technical support staff: Marc Friebel, Jolanda Haagen-Donker, Karel Heller, Joost van Meel, Ellen Meijvogel-de Koning, and Han de Visser. Jens van den Berg is thanked in particular for his endless patience when coring mudstone plugs. I very much appreciate the feedback of fellow researchers, such as Maartje Houben, who helped me during the entire four years of my PhD; Quentin Fisher, who discussed (shale) geomechanics over a good bottle of wine; Silvio Giger who also provided core material of the Opalinus shale; and Russell Ewy who provided feedback on the mechanical response and pore pressure evolution. I also value the time and effort put in assessing this thesis and being part of the doctoral committee by David Dewhurst, Alessio Ferrari, Suzanne Hangx, David Bruhn, Giovanni Bertotti, and my promotor and co-promotor.

I would also like to thank those who had an indirect impact on my personal development during my PhD. My fellow team mates of the Imperial Barrel Awards, Axel, Thore, Fu Kai, and Duaa, as well as the excellent group of supervisors, Gerhard Diephuis, Jan de Jager, Harry Doust, and Evert van de Graaff, are thanked for the enjoyable time. I very much appreciate the opportunity given by Sander Hol and Axel Makurat to work in Shell's geomechanics laboratory on rocks other than shales. The staff from the TU Delft who supported me during the years is also thanked, in particular Jan Kees Blom who brought me along to France as a teaching assistant. The support staff is also thanked, in particular Ralf Haak, who spend one hour to search for a fashionable (pink) laptop bag.

I would like to thank my closest colleagues, friends and family, who supported me all in their own way during these four years. Myrna, Karlien, Reuben, Christian, Ranjani, Sixue, Anne, and Richard, thank you for making the time at the TU Delft enjoyable. Juliette, Linda, Faye, and Marianne, many thanks for your lasting friendship and 'mondelinge verslagen'. The serieclub: Loes, Paul, Silvestre, Erik, Nard and Luuk, thanks for the enjoyable Tuesday evenings, even though we are not watching any series. My sisters, Laura and Larissa, and my parents, Maya and Douwe, thank you for your loving support, for listening to my complaints, for taking care of the horses, and so much more. And Finally: Koen, thank you for your endless patience, love and support on the way. You have taught me to push myself further, not to give up, and to always have a sense of humour when things get rough. We did it!

Curriculum Vitæ

Lisanne Aurora Natascha Rosalie Douma

30-05-1991	Born in Groningen, the Netherlands.

Education

2003–2009	Pre-university education (*Economics and Society*) d'Oultremont College, Drunen.
2009–2010	Pre-university education (*Science and Health*) James Boswell Institute (Boswell-Beta), Utrecht.
2010–2013	B.Sc. Earth Sciences Utrecht University, Utrecht.
2013–2015	M.Sc. Earth Sciences (*Earth, Structure, and Dynamics*) Utrecht University, Utrecht. *Thesis:* The effect of evolving grain contact and pore wall area on compaction creep of granular NaCl by pressure solution *Supervisors:* Prof.dr. C.J. Spiers and dr. C. Arson
2015–2020	Ph.D. Applied Geophysics and Petrophysics Delft University of Technology, Delft.

List of publications

Journal publications

[7] Zotz-Wilson, R., **L.A.N.R. Douma**, J. Sarout, J. Dautriat, D.N. Dewhurst, and A. Barnhoorn, Ultrasonic Imaging of the onset and growth of fractures within Partially Saturated Whitby Mudstone using coda-wave decorrelation inversion. *Under review.*

[6] **Douma, L.A.N.R.**, J. Dautriat, J. Sarout, L. Esteban, D.N. Dewhurst, and A. Barnhoorn, The deformation behaviour of the Whitby Mudstone with variable water saturations. *Under review.*
Chapter 5 of this thesis

[5] Boersma, Q.D., **L.A.N.R. Douma**, G. Bertotti, Q.D. Boersma and A. Barnhoorn (2020), Mechanical controls on horizontal stresses and fracture behaviour in layered rocks: a numerical sensitivity analysis, *Journal of Structural Geology*, 130, 103907.

[4] **Douma, L.A.N.R.**, J. Dautriat, J. Sarout, D.N. Dewhurst, and A. Barnhoorn (2019), Impact of water saturation on the elastic anisotropy of the Whitby Mudstone, United Kingdom, *Geophysics*, 85(01), 1-82.
Chapter 4 of this thesis

[3] **Douma, L.A.N.R.**, J.A. Regelink, G. Bertotti, Q.D. Boersma and A. Barnhoorn (2019), The mechanical contrast between layers controls fracture containment in layered rocks, *Journal of Structural Geology*, 127, 103856.
Chapter 7 of this thesis

[2] **Douma, L.A.N.R.**, M.I.W. Primarini, M.E. Houben, and A. Barnhoorn (2017), The validity of generic trends on multiple scales in rock-physical and rock-mechanical properties of the Whitby Mudstone, United Kingdom, *Marine*

and Petroleum Geology, 84, 135-147.
Chapter 3 of this thesis

[1] ter Heege, J., M. Zijp, S. Nelskamp, **L.A.N.R. Douma**, R. Verreussel, J. ten Veen, ..., R. Peters, (2015), Sweet spot identification in underexplored shales using multidisciplinary reservoir characterization and key performance indicators: example of the Posidonia Shale Formation in the Netherlands, *Journal of Gas Science and Engineering*, 27, 558-577.

Conference proceedings

[10] **Douma, L.A.N.R.**, J. Dautriat, J. Sarout, D.N. Dewhurst, and A. Barnhoorn (2019, April), Impact of the degree of saturation on the mechanical behaviour of the Whitby Mudstone. In *Sixt EAGE Shale Workshop.*

[9] **Douma, L.A.N.R.**, J. Dautriat, J. Sarout, D.N. Dewhurst, and A. Barnhoorn (2019, April), The elastic anisotropy of the Whitby Mudstone Formation at varying water saturations. In *Sixt EAGE Shale Workshop.*

[8] Barnhoorn, A., R. Bakker, **L.A.N.R. Douma**, A. Pluymakers, G. Bertotti (2019), Porosity controls the fracturing mode in rocks in unconfined compressive strength tests. *EGU General Assembly 2019.*

[7] **Douma, L.A.N.R.**, J. Dautriat, J. Sarout, D.N. Dewhurst, and A. Barnhoorn (2018), Impact of water saturation on the mechanical properties and elastic anisotropy of the Whitby Mudstone. *SEG EPFL.*

[6] Barnhoorn, A., **L.A.N.R. Douma**, F. Janmahomed, (2018, April), Experimental load cycling in the brittle field produces a more distributed fracture network. In *EGU General Assembly Conference Abstracts* (Vol.20, p.7938)

[5] Houben, M., J, van Eeden, S. Hangx, **L.A.N.R. Douma**, A. Barnhoorn, and M. Drury (2018, April), Impact of mechanical damage on fluid flow in mudstones: matrix versus fracture permeability of deformed Whitby Mudstone (UK). In *EGU General Assembly Conference Abstracts* (Vol.20, p.858)

[4] **Douma, L.A.N.R.**, F. Janmahomed, G. Bertotti, and A. Barnhoorn (2017, August), The influence of rock-mechanical properties on fracture characteristics in finely-layered reservoirs. In *51st US Rock Mechanics/Geomechanics Symposium*, American Rock Mechanics Association.

[3] **Douma, L.A.N.R.**, F. Janmahomed, G. Bertotti, and A. Barnhoorn (2017, April), The propagation of fractures in finely-layeredd reservoir rocks. n *EGU General Assembly Conference Abstracts* (Vol.19, p.6735).

[2] Houben, M., A. Barnhoorn, N. Hardebol, M. Ifada, Q. Boersma, **L.A.N.R. Douma**, ... and M. Drury (2016, December), Porosity, petrophysics and permeability of the Whitby Mudstone (UK). In *AGU Fall Meeting Abstracts.*

[1] **Douma, L.A.N.R.**, M.E. Houben, M.I.W. Primarini, and A. Barnhoorn (2016, May), The effect of temperature and pressure on the rock mechanical behaviour of the Whitby Mudstone Formation, UK. In *Fifth EAGE Shale Workshop.*